Design and Evaluation of Tunable Microstrip Liquid Crystal Devices

Ming Lei

A dissertation submitted in partial fulfilment of the requirements for the degree of

Doctor of Philosophy

of

University College London

Department of Electronic and Electrical Engineering

University College London

April 2019

I, Ming Lei confirm that the work presented in this thesis is my own. Where information has been derived from other sources, I confirm that this has been indicated in the thesis.

Abstract

Liquid crystals (LCs) are a promising microwave material due to their advantages of low voltage tuning, low cost, low power consumption. The first objective of this thesis is to develop a general design method for tunable microstrip devices using LCs working at microwave frequencies for wireless communications. As a second objective, the method was then applied to design, simulate and fabricate three types of filter to achieve different bandwidths and to maximise the tuning range.

A novel general design method for tunable microstrip devices based LCs is first proposed. The design process consists of two stages, the first uses a lumped element modelling and the second, full wave simulation to optimise the dimensions. The design process was tested and verified by designing tunable bandpass filters using ELC (Electric, inductive, capacitive) resonators. Three types of ELC resonators have been designed, simulated and fabricated. The comparison between the simulation and measured results shows that the proposed design method is effective, providing the electric field of the microwave signal is considered and is compatible with the LC switching.

For the second objective, interdigital capacitor (IDC) filters and ring filters were investigated. The IDC filters were designed for 2.4GHz and 5GHz. Compared with LC devices working at 5GHz in the literature, the designed IDC filter using LCs has the largest tuning range. The tunable ring resonators were designed to have compact size and narrow bandwidth so that high frequency selectivity can be realized.

Impact Statement

Due to the increasing demand for new wireless communication applications, there is a trend to integrate multi-band operations into a single device. More specifically, tunable filters allow selection of the multiple frequency bands, which have potential to reduce the size. Liquid crystals (LCs) are a promising microwave material due to their advantages of low cost, low power consumption. The use of LC as a tunable material has been considered in the development of microwave and Terahertz (THz) LCs applications in tunable phase shifters, resonators and filters.

However, there is no clear methodology for a design process that can be widely applied to LC microwave devices based on microstrip configuration. In this thesis, a general design method for tunable microstrip devices using LCs working at microwave frequencies is developed and proposed. The method has been tested and verified by designing and measuring a variety of tunable LC devices, working at 2.4GHz and 5GHz. The proposed design methodology uses standard microwave design software and so can be directly used by other researchers.

As well as the use in academic research, the designed filters can be used for industrial purposes. Nowadays, there are some liquid crystals tuanble bandpass filters available in the market, such as the KURIOS LC tunable bandpass filters by THORLABS and the tunable LC antennas by Merck, which allows them to pick up TV signals in the car. The proposed design method can be directly used by the industry or they can develop their own design procedures based on the proposed design method. Moreover, the LC devices designed and fabricated in this thesis are compact size, and they can be directly used to incorporate into the commercial products.

Acknowledgements

First and foremost, I would like to express my thanks to my supervisor Professor Sally Day for her invaluable guidance, encourage and support through my PhD. I learned a lot from Sally both about the technical issues and professional spirit. She helped me to practice my problem solving skills, critical thinking and logical thinking. She also encouraged me when I failed to deliver the outcome and helped me to analyse the problem. I want to express my thanks again to my supervisor, Professor Sally Day.

I also want to thank Dr Anibal Fernandez for his help in revising the paper. He gave me many valuable suggestions which helped me to publish my first paper successfully. I want to say thank to Dr Chin-Pang Liu for helping to measure my devices.

I would like to thank my colleagues, Dr Mengyang Yang and Mr Zijun Nie. Thank you for doing the modelling of liquid crystal for me so that I have the modelling results to compare with my results.

Lastly, my deepest appreciations go to my beloved parents for their love and support. Without my parents' support in terms of both emotionally and financially, I cannot complete my PhD study. Thank you and I love you. I also want to thank my dearest girlfriend. Thank for appearing to shine my life, supporting and companying me. I Love you.

Table of Contents

List of Figures

List of Tables

Glossary

AC	Alternating current
ADS	Advanced Design System
AFM	Atomic Force Microscope
BPFs	Bandpass filters
BST	Barium strontium titanate
BW	Bandwidth
CR	Cognitive radio
CST	Computer simulation technology
dB	Decibel
DC	Direct current
DUT	Device under test
FBW	Fractional bandwidth
GHz	Gigahertz
ITO	Indium tin oxide
kHz	Kilohertz
L_A	Insertion loss
L_R	Return loss
LCs	Liquid crystals
LTCC	Low temperature co-fired ceramic
MEMS	Microelectromechanical systems
MHz	Megahertz
mm	Millimetre
ms	Microsecond
PCB	Printed circuit board
PDLC	Polymer dispersed liquid crystals
PGMEA	Propylene glycol methyl ether acetate
RPM	Revolutions per minute
PVA	Polyvinyl alcohol
Q	Quality factor
S_{11}	Reflection coefficients
S_{21}	Transmission coefficients
S-parameters	Scattering parameters
SMA	SubMiniature version A
TEM	Transverse electromagnetic
THz	Terahertz
µm	Micron
UV	UltraViolet
YIG	Yttrium-iron-garnet

Chapter 1 Introduction, Motivation and Objectives

1.1 Motivation

Microwave frequencies (300MHz – 300GHz) are widely used in telecommunication systems (satellites, radar, mobile communications and wireless communications), due to the advantages in bandwidth and low interference [Torrecila, 2015]. The demand for communication systems is increasing and becoming complex of integrating multi-functions in one system [Chun, 2008]. The front end devices need to satisfy several functions of communication systems [Chun, 2008], such as working at multi-frequencies, compact size, etc.

Tunable devices, that can realize multiple allocated frequencies in a single device and achieve a tunability ($\frac{\Delta f_c}{f_c}$) of more than 10% for multi-band, have become popular in recent years in modern commnunication systems [Zhang, 2012]. Common applications using tunable filters and resonators include cognitive radio (CR) systems, next generation and 4G/5G smart phones, telecommunication systems, radars and WiFi communication systems [Naglich, 2012; Li, 2015; Nath, 2005; Fouladi, 2013]. Tunable filters used in multifunctional, multiband systems offer a number of advantages over fixed filter solutions over the same multiple bands which include: reduced size, low power consumption, a convenient tuning mechanism while maintaining low loss operation [Nath, 2005; Chaudhary, 2013].

Many types of technology can be used to realize tunable microwave filters and resonators. The methods are generally separated as discrete tuning techniques and continuous tuning techniques. For the discrete tuning, the technologies used are PIN diodes and MEMS switches [Koochakzadeh, 2010; Goldsmith, 1999]. As for the continuous tuning, varactor diodes, MEMs capacitors, mechanical tuning and tunable materials are frequently used [Zhang, 2016; Rebeiz, 2009; Yun, 2002; Li, 2014].

Liquid crystals (LCs) are an example of a suitable tunable material for microwave applications. In the last two decades, liquid crystal materials have been widely used to make electro-optical devices, and flat panel displays [Prost, 1995]. Recently, however, the trend has shifted from optical applications to non-optical applications for LC materials. The anisotropy used to allow electro-optical switching can also be applied to switch the dielectric constant of LC layers used in devices covering other wavelengths (or frequencies in the electromagnetic spectrum). For example, liquid crystal tunable filters, resonators, shifters and antennas for microwave and Terahertz (THz) systems have been reported. This thesis is concerned with the use of liquid crystal layers in microwave devices for communication systems. In the section 1.2, a review is given of different techniques to build tunable devices, and it provides reasonable support to focus the research on designing tunable devices using LCs.

1.2 Tunable Devices at Microwave Frequencies

In this section, different technologies to build tunable devices at microwave frequencies are reviewed and the advantages and disadvantages of each technologies are summarized. The comparison between the technologies makes LCs are suitable alternatives to construct tunable devices at microwave frequencies. Some examples of LC based devices are described so that the objectives of the thesis can be proposed.

1.2.1 Tunable Devices Based on Other Technologies

Mechanical tuning technique is one of the earliest tuning techniques used to build tunable filters and resonators. The mechanical tuning achieves tunability by physically moving a material or tuning screws to tune the resonant frequency [Yun, 2002; Huang, 2009]. Mechanical tuning has the advantages of high quality factor and high power handling capabilities, but their bulky size and low tuning speed are the main drawbacks [Naglich, 2012].

PIN diode is commonly used to realize devices to switch in multiple frequency channels. PIN diode switches have high linearity, good isolation, and enable digital frequency tuning [Koochakzadeh, 2007]. But one of the drawbacks is that the bandwidth of these filters cannot be kept constant during the centre frequency tuning [Koochakzadeh, 2010].

MEMS-based tunable switches and capacitors can be excellent candidates for developing compact, reconfigurable, and tunable RF systems such as mobile phones, radar systems, and wide-band tracking receivers [Goldsmith, 1999; Gu, 2010; Rebeiz, 2009]. MEMS devices mostly use micrometre level movement to obtain a switching or adjust capacitance with the applied dc voltage. They have small size, low loss, and their linearity is high with low signal distortion [Rebeiz, 2003], [Dussopt, 2003], but the driving voltage is very high, which normally ranges from 20V to 100V. There are two different types of frequency-tuning methods for MEMS-based filters, analogue and digital. Analogue tuning is comparatively easy with MEMS varactors and provides continuous frequency variation, but the tuning range has been limited to 5%–15%. For example, the tuning range in [Kim, 1999; Kim, 2002; Abbaspour-Tamijani] is 4.2%, 10%, and 14%, respectively. In digital MEMS filters, discrete centre frequencies and wide tuning ranges are possible to realize. The advantage of digital MEMS filters is that they are less sensitive to bias, and the centre frequency has little change with temperature [Pothier, 2005]. However, existing digital MEMS filters at microwave frequencies do not have enough resolution to result in near continuous coverage of the frequency band [Peroulis, 2001]. The MEMS filter in [Fourn, 2003] shows a filter has a tuning range of 44% but with poor frequency resolution.

Varactor diodes are widely used in the design of microstrip tunable bandpass filters (BPFs) [Long, 2011; Zhang, 2016]. The varactor diode can achieve tuning by varying capacitance as a function of the reverse voltage applied across its p-n junction, and the variable capacitance is inversely proportional to the square root of applied voltage [Varactor, 2018]. Though varactor diodes have the drawbacks of low quality factor, poor linearity, and high driving voltage from 0V to 30V [Genc, 2009], they are widely used for building tunable

filters as they have fast tuning speed, high tunability even at lower microwave frequencies, compact size, low cost and good reliability. [Huang, 2014] uses coupled line filters to achieve a tuning range of 500MHz when the working frequency is designed to 1.8GHz. The tuning range of 1.1GHz is realized in [Boutejdar, 2016], which is designed to work at 5GHz.

1.2.2 Tunable Devices Based on Tunable Materials

Tunable materials, such as ferrites, ferroelectrics and semiconductors, are used to achieve the tunability by using external field in terms of electric or magnetic field to change the permittivity or permeability of the materials [Li, 2014]. However, material loss and high voltage are the particular problems for these tunable materials used in microwave frequencies [Liu, 2015].

YIG (yttrium-iron-garnet) filters, one of the most popular type among the magnetically tunable filters [Fjerstad, 1970; Tsai, 2009], are controlled by the change in ferromagnetic resonance frequency with an externally applied DC magnetic field [Bao, 2008]. The YIG filters have the advantages of a multi-octave tuning range, low insertion loss and high power handling capability; however, they are high power consumption, large in size, difficult to integrate with monolithic microwave-integrated circuits, and their tuning speed is slow (GHz/ms), limiting their use in certain areas[Vendik, 1999].

Ferroelectrics have been widely proposed as an alternative material for tunable filters. The most intensively studied ferroelectric material at room temperature in this application is barium strontium titanate (BST). BST thin-film varactors are small and light, and offer a good tunability and fast tuning speed to nanosecond and have low power consumption [Tsai, 1999]. In addition, ferroelectric devices can have high power handling capability and high linearity, at a cost of high DC tuning voltage [Vendik, 1999]. The relatively high loss of room-temperature microwave devices based on BST tunable filters has been a significant drawback which limits their microwave applications [Tombak, 2002].

1.2.3 Comparison of the Various Tuning Techniques

The advantages and disadvantages of the various tuning techniques are summarized in Table 1.1.

Technology	Advantage	Disadvantage
PIN diodes	high linearity Good isolation Enable digital frequency tuning	Limited phase shift resolution
MEMS	Low loss High linearity	Analogue MEMS: limited tuning range Digital MEMS: Low frequency resolution
Varactor diodes	Large tuning range	High power consumption above 1GHz High bias voltage
YIG	Small in-band insertion loss High power handling capability	High power consumption Large in size Low tuning speed
Ferroelectrics	Large tuning range Low loss	High bias voltage High power consumption

Table 1. 1 Comparison of advantages and disadvantages for different tuning methods

1.3 Liquid Crystal Microwave Devices

Recently liquid crystals have attracted a lot of attention as electrically controllable dielectric media for microwave and Terahertz applications [Schaub, 2011]. In many ways, LCs are ideal for tunable devices. LCs has the advantages such as low cost, broadband operation (several GHz to 100s of

GHz), low voltage requirement, low power consumption, and constant value of group delay [Gennes, 1995; Camley, 2018]. Typical examples are their use in phase shifters, tunable filters, phased array and reflect array antennas. The description of these devices is divided into four main groups: (1) phase shifters and delay lines, (2) resonators, (3) filters. In the next section, liquid crystal tunable devices designed for operation at microwave frequencies are discussed.

1.3.1 Phase Shifters Using LCs

The first microwave devices using LCs was phase shifters in the early 1990s, where [Dolfi, 1993] developed a phase shifter using microstrip line on alumina substrate with K15 LC. Though only a phase shift of 5°/cm at 10.5GHz is reported [Dolfi, 1993], this phase shifter has found the possibility of using LC for microwave devices.

[Martin, 2004] proposes two-phase shifters using inverted microstrip line, and the difference between the two devices are the line topology and the length of the active part. The first device works at the setting frequency of about 1GHz and the active part of the cell is 30mm long. The insertion loss is higher than -4dB and return loss is lower than -10dB. The second device uses a periodic stub-filter line, and the setting frequency is 20GHz. The insertion losses are greater than -5dB and a return loss lower than -10dB. However, the results of both the phase shifter show that these shifters needs to be improved to achieve better return loss, as the return loss in these two devices are too small.

Ring resonator is also used for the compact tunable Ka-band (20GHz~30GHz) phase shifter based on liquid crystal [Moessinger, 2010]. In the cavity, a 100μm thick LC layer is embedded, which is a proper thickness for LCs. The measurement results show that the centre frequency can be shifted in between $f_0 = 33.1\ to\ 35.4GHz$ with the tunability of 6.7%. The operating frequency is 34.32GHz, and a continuously tunable phase shift of $\Delta\varphi$=0 to 117.12°with a DC bias voltage of 0 to 40V. Due to the small size of the ring resonator ($2 *$

$2mm^2$), this resonator can be connected in series and placed within the area of a unit cell employed in reflect-array antennas.

Many phase shifters using LCs are designed to work at higher microwave frequencies. A W-band phase shifter is proposed using liquid crystal as a tunable dielectric layer underneath fixed MEMs bridges [Fritzsch, 2011]. The single unit consists of a CPW (coplanar waveguide) line on a 300um thick fused silica substrate, the ground planes are made of gold layer and the inner conductor is multi-metal layer. The results shows that with using the 14 unit cell of the resonator, it can achieve a phase shift of 92° with 2.4dB insertion loss at 76GHz, The tuning time is around 2ms for increasing and 21.2ms for decreasing the phase shift. The large difference between rise and fall time occurs and is normal for LC devices, as the LC molecule alignment with an electrical field is much faster than the self-alignment process from the alignment of molecules along the surface. In order to increase the response time, polymer dispersed liquid crystals (PDLC) can be employed. This work also shows a possibility use of combining the MEMS and liquid crystal, which might be a good way to combine the MEMS and liquid crystals to design a tunable filter.

Another inverted microstrip structure is used for the phase shifter [Garbovskiy, 2012]. LC W1804 was used with a large Δn and low losses. The phase shift can be changed continuously from 0 to 300°/cm at 110GHz. A phase shift of about 600°/cm at 220GHz can be expected. This phase shifter shows no dispersion over the entire frequency, and due to the speed of delay of 2.5ps/cm, it is a tunable true time delay at all frequencies. It is a very efficient phase shifter, and the continuous shift over the frequency makes it possible to work at even higher frequency with good performance, and it opens the possibilities of using liquid crystal at very high frequency.

1.3.2 Resonators Using LCs

The major objective for the tunable resonators based on LCs is to characterize the liquid crystal materials at microwave frequencies [Camley, 2018]. There

are two techniques can be used to characterize the properties of LCs, the first involving measurement of a resonant circuit and computing the dielectric constant and loss tangent at resonant frequency and the second generating the electromagnetic properties of the scattering parameters which are influenced by replacing dielectric with LCs, respectively [Deo, 2015, Camely, 2018].

The photonic group of UCL and RF & Microwave research lab at Essex have published several papers on characterization of LC properties. [Yazdanpanahi, 2010] use the first method and report a mm-wave planar patch resonator to measure the dielectric constant of LC E7 at 40GHz, which shows good agreement with existing literatures. It is the first time a comparison between using longitudinal and transverse preconditioned surface for the resonator. The second method is used by [James, 2011] who use a strip electrode separated from a ground plane by a dielectric layer. The dielectric properties and loss tangents of several types of LCs are characterized, and agree well with previous literatures. [Deo, 2015] use coplanar waveguide terminals with two dielectric layer microstrip structure to measure the dielectric constants and loss tangents of nematic LCs with 15GHz to 65GHz.

The first method is also used by [Schaub, 2011], who present a method of performing microwave characterizations of nematic liquid crystals using a circular patch resonator and finite-element software. BL006 LC is used over the frequency range of 4.8–8.7 GHz. The computed values for BL006 agree well with those found in the literature. This method benefits from simple resonator construction, straightforward simulations, and accuracy that derives from the finite element's detailed modelling of coupling and geometry of the fabricated device.

A tunable S-band resonator with an operational frequency of 3.5GHz was presented by [Yaghmaee, 2012]. The two sandwiched liquid crystal samples (K15 and GT3-23001) in this resonator allowed for 4% and 8% tuning range, respectively. The results show that the measured frequency moves from 2.93GHz to 2.70GHz with the bias voltage of 0 to 30V, when using GT3-23001.

Another work of [Yaghmaee, 2013] proposes a five-layer tunable bandpass filter operating at a frequency of around 3.0GHz. When using K15 LC, the prototype measurement of tuning range is 4%, compared with the tuning range of 4.4% computed in CST. When using GT3-23001, 8.3% and 8.2% are the tuning range for simulation and measurement. These works suggest new possibilities for applications of LC at even a lower microwave frequencies, for example, it could be used for body-centric communications or WiFi applications which require tunability at a low microwave frequencies. However, the tuning ranges reported in these literatures are relatively small. Using LCs with wider range of dielectric constant might be a good way to increase the tuning range.

1.3.3 Filters Using LCs

Filters are very important components in modern telecommunication systems. However, in spite of the importance, there are not many reported studies of tunable filters based on LCs [Camley, 2018]. The reported tunable filters based on LCs are notch filters and bandpass filters. One of the earliest proposed tunable filters based on LCs is reported by [Bernigaud, 2006]. They use a half wavelength open-circuited stub resonator and a second-order dual behaviours resonator filters to achieve a few percent of tunability at lower microwave frequencies. The advantage of this design is that a LC cavity is drilled in the substrate, which will prevent LC from leaking. It may be a good way to create LC cavity, but it is difficult to control the thickness of drill, and thicker layer of LCs decrease the response time of LCs. Also, if the surface is damaged by the drill, it is difficult to maintain a flat surface for the alignment layer. Another liquid crystal tunable bandpass filter is presented by [Goelden, 2010]. The proposed three-pole filter designs to work at around 20GHz, and it can achieve a tuning range of 2GHz, which corresponds to a tunability of 10%. Due to the metallic loss, the insertion loss is rather high. Therefore, the measured results are not so close to the simulated results.

Tunable coupled microstrip line filter is also used for bandpass filter [Yazdanpanahi, 2012], which is based on parallel-coupled line structure. This

filter has been developed with an operational frequency of 33GHz, and the E7 liquid crystal employed in this structure demonstrates the frequency tuning of up to 2GHz. As the first tunable parallel-coupled microstrip lines filter based on liquid crystal, the main drawback of this design is that the insertion loss needs to be significantly improved.

Except for the high microwave frequencies using tunable filters based on LCs, lower microwave frequencies has also drawn researchers' attention. In order to achieve higher tunability, dual-mode technology, which can realize a two pole filter with only one (physical) resonator, is used in the design of microwave bandpass filters due to its advantages in size and compactness [Torrecilla, 2013]. The filter central frequency has been tuned from 4.54GHz to 5.19GHz, and tuning range relative to the central frequency is 13.4%. Though the tuning range is good, the resonant bandwidth is very wide, which may lead to poor frequency selectivity.

Not only can liquid crystal be used for bandpass filters, but also notch filters can employ liquid crystal. The research group from University Carlos III de Madrid has reported several studies about bandstop filters using LCs. It is a band-rejection filter with a narrow stopband and it is based on inverted microstrip line technology. Conventional microstrip line structure is not compatible to use as the LCs devices, since a cavity is needed to contain LCs. Therefore, using inverted microstrip is a good alternative to use for LC devices. The rejection frequency of the notch filter is from 4.85GHz to 4.45GHz, with the tunability of 9%. The stopband filter attains a rejection of about 24dB which remains almost constant as the voltage is increased from 0 to 15 Vrms. It used the thickness of 250μm for the spacer, and this thick layer can decrease the tuning speed of LCs. The thickness of around 100μm of LCs layer is preferred to use. A spiral structure [Torrecilla, 2013] is also used for tunable notch filter based on liquid crystal, which provides a reduction of the device size with respect the conventional spurline topology. The liquid crystal used is nematic liquid crystal, 1631E, which dielectric constant and losses are unknown. The results indicate that the centre frequency f_0= 3.75 to 3.40GHz with the voltage of 0 to 12 Vrms. The tunability is 9.8%. The dielectric constant of this LCs is

approximately known by comparing the measured results and simulation results to find out the corresponding dielectric constant. This method is an easy way to get to know some characteristics of the LCs used in this paper.

[Skuski, 2013] propose a tunable microwave band stop filter which is based on the use of inverted microstrip line technology. It used the liquid crystal 1825 produced at the Military University of Technology in Warsaw. The tuning range of this filter is 275MHz when the bias voltage changes between 0V and 6V. LCs with lower dielectric loss can be used to obtain narrower stop bands.

1.3.4 Consideration for Optimizing the Performance of Liquid Crystal Devices

In order to optimize the performance of liquid crystal based tunable microwave devices, there are some factors need to be considered [Camley, 2018]

1. The thickness of the microstrip line needs to be considered. In order to optimize the performance, the thickness of the line should be chosen at least 3 times bigger than the skin depth.

2. The dielectric substrate used to support the microstrip line needs to be low loss microwave materials. Rogers Duroid materials are chosen to use in this project due to their low loss at microwave frequencies.

3. The losses associated with the devices and liquid crystals materials are important factors. Though LC has relatively low loss, but it is not zero loss in microwave region. The loss tangent of LCs varies from 0.001 to 0.09.

4. The driving voltage to switch the LC directors is important. Using AC voltage is preferred.

5. The tuning speed of LC is also important. Thicker layer of LC

increases the response time of LCs. Therefore, the proper thickness is needed to allow fast switching.

All of the considerations need to be evaluated and optimized so that best performance of the LC based devices can be achieved [Camley, 2018].

1.4 Objective of the Thesis

Based on the literature review demonstrated above, the primary motivation and objective of this thesis is to design tunable resonators and filters using liquid crystals for modern wireless communication systems. In the design of LC devices, the LC layer requires a ground plane to apply the modulating voltage to control the dielectric constant to provide the frequency tuning. This requirement of the LC layer make the microstrip configuration the most compatible. The motivation and objective help to divide the task into two research objectives as follows.

1. A novel general design method for tunable microstrip devices using LCs needs to be proposed and verified. The design method can be used as a guide to design tunable microstrip devices using LCs at microwave frequencies.

2. Another goal of this thesis is to design, fabricate and measure of different types of tunable devices and applications using LCs at microwave frequencies. The proposed design method is used to design the different types of LC devices.

1.5 Organization of the Thesis

This section presents the organization of the thesis. In this chapter, the motivation, relevant literatures about technologies to realize tunable devices at microwave frequencies are studied, followed by the objectives of the thesis.

In Chapter 2, in order to realize the objectives of the thesis, the theories behind tunable microstrip resonators and filters using LC are investigated. The tuning mechanism of how LC directors responds to the external bias voltage and how to model LCs in full wave simulations are explained in the first section. Since the thesis focuses on designing tunable resonators and filters, the parameters used to measure the performance of the resonators and filters are studied. With the understanding of LCs, the inverted microstrip structure is determined to use to build LC devices as this structure is compatible to use for LC devices with the advantages of containing a cavity for LCs and can apply external voltage to switch LCs. The frequently used microstrip discontinuities are demonstrated in the last section.

In Chapter 3, the fabrication process of tunable devices based on LCs are stated. Different methods to pattern electrodes have been investigated and the different methods have been chosen to use for this thesis with the consideration of the resolution for the devices. The assemble process and LCs injection have also been studied to make sure LCs are well sealed in the devices and bubbles in LCs should be avoided. The measurement setup is also described, which is used to measure all the fabricated devices in the thesis.

In Chapter 4, the novel general design method for tunable microwave LC devices based on microstrip configurations is proposed. The design process consists of lumped element modelling and full wave simulation, respectively. The approximation of using LCs as homogeneous anisotropic materials is also checked by comparing the electric field at resonant frequency from full wave simulation and the detailed switching of LC directors from an in-house finite element modelling package.

Chapter 5 focuses on testing and verifying the general design method stated in Chapter 4. Three types of tunable resonators using electric capacitive inductive (ELC) resonators are designed, simulated and fabricated. The comparison between the results shows that the proposed novel general design

method is correct and effective to use. Therefore, this design method is used for the following designs.

In order to satisfy the second objective of the thesis, Chapter 6 and 7 focus on designing different types of tunable resonators for different use. In Chapter 6, the tunable resonators are designed with using the interdigital capacitors (IDCs). The tunable resonators are designed to work at 2.4GHz and 5GHz, respectively. The tunable resonator using IDC at 5GHz has the largest tuning range, compared with other tunable resonators and filters using LCs in the literature. In Chapter 7, the ring resonators are used to design tunable resonators with narrow bandwidth. The tunable resonator using ring resonator also have the advantages of narrow bandwidth, good return loss and low insertion loss. However, compared with tunable resonator using IDCs, the size is relatively bigger.

Finally in Chapter 8, the work in the thesis is summarized, and the future work of the research is also presented.

Chapter 2 Background of LCs and Microstrip Lines

In the previous chapter, the objectives of the thesis are determined to be developing a general design method for tunable microstrip devices using LCs and to design and build different types of tunable resonators and filters. Therefore, in this chapter, it is important to understand the considerations and basic theories for designing tunable devices using LCs. In order to understand how LC can be used as the tuning layer to realize tunable devices, in the first section, the types of LCs to use and how LCs are switched by external voltage to realize tuning are explained. After understanding the principle behind LC switching, the LC response time, which affects the choice of the thickness of LC cavity and how to calculate the tunability are explored. Next, how to model LCs in the full wave simulation software at unswitched and switched state are explained. Based on different situations, LCs can be simulated as a single block or multiple blocks.

Microwave filters are the devices designed and built in this project. The background description of microwave filters is stated, and most of them can be treated as a two-port network. Under this context, the scattering parameters and how to use the parameters to quantify the performance of the microwave filters are explained. The quality factor of the microwave resonators, another important parameter, is used to illustrate the performance in terms of the filter selectivity. Transmission line technology is chosen to realize the filter design with the considerations of achieving high quality factors and the compatibility with LC devices.

The requirements of the LC layer leads to the fact that inverted microstrip lines are best suited to use to design the LC devices, which is a special configuration of microstrip line, is introduced. It allows to form the cavity to contain LCs between ground plane and electrode structures and makes it easy to apply external voltage to switch the LCs. In the last section, some types of microstrip discontinuities, frequently used in microstrip structure, are described.

2.1 Properties of Liquid Crystal

Liquid crystals are mesophases between solid/crystalline and liquid/isotropic [Gennes, 1995]. The constituents of LCs are organic molecules with rod-like or disk-like shapes. The size of the LC molecules is typically a few nanometres [Gennes, 1995]. At higher enough temperatures, the molecules of LCs are in the isotropic liquid state, and they do not have positional and orientational order. The molecules easily moves around and behaves like regular liquid [Kelker, 1980]. When the temperature is decreased, it transforms into the nematic phase, which has orientational order but no positional order [Kelker, 1980].When the temperature is decreased further, the molecules may transform into smectic phase, where there is orientational order and partial positional order [Kelker, 1980]. The nematic LCs are the most commonly used LCs for displays and used at microwave frequencies, because of their suitability for thick layers, cheapness and compactness [Bahadur, 1992]. In this project, only the nematic LCs are used.

2.1.1 Nematic Liquid Crystal

The ‘nematic’ is derived from Greek which means thread, and it represents the appearance of this crystalline phase under crossed polarisers [Bahadur, 1992]. Though the molecules in this state can still diffuse around, the average direction of the long axis of a molecule is well defined [Chigrinov, 1999]. The average direction of the long molecular axis is denoted by $\vec{n}$, which is a unit vector called the liquid crystal director [Chigrinov, 1999]. The short axis of the molecules do not have orientational order and so nematic LCs are uniaxial.

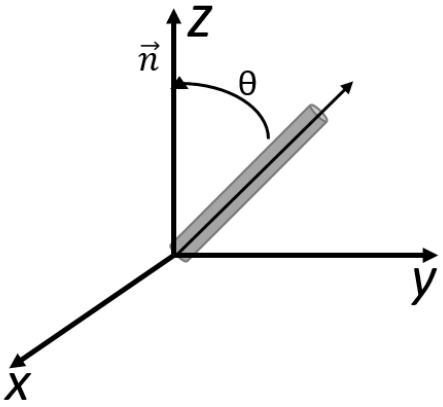

Figure 2. 1 Schematic diagram showing the orientation of rod-like molecules

A diagram of the orientation of the rod-like molecules is shown in Figure 2.1. The z axis is chosen parallel to $\vec{n}$. The order parameter S describes quantitatively how the LC is arranged and it is the average over a large number of molecules and is defined as [Kelker, 1980]:

$$S = \langle \frac{3cos^2\theta - 1}{2} \rangle \qquad 2\text{-}1$$

θ is the angle between a molecule at a given instant and the director orientation $\vec{n}$. The angled brackets indicate an average over a large number of molecules. When S=0, there is no orientational order, which means a randomly aligned material, for example, the isotropic state [Yaghmaee, 2013]. When S=1, all the molecules are parallel to the director [Yaghmaee, 2013]. The typical values for the order parameter as a liquid crystal is 0.9 above the solid-nematic transition temperature, going down to 0.3 when the temperature rises to below the nematic-isotropic transition [Kelker, 1980].

2.1.2 Tuning Mechanism and Dielectric Anisotropy of LC

As explained previously, the nematic LCs is uniaxial and in order to define the permittivity of LCs, two permittivity values described as $\varepsilon_{r\parallel}$ and $\varepsilon_{r\perp}$ are defined, which correspond to the parallel and perpendicular directions of the LC director [Garbovskiy, 2011]. The parallel and perpendicular directions are the directions between the director $\vec{n}$ and to direction of the applied electric field.

The LCs are initially aligned with the alignment layers which fix the LC directors and along the desired direction without voltage applied.

As shown in Figure 2.2(a), when LCs are pre-aligned with alignment layer and no voltage applied, the director $\vec{n}$ is parallel to the metallic layers which contains the LCs and presents a dielectric permittivity of $\varepsilon_{\mathrm{r}\perp}$ to electric fields applied between the electrodes, and known as the perpendicular state. The effective relative permittivity is $\varepsilon_{eff} = \varepsilon_{\perp}$, since directors orient parallel to the metallic layer and perpendicular to the direction of the applied electric field. In this case, the permittivity tensor is defined as

$$\underset{\varepsilon_{\perp}}{\leftrightarrow} = \begin{pmatrix} \varepsilon_{\parallel} & 0 & 0 \\ 0 & \varepsilon_{\perp} & 0 \\ 0 & 0 & \varepsilon_{\perp} \end{pmatrix} \qquad 2\text{-}2$$

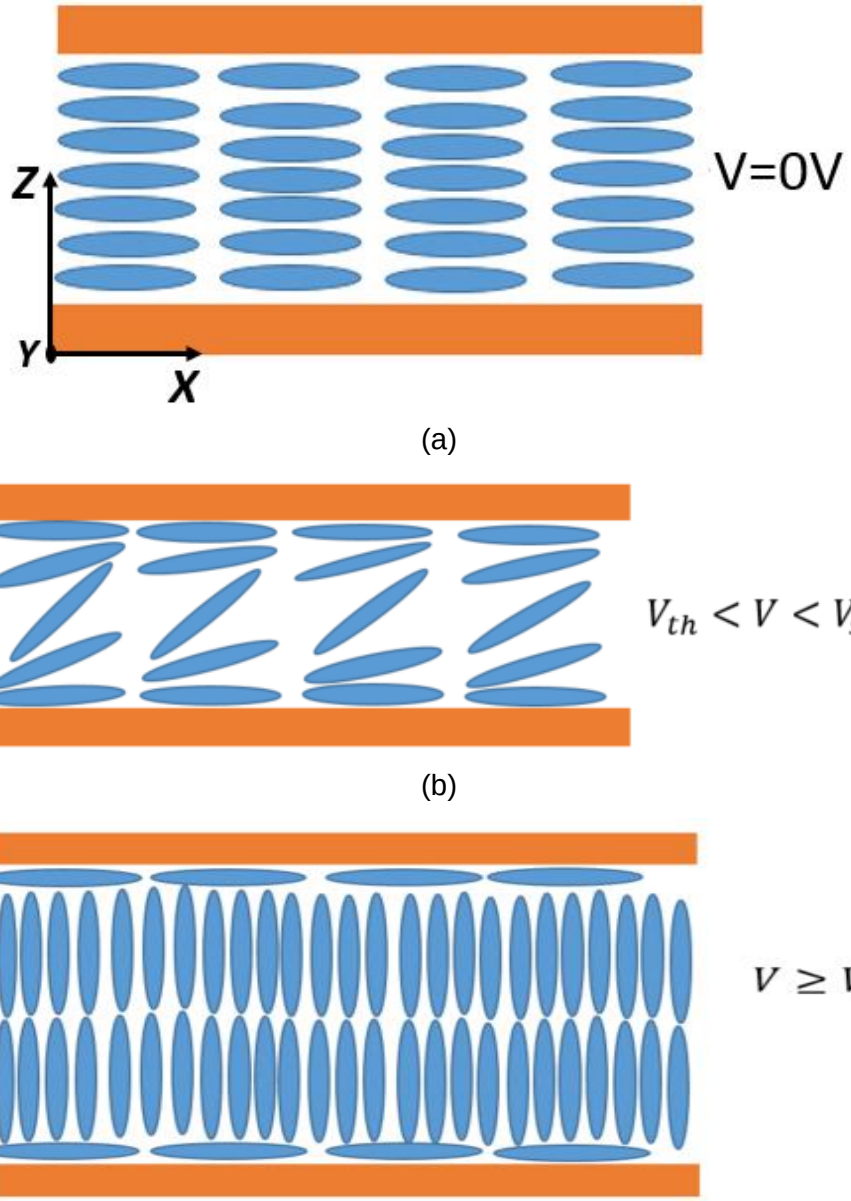

Figure 2. 2 Liquid crystal molecule orientation at (a) No voltage applied and with alignment layer (b) Voltage applied, but not reach the saturation voltage (c) At the saturation voltage

As the bias voltage V starts to increase to pass the threshold voltage and not reach the saturation voltage, the LC directors start to continuously switch from perpendicular to parallel state, as shown in Figure 2.2(b). The dielectric anisotropy $\Delta\varepsilon$ is the difference between the perpendicular and parallel state and can be expressed as [Yaghmaee, 2013]

$$\Delta\varepsilon = \varepsilon_{\parallel} - \varepsilon_{\perp} \qquad 2\text{-}3$$

The permittivity tensor in this state can be described as

$$\overleftrightarrow{\varepsilon} = \begin{pmatrix} \varepsilon_{\perp} + \Delta\varepsilon\sin^2\alpha & 0 & \Delta\varepsilon\sin\alpha\cos\alpha \\ 0 & \varepsilon_{\perp} & 0 \\ \Delta\varepsilon\sin\alpha\cos\alpha & 0 & \varepsilon_{\perp} + \Delta\varepsilon\cos^2\alpha \end{pmatrix} \quad 2\text{-}4$$

where the α is the average angle between the molecule axis and the director $\vec{n}$. The dielectric anisotropy $\Delta\varepsilon$ can be positive or negative. In this thesis, due to better performance at microwave frequencies, the LCs with positive dielectric anisotropy are used, where $\varepsilon_{r\parallel}$ is generally greater than $\varepsilon_{r\perp}$. For nematic LCs, it is easier to spin around the long molecular axis than to rotate around a short molecular axis [Chigrinov, 1999], which means that the characteristic frequency for $\varepsilon_{\perp}$ is higher than the characteristic frequency for $\varepsilon_{r\parallel}$ [Chigrinov, 1999].

When the saturation voltage is reached, most of the LC directors are parallel to the direction of electric field and perpendicular to the metallic layers. This is generally referred to as the parallel state as shown in Figure 2.2(c). In this state, the relevant effective permittivity (ε_{eff}) becomes $\varepsilon_{\parallel}$, and the permittivity tensor at this state can be expressed as

$$\underset{\varepsilon_{\parallel}}{\leftrightarrow} = \begin{pmatrix} \varepsilon_{\perp} & 0 & 0 \\ 0 & \varepsilon_{\perp} & 0 \\ 0 & 0 & \varepsilon_{\parallel} \end{pmatrix} \quad 2\text{-}5$$

Upon removal of the voltage, the LC returns to the direction defined by the surface alignment. This is achieved by the elastic constants, which are the parameters describe the restoring forces on the director with a liquid crystalline phase. The three types of distortion in the director field, splay, twist and bend, leads to three elastic constants of K_{11}, K_{22} and K_{33}, and more description of these elastic constants can be found in [Prost, 1995]. When removes the voltage, the defined direction is restored by the elastic forces originating at the surface between the liquid crystals and the alignment layers.

Figure 2.3 shows the switching and change of permittivity with different bias voltages. The LCs has a threshold voltage V_{th}, above which the reorientation of the LC molecules take place [Prost, 1995]. After the threshold voltage, there is a sharp rise in the permittivity until the fully saturation voltage is reached. Above the saturation voltage, the permittivity almost remains unchanged.

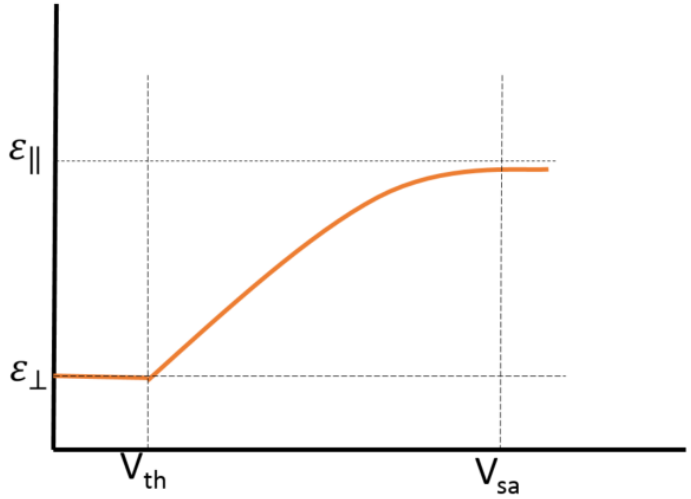

Figure 2. 3 Permittivity of LC versus bias voltage change

As discussed above, when applying the external voltage to the LC layer, the effective permittivity has a continuous variation from perpendicular to parallel states. The permittivity at perpendicular and parallel state can be used as the effective permittivity to achieve tuning. Based on this tuning mechanism, LC is compatible to be used to design tunable devices. The larger the dielectric anisotropy, the larger tuning range can be achieved.

2.1.3 Response Time

The LC director response time τ can be expressed using the following equations [Prost, 1995]

$$\tau_{on} = \frac{4\pi\gamma_1 d^2}{\Delta\varepsilon V^2 - 4\pi^3 K_i} \quad 2\text{-}6$$

$$\tau_{off} = \frac{\gamma_1 d^2}{K_i \pi^2} \quad 2\text{-}7$$

where γ_1 is the rotational viscosity, *d* is the thickness of the LC layer, V is the applied external voltage, $\Delta\varepsilon$ is dielectric anisotropy, K_i is elastic constant

corresponding to different electrooptical effect. For nematic LCs, the response times are proportional to d^2.

As can be seen from the equation 2-6 and 2-7, thickness *d* of the LC layer affects the response time of LCs, especially when using thick layer of liquid crystal, the response time will become very slow [Garbovskiy, 2011]. If it is required to use a thick layer of LCs and the switching time is not slowed, the polymer network, such as the polymer dispersed liquid crystals (PDLC) are considered to use. PDLC is not a new phase like smectic or nematic, it is simply a different way of packaging the LCs.

The most common PDLC is polymer dispersed nematic liquid crystal, and the director configuration inside a nematic droplet is determined by the droplet shape and size, the anchoring condition on the droplet surface and the externally applied field, as well as the elastic constants of the liquid crystal [Yang, 2006]. The high electric field might be a disadvantage of using PDLC, because it requires a higher voltage compared with using normal liquid crystals, which uses voltage up to tens of volt. Compared with normal liquid crystal, the external voltage used for PDLC will be higher and it will be around 50V.

2.1.4 Tunability and Tuning Range of LC Microwave Devices

The continuous variation of the effective permittivity between perpendicular and parallel states is achieved by the continuous change in the bias voltage. As discussed above, the changes in permittivity results in the changes of resonant frequency. The performance of the tunable devices can be measured with the tunability and tuning range, which quantitatively describe the maximum tuning of the devices and are useful to directly compare the performance of the devices working at same frequency range. The tunability can be expressed as a function of the highest and lowest resonant frequencies f_h and f_l as [Yaghmaee, 2013]

$$Tunability = \left(\frac{f_h - f_l}{f_h}\right) * 100\% \qquad 2\text{-}8$$

or

$$Tunability = \left(\frac{f_h - f_l}{f_l}\right) * 100\% \quad \text{2-9}$$

depending on which frequency is the reference frequency.

2.1.5 Modelling of LC in Full Wave Simulation

LCs have different effective dielectric constant, and they are anisotropic material. Therefore, LCs can be modelled with electromagnetic simulation software as a material with varied permittivity and loss tangent based on the switching of the LC directors. In most cases in this project, LCs are reasonable to be modelled as a single block of homogenous anisotropic material, which is clearly explained in Chapter 4. As shown in Figure 2.4 (a) and (b), the LCs between the two metallic layers are simulated as homogeneous anisotropic material in both unswitched and switched state, and the values for these states can be found using equation 2-2 and 2-5.

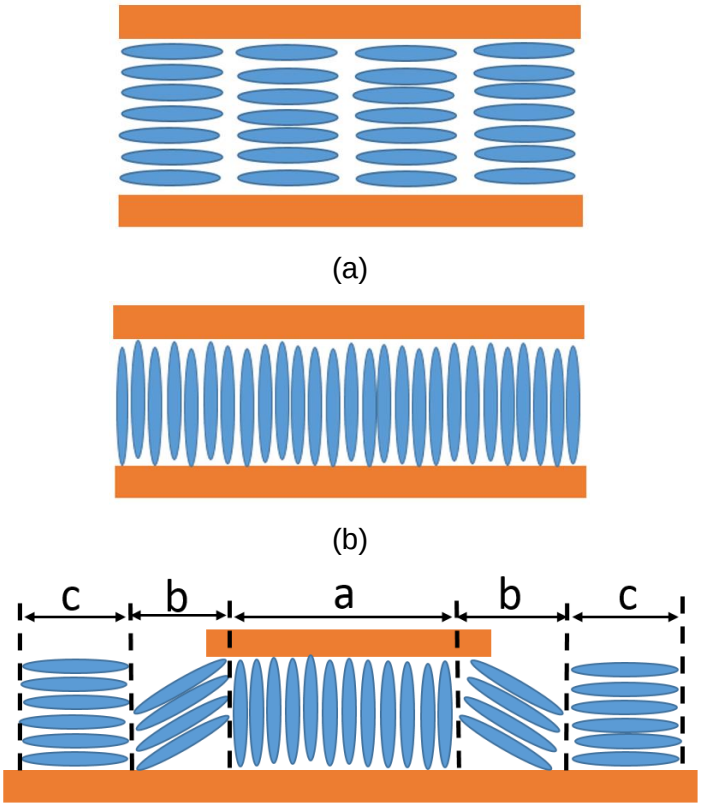

Figure 2. 4 The modelling of LC director at (a) unswitched state using single block (b) switched state using single block (c) switched state using multiple blocks

For the edge of the electrodes at the switched states, LCs can be modelled in a different way. Figure 2.5 shows the detailed switching of LC directors at switched case for the edge of electrodes using in house finite element modelling package-QLC3D [Deo, 2015]. Figure 2.5 shows that beyond the edge of the electrodes, the LC is only partially switched contributing to a lowering of the effective permittivity for this region. In this situation, the LC region can be divided into several homogeneous parts. In this thesis, as shown in Figure 2.4(c), the LCs are divided into three parts a, b and c, which corresponds to fully switched, partial switched and no switch. In the part a, most of the directors are fully switched and the value used for part a can be found with equation 2-2. In the part b, LCs are partially switched, and the permittivity can be found with equation 2-4, where the angle θ is defined as $\alpha = 45°$. In the part c, LCs are not affected by the electric field, which means the LC directors do not switch. The value used for this situation can be found with equation 2-5.

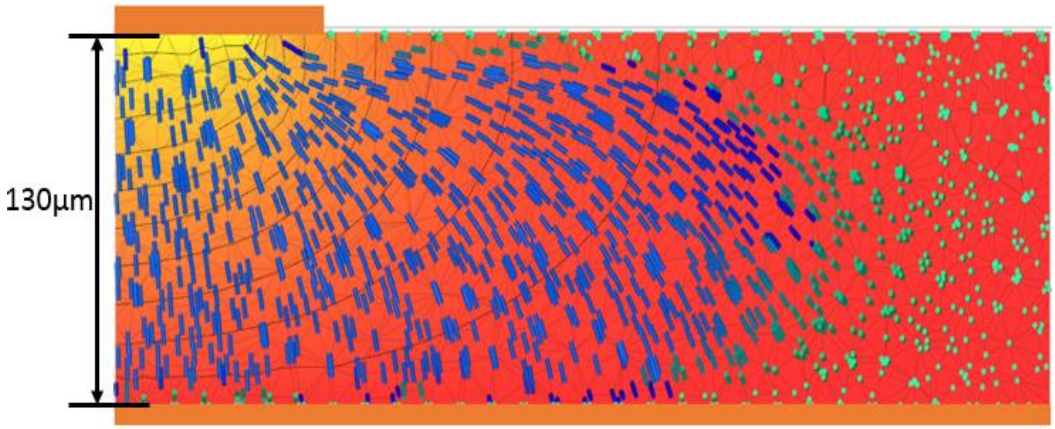

Figure 2. 5 The LC directors distributions for the switched state at the edge of electrodes. The thick brown lines added to the pictures indicate the position of the electrodes. The ground electrode covers the whole of the bottom surface. Ground plane is the bottom layer, and its size is 40×32mm. Top electrode is half of the IDC fingers, it is around 0.15mm.

2.2 Overview of Microwave Resonators and Filters

Filters are an important and frequently occurring part of the modern communication systems. A filter is a frequency selective device, and it usually has two ports. From the input to output port, a filter can pass through the

desired frequency band and reject the undesired frequency [Temes, 1973]. There are five types of filters, which are lowpass filter, bandpass filter, bandstop filter, highpass filter and all-pass filter. Lowpass filters can serve as a prototype to design many practical filters with frequency and element transformations. Based on different transfer functions, there are different kinds of responses, such as Chebyshev response, Butterworth response and Quasi-elliptic response [Temes, 1973].

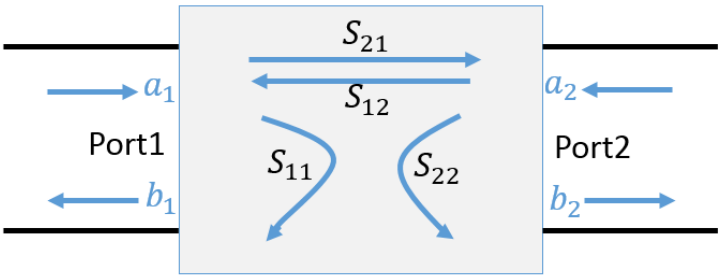

Figure 2. 6 S-parameters for two port network

At microwave frequencies, most resonators and filters can be represented as a two-port network shown in Figure 2.6. It is difficult to measure the voltage and current at microwave frequencies, therefore, the scattering parameters (S-parameters) are introduced to measure the performance of the resonators and filters at microwave frequencies. The S-parameters are obtained when there is perfect impedance matching at both input and output ports [Poole, 2015]. The S-parameters are transmission and reflection coefficients and S_{12} and S_{21} are the transmission coefficients and S_{11} and S_{22} are the reflection coefficients. In this thesis, the resonators and filters are reciprocal and symmetric two-port network, thus $S_{12} = S_{21}$ and $S_{11} = S_{22}$. These S-parameters can be expressed as a function of the ratio of the power between the input and output of a two-port network. The a_1 is the power entering port 1 and leaves as the power of b_2 at port 2. Any power a_2 entering the output port, such as the reflection, leaves port 1 as the power of b_1. The matrix containing the S-parameters is referred to as the scattering matrix and can be written as

$$\begin{bmatrix} b_1 \\ b_2 \end{bmatrix} = \begin{bmatrix} S_{11} & S_{12} \\ S_{21} & S_{22} \end{bmatrix} \begin{bmatrix} a_1 \\ a_2 \end{bmatrix} \quad \text{2-10}$$

The measurement of the S-parameters can reflect the performance of the designed microwave resonators and filters. In particular, the insertion loss (L_A) and return loss (L_R) derived from S-parameters are the parameters which are important in filter characterization. These two losses are given in decibel (dB) with the logarithm operation is base 10.

The insertion loss is the ratio of the power leaving output port 2 and the power entering input port 1. The insertion loss occurs if there is impedance mismatch at the input or output of the filter, or the dissipative loss with each reactive element [Poole, 2015], and L_A can be expressed as

$$L_A = 20log|S_{21}|dB = 10log\frac{b_2}{a_1} \quad \text{2-11}$$

The value of the insertion loss should be very low in the passband and very high at reject band. The acceptable loss will depend on the applications. For bandpass filter, there is no specific value that the insertion loss should be less than, but the insertion loss should be as small as possible. As shown in Figure 2.7, which shows a typical filter response for the bandpass filters with the S-parameters, the S_{21} indicates an insertion loss of 0.05dB at resonant frequency.

The return loss is the ratio of the power reflected at port 1 and the power entering at port 1. It happens when mismatching the impedance between components, and it is determined by the material properties and dimensions of the structures, and L_R can be expressed as [Poole, 2015]

$$L_R = 20\log|S_{11}|dB = 10log\frac{b_1}{a_1} \quad \text{2-12}$$

The L_R measures how much power is reflected for the device. For bandpass filters, the return loss should be high at the passband frequency and low at the reject frequency. The larger value for the return loss indicate a better quality for the device. The S_{11} shown in Figure 2.7 has a return loss of -26dB at the resonant frequency of 4.9GHz.

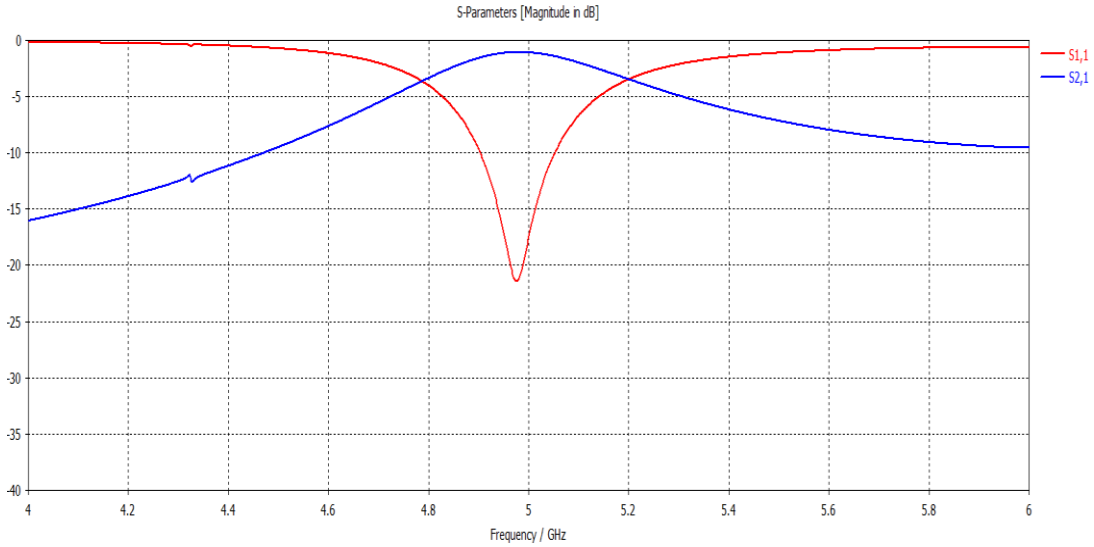

Figure 2. 7 A typical filter response of the bandpass filters with S-parameters

In order to design a tunable filter with good performance, not only do the insertion loss and return loss need to be considered, but also the frequency selectivity of the filter needs to be considered. The selectivity can be measured by the quality factor (Q), and it is defined as the ratio between the centre frequency (f_0) of the filter and the 3dB bandwidth (*BW*) for a single resonator ($Q = \frac{f_0}{BW}$). If a filter has a high Q, it is narrowly selective.

Distributed elements and transmission lines can be used to design devices at microwave frequencies while maintaining high quality factor [Hong, 2004]. In order to be compatible with the LC device structures, transmission lines, more specifically, microstrip lines are the most appropriate structures to use to design the LC devices.

2.3 Microstrip Lines Used for LC Devices

Microstrip line is one of the most widely used transmission lines for designing microwave devices, it is used to design resonators [Hong, 2000; Hong, 1996], phase shifters [Osadchiy, 2003; Weil, 2002], antennas [Varadan, 1999], and filters [Swanson, 2007; Yi, 2009], etc.

2.3.1 Microtrip Line Structure

A microstrip transmission line consists of a conductive strip of width *W* and thickness of *t* and a ground plane, separated by a dielectric layer (substrate) of thickness of *h*, and the dielectric constant of ε_r as shown in Figure 2.8 [Bahl, 1977]. Using microstrip technology, it is possible to mount all the active components on the top of the board [Bahl, 1977]. If the dielectric substrate is thin ($h \ll \lambda$), the electromagnectic field can be modelled as a quasi-TEM wave, and it simplifies the analysis of microstrip line [Poole, 2005].

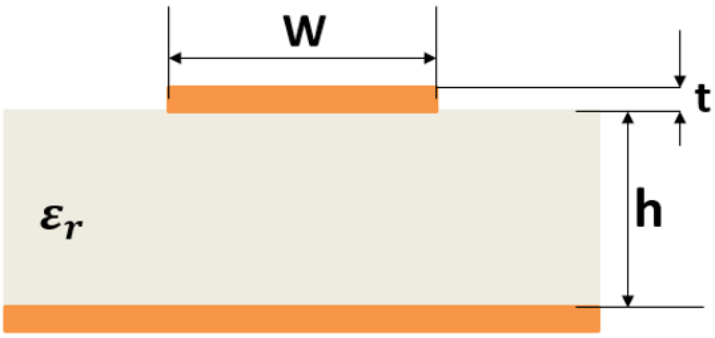

Figure 2. 8 Microstrip structure

The transmission characteristics of the microstrip line are described by two parameters, namely, the effective dielectric constant ε_{eff} and characteristic impedance Z_0. According to [Bahl, 1977], the design equations for microstrip line are as follows

The guided wavelength is

$$\lambda_g = \frac{c}{\sqrt{\varepsilon_{eff}} f_0} = \frac{\lambda}{\sqrt{\varepsilon_{eff}}} \qquad 2\text{-}13$$

The effective dielectric constant

$$\varepsilon_{eff} = \frac{\varepsilon_r+1}{2} + \frac{\varepsilon_r-1}{1\sqrt{1+12(\frac{h}{W})}}, \ \frac{W}{h} > 1 \qquad 2\text{-}14$$

$$\varepsilon_{eff} = \frac{\varepsilon_r+1}{2} + \frac{\varepsilon_r-1}{2}\{\left[1+12\left(\frac{h}{W}\right)\right]^{\frac{-1}{2}} + 0.04(1-\frac{h}{W})^2\}, \ \frac{W}{h} < 1 \qquad 2\text{-}15$$

The characteristic impedance Z_0 is found as follows if width (W) of the microstrip and thickness (h) are known [Bahl, 2003]

For high impedance $\frac{W}{h} < 1$

$$Z_0 = \frac{\eta}{2\pi\sqrt{\varepsilon_{eff}}} \ln\left(\frac{8h}{W} + \frac{W}{4h}\right) \quad 2\text{-}16$$

For low impedance $\frac{W}{h} > 1$

$$Z_0 = \frac{\eta}{\sqrt{\varepsilon_{eff}}} \{W/h + 1.393 + 0.677ln(W/h + 1.444)\}^{-1} \quad 2\text{-}17$$

Where $\eta = 120\pi$ ohms in the wave impedance in free space.

However, if the microstrip line is to be designed with a particular impedance, then for a given h, the width *W* is calculated by following equations. With the h, ε_r and Z_0 already known, rough estimate of the necessary ratio of W/h to achieve the desired impedance [Bahl, 2003] is found. If the estimated W/h ratio is >2, then the low impedance design equations are used, and if the W/h ratio is ≤ 2, then the high impedance design equation are used.

For low impedance ($\frac{W}{h} > 2$)

$$\frac{W}{h} = \frac{2}{\pi}[B - 1 - \ln(2B - 1) + \frac{\varepsilon_r - 1}{2\varepsilon_r}(\ln(B - 1) + 0.39 - \frac{0.61}{\varepsilon_r})] \quad 2\text{-}18$$

$$B = \frac{377\pi}{2Z_0\sqrt{\varepsilon_r}} \quad 2\text{-}19$$

For high impedance ($\frac{W}{h} \leq 2$)

$$\frac{W}{h} = \frac{8e^A}{e^{2A} - 2} \quad 2\text{-}20$$

$$A = \frac{Z_0}{60}\sqrt{\frac{\varepsilon_r + 1}{2}} + \frac{\varepsilon_r - 1}{\varepsilon_r + 1}(0.23 + \frac{0.11}{\varepsilon_r}) \quad 2\text{-}21$$

2.3.2 The Inverted Microstrip Line Structure

For the microstrip line shown in Figure 2.8, it is not possible to contain the liquid layer which makes it incompatible with LC devices. Therefore, in order to use the transmission line to design LC devices, the inverted microstrip structure is employed. It is compatible to use as it is convenient to use spacers to form the cavity between the dielectric substrate supporting microstrip

structures and the ground plane to contain the LCs. The detailed inverted microstrip structure is shown in Figure 2.9.

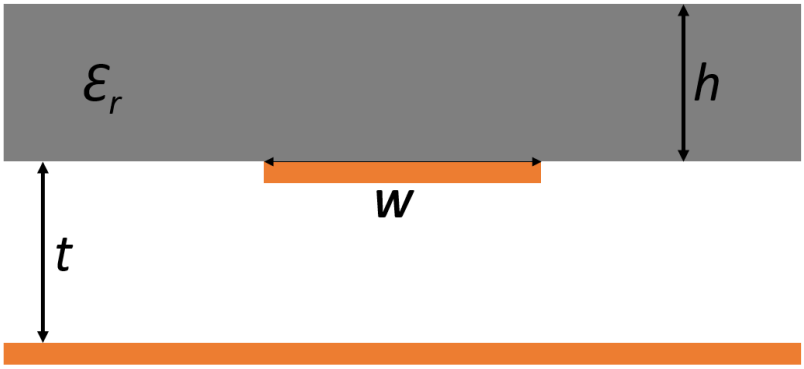

Figure 2. 9 The typical structure of inverted microstrip line

As shown in Figure 2.9, the typical inverted microstrip structure consists of a conductor electrode with the width of *W*, which is supported by the dielectric substrate with the thickness of *h* and the dielectric constant of ε_r and the thickness *t* between electrode and ground plane.

The effective dielectric constant ε_{eff} and the characteristic impedance Z_0 of the inverted microstrip line can be determined considering the width of the electrode *w*, the thickness of the substrate h, the dielectric constant ε_r and the thickness t of the material filled in the gap between electrode and ground plane. The expression for ε_{eff} is presented as [Bahl, 2003], where the dielectric constant in the gap is assumed to be air:

$$\varepsilon_{eff} = 1 + \frac{h}{t}((0.5173 - 0.1515ln\frac{h}{t})^2 - (0.3092 - 0.1047ln\frac{h}{t})^2 ln\frac{t}{h})(\sqrt{\varepsilon_r} - 1) \quad 2\text{-}22$$

The characteristic impedance Z_0 of the inverted microstrip structure is calculated as:

$$Z_0 = \frac{60}{\sqrt{\varepsilon_r}} \ln[t\left(\frac{6+(2\pi-6)e^{-\left(30.666\frac{t}{w}\right)^{0.7528}}}{w}\right) + \sqrt{1+(\frac{2t}{w})^2}] \quad 2\text{-}23$$

The equation for the effective dielectric constant of the inverted microstrip line is not suitable to use in LC devices, as it does not account for the dielectric constant between the strips and ground plane. Since it is also a quasi-TEM wave propagation, it is suitable to calculate the effective dielectric constant of inverted microstrip line using the equations for normal microstrip lines.

2.3.3 The Configuration of Inverted Microstrip Structure Compatible with LC Devices

The configuration of the specific inverted microstrip structure used in this project is shown in Figure 2.10. As can be seen from Figure 2.10, in order to make the device compatible with LC technology, the surface of microstrip electrodes and ground plane are separated by the spacer to form the cavity for containing the LC material. The spacer is made by another thin dielectric layer. Another piece of dielectric substrate is used to support the ground plane so that a low frequency voltage applied between microstrip electrodes and ground plane can be used to control the LC orientation. SMA connectors are used to connect the microstrip input to the resonator or filter, and make it easier to integrate into other microwave systems.

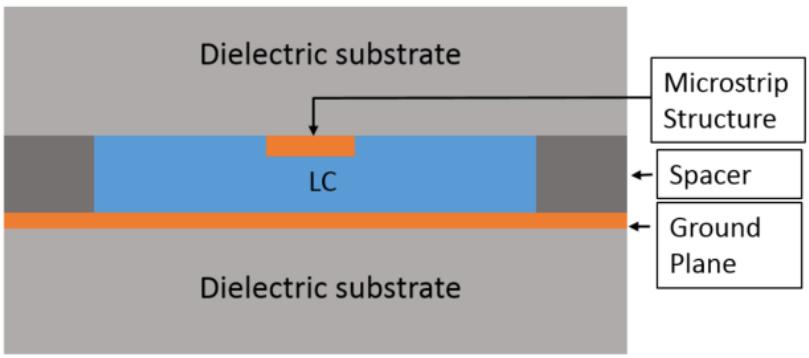

Figure 2. 10 Cross section view of the inverted microstrip (Not drawn to scale)

2.3.4 Microstrip Discontinuities

A complete understanding and design of microstrip circuits require characterization of various discontinuities included in the circuit [Poole, 2005]. A discontinuity in a microstrip is caused by an abrupt change in the geometry

of the strip conductor [Wadell, 1991]. Therefore, electric and magnetic field distributions are modified near the discontinuity. The change in electric field distribution gives rise to a change in capacitance, and the change in magnetic field distribution is expressed by an equivalent inductance. In this way, the discontinuities in microstrip can be expressed by capacitance and inductance, which means lumped elements can be used to analyse these discontinuities.

Microstrip discontinuities are commonly encountered in the layout of practical filters include steps, open-ends, bends, gaps and junctions [Hong, 2004]. Figure 2.11 illustrates some typical structures and their equivalent circuit. Closed-form expressions for equivalent circuit models of these discontinuities are useful when appropriate, and some typical ones are given as follows where h is the thickness of the substrate. The equations for these discontinuities can be used for both the normal microstrip line and inverted microstrip line.

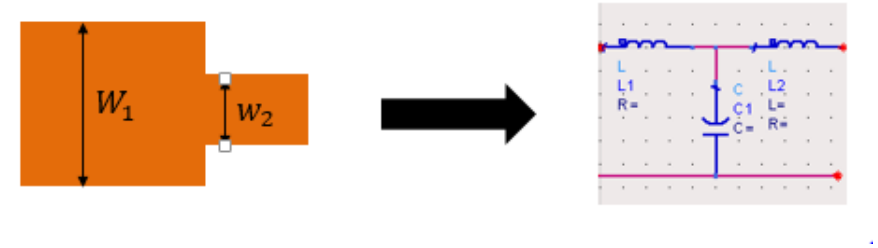

(a)

(b)

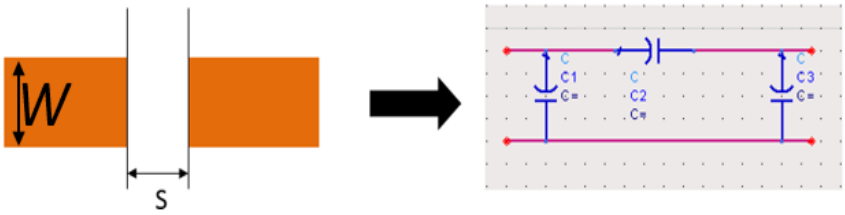

(c)

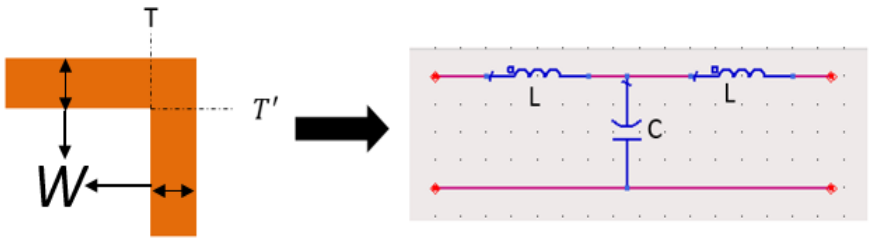

(d)

Figure 2. 11 Microstrip discontinuities: (a) step; (b) open-end; (c) gap; (d) bend

2.3.4.1 Steps in Width

For a symmetrical step, the capacitance and inductances of the equivalent circuit indicated in Figure 2.11(a) may be approximated by the following formulation [Gupta, 1996]

$$C = 0.00137h\frac{\sqrt{\varepsilon_{eff}}}{Z_0}\left(1-\frac{W_2}{W_1}\right)\left(\frac{\varepsilon_{eff}+0.3}{\varepsilon_{eff}-0.258}\right)\left(\frac{\frac{W_1}{h}+0.264}{\frac{W_1}{h}+0.8}\right) \quad 2\text{-}24$$

$$L_1 = \frac{L_{w1}}{L_{W1}+L_{W2}}L \quad 2\text{-}25$$

$$L_2 = \frac{L_{w2}}{L_{W1}+L_{W2}} L \quad \text{2-26}$$

$$L_{wi} = Z_{0i} \frac{\sqrt{\varepsilon_{effi}}}{C} \quad \text{2-27}$$

$$L = 0.000987h(1 - \frac{Z_{01}}{Z_{02}} \sqrt{\frac{\varepsilon_{eff1}}{\varepsilon_{eff2}}})^2 \quad \text{2-28}$$

Where L_{wi} for i=1,2 are the inductances per unit length of the appropriate microstrips, having widths W_1 and W_2, respectively. While Z_{0i} and ε_{effi} denote the characteristic impedance and effective dielectric constant corresponding to width W_i, c is the light velocity in free space, and h is the substrate thickness in micrometers.

2.3.4.2 Open Ends

At the open end of a microstrip line with a width of W, the fields do not stop abruptly but extend slightly further due to the effect of the fringing field. This effect can be modelled either with an equivalent shunt capacitance C_p or with an equivalent length of transmission line ∆l, as shown in Figure 2.11(b). The equivalent length is more convenient for filter design. The relation between the two equivalent parameters may be found by [Edwards, 1992]

$$\Delta l = \frac{C Z_0 C_p}{\sqrt{\varepsilon_{eff}}} \quad \text{2-29}$$

where c is the light velocity in free space. A closed-form expression for ∆l/h is given by (Kirschning, et. al, 1981)

$$\frac{\Delta l}{h} = \frac{\xi_1 \xi_3 \xi_5}{\xi_4} \quad \text{2-30}$$

Where

$$\xi_1 = 0.43907 \frac{\varepsilon_{eff}^{0.81} + 0.26(\frac{W}{h})^{0.8544} + 0.236}{\varepsilon_{eff}^{0.81} - 0.189(\frac{W}{h})^{0.8544} + 0.87} \quad \text{2-31}$$

$$\xi_2 = 1 + \frac{(\frac{W}{h})^{0.371}}{2.35\varepsilon_r + 1} \quad \text{2-32}$$

$$\xi_3 = 1 + \frac{0.5374 tan^{-1}[0.084(\frac{W}{h})^{\frac{1.9413}{\xi_2}})}{\varepsilon_{eff}^{0.9236}} \quad \text{2-3}$$

$$\xi_4 = 1 + 0.037 tan^{-1}\left[0.067\left(\frac{W}{h}\right)^{1.456}\right]\{6 - 5\exp[0.036(1-\varepsilon_r)]\} \quad \text{2-34}$$

$$\xi_5 = 1 - 0.218\exp(\frac{-7.5W}{h}) \quad 2\text{-}35$$

The accuracy is better than 0.2% for the range of $0.01 \leq \frac{W}{h} \leq 100$ and $\varepsilon_r \leq 128$.

2.3.4.3 Gaps

A microstrip gap can be represented by an equivalent circuit, as shown in Figure 2.11 (c). The shunt and series capacitances *Cp* and *Cg* may be determined by [Gupta, 1996]

$$C_p = 0.5C_e \quad 2\text{-}36$$

$$C_g = 0.5C_o - 0.25C_e \quad 2\text{-}37$$

where

$$\frac{C_o}{W}\left(\frac{pF}{m}\right) = (\frac{\varepsilon_r}{9.6})^{0.8}(\frac{s}{W})^{m_o}\exp(k_o) \quad 2\text{-}38$$

$$\frac{C_e}{W}\left(\frac{pF}{m}\right) = 12(\frac{\varepsilon_r}{9.6})^{0.9}(\frac{s}{W})^{m_e}\exp(k_e) \quad 2\text{-}39$$

with

$$m_o = \frac{W}{h}[0.619\log\left(\frac{W}{h}\right) - 0.3853] \quad 2\text{-}40$$

$$k_o = 4.26 - \frac{1}{453\log(\frac{W}{h})}, 0.1 \leq W \leq 1.0 \quad 2\text{-}41$$

$$m_e = 0.8675 \quad 2\text{-}42$$

$$k_e = 2.043(\frac{W}{h})^{0.12}, 0.1 \leq W \leq 0.3 \quad 2\text{-}43$$

$$m_e = \frac{1.565}{(\frac{W}{h})^{0.16}} - 1 \quad 2\text{-}44$$

$$k_e = 1.97 - \frac{0.03}{\frac{W}{h}}, 0.3 \leq W \leq 1.0 \quad 2\text{-}45$$

Those accuracy of these expressions is within 7% for $0.5 \leq \frac{W}{h} \leq 2$ and $2.5 \leq \varepsilon_r \leq 15$.

2.3.4.4 Bends

Right-angle bends of microstrip may be modelled by an equivalent T-network, as shown in Figure 2.11(d). [Gupta, 1996] have given closed-form expressions for evaluation of capacitance and inductance:

$$\frac{C}{W}(pF/m) = \frac{(14\varepsilon_r+12.5)\frac{W}{h}-(1.83\varepsilon_r-2.25)}{\sqrt{\frac{W}{h}}} + \frac{0.02\varepsilon_r}{\frac{W}{h}} \quad for\ \frac{W}{h} \leq 1 \qquad 2\text{-}46$$

$$\frac{C}{W}(pF/m) = (9.5\varepsilon_r + 1.25)\frac{W}{h} + 5.2\varepsilon_r + 7.0 \quad for\ \frac{W}{h} > 1 \qquad 2\text{-}47$$

$$\frac{L}{h}\left(\frac{nH}{m}\right) = 100\{4\sqrt{\frac{W}{h}} - 4.21\} \qquad 2\text{-}48$$

The accuracy on the capacitance is quoted as within 5% over the ranges of $2.5 \leq \varepsilon_r \leq 15$ and $0.1 \leq \mathrm{W/h} \leq 5$. The accuracy on the inductance is about 3% for $0.5 \leq \frac{W}{h} \leq 2.0$.

2.4 Conclusion

In order to design tunable bandpass LC filters, in the first part of this chapter, the tuning mechanism of LCs and how to model LCs in the full wave simulation software are studied. As stated in Chapter 1, the second objective of this thesis is to design and build different types of tunable bandpass filters. In the second part of this chapter, a brief introduction of microwave bandpass filters is given. The parameters used to measure the filters' performance are also explained. Next, with the understanding of how to use LCs as the tuning material, the microstrip line technology, specifically the inverted microstrip line, is compatible to use to design the tunable bandpass filters since a cavity for LCs can be created in the inverted microstrip structure. In the last section of this chapter, the microstrip discontinuities, which are frequently used in designing microstrip structures, are described.

Chapter 3 Fabrication and Measurement Setup of Microwave Liquid Crystal Devices

Precise manufacture of microwave liquid crystal devices is important for the performance of the devices. The process of manufacturing of the microwave devices can be described in terms of two stages, first the patterning electrodes and second the assembly of the devices. In the stage of patterning electrodes, there are some criteria to meet. Devices working at low and high microwave frequencies require different resolution for the devices' structures, and lower microwave frequencies may require high resolutions, for example, the devices stated in Chapter 7 requires the minimum gap of 10μm. The flatness of the substrate after patterning electrodes is another consideration, as the LC devices need flat substrates to deposit a good alignment layer for the LCs. Stability and reproducibility are also important considerations in producing electrodes. In the first section of this chapter, based on the criteria, developing and testing methods to pattern electrodes with different resolutions are stated. The physical processes, such as milling and laser cutting which directly remove the unwanted part of the materials, are tested with the criteria. The chemical process which includes the traditional etching methods and a new possible method using Microplotter to directly pattern the photoresists are tested. The second section considers the assembly process: how to make the alignment layer; how to fill LC without bubbles; and the choice of connectors based on the working frequency. In the last section, the detailed setup to measure the devices are stated.

3.1 Overall Process of Fabrication of Microstrip LC Devices

The overall procedure of the fabrication are stated as follows

1. *Electrodes patterning and spacer patterning*. In the section 3.2, how to develop the specific methods and process to pattern the electrodes on the dielectric substrates are stated.

2. *Substrate preparation and sealing the device.* What material is used as the alignment layer, how to make the alignment layer and the method for rubbing are explained in section 3.3.1

3. *LC injection.* How to put the LC in the cavity without bubble is very important, and it is explained in 3.3.2.

4. *Connect to proper connectors.* The choices of the connection depend on the working frequency and the choice is stated in 3.3.3.

3.2 Methods and Process of Producing Metallization Pattern

The precision of the patterning can be measured under the microscope, and the results are compared with the designed dimensions to make sure the structures are precisely fabricated. The resolution is depended on the designed structures, and different resolution may need to use different methods to make. The stability can be observed with the success rate in producing the structures. The physical processes, such as milling and laser cutting are tested first, followed by the chemical process, such as the possible new method using Microplotter and the traditional etching method.

The materials used in this project are Roger Duroid 5880, and it has the dielectric constant of 2.2, substrate's thickness of 0.79mm and thickness of copper of 35µm. The low dielectric loss of this material makes it very suitable to use for high frequency applications where dispersion and losses need to be minimized [Rogers, 2018]. It is also resistant to all solvents and reagents normally used in etching process [Rogers, 2018].

3.2.1 Milling

Milling is the most common method to be used to create a variety of features on a part of the material by cutting away the unwanted material [Koenigsberger,

2013]. The milling can work at different scales from small to large, and the highest resolution the milling machine can achieve is 0.01mm.

There are two major classes of milling process [Koenigsberger, 2013]:

1. Face milling. In face milling, the cutting action occurs primarily at the end corners of the milling cutter. Face milling is used to cut flat surfaces into the workpiece, or to cut flat-bottomed cavities.

2. Peripheral milling. In peripheral milling, the cutting action occurs primarily along the circumference of the cutter, so that the cross section of the milled surface ends receiving the shape of the cutter. In this case, the blades of the cutter can be seen as scooping out material from the work piece. Peripheral milling is well suited to the cutting of deep slots, threads, and gear teeth.

In this project, the Roland Modela Pro II MDX-540E to cut the electrodes. With the advent of computer numerical control [Beck, 1997], milling machines can automatically change the tools to cut. Therefore, the milling process is a very simple process as follows:

1. The structure is drawn with Diptrace, which is a specific software for PCB manufacture. The designed structure will be stored and exported as the DXF file for the milling machine to use.

2. The DXF file is imported into the milling machine.

3. The milling machine will automatically cut the structure.

4. Check the structure with microscope to find whether it meets the satisfaction.

Though the milling machine is very easy to use, there is one main drawback which makes it not suitable for the fabrication process. The cut electrodes were checked under microscope, and it was found that the milling machine removed not only the surface but also the substrate. However, for LC devices, a flat substrate surface is needed to deposit the alignment layer for the LCs. Therefore, milling is not recommended to use in the project as it damaged the substrate for the material used in this project.

3.2.2 Laser Cutting

Laser cutter works by directing the output of a high-power laser through optics [Wang, 2008]. The focused laser beam is directed at the material, which then either melts, burns, vaporizes away [Wang, 2008], leaving well defined sharp edge corner finish.

The LPKF ProtoLaser U3 is the laser cutter used in this thesis, and this laser cutter is an ultraviolet system with a 20µm focused beam diameter for processing printed circuit boards, as shown in Figure 3.1 [LPKF, 2016]. This laser cutter can etch circuitry, drill holes, and depanel PCBs all in a single step [LPKF, 2016]. It can deal with a variety of PC board substrates [LPKF, 2016], such as FR4, fired ceramics, green and co-fired LTCC, flexible and rigid-flex materials, high-frequency and microwave materials (Rogers TMM, RT/duroid, etc.).

Figure 3. 1 The LPKF ProtoLaser U3

The process of using laser cutter is as follows:

1. The patterns of electrodes are drawn through CST Microwave Studio and exported as the gerber file.
2. The gerber file is then imported into the CircuitMaster, which is a software from LPKF to generate the automatic cutting process. After generating the automatic cutting process, the LMD file is exported for use.
3. The LMD file is imported into the LPKF CircuitPro, which is the software to control the The LPKF ProtoLaser U3 laser cutter. After the LMD file importing, what needs to be cut and how to finish the cutting are set.
4. The board to be cut needs to be put in the reference position to fix the position for board, and the laser works based on the reference position. The reference positions are clearly labelled in the working plate.
5. The laser cutter finishes the cutting job automatically, except for the temperature of the laser cutter. The working temperature for the laser cutter should be kept no higher than 27º, which is shown on the screen.
6. After the cutting process, the board needs to be cleaned with a standard vacuum machine and the structures are then checked with microscope to see whether the cut matches the requirements.

With the excellent reproducible of the structures, laser cutter is considered to have good stability. The patterned electrodes and spacers are shown in Figure 3.2. As can be seen from the Figure 3.2, compared with the designed dimensions indicated in the following chapter, the patterned electrodes show very good precision. The measured results for Figure 3.2(a) are 0.51mm for the lines and 0.2mm and 0.5mm for the gap, where the designed dimensions are 0.5mm, 0.2mm and 0.5mm. These observations and results make the laser cutting a very suitable method to pattern electrodes. However, due to the size of laser beam of 20µm, for the purpose of accuracy of the gaps and lines, this laser cutter should not be used to cut gaps or lines which are less than 20µm. Small features may be possible and results are dependent on copper/metal thickness and substrate type. Therefore, when dealing with small size devices which requires the gaps or lines smaller than 20µm, the laser cutting is not recommended to use. For the spacers, laser cutter can be used to cut all the spacers as spacers do not have dimensions less than 20µm.

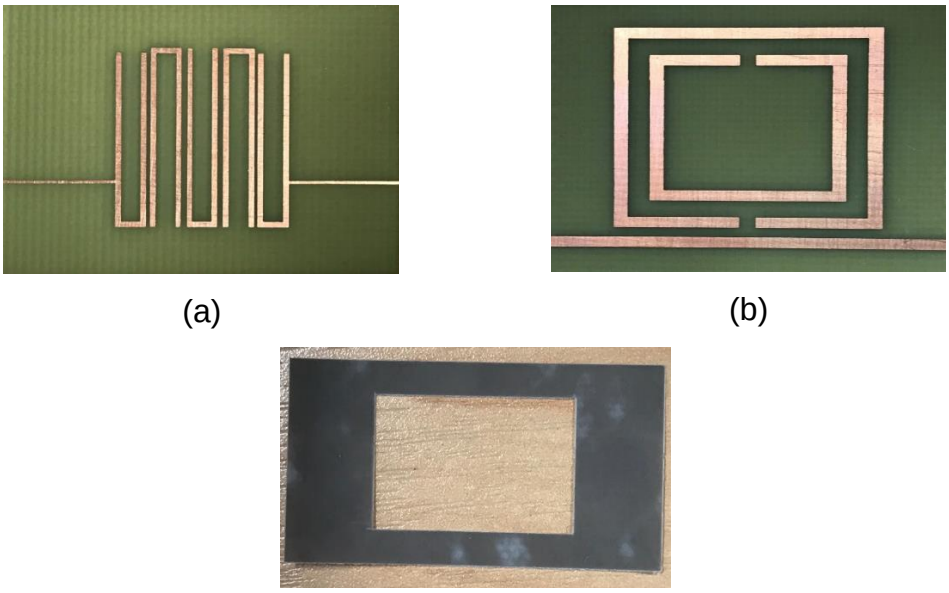

(a) (b)

(c)

Figure 3. 2 Patterned structures using laser cutter (a) Hairpin resonator (b) Split ring resonator (c) spacers using Rogers Duroid 5880

3.2.3 Patterning Photoresist for the Etching Process

Etching is not only suitable to work with resolution smaller than microns, but can also deal with very thin surface without damaging the substrate [Lei, 2012]. In order to pattern gaps or lines smaller than 20 μm, the use of etching is considered. The conventional method of patterning electrodes using etching is to use a metal or plastic mask with the printed patterned on the photoresist, which allows the illumination of UV light to cure the photoresist and protect the pattern under the photoresist. Once the photoresist is cured under the UV light, etching is used to remove the unprotected part of the metal surface and leave the wanted patterns. However, making masks with high resolution takes time to produce, therefore, a method to directly print photoresist on the surface without using masks is developed and tested.

3.2.3.1 Introduction of Microplotter

GIX microplotter manufactured by Sonoplot was considered to be a good alternative method to replace the masking process which can print the photoresist directly on the copper with the required patterns. The microplotter is a leading-edge tool which is used for microarrays, polymer electronics, and other applications which require precise and accurate dispensing of extremely small liquid volumes, such as a few microns [Lei, 2012]. This system can deposit discrete spots or continuous traces such as lines or arcs onto any planar surface with a wide range of solutions [Lei, 2012].

Figure 3. 3 GIX Microplotter

This microplotter consists of a positioning system, which contains printhead and optics system already mounted, iMac control computer with keyboard and

a wireless mouse, and control electronics, as shown in Figure 3.3. The positioning system can create features in the area as small as 5μm wide. And it can print liquid with viscosity of less than 450cP, and anything having more viscosity will not be printed from the glass capillary.

3.2.3.2 Experimental Results

In order to test whether microplotter is suitable to use for patterning structures, both small and large size structures, such as several microns tens and tens of millimetre are designed and tested. The photoresist S1818 from Shipley is mixed with its solvent PGMEA from Sigma Aldrich is chosen to meet the viscosity requirement to use, and this mixture is used to draw the patterns directly on the copper. The processes of using Microplotter are as follows:

1. The structures are drawn with Sono draw, which is the build-in software of microplotter.
2. The drawn structures are imported into the Sono guide, which is the software to control the microplotter. After loading the structures, the proper position to absorb solutions (photoresist mixtures) and the position of the board to draw are set for the microplotter.
3. With the pre-set data, the printing job can be finished automatically.
4. The printed patterns is then etched using the method stated in 3.2.4 and checked with microscope and Atomic Force Microscope (AFM).

Three types of the filters and resonators structures are designed and drawn with Microplotter, and Figure 3.4 and 3.5 are the designed structures and the correponding structures after etching. The dimensions for the three structures excluding the feed lines shown in Figure 3.4(a), (b) and (c) are 14mm×14mm, 18mm×18mm and 15mm×15mm. Compared the (a) in Figure 3.4 and 3.5, the electrodes are not precisely patterned, where the patterned central plates are not parallel and not constant width. Figure 3.5(b) shows a discontinuity gap in the line and different width of the lines, which are not what they designed in Figure 3.4(b). While Figure 3.4(c) shows different gap width and different line width, and the corner of the microstrips are not perpendicular. Based on the

comparison between the three structures, microplotter is not suitable to use for structures with tens of millimeters.

(a) (b) (c)

Figure 3. 4 Designed patterns (a) ELC resonator (b) edge coupled filter (c) split ring

(a) (b) (c)

Figure 3. 5 Patterned electrodes using Microplotter (a) (b) (c) are the correponding strctures in Figure 3.4

As millimeter scale structures are not suitable to print with the microplotter, small scale structures, such as several microns, are also designed and tested to find out whether it is suitable for several structures with microns. Seperate lines and meander line structure, as shown in Figure 3.6, are designed, patterned and etched. The etched pattern are then checked with Atomic Force Microscopy (AFM) to measure whether the width matches the width designed.

(a) (b)

Figure 3. 6 Designed patterns with microns (a) separate lines (b) meander line

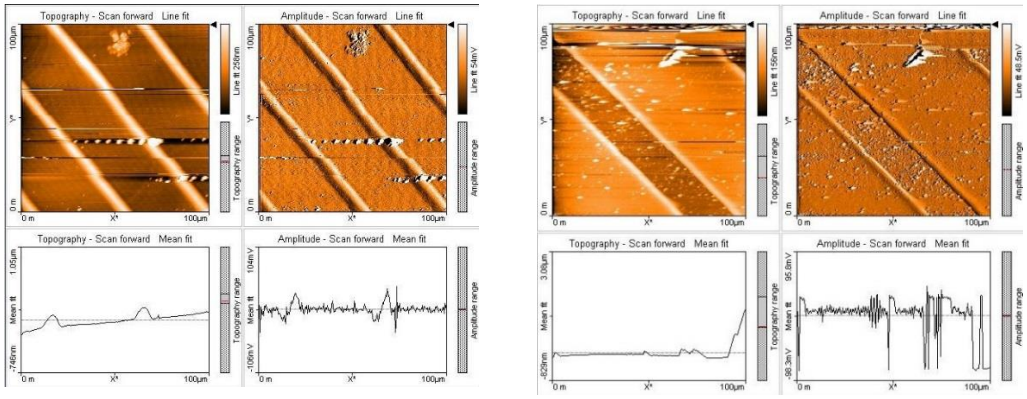

(a) (b)

Figure 3. 7 AFM results of printed patterns (a) Separate lines (b) meander lines

Figure 3.7 shows the AFM results for separate lines and meander lines. As can be seen from Figure 3.7 (a), the results shows that the average distance between the two peaks is 50.89µm, which is slightly larger than the designed value of 50 µm. It is believed that the reason why the distance is larger than 50µm is the coffee ring effect, which is that after droplet evaporation, the particles are highly concentrated along the original edge of the drop [Yunker, 2011]. Figure 3.7 (b) indicates that for the meander structure, the average width for the line is 49.73µm, and the average width of the space is 19.79µm. The proposed width for the line is 50 µm and the space drawn between two lines is 20 µm, and the results shows the printed width and space are slightly less than the proposed width and space. The discrepancies between designed and patterned structures are very small, which are around 2%, therefore, the discrepancies are acceptable.

Based on the experiment results shown above, the microplotter is not suitable for structures of tens of millimetres, but it can be used for small scale devices, such as several microns. However, due to the un-stability and high failure rate to print the whole small scale structures, microplotter is not recommended to use. Therefore, microplotter is not suggested to use to replace the mask procedure, and the traditional process of using mask is continued to use in the etching process.

3.2.4 Pattern Electrodes using Traditional Etching Process

The conventional etching method is used, and the specific process of etching for this project is stated as follows:

1. The surface of the substrate, which is Rogers Duroid 5880 in this thesis, needs be cleaned first. Acetone is recommended to use for cleaning. Acetone can be sprayed all over the surface and wiped using clean soft brush. Then the surface is thoroughly washed under water and dried with a blower if possible.

2. After cleaning the surface, positive photoresist S1818 from Shipley is applied over the surface. The board with photoresist is then spinned with the spin coater to help the board to have a flat surface of the photoresist. The speed for the spin coater in this process is RPM 3500 for 1 minute. Softbaking of the photoresist is conducted on a hotplate for 1 minute at 100 °C.

3. Masks which have the designed patterns is attached on the surface, and the position is fixed by using two thick transparent layers to press together. This three-layer structure is then exposed under UV light for a period of time. The time for exposing under UV light varies with the types of UV light and the photoresist used. Here, the UV light used is The Spectroline® CL-150 and time used in this experiment is 45s. Masks are made of plastic, and for high resolution, such as smaller than 10μm, the masks are sent to special manufacture to produce. For low resolution, such as larger than 30μm, the masks are made in house using standard printer to print the masks.

4. After exposing to the UV light, the photoresist developer, PGMEA from Sigma Aldrich, is used to remove the photoresist on the unprotected part.

5. The exposed board is put into the etching bath which uses ferric chloride to remove the unprotected copper on the surface, and the etching time depends on the temperature of the etchant and how long the etchant has been used. The temperature used in this project is 40º and the etching time is around 4 to 5 minutes.

6. After the etching process, the photoresist remover is used to remove the remaining photoresist, and acetone could be the remover.

7. The surface is then cleaned with water and checked under the microscope to see the etching results, which is based on the discontinuity and continuity of the microstrip.

Figure 3.8 shows some electrodes structures after etching using Rogers Duroid 5880. Compared with the designed dimensions shown in later chapter, these electrodes dimensions are measured under microscope, and the results shows that etching can produce very precise patterns. However, in order to produce small features electrodes, such as smaller than 20μm, high resolution masks are needed, which requires to send the designed pattern to special manufacturer to make the masks.

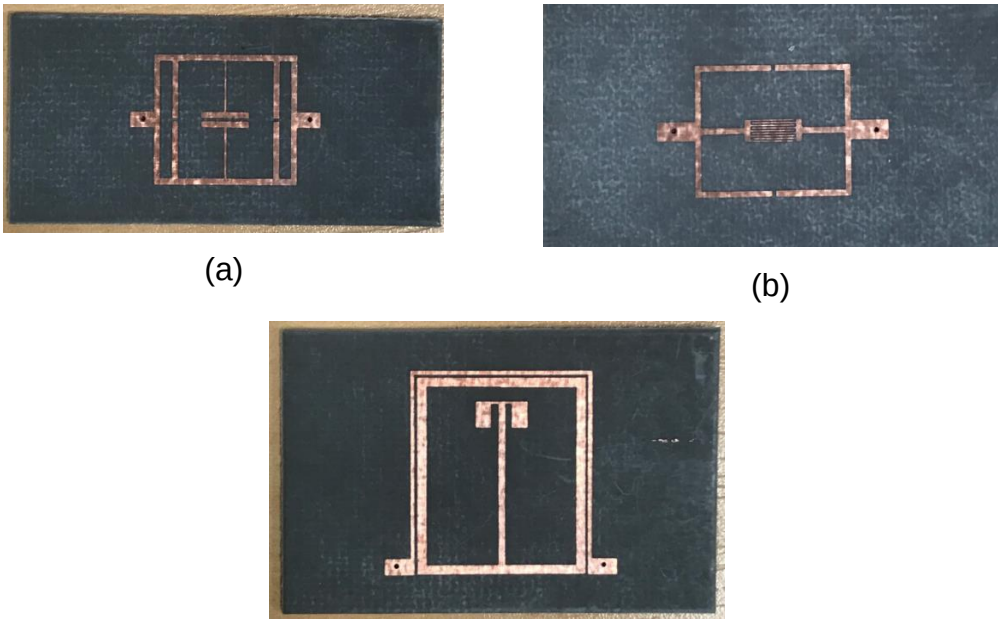

(a) (b)

(c)

Figure 3. 8 Patterned structures using etching (a) ELC resonator (b) IDC filter (c) Dual-mode filter

In conclusion, in order to develop the methods for patterning electrodes, the methods of milling, laser cutting, patterning photoresist with Microplotter and the conventional etching are tested. For thick layer of copper film, such as thicker than 0.15mm, milling machine is recommended to use. For thin layer of copper film, such as the copper layer of 35μm PCB and Rogers Duroid 5880 used in this project, etching and laser cutting are the suitable methods. For structures' dimensions larger than 20μm, laser cutter is preferred to use, due to its reliability and fast speed to cut, and etching is used when the structures have dimensions less than 20μm. As for the spacers, laser cutter is used to cut the desired shape of the spacers.

3.3 Assembly Process of Liquid Crystal Microwave Devices

Section 3.2 discusses the process to develop the methods for patterning electrodes, and in this section, how to develop a specific process to assemble microstrip LC devices are stated.

The general assembling process for microstrip LC devices are as follows:

1. Alignment layer is coated and rubbed with the chosen alignment methods stated in 3.3.1.

2. Spacers need to be attached on the surface using glue to form the cavity of LC.

3. After attaching the spacers, the device needs to be sealed with glue gun, as shown in 3.3.2.

4. LC is loaded after sealing the device.

5. The suitable connectors will be soldered on the board, and the connector are chosen depending on the working frequency as discussed in 3.3.3.

In the process of assembling the devices, there are some issues which needs to be addressed, such as how to make the alignment layer, seal the device, deposit LC and choose the connectors. In the following sections, the process of developing the methods to address these issues are demonstrated.

3.3.1 Alignment Methods

In most LC devices, it is necessary to align the LCs uniformly and in a defined direction without the application of an electric or magnetic field. An aligning force defines the off-state of a device and returns the LCs to that state after an applied field is removed. Homogeneous alignment is required for most devices, and in order to make LC be homogeneously oriented in the same direction, the surfaces must be initially prepared with the alignment layer which are coated and rubbed. The alignment layer planarize and provide the anchoring and pre-alignment of the LC. The material used as the alignment layer is the polyvinyl alcohol (PVA) made by Sigma-Aldrich, and the concentration for the PVA is 5%. In order to coat the alignment layer on the surface, two methods

for coating are used in this project. The first method is the spin coating, which uses the spin coater to coat. Based on the experiments conducted for the flat coating, the spin coater is set to work with the spin speed 2500 for 1 minute and 10 seconds to get the best coating results. The second method used is dip coating. Dip coating is conducted with directly putting the surface into the PVA which is also suitable to use. After coating the alignment layer on the surface, the alignment layer needs to be rubbed so that micro-grooves are created. With the created micro-grooves, a pre-alignment orientation is achieved. In this way, the LC is pre-aligned when no voltage applied. When the voltage is removed, LC can return to the pre-aligned direction with the alignment layer. In this project, the alignment layer is rubbed with rubbing cloth using a constant force to rub. This method to make alignment is checked with ITO glasses, and the alignment can be observed under microscope to see the LCs are tuned with external voltage applied to ITO glass.

3.3.2 Seal the Device and Deposit the LC

The microstrip LC devices are needed to be sealed**.** The top substrate and bottom substrate are sealed together to avoid the leakage of the LC. A glue gun with the small diameter head is used to seal the devices, as shown in Figure 3.9(a). After sealing the devices properly, the LC can be deposited into the cavity. In this project, this is achieved with using filling holes. The filling holes are two small holes on the dielectric substrate, which is shown in Figure 3.9(b). LC can be put into the hole with a fine syringe. The holes are sealed once the LC is loaded. The ITO glasses and the substrate with filling holes are used to verify the LC filling process, and it confirms that with the fine syringe to fill LCs, there is no bubble seen in the cavity.

(a) (b)

Figure 3. 9 (a) Glue gun used to seal the LC device (b) Filling holes to put LC

3.3.3 Choose the Connectors

The connectors are needed to be soldered to the device so that it can connect to the measurement applications. The connectors are chosen from the working frequency. If the working frequency is below 18GHz, SMA connectors should be chosen, while if the working frequency is above 18GHz, V connectors is the choice. In this project, the working frequency is below 18GHz, therefore, the SMA connectors are chosen to use.

3.4 Measurement Setup for the Microwave Resonator and Filters based on Liquid Crystals

After assembling the device, the device can be measured with the following measurement setup, where the S-parameters can be measured. The general measurement setup is shown in Figure 3.10. The frequency response is measured using a Keysight E5071C network analyser. The input port of the resonator or filter is connected to the analyser through a Bias-T, then connected to the device under test (DUT). A 1 kHz voltage was used to provide the voltage to switch the LC. Measurements were taken with the biasing voltage amplitude varying from 0 V to 16 V in 0.5 V steps. Each equipment are explained as follows.

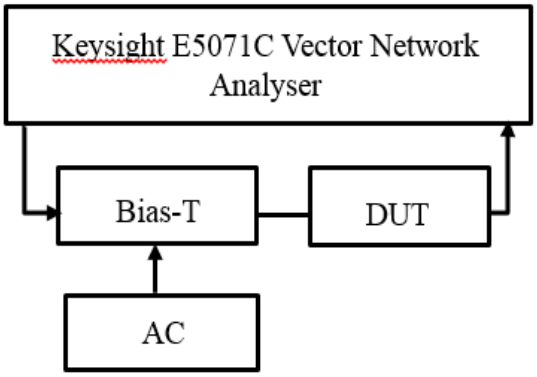

Figure 3. 10 Measurement Setup of the Microwave Resonator or Filters based on Liquid Crystals

3.4.1 Keysight E5071C Network Analyser

In this project, the working frequency is mainly under 8.5 GHz, therefore, the Keysight E5071C network analyzer, as shown in Figure 3.11, is chosen to measure the S-parameters. This network analyzer can work from 0 to 8.5 GHz, which satisfies the need for measurement of the resonant frequency. As can be seen from Figure 3.10, the microwave signal is applied to the Bias-T through the port, and the response through the DUT is received in another port for the analyzer to process and produce the S-parameters. In order to use it to measure the S-parameters correctly, the calibration needs to be done. The open, short and load calibration are needed to complete the calibration process.

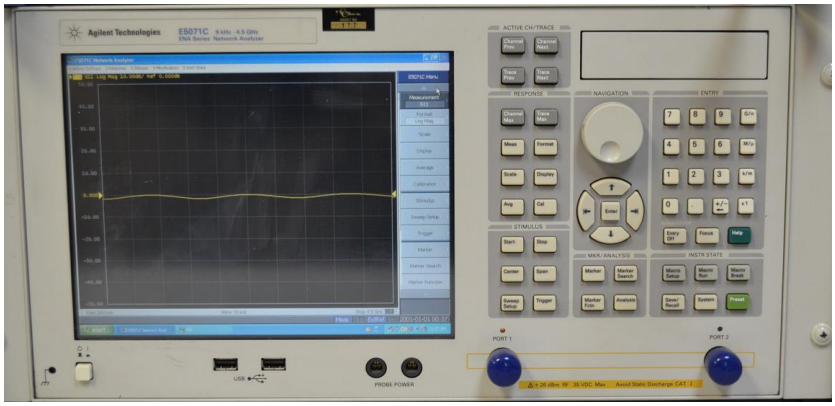

Figure 3. 11 Keysight E5071C network analyser

3.4.2 Bias-T

Bias-T is used to decouple the bias voltage source and the microwave signal, and it will pass through the AC voltage into the LC device so that LC can be tuned by the external voltage. The Bias-T used in this project is Hewlett Packard 33150A shown in Figure 3.12, which can work from 0.1 to 18 GHz. Because the working frequencies in this project are designed below 8.5GHz, this Bias-T can work very well with the designed frequency.

Figure 3. 12 Hewlett Packard 33150A Bias-T

3.4.3 AC Voltage

A DC voltage is not normally used as the bias voltage in LC devices because it can cause impurity ions in the LC to drift towards the electrodes and effectively shield the low frequency field. Instead, a 1 kHz AC voltage generated from the Agilent 33120A is used, as shown in Figure 3.13.

Figure 3. 13 Agilent 33120A generator

3.5 Conclusion

In this chapter, the fabrication process of the LC based devices and the measurement setup are studied. In the first stage of fabrication process, four different methods to pattern electrodes have been investigated and compared. Milling is a suitable method for thick layer because it does not damage the surface.However, for the Duroid 5880, the copper layer is 35µm, which is too thin to use milling machine. Laser cutter is convenient to use and it can be used to pattern electrodes, which is larger than 20 µm. Microplotter is not suitable to use due to its reliability problem and high error rate. Etching is the preferred method as it can be used for both low and high resolutions. The second stage is to assemble the LC based devices. How to make the alignment layer, LC injection and how to seal the devices are stated. In the second part of this chapter, the measurement setup is described, followed by the description of each components used for the measurement. The measurement setup is used to measured all the fabricated devices in the thesis.

Chapter 4 A General Design Method for Tunable Microstrip Devices Using LCs

There are a number of different applications of LC at Microwave frequencies and the details are given in Chapter 1. However, it is clear from these that there is no clear methodology for a design process that can be applied more widely to LC microwave devices based on microstrip configuration. Therefore, in the first part of this chapter, a novel general method for how to design LC devices based on microstrip configuration is put forward. The novelty of this method are that it integrates the use of the lumped element modelling and full wave simulation and it is the first paper published to demonstrate the whole design process of designing tunable microstrip devices using LCs. The design process is separated into two stages, where two types of software, ADS and CST, are used to run the simulations. The reason why to use ADS in the first stage is that the simulation using ADS is fast and can estimate the performance of the designed devices in a short time, while using CST for the full wave simulation takes much longer time but more precise results. In the first stage, the lumped element modelling using equivalent circuits is conducted by ADS, and the working frequency and tuning range is firstly optimized. The second stage involves using CST to run the second optimization to get the required frequency and maximize the tuning range. The final dimensions after second optimization are then used to run the full wave simulation to get the final results. LCs are treated as isotropic materials in the ADS simulation and anisotropic materials in the CST, respectively. The use of LCs as homogeneous anisotropic materials in the CST is a reasonable approximation through checking and comparing the electric field from CST and the detailed switching of LC directors from an in-house finite element modelling package.

4.1 General Method to Design Tunable Microwave Devices

The general design process diagram is shown in Figure 4.1. The design method consists of two main stages; lumped element modeling followed by

full-wave simulation. As shown in Figure 4.1, in the first stage, the elements of the basic microstrip line circuit are identified and then converted to equivalent lumped elements using theoretical and empirical equations. The lumped element equivalent circuit is then modeled using Advanced Design System (ADS) [ADS, 2012] to optimize the element values to give the desired working frequency and the widest tuning range. The LC is considered as an isotropic material in this stage. The first optimization, using ADS, allows the sensitivity of the resonant frequency to various dimensions of the structure to be investigated. In addition the tuning range can be maximized as the different dimensions are varied.

In the second stage, as the optimized elements are converted back to microstrip segments and the structures used in CST Microwave Studio [CST, 2017] for full-wave simulation of the device. In the first step, as shown in Figure 4.1, the full wave simulation results from CST are compared with the lumped element modelling results to make sure the initial lumped element model provides the correct estimation. It is possible that some microstrip structures are not identified as giving significant lumped elements to be used in the ADS simulation. So if poor agreement is found with the initial CST results it may be necessary to repeat the ADS modelling with additional lumped elements.

A final check is made before final optimization in the CST. An output from CST allows the detail of the electric (and magnetic) fields to be visualized. Running the final full wave simulation at the resonant frequency, the electric field is plotted to allow consideration of the way that the un-switched and switched LC may present to the electric field. In the CST simulation, the LCs are approximated as a single block of homogeneous anisotropic materials, and this approximation is checked by comparing the direction and location of the electric field from CST and the detailed switching of LC director structure from an in-house finite element modeling package QLC3D [Yazdanpanahi, 2010]. If necessary, the LC region can be divided into several homogeneous parts, as stated in Chapter 2.

Providing the initial agreement and final check of electric field are good, the

second optimization is then performed and the required working frequency and the tuning range are generated. The adjusted dimensions are generated in the second optimization using CST, and these dimensions can be used in fabricating the tunable device.

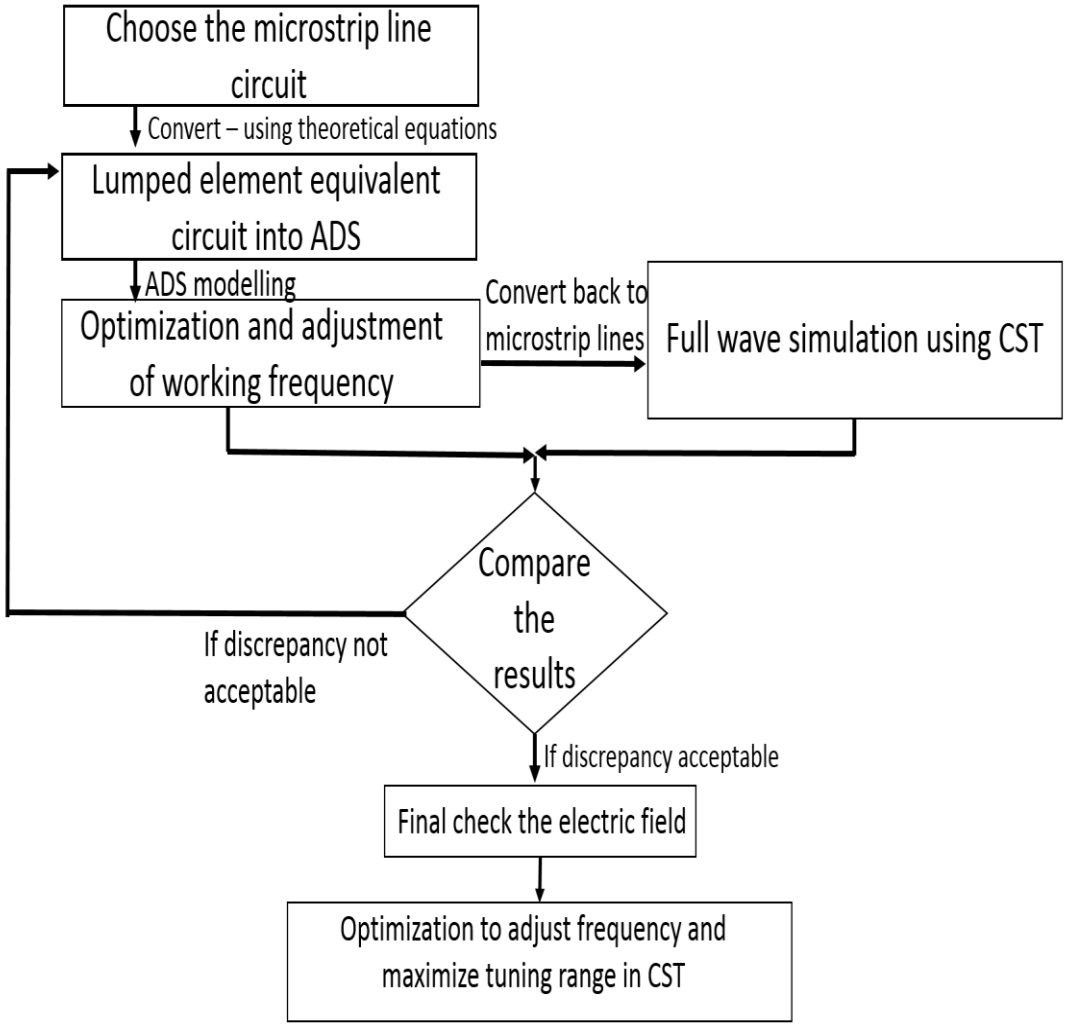

Figure 4. 1 General design process diagram

4.1.1 The Software Used in the Design Process

The lumped element model is simulated with ADS, which is an electronic design software for RF and microwave applications. In this thesis, the equivalent circuit is generated with using the theoretical and empirical equations from books and literatures. In the ADS, in order to carry out the optimization, the values for the lumped elements are varied by changing the dimensions of the microstrip lines through the equations. With the changes in

the values of lumped elements, the working frequency is adjusted and the tuning range is optimized.

The second stage of design uses the software CST Microwave Studio to run the full wave simulation, and it is widely used in electromagnetic analysis and in the microwave frequencies range [CST, 2017]. In the CST, the 3D model of the designed structure are constructed and simulated within specific frequency range under correct boundry conditions to figure out the resonant frequency. Second optimization is also performed with CST to adjust the required working frequency and maximize the tuning range. Besides the resonant frequency, CST can also generate the electric field, quality factor, power flow, current and the farfields for antennas. The use of CST makes the design method suitable for a variety of applications, such as filters, resonators and antennas.

4.2 Verification of Using CST to Model LC as a Homogeneous Anisotropic Material

CST can only deal with homogeneous blocks of isotropic or anisotropic material, therefore, the LC is assumed in the simulations to be a single homogeneous anisotropic layer. However, the LC switches into a non-uniform structure. In order to examine the validity of approximation LCs as homogeneous anisotropic material in this thesis at microwave frequencies, the electric field distribution calculated with CST and the LC director distribution are compared for the case of saturation voltage (maximum switching). With no voltage applied, the LC orientation is uniform and in the direction given by the surface alignment, so the simulations are expected to be accurate in the unswitched case. The director distribution is calculated using QLC3D, which is an in-house finite element LC modeling program [Yazdanpanahi, 2010].

Figure 4.2 (a) and (b) show the electric field below and between the interdigital capacitor (IDC) electrodes and at the edge of the IDC for the case when the maximum voltage is applied in the CST. The arrows in (a) and (b) indicate the direction of the field and their colors represent its intensity, where those in red show the highest field intensity. It can be seen that the field is largely confined

between the IDC electrodes and the ground plane.

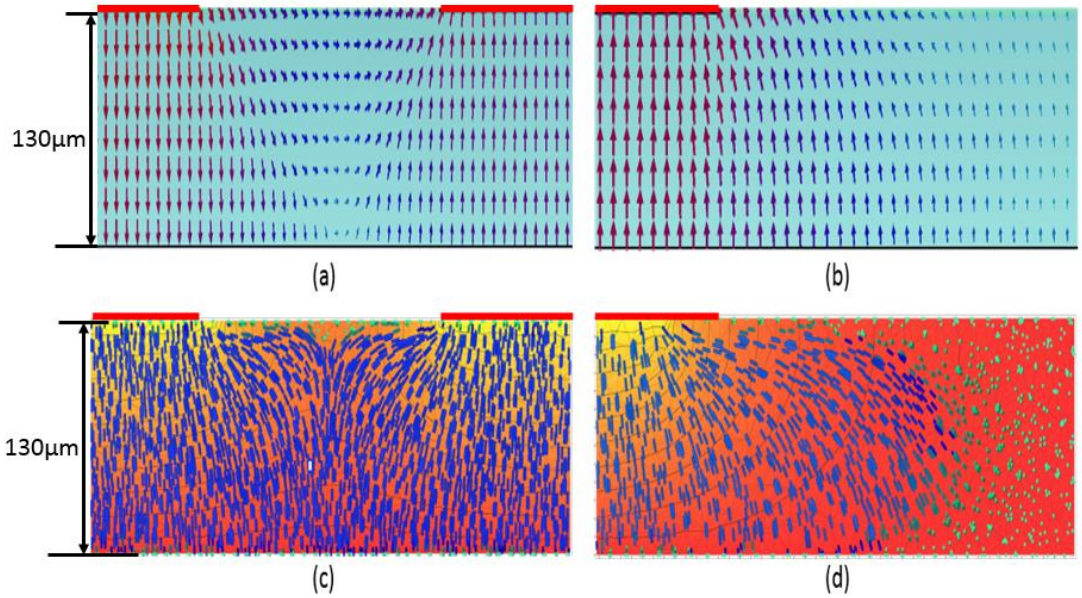

Figure 4. 2 Electric field distribution for the saturation voltage (16 V) in the region below and between the IDC electrodes (a) and at the edge of the electrodes and beyond (b). The corresponding director distributions are shown in (c) and (d) respectively. The thick red lines added to the pictures indicate the position of the electrodes. The ground electrode (not marked) covers the whole of the bottom surface. Gap between electrodes is *g*= 0.2mm, the bottom electrodes is whole ground plane, size is 40×32mm. Top electrode is half of the IDC fingers, it is around 0.15mm

Figure 4.2 (c) and (d) show the corresponding director distributions in the same regions as (a) and (b) using QLC3D. We can observe that although the LC in Figure 4.2(c) is almost fully switched, it is not fully vertical across the whole of the cross section as some LCs near the electrodes and ground plane are not switched and shown in blue color, which would represent a homogeneous permittivity. Compared with Figure 4.2(a), the LC directors largely follow the direction of the electric field, which in fact would maximize the tuning effect by increasing the actual effective permittivity and in turn shows a larger tuning range in the measurement. However, there is a narrow layer next to the alignment layers that will remain unswitched and this will contribute to a small decrease of the effective permittivity, the assumption of uniform, vertically aligned permittivity ellipsoid here will overestimate the effective permittivity. Beyond the edge of the electrodes (Figure 4.2(b) and (d)), the LC orientation is not vertical and the assumption of vertically oriented permittivity will underestimate the effective permittivity. However, the field values in this region

decrease sharply away from the electrodes so the approximation has a lower effect. Since the effect of assuming a vertically oriented permittivity in the different regions tends to compensate each other, we have considered it reasonable to use this approximation in the CST simulations.

The work in this thesis is concerned with lower microwave frequencies, however, it should be noted that there may be differences at higher microwave frequencies, where the electric field may be concentrated close to electrodes and less likely to go from one electrode to the ground plane. A metadevice using LCs and Au electrodes is designed by [Shen, 2018], and the electric field at resonant frequency of 1.08THz is shown in Figure 4.3. As can be seen from Figure 4.3, between the electrode and the ground plane underneath, the electric field is concentrated along the edges of the electrodes, and it is not concentrated between electrodes and ground plane, where assuming LCs as homogeneous anisotropic material is not appropriate.

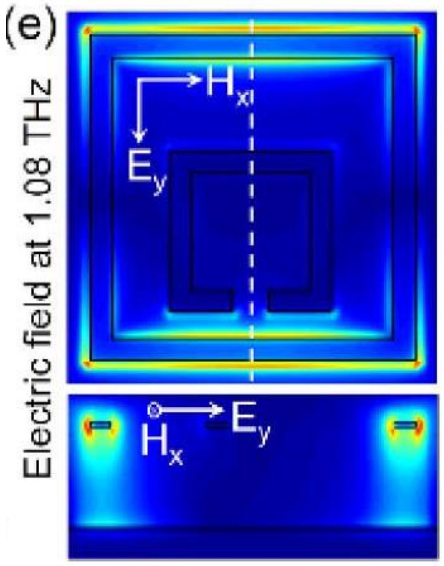

Figure 4. 3 The electric field at 1.08THz (Shen et. al, 2018)

Chapter 5 Tunable LC Resonators Using Electric Inductive Capactive Resonators

In the Chapter 4, a general design method for tunable microstrip devices using LCs is proposed. In this chapter, the proposed design method is tested and verified by designing tunable LC resonators using electric inductive capacitive (ELC) resonators, so called because of working with a fundamental mode that couples strongly to electric field, and negligibly to magnetic field [Schurig, 2006]. Strong coupling to electric field is particularly important for LC tunable device, because LC directors are switched by the external voltage and largely follow the distribution of microwave electric field, as discussed in Chapter 4. With strongly coupling to electric field, more LC directors can be fully switched and more tuning can be achieved. Therefore, tunable resonators using ELC resonators are compatible to construct tunable LC devices.

Three types of tunable LC resonators are considered, starting from one derived from [Schurig, 2006], followed by two improved versions of ELC resonators are proposed and designed using the design methodology. The three types of tunable resonators are then fabricated and measured. The measured results and simulated results are compared to check and verify the design method.

5.1 ELC Resonator Calculation

As stated in Chapter 4, the general design method consists of two stages. In the first stage of the design, the microstrip structure is first converted into equivalent lumped elements using empirical equations. A ELC resonator can be described qualitatively in terms of its equivalent circuit as shown in Figure 5.1. A capacitor-like structure couples to the electric field and is connected in parallel, to two loops, which provide inductance to the circuit. The two inductive loops are connected in parallel, so that the resonant frequency of the circuit model is $w_0 = \sqrt{2/LC}$ [Schurig, 2006]. This simplified lumped element does not include the capacitance C_P between ground plane and resonator structure,

and whether it is appropriate to not include the C_P is investigated later.

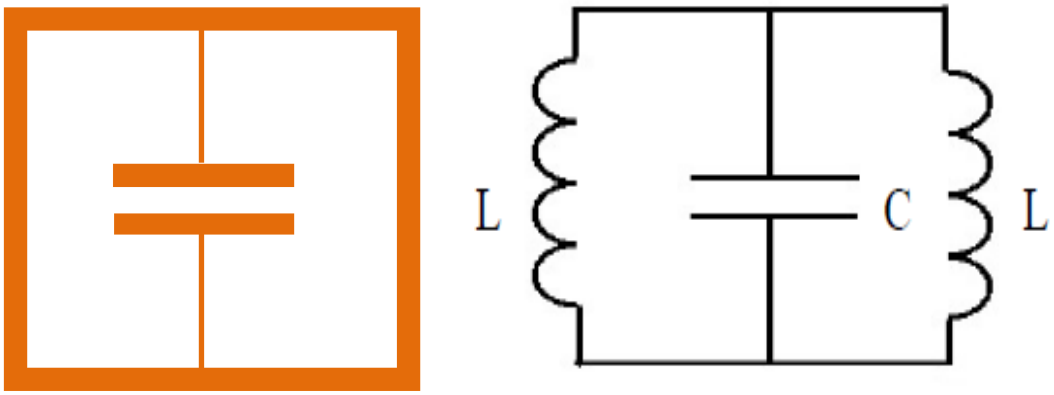

(a) (b)

Figure 5. 1 (a) Structures of ELC resonator (b) equivalent circuit of ELC resonator

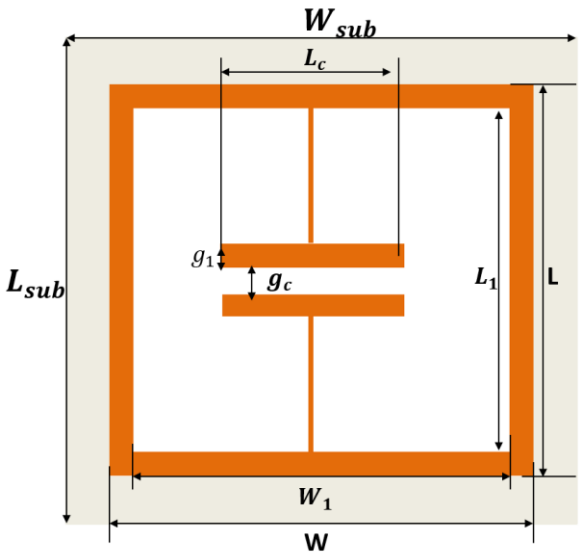

Figure 5. 2 Parameters for ELC resonator

The parameters of the ELC resonator is shown in Figure 5.2, and these parameters are used for calculating the resonant frequency. A design equation using the partial capacitance method [Bahl, 2003] to find the capacitance and inductance of the structure has been improved by [Gevorgian, 2001] by using closed form formula, and the capacitance *C* is given by

$$C = \frac{\varepsilon_{eff}}{18\pi} \frac{K(k)}{K'(k)} L_c \qquad 5\text{-}1$$

where L_c is in mm, C is in pF.

The ratio of complete elliptic integral of first kind *K(k)* and its complement $K'(k)$ are calculated as follows

$$\frac{K(k)}{K'(k)} = \frac{\pi}{\log(\frac{2(1+\sqrt{k'})}{1-\sqrt{k'}})} \; for\; 0 \le k \le \frac{1}{\sqrt{2}} \quad 5\text{-}2$$

$$\frac{K(k)}{K'(k)} = \frac{\log(\frac{2(1+\sqrt{k})}{1-\sqrt{k}})}{\pi} \; for\; \frac{1}{\sqrt{2}} \le k \le 1 \quad 5\text{-}3$$

$$\frac{K(k_1)}{K'(k_1)} = \frac{\pi}{\log(\frac{2(1+\sqrt{k_1{}'})}{1-\sqrt{k_1{}'}})} \; for\; 0 \le k_1 \le \frac{1}{\sqrt{2}} \quad 5\text{-}4$$

$$\frac{K(k_1)}{K'(k_1)} = \frac{\log(\frac{2(1+\sqrt{k_1})}{1-\sqrt{k_1}})}{\pi} \; for\; \frac{1}{\sqrt{2}} \le k_1 \le 1 \quad 5\text{-}5$$

Where the *k*, k_1, $k'$and k_1' are generated by

$$k = \frac{g_c}{2g_1+g_c} \quad 5\text{-}6$$

$$k_1 = \frac{\tanh(\frac{\pi g_c}{4h})}{\tan(\frac{\pi(g_1+g_c)}{2h})} \quad 5\text{-}7$$

$$k' = \sqrt{1-k^2} \quad 5\text{-}8$$

$$k_1' = \sqrt{1-k_1^2} \quad 5\text{-}9$$

The effective permittivity ε_{eff} and the inductance *L* are given by

$$\varepsilon_{eff} = \varepsilon_0(1 + \frac{(\varepsilon_r-1)}{2}\frac{K(k_1)}{K'(k_1)}\frac{K'(k)}{K(k)}) \quad 5\text{-}10$$

$$L = \mu_0\mu_r h(2\frac{g_1}{W} + 2\frac{L}{g_1} + \frac{L-2g_1-g_c}{g_1}) \quad 5\text{-}11$$

$$f = \frac{1}{2\pi\sqrt{LC}} \quad 5\text{-}12$$

For the above equations, *h* is the thickness of the substrate, the permeability μ_r of the LC can be approximated by $\mu_r = 1$, *L* is the total inductance of the loop, *C* is the total capacitance, f is the resonant frequency. With the designed method discussed above, the capacitance *C*, the inductance *L*, and resonant frequency f can be calculated.

5.2 Tunable LC Resonator Using Type I ELC Resonator

5.2.1 Verification Equivalent Circuit of ELC Resonator

The ELC resonator in Figure 5.2 is designed to work at 4.8GHz with using the empirical equations from 5-1 to 5-11, and the calculated dimensions are shown in Table 5.1. In the first stage of the design, the simulated results from lumped element modeling using ADS and the full wave simulated results from CST needs to be compared to ensure the equivalent lumped element circuit is chosen correctly to predict the working frequency.

L_{sub}	L	W	L_1	W_1	L_c	g_c	g_1
16	14	14	13	13	4.5	0.2	3

Table 5. 1 Dimensions of ELC resonator using empirical equations (Unit:mm)

The dimensions in Table 5.1 are used in the CST to build the 3D model of the ELC resonator. The schematic view of an ELC resonator [Schurig, 2006] from CST is shown Figure 5.3 (a) which has been modified with the materials used in this project. The cross section view of the structure is shown in Figure 5.3 (b). The bottom substrate is Roger Duroid 5880 with the thickness of *h*=0.79mm. The resonator structure is on the top of the bottom Rogers Duroid 5880, and the resonator structure is copper with the thickness of *t*=35μm. The spacers, another piece of Rogers Duroid 5880 with a thickness of $h_{spacer} = 130\mu m$, are used to form the cavity for LC, which is shown as the blue region in the Figure 5.3(b). Rogers Duroid 5880 with a thickness of 0.79mm is used as the top layer, and copper layer underneath the Duroid 5880 acts as the ground plane.

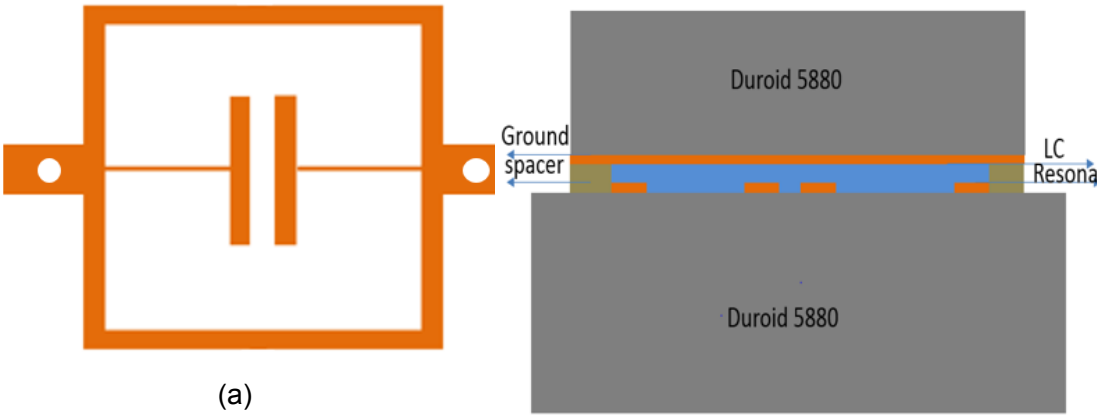

(a)

(b)

Figure 5. 3 (a) Structure of ELC resonator (b) Cross section view of ELC resonator (Not drawn to scale), $\varepsilon_{substrate} = 2.2$, $h = 0.79mm$, $t = 35\mu m$, $h_{spacer} = h_{lc} = 130\mu m$

The results from lumped element modelling using ADS and full wave simulation results are shown in Table 5.2. The LCs from Merck E7 is used in the simulation for the whole project as it is used in the fabricated devices, which has the permittivity of $\varepsilon_{r\perp} = 2.72$ and $\varepsilon_{\parallel} = 3.17$ at room temperature [Yaghmaee, 2013]. As can be seen from Table 5.2, the resonant frequency is 4.78GHz for lumped element modelling using ADS, where the dielectric constant of 2.72 is used. The CST simulation shows the resonant frequency of 4.72 at unswitched state. While for the switched state, the CST simulation results is 4.21GHz and ADS simulation results is 4.20GHz. With changing the dielectric constant of LC from 2.72 to 3.17, the biggest discrepancy between ADS and CST is 0.06GHz, which corresponds to 1.26%. Since the discrepancy between the ADS and CST is small, there is good agreement between ADS and CST simulation, which means that the equivalent lumped element model is appropriate to use.

Dielectric constant (ε)	Resonant frequency (GHz) of S11 from ADS	Resonant frequency (GHz) of S11 from CST
2.72	4.78	4.72
2.8	4.58	4.52
2.9	4.41	4.42
3.0	4.39	4.41
3.1	4.22	4.25
3.17	4.20	4.21

Table 5. 2 Resonant frequency from ADS and CST simulation

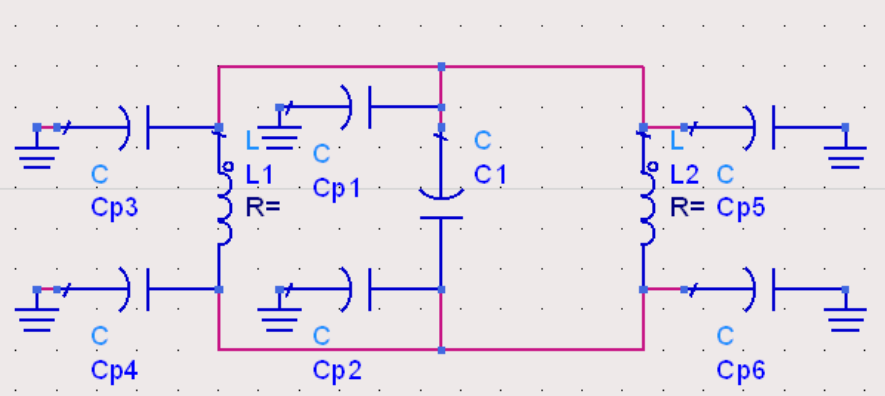

Figure 5. 4 Equivalent circuits of ELC resonator with C_p

In the next step, the capacitance C_p between ground and resonator structures needs to be verified. In the simplified equivalent circuit of ELC resonator, the capacitance C_p between resonator structure and ground plane is not included. One of the issues for LC devices is that a ground plane is required to apply the external voltage for the LC. Therefore, this may affect the equivalent lumped circuit used in the first stage of the resonator design. Whether C_p is included or excluded in the equivalent circuit needs to be analyzed. Figure 5.4 shows the equivalent circuits of ELC resonator which considers and adds the capacitance between ground and microstrip lines, C_p.

Dielectric constant (ε)	Resonant frequency (GHz) of S11 from ADS	Resonant frequency (GHz) of S11 with only changing C_p (ADS)
2.72	4.78	4.73
2.8	4.58	4.73
2.9	4.41	4.72
3.0	4.39	4.72
3.1	4.22	4.70
3.17	4.20	4.69

Table 5. 3 Simulation results for equivalent circuit with and without *Cp*, $h_{lc} = 130\mu m$

In order to analyze the influence of C_p for the ELC resonator, the simulation using ADS is carried out with using the equivalent circuit in Figure 5.1(b) and in Figure 5.4. Figure 5.1(b) shows the simplified equivalent circuit while Figure 5.4 shows the equivalent circuit including C_p. The simulation using ADS starts with using the equivalent circuit in Figure 5.1(b), where all the capacitances are changed with changing the dielectric constant of LCs from 2.72 to 3.17. While for the ADS simulation using the equivalent circuit in Figure 5.4, only the capacitance C_p is changed with varying the dielectric constant from 2.72 to 3.17 and other capacitance and inductance are fixed. In this way, how the capacitance C_p affects the resonant frequency is figured out. The comparison of the results from lumped element modeling using Figure 5.1(b) and Figure 5.4 is shown in Table 5.3. As can be seen from Table 5.3, the resonant frequency of only changing C_p shifts from 4.73GHz to 4.69GHz, which is a tuning range of 0.04GHz. Compared with the tuning range of 0.04GHz, the tuning range from changing all the capacitance and inductance is 0.58GHz, and it is 14.5 times bigger than the tuning range of only changing C_p. Therefore, it is appropriate to exclude the C_p in the equivalent circuit. The comparisons of simulated results of using ADS and CST are plotted in Figure 5.5. The resonant frequency in the ADS and CST shows that there is greater decrease when changing the dielectric constant from 2.7 to 2.9 and from 3 to 3.17. From 2.9

to 3, there is small decrease in the resonant frequency, which is very interesting to find out whether the same changes can be found from measurement results.

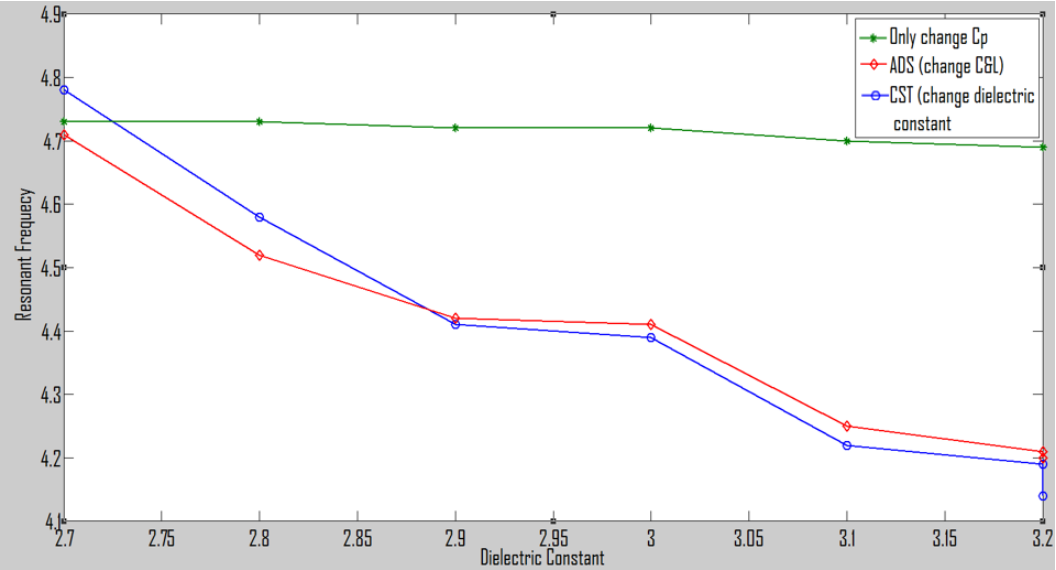

Figure 5. 5 Comparison of simulation results using ADS and CST

5.2.2 Verification of the Thickness of LC Layer

Although C_p does not need to be considered in the lumped element, capacitance and inductance do depend on the thickness of LC layer. The range of the appropriate thickness for LC layer need to be considered. The resonant frequencies from CST and ADS are generated with changing the thickness of LCs. After considering the ease of fabrication and tuning response time of LCs, the thickness is chosen to change from 50μm to 200μm. For ADS simulation, the changes in thickness will change the capacitance and inductance of the lumped elements. The results from ADS and CST are shown in Table 5.4, which shows the different thicknesses and the corresponding resonant frequency.

h(μm)	Resonant frequency of S11 (GHz) from ADS	Resonant frequency of S11 (GHz) from CST
50	4.65	4.61
60	4.68	4.62
70	4.70	4.67
80	4.73	4.72
90	4.75	4.73
100	4.78	4.74
110	4.80	4.69
120	4.81	4.67
130	4.80	4.63
140	4.79	4.61
150	4.76	4.59
160	4.72	4.56
170	4.71	4.52
180	4.65	4.50
190	4.55	4.48
200	4.40	4.45

Table 5. 4 Resonant frequency from CST and ADS results of changing thickness of LC

Figure 5.6 plots the comparison between the ADS and CST results. As can be seen from Figure 5.6, the results from 50μm to 100μm of CST and ADS have matched with accepted error. However, when increasing the thickness from 100μm to 200μm, there are very big discrepancies between two groups of results. The reason attributes to this problem might be the conditions to use the equations, which is the W/h ratio. When increasing the thickness, the ratio of W/h decreases, and if this decrease is out of the range to use the equations, it causes the discrepancies. However, as long as the discrepancy is known, it will not affect using it as the first stage of simulation and optimization.

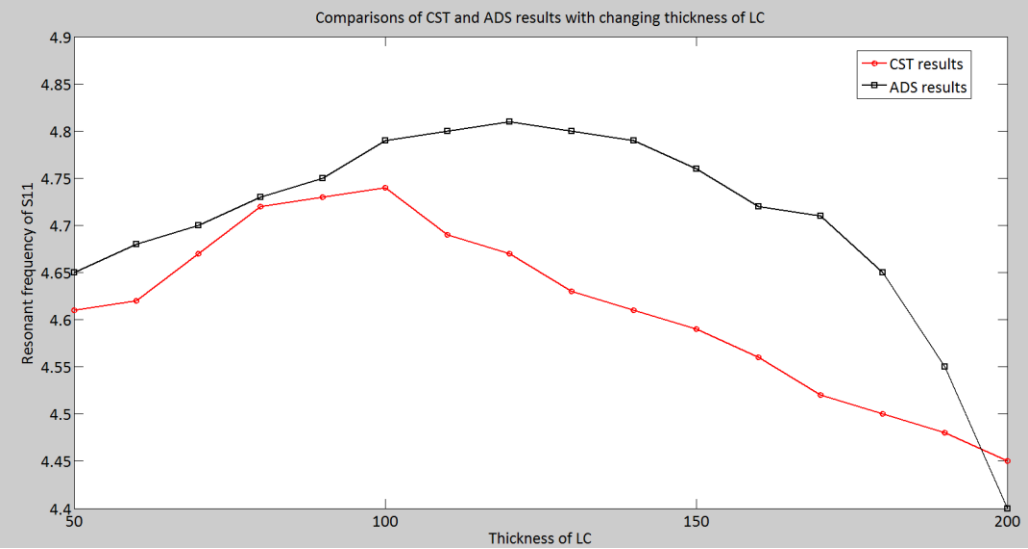

Figure 5. 6 Comparisons of CST and ADS results with changing thickness of LC

5.2.3 Verification of the LC Region

Also, since LCs are switched between electrodes and ground plane, it is also interesting to find out whether the tuning is affected if LCs are only deposited on electrodes and the rest of the area uses spacers. As can be seen from Figure 5.7, the blue region indicates the area of LCs and the grey region is modelled with spacers using four types of materials, namely acrylic plastic, PTFE, Mylar and PMMA. The dielectric constant for acrylic plastic, PTFE, Mylar and PMMA are 1.9, 2.1, 3.1 and 4, respectively.

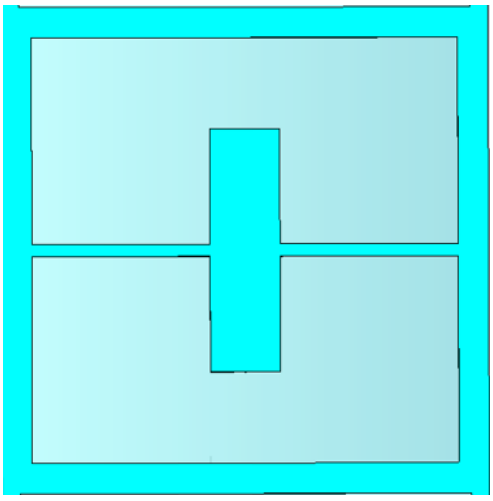

Figure 5. 7 The LC and spacer region

Two types of liquid crystals, liquid crystal E7 (ε_r from 2.7 to 3.17) and liquid crystal GT3-23001 (ε_r from 2.5 to 3.3), are used to get more results to compare. The results for the four different materials are summarized in Table 5.5, and the table shows both the tuning range and tunability of using these materials. As can be seen from Table 5.5, from the simulation results, the tuning ability reduces with the increase of dielectric constant of the materials (ε_r from 1.9 to 4),.

Spacer	Tuning range & Tunability	
	Merck E7 (ε_r=2.7 to 3.17)	GT3-23001 (ε_r=2.5 to 3.3)
Acrylic Plastic (ε=1.9)	370MHz (4.93 to 4.56GHz)	400MHz (4.98 to 4.58GHz)
	7.6%	8.1%
PTFE (ε=2.1)	330MHz (4.91 to 4.58GHz)	340MHz (4.93 to 4.59GHz)
	6.7%	6.9%
Mylar (ε=3.1)	260MHz (4.73 to 4.47GHz)	280MHz (4.78 to 4.5GHz)
	5.5%	5.9%
PMMA (ε=4)	200MHz (4.65 to 4.45GHz)	210MHz (4.7 to 4.49GHz)
	4.3%	4.5%

Table 5. 5 The tuning range and tunablity with different spacers

As can be seen from the simulation results, using Acrylic has the largest tuning range and tunability, which corresponds to 370MHz and 400MHz and 7.6% and 8.1%. However, using LCs in the whole region provides a tuning range of 510MHz and a tunability of 11%. Therefore, from the discussion above, it is better to apply LCs in the whole region which not only can have better tuning range but also is ease for fabrication process.

5.2.4 First Optimization of ELC Resonator

After verifying the equivalent circuits, the equations and the proper thickness of LCs, the first optimization is conducted with ADS. Since there are some dimensions can be optimized, it is important to find out which dimension should be optimized. Figure 5.8 shows the electric field of this resonator at resonant frequency, and orange and red colors represent the higher electric field. It can be clearly seen that the higher intensity of electric field concentrates on the central plates, which are the capacitive elements. Therefore, the optimization focuses on changing the dimensions of the central plates, which are g_1, g_c and l_c, as shown in Figure 5.1.

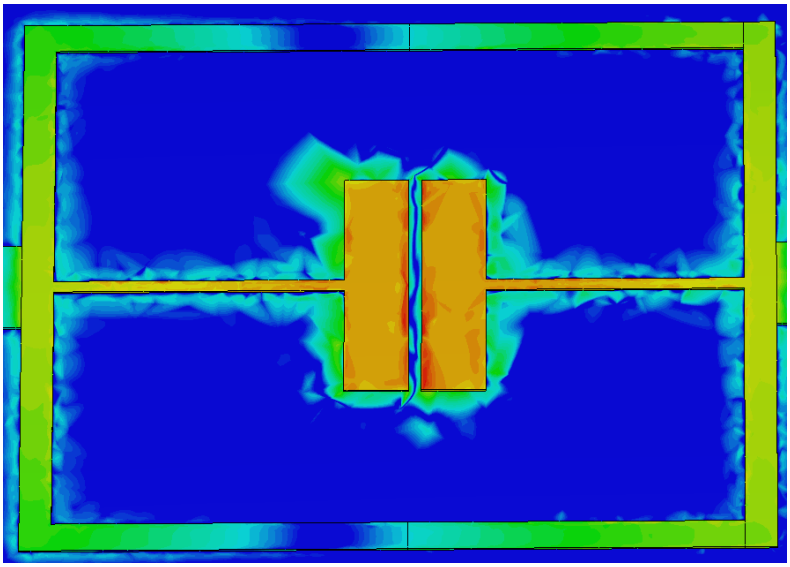

Figure 5. 8 Electric field at resonant frequency for ELC resonator

After considering the fabrication resolution, the ranges for the dimensions can be changed as: the g_c is chosen from 0.2mm to 0.6mm, g_1 is chosen to change from 2mm to 6mm, and L_c is chosen from 3mm to 7mm as increasing the length to the inductive loops means that the coupling between central plate and inductive loops needs to be considered.

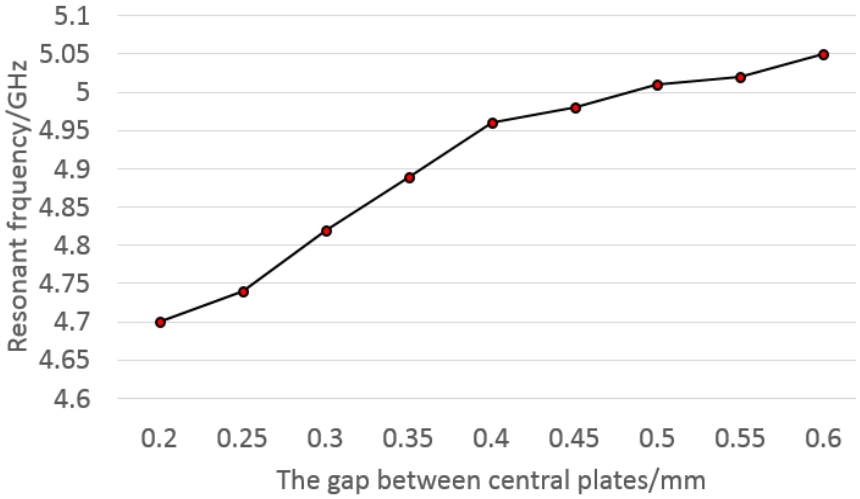

(a)

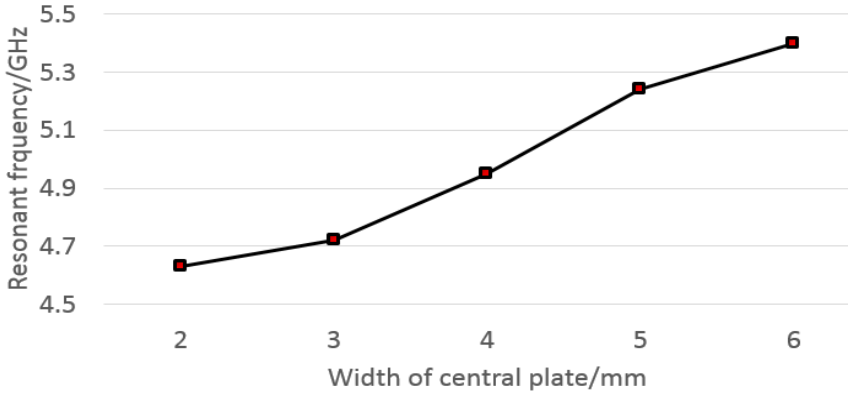

(b)

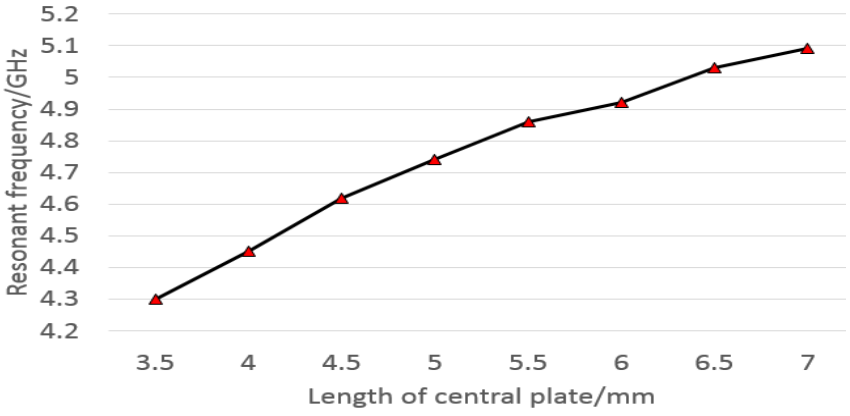

(c)

Figure 5. 9 First optimization of (a) changing gap g_c between central plate (b) changing width g_1 of central plate (c) changing length L_c of central plate

The optimization results are shown in Figure 5.9. Figure 5.9 (a) shows the simulation results of changing the gap g_c between central plates. With increasing the gap, the resonator frequency increases from 4.7GHz to

5.05GHz. There is greater increase in the resonant frequency from 0.25mm to 0.4mm, which means the resonant frequency is more sensitive in this range. Figure 5.9 (b) indicates the simulation results of increasing width g_1 of central plates. There is an average increase of 0.2GHz when increases the width with a step of 1mm, and the largest increase happens in changing from 4mm to 5mm. Figure 5.9 (c) shows the changes in resonant frequency as a function of increasing the length l_c of the central plates. As can be seen from Figure 5.9(c), increasing the length of central plates from 3.5mm to 5.5mm shows bigger changes than from 5.5mm to 7mm. The simulation results indicate the influences of changing these dimensions, and the changes in the width g_1 and length l_c of central plates are more sensitive to the resonant frequency. Therefore, if the optimization involves changing the resonant frequency greatly, it is better to optimize the length and width of the central plates. If the optimization focuses on small changes, changing the gap between central plates is more effective.

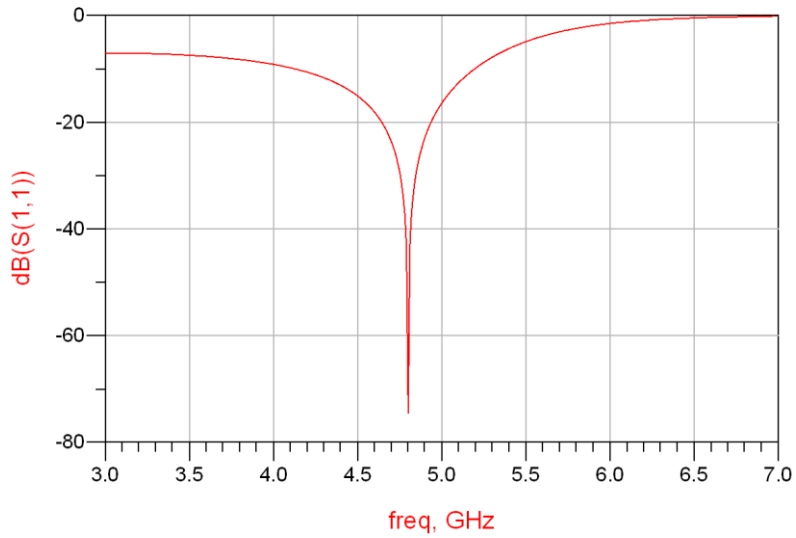

Figure 5. 10 The optimized resonant frequency of 4.8GHz using ADS

The resonant frequency using dimensions in Table 5.1 is 4.78GHz, which is close to the designed working frequency of 4.80GHz. As stated above, it is better to change the gap between central plates to adjust the working frequency for small changes. With changing the dimensions g_c from 0.2mm to 0.25mm, the resonant frequency can achieve 4.8GHz, as shown in Figure 5.10. The optimized dimensions using ADS are shown in Table 5.6.

L_{sub}	L	W	L_1	W_1	L_c	g_c	g_1
16	14	14	13	13	4.5	0.25	3

Table 5. 6 Dimensions after first optimization using ADS (unit:mm)

5.2.5 Second Optimization Using CST and Full Wave Simulation Results

After the first optimization with ADS, the second optimization is carried out with CST. The reason why the second optimization is necessary are that LCs are used as homogeneous anisotropic materials in CST and it provides more accurate simulated results than ADS using isotropic value. The second reason is that since CST is full wave simulation, the magnitude of S-parameters can be optimized.

The dimensions in Table 5.6 are used to build the 3D model of the tunable bandpass resonator using ELC resonator in CST, and the 3D model is shown in Figure 5.11. As can be seen from Figure 5.11, the resonator structure and feed lines are placed on different sides of Roger Duroid 5880 substrate and are connected through metallic vias. The LC layer, top ground plane and top substrate are chosen to be transparent so that the ELC resonator structure can be clearly seen.

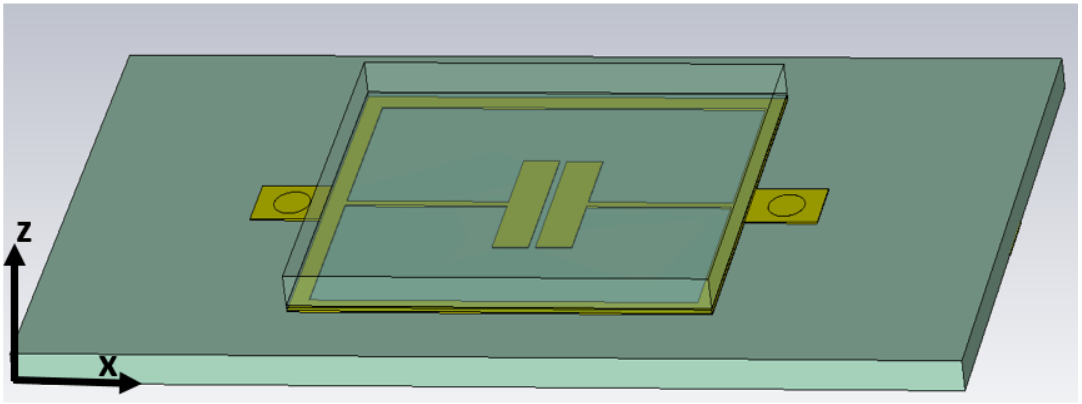

Figure 5. 11 The 3D model of the tunable bandpass resonator using ELC resonator in CST

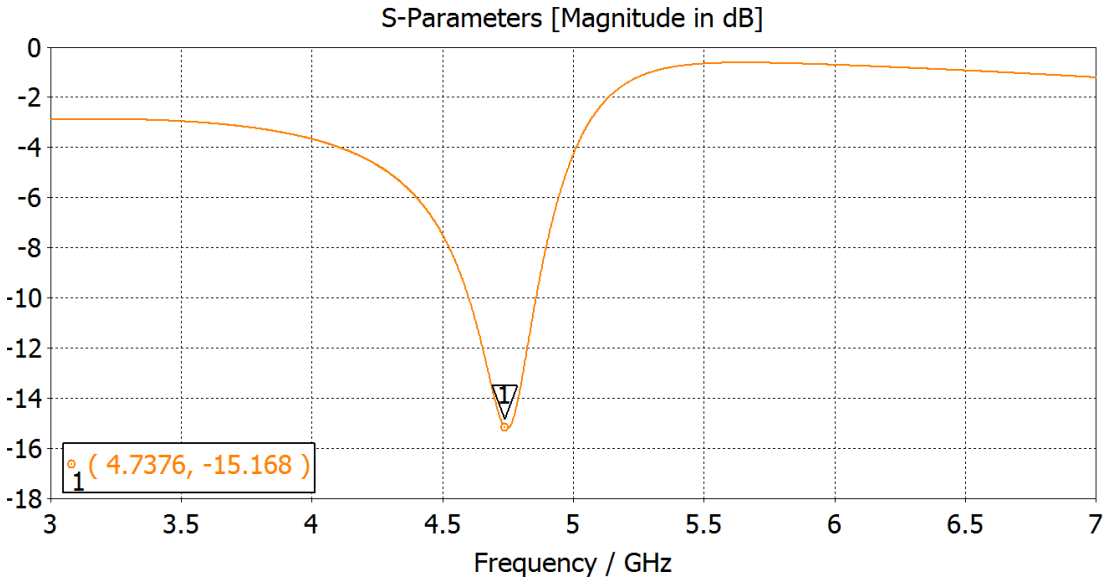

Figure 5. 12 S_{11} generated from CST

The full-wave electromagnetic simulations using CST demonstrates that using the dimensions from first optimization, the resonant frequency in CST is 4.73GHz, as shown in Figure 5.12. In order to achieve the designed frequency of 4.80GHz, the three dimensions stated in the first optimization are used to carry out the second optimization. The three dimensions are changed separately to find out how each dimension affects the resonant frequency.

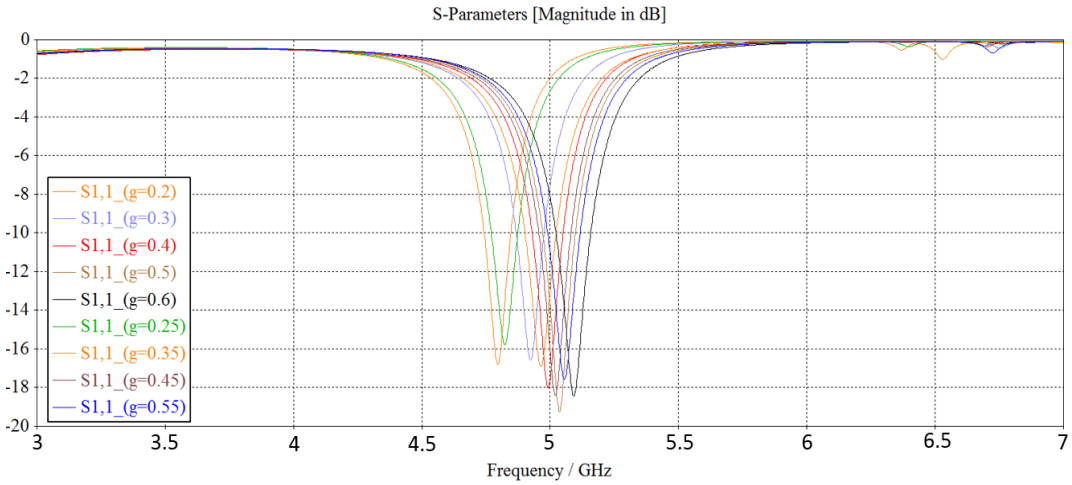

(a)

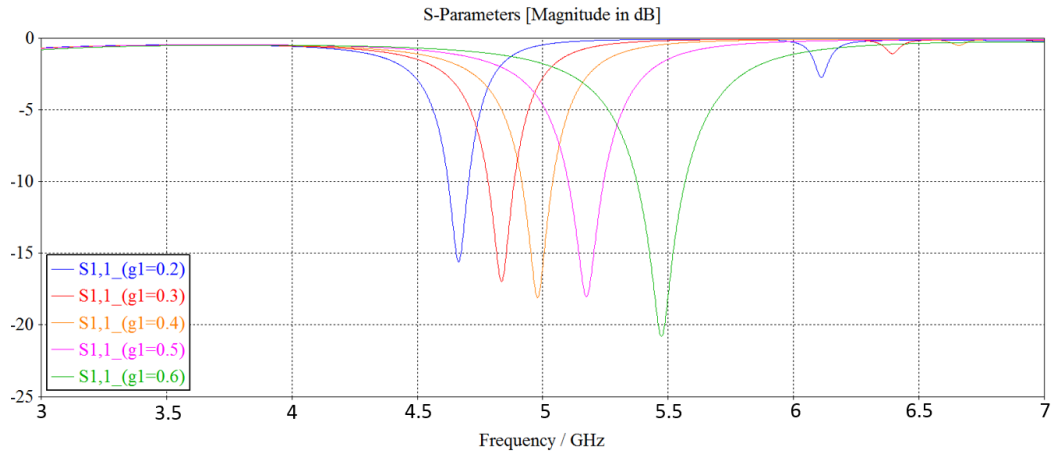

(b)

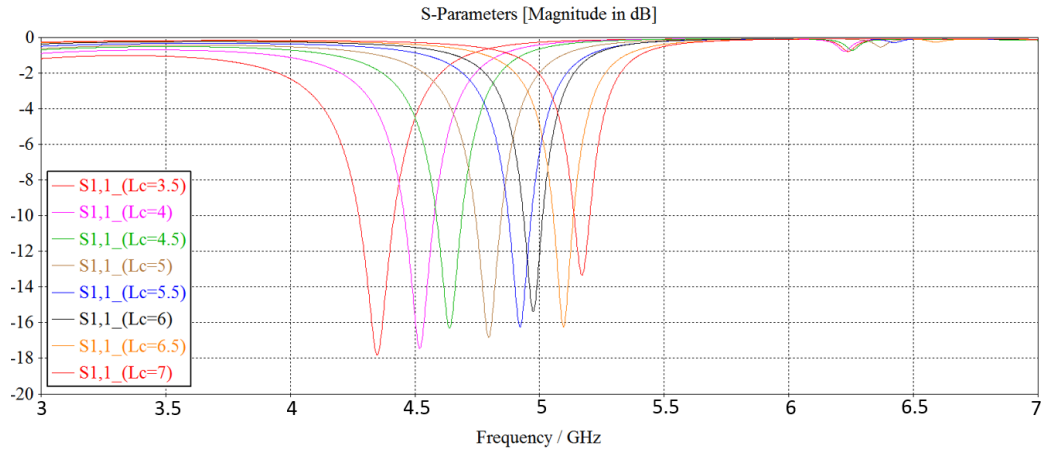

(c)

Figure 5. 13 (a) The resonant frequencies with changing gaps g_c (b) The resonant frequencies with changing the width of central plate g_1 (c) The resonant frequencies with changing length of central plate L_c

The gap g_c between the central plates are first changed from 0.2mm to 0.6mm, and the simulation results are shown in Figure 5.13 (a). As can be seen from Figure 5.13(a), when changing the gap from 0.2mm to 0.6mm, the resonant frequency shifts from 4.72GHz to 5.1GHz with the magnitude fluctuating from -16dB to -19dB. The 4mm increase in the gap indicates a frequency change of 0.38GHz, which means that resonant frequency is sensitive to the increases in the gap. Therefore, a high resolution mask is required to pattern the electrodes precisely to minimize the influence of the fabrication error. The width g_1 of the central plate is then changed from 0.2mm to 0.6mm, and Figure 5.13(b) shows the simulation results. As can be seen from Figure 5.13(b), the resonant frequency changes from 4. 7GHz to 5.46 GHz with changing the g_1 from 0.2mm to 0.6mm, which means an average increase of 0.2GHz with an increase of 0.1mm in the width. Changing the width of central plate has a significant change in the resonant frequency, which means the resonant frequency is very sensitive to the changes in the central plate's width. Again, it proves a high resolution mask is a must in the fabrication process.

The length of the central plate L_c is also investigated to figure out the influence on the resonant frequency. The length L_c of the central plate is varied from 3.5mm to 7mm, and the simulation results are shown in Figure 5.13. From Figure 5.13(c), the resonant frequency shows a clear shift from 4.34GHz to 5.16GHz when changes the L_c from 3.5mm to 7mm. The magnitude goes smaller with changing the length L_c, which changes from -18dB to -13dB. Increasing the length L_c decreases the magnitude of S_{11}, and in order to have good return loss, the length L_c should not be too long. Also, changing the length of 0.5mm increases about 0.1GHz in the resonant frequency, which also indicate the necessity of high resolution mask used in the fabrication process.

The simulations results above show that all the three dimensions affect the resonant frequency. With the understanding of how the three dimensions affect resonant frequency, the second optimization is conducted with changing the three dimensions to figure out the dimensions which can achieve the working frequency of 4.80GHz and largest tuning range. The optimization process suggests that with g_c of 0.25mm, g_1 of 0.3mm and L_c of 4.5mm, the resonant

frequency is 4.80GHz, and Table 5.7 shows the dimensions after second optimization.

L_{sub}	L	W	L_1	W_1	L_c	g_c	g_1
16	14	14	13	13	4.5	0.25	3

Table 5. 7 Dimension after second optimization using CST (unit:mm)

After the second optimization, the full wave simulation using CST is conducted, where LCs are used as homogeneous anisotropic materials. The alignment direction is chosen to be along *x*, as shown in Figure 5.11, and the LCs are switched from along *x* to along *z* direction. Figure 5.14 shows the full wave simulation results. It can be seen from Figure 5.14, with LC directors switching from along *x* to along *z*, the resonant frequency shift from 4.8GHz to 4.23GHz, and it corresponds to a frequency change of 570MHz and a tunability of 11.8%. The return losses at resonance are -19dB for the unswitched state and -21dB for the switched state, and insertion loss are no larger than -2dB. 11.8% of tunability is relatively a very good tunability, and this structure is fabricated and measured in later section.

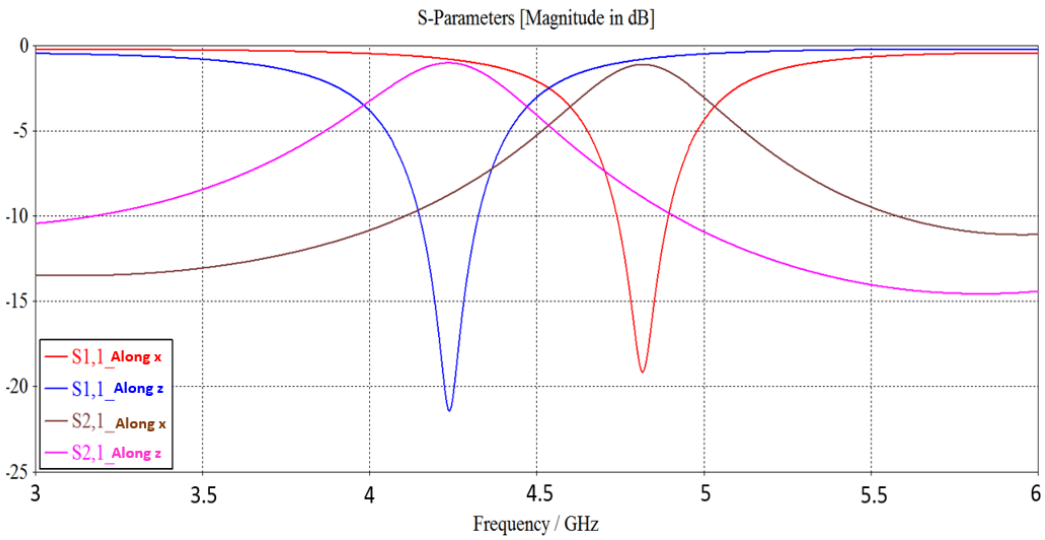

Figure 5. 14 The resonant frequency with LC director switching from unswithced to switched state

5.3 Tunable LC Resonator Using Type II ELC Resonator

An alternative structure to the ELC resonator is shown in Figure 5.15(a). Compared with the previous structure, this improved structure has two gaps in the inductive loops. The equivalent circuit for the improved structure is shown in Figure 5.15(b). The central plates and the gap in the inductive loops form the capacitors, and the inductive loops form the inductors. The total capacitance can be increased with the two additional gap capacitances, and the area to higher intensity to the electric field is also increased and observed from CST. In this way, larger tuning range can be generated as more LC can be fully switched with more area of higher intensity to the electric field.

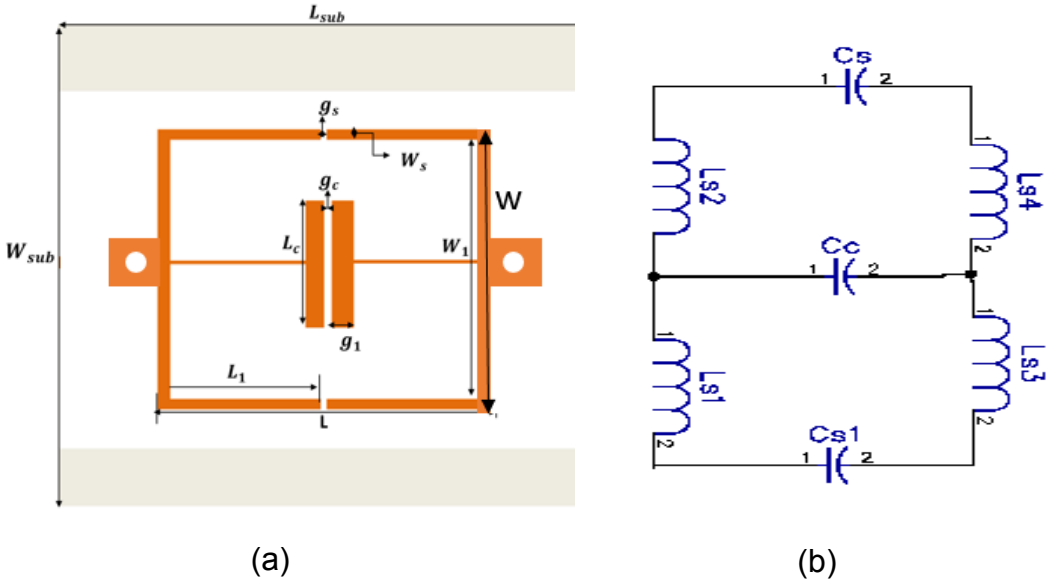

(a) (b)

Figure 5. 15 (a) Structure of the type II ELC resonator (b) Equivalent circuit of the Type II ELC resonator

As can be seen from Figure 5.15 (b), C_s and C_{s1} are the same capacitances derived from the gap of the conducting loops. L_{s1}, L_{s2}, L_{s3} and L_{s4} are the inductance of the conducting loops and they are the same value, so L_s is used to represent in the following equations. According to [Arritt, 2011] and [Withayachumnankul, 2011], the resonant frequency, capacitance and inductance of the ELC resonator could be calculated as follows

$$f_0 = \frac{1}{2\pi\sqrt{(C_c+C_s)(L_{s1}+L_{s3})}} \quad 5\text{-}13$$

$$C_s = \varepsilon_0 \frac{2}{\pi}\ln(2\alpha\frac{L_1}{g_s})W_s \quad 5\text{-}14$$

$$L_s = \frac{\mu_0(L-g_s)}{2\pi}\left[\ln\left(\frac{2(L-g_s)}{W_s}\right)+\frac{1}{2}+\frac{W_s}{3(L-g_s)}+\frac{g_s^2}{24(L-g_s)^2}\right] \quad 5\text{-}15$$

α is the propagation constant and it is 5/2 [Arritt, 2011]. C_c is the capacitance of the central strip, and it can be calculated using the equations from previous section. The working frequency is designed to be 5GHz and the initial dimensions using empirical equations for the resonator is shown in Table 5.8.

Optimization	L_{sub}	L	W	L_1	W_1	L_c	g_c	g_1	g_s
Before	16	14	14	13	13	4	0.3	2.5	0.3
After	16	14	14	13	13	4	0.2	3	0.2

Table 5. 8 Dimensions of amended ELC resonator shown in Figure 4.33(a) (Unit:mm)

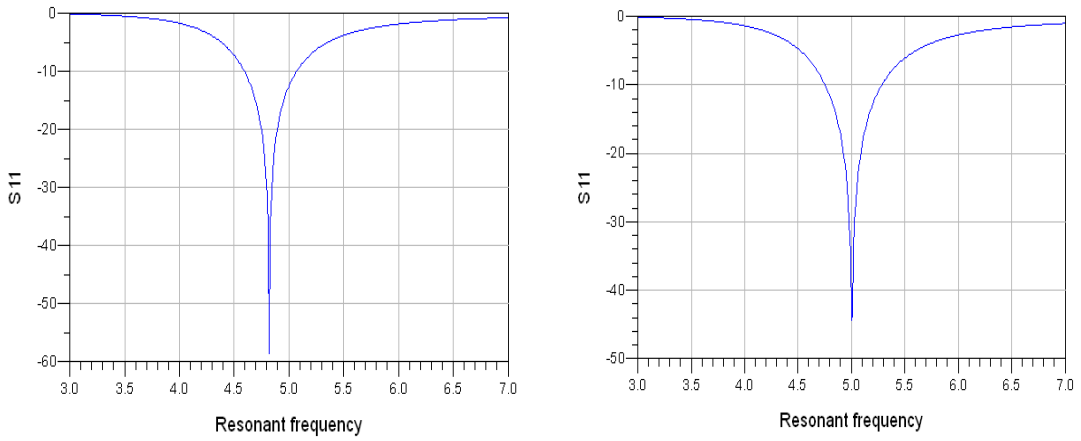

(a) (b)

Figure 5. 16 ADS results (a) before optimization (b) after optimization

The resonant frequency from ADS is shown in Figure 5.16 (a), and the resonant frequency is 4.86GHz, which indicates a discrepancy of 2.8% and it is an acceptable error. With the initial resonant frequency, the first optimization can be conducted to adjust the working frequency. The optimization involves changing the g_1, g_c, g_s and L_c. As shown in Figure 5.16 (b), the first optimization

shows that the working frequency of 5GHz is achieved when g_c *and* g_s are 0.2mm, g_1 of 3mm, and other dimensions remain the same, as shown in Table 5.8.

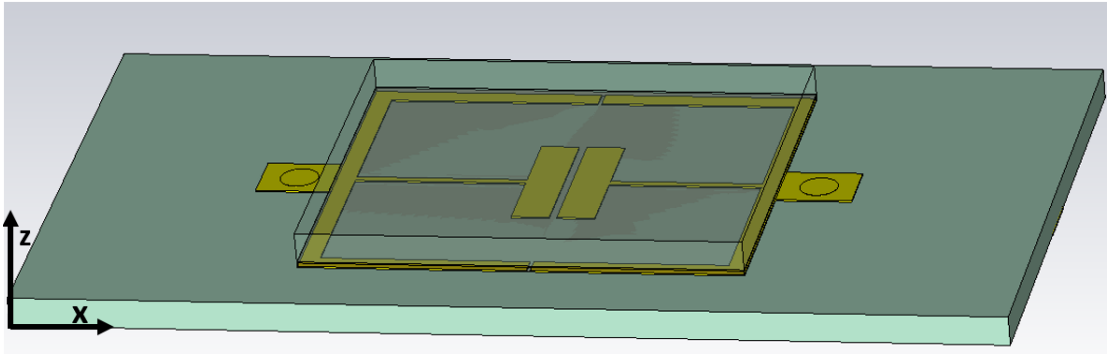

Figure 5. 17 3D structure of the type II ELC resonator

The 3D model is constructed in CST with the dimensions after first optimization using ADS, and it is shown in Figure 5.17. The full wave simulation is carried out using CST and the result of the resonant frequency is shown in Figure 5.18. It shows the resonant frequency of 4.9GHz with using the dimensions after first optimization. As the working frequency is 5GHz, second optimization is carried out to satisfy the requirement.

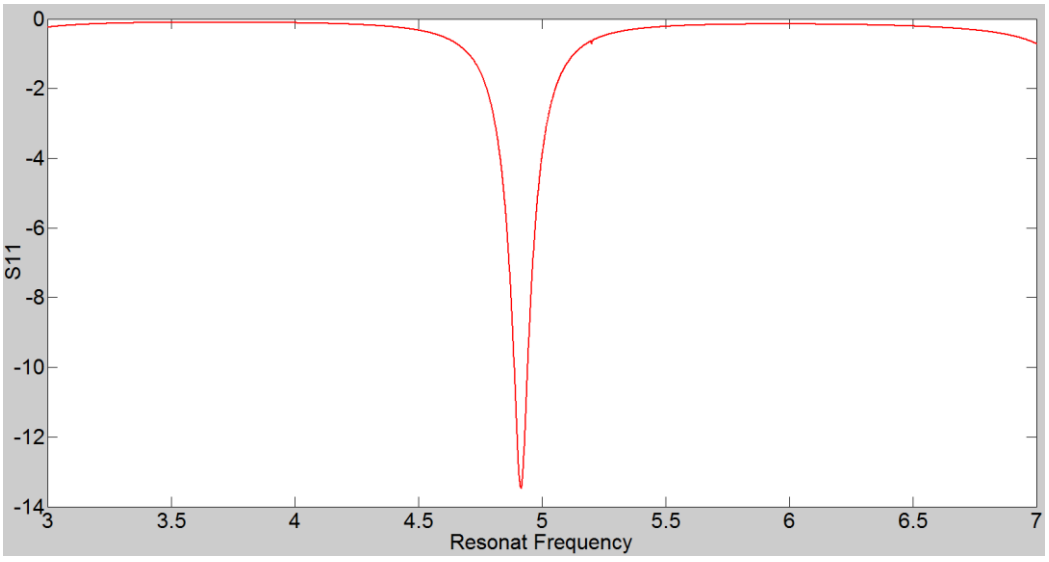

Figure 5. 18 Resonant frequency using dimensions after first optimization in CST

From the previous section, it is known that g_1, g_c, and L_c all affect the resonant frequency, and the resonant frequency is very sensitive to the change of g_1

and L_c. How g_s affects the resonant frequency needs to be figured out. Therefore, the gap g_s in the inductive loops is changed from 0.1mm to 0.4mm to find out the influence on resonant frequency. Figure 5.19 shows the resonant frequencies changes from 4.95 GHz to 4.8 GHz when changes the gap g_s from 0.1mm to 0.4mm, which means every increase of 0.1mm leads to an average decrease of 0.04 GHz. It means that changing in the gap g_s is not very sensitive to the resonant frequency.

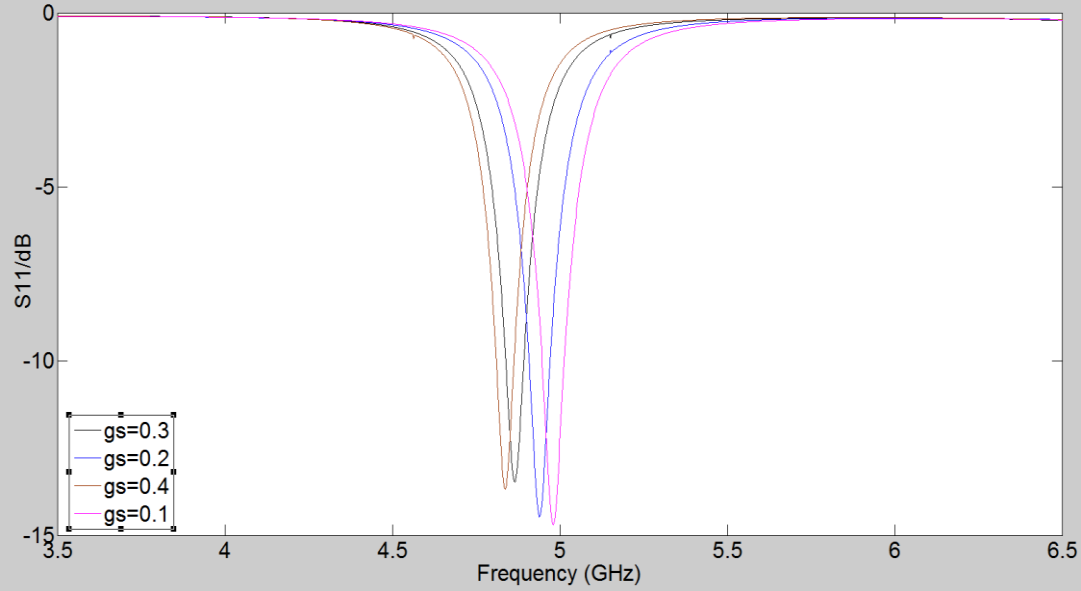

Figure 5. 19 Resonant frequency with different gap g_s

After understanding the influence of gap g_s, the second optimization is carried out with changing g_1, g_c, g_s and L_c. Since the resonant frequency using the dimension after first optimization is close to the designed working frequency, these dimensions do not need to change to a wide range to achieve the working frequency. After considering the fabrication limitations, g_1 *and* g_s are chosen to change from 0.1mm to 0.5mm, g_1 changes from 2mm to 3mm with a step of 0.1mm, and L_c varies from 3.5mm to 6mm as not to consider the coupling between central plates and inductive loops. The optimization starts with changing L_c and fixing other three variables. When the optimized L_c is found, the optimization is carried out with another dimension with fixing other three dimensions. In this way, the second optimization is completed with the final dimensions, as shown in Table 5.9.

L_{sub}	L	W	L_1	W_1	L_c	g_c	g_1	g_s
16	14	14	13	13	4.5	0.2	2.4	0.3

Table 5. 9 Final dimensions of the improved ELC resonator

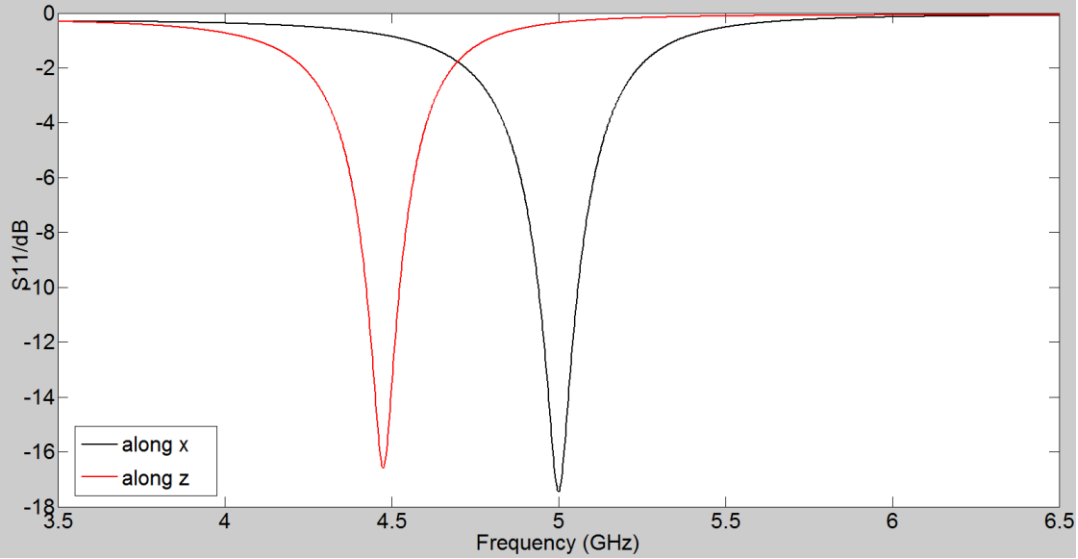

Figure 5. 20 Resonant frequency using final dimensions at unswitched and switched state

The 3D model is updated with the final dimensions, and the full-wave simulations using CST is conducted to figure out the working frequency, tuning range and tunability. Figure 5.20 shows simulation results of resonant frequency when switching LC directors from along *x* to along *z* as shown in Figure 5.17. Figure 5.20 indicates that by switching the LCs from along *x* to along *z*, the resonant frequency shifts from 5 GHz to 4.47 GHz, which shows a tuning range of 530MHz and a tunability of 10.6%.

5.4 Tunable LC Resonator Using Type III ELC Resonator

The third alternative to the ELC resonator is designed and shown in Figure 5.21(a). This alternative adds two additional inductive loops to the previous model, which forms two more inductances for the resonators. The equivalent circuit of the Type III ELC resonator is shown in Figure 5.21(b). Compared with previous model, if the additional inductive loops have wider width than the loops with gap, the additional inductive loops are acted as the dominant inductance, which decrease the total inductance and increase the working

frequency. Therefore, in order to maintain the working frequency, the capacitance *C* needs to be increased, and it can be realized by changing in either the gap or the width or length of central plate. The increase in the capacitance means a bigger change in the resonant frequency.

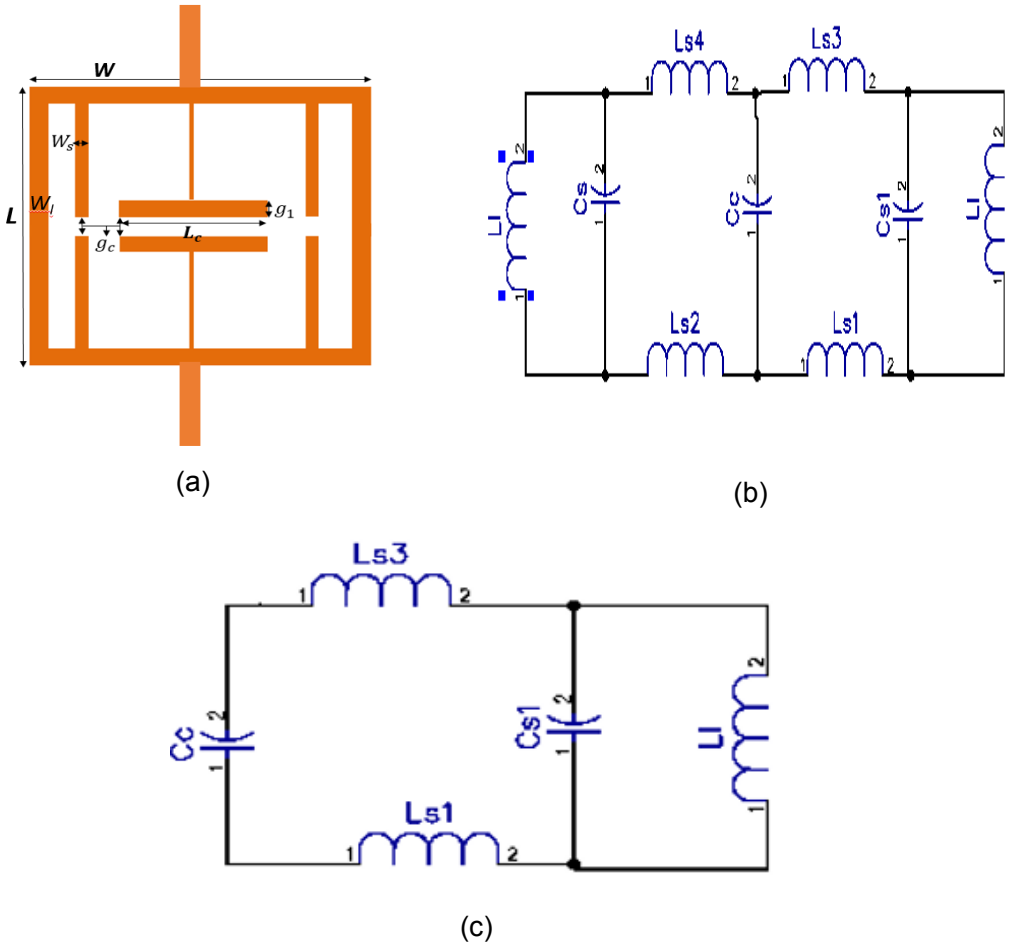

Figure 5. 21 (a) Structure of type III ELC resonator (b) equivalent circuit for type III ELC resonator (c) Simplified equivalent circuit for calculating resonant frequency

As the equivalent circuit is symmetric, this equivalent circuit can be simplified as Figure 5.21(c) when calculating the resonant frequency. The resonant frequency can be calculated as follows

$$f_0 = \frac{1}{2\pi}\sqrt{\frac{L_{s1}+L_1+L_{s3}}{(C_{s1}+C_c)(L_{s1}+L_{s3})L_1}} \qquad 5\text{-}16$$

In order for this resonator to work at 5GHz, the initial dimensions for the structure are calculated using the equations stated in section 5.1 and 5.3, and the dimensions are shown in Table 5.10 as the initial values. The equivalent circuit using ADS shows that with the initial calculation, the resonant frequency

is 4.84GHz, as shown in Figure 5.22 (a).

Optimization	L_{sub}	L	W	W_s	W_l	L_c	g_c	g_1
Initial	20	14	14	0.3	0.5	4	0.25	1.5
After	20	14	14	0.3	0.5	4	0.2	1.7

Table 5. 10 Dimensions for Type III ELC resonator after initial calculation (Unit: mm)

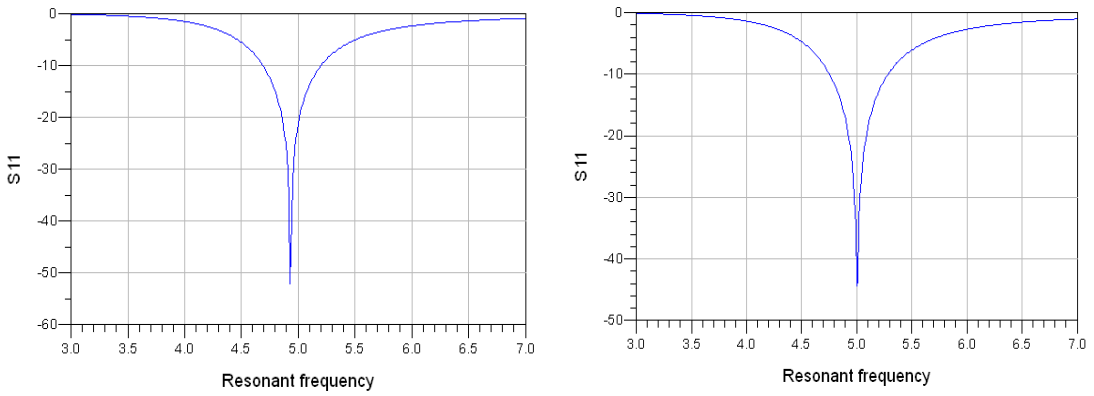

(a) (b)

Figure 5. 22 (a) The resonant frequency with initial calculation (b) The resonant frequency after first optimization

The first optimization is conducted to adjust the working frequency. The optimization mainly focuses on the dimensions affecting the capacitance, as higher intensity of electric field concentrates on capacitive elements, which are L_c, g_c and g_1. The value after optimization is shown Table 5.10 as the after value, and Figure 5.22 (b) shows the resonant frequency after first optimization.

After the first optimization, the dimensions are used to construct the 3D model in CST and shown in Figure 5.23. Compared with previous model, this model uses a different configuration of feed line, and they are put on the same side with the resonator structure. In the simulation with CST, as long as the impedance matching is well matched, it makes no difference to put feedline on the same side or the other side. The choice can depend on the own preference and ease of fabrication. The material used is Rogers Duroid 5880 with the thickness of 0.79mm as the dielectric substrate and the copper to pattern the electrodes has the thickness of 0.035mm.

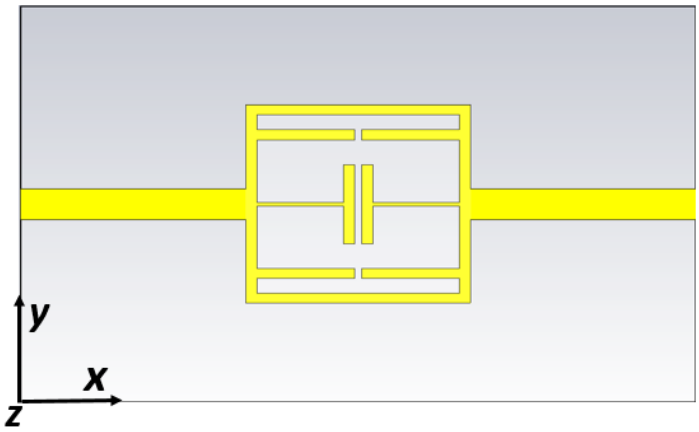

Figure 5. 23 3D of the type III ELC resonator in CST

Figure 5.24 shows the simulation results using the dimensions after first optimization. As can be seen from Figure 5.24, the resonant frequency shifts from 4.92GHz to 4.39GHz, and it corresponds to a tuning range of 540MHz and a tunability of 11%.

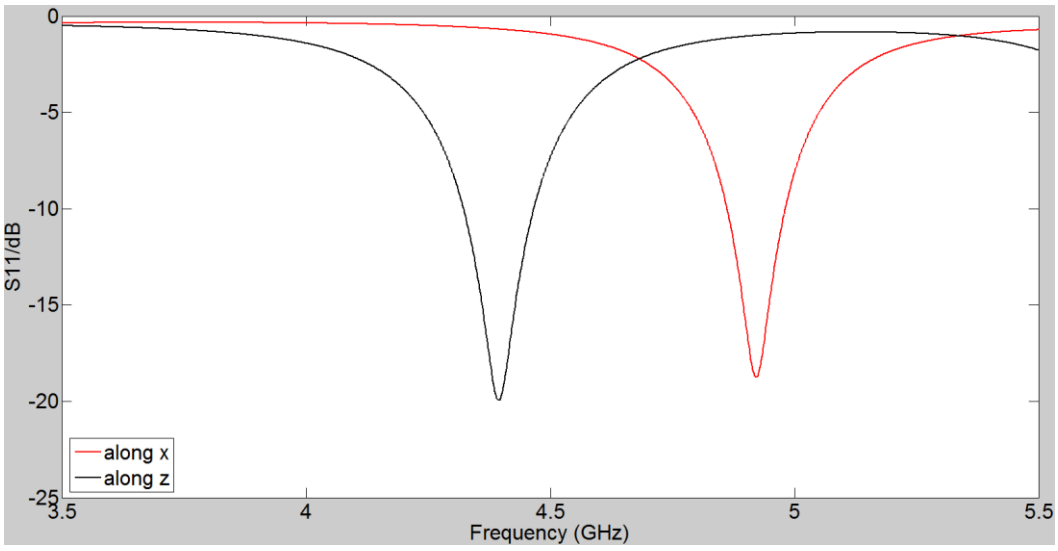

Figure 5. 24 Resonant frequency using the dimensions after first optimization

The second optimization involves adjusting the working frequency and optimizing tuning ragne by changing the dimensions of L_c, g_c and g_1. The gap g_c changes from 0.1mm to 0.5mm, g_1 changes from 1mm to 3mm with a step of 0.1mm, and L_c varies from 3mm to 5mm with a step of 0.5mm. The optimization suggests that with the dimensions shown in Table 5.11, the working frequency of 5GHz and the optimized tuning range are achieved.

L_{sub}	L	W	W_s	W_l	L_c	g_c	g_1
20	14	14	0.3	0.5	4	0.25	1.5

Table 5. 11 Dimensions for the resonator after second optimization (unit: mm)

With the final dimensions from the second optimization, the working frequency and the tuning range can be simulated with CST. Figure 5.25 shows the resonant frequency and tuning range when switches LC directors from along x to along z. It can be seen from Figure 5.25, the resonant frequency shifts from 5GHz to 4.42GHz, which corresponds to a tuning range of 570MHz and a tunability of 11.4%. The return losses at resonance are -28.7dB for the unswitched state and -26.4dB for the switched state, and insertion loss no bigger than -2dB. Compared with the previous two models, this alternation has the largest tuning range, and it needs to be fabricated and tested.

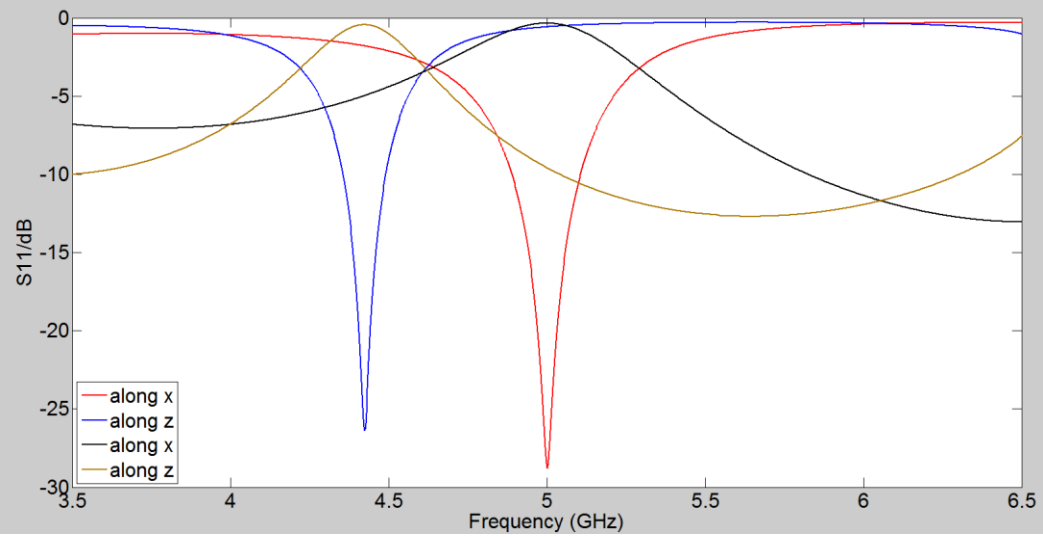

Figure 5. 25 Resonant frequency using dimensions after final optimization at unswitched and switched state

The performance of the three types of the ELC resonators are summarized in Table 5.12. As can be seen from the Table 5.12, Type I and type III ELC resonators have the tuning range of 570MHz, and the tuning range of Type II ELC resonator is 0.53GHz. The fractional bandwidth (FBW) is the bandwidth of the device divided by its centre frequency, and it means that the smaller the FBW, the narrower the bandwidth is. Compared with Type I and Type III ELC

resonator, type II ELC resonator has it has narrower bandwidth at both unswitched and switched state, since the FBW is smaller than them. All the three types of the ELC resonators are fabricated and measured so that the simulation and measured results can be compared to verify the design method.

	Switching state	Centre Frequency (GHz)	FBW	Tuning Range (GHz)	Tunability
Type I ELC	Unswitched	4.8	10.6%	0.57	11.8%
	Switched	4.23	13.4%		
Type II ELC	Unswitched	5	7.6%	0.53	10.6%
	Switched	4.47	7.8%		
Type III ELC	Unswitched	5	13%	0.57	11.4%
	Switched	4.42	10.2%		

Table 5. 12 Summary of three types of ELC resonators

5.5 Measurement Results for Tunable LC Resonators Using ELC resonators

5.5.1 Measurement for Tunable LC Resonator Using Type I ELC resonator

Component	Material	Thickness (mm)
Microstrip line substrate/Ground plane substrate	Rogers Duroid 5880	0.79
Microstrip line and ground plane	Copper	0.035
Spacer	Rogers Duroid 5880	0.13
Liquid Crystals	Merck E7	0.13

Table 5. 13 The dimensions for the component to build the device

The material of Rogers Duroid 5880 has been chosen as the dielectric substrate because its low permittivity allows higher field confinement in the LC region, increasing the effect of the LC switching. The board is cleaned first by using acetone, and it uses the traditional etching method stated in Chapter 3 to pattern electrodes. Another piece of Rogers Duroid 5880 is used as the spacer, which is etched first to remove the copper and laser cutter is then used to cut the shape of the spacer. The device is then assembled using the process stated in Chapter 3. The dimensions for the material is shown in Table 5.13, and the Figure 5.26 shows the patterned electrodes, the shape of spacer and the assemble device. Liquid crystal E7 from Merck is used for the all the fabricated devices in the thesis.

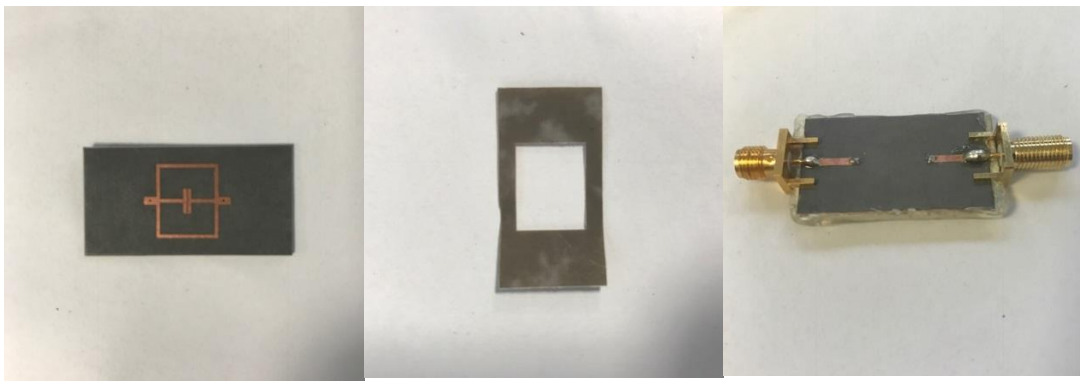

(a) (b) (c)

Figure 5. 26 (a) Patterned ELC resonator (b) the shape of spacer (c) the assemble device

The device is measured using the measurement setup discussed in Chapter 3. Measurements were taken with the biasing voltage amplitude varying from 0 V to 16 V in 0.5 V steps with using the 1kHz AC voltage, as stated in Chapter 3.4.3. Figure 5.27 shows the measurement results with different external voltage applied. As can be seen from Figure 5.27(a), the resonant frequency shifts from 4.76GHz to 4.29GHz with changing the external voltage from 0V to 16V. The tuning range is 470MHz and the tunability is 9.8%. The return losses are -21.6dB for 0V and -16.5dB for 16V. The insertion loss shows in Figure 5.27 (b), and the insertion losses are under -3dB at resonant frequencies for all the measurement external voltage.

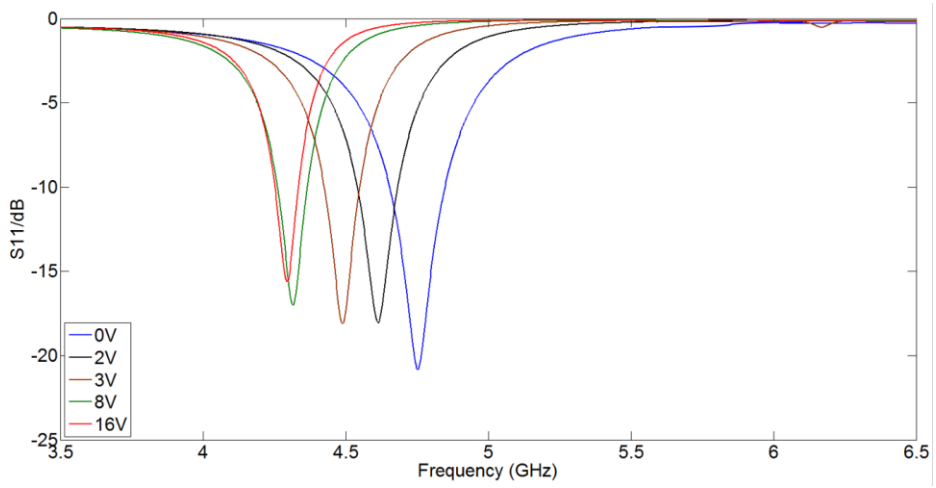

(a)

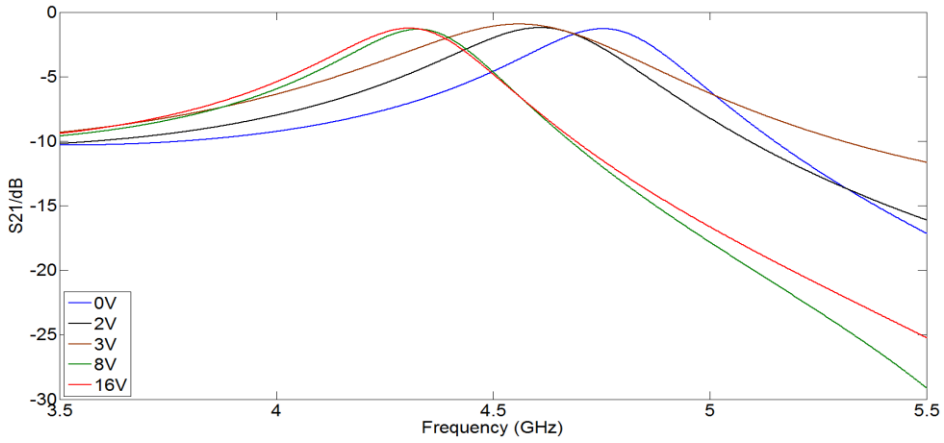

(b)

Figure 5. 27 (a) The measured results of S_{11} (b) The measured results of S_{21}

Figure 5.28 shows the centre frequency as a function of the LC bias voltage. When a voltage is applied across an LC cell there is a threshold voltage before the LC starts gradually to re-orient itself to the applied field (Fréedericksz transition). For E7 this threshold is about 0.5 V and Figure 5.28 shows this behavior for the centre frequency. After 0.5V, the central frequency decreases slowly and continuously for intermediate values between 0.5V to about 8V and there is little change after that. When the bias voltage increases to more than 8V, the LC reaches a saturation state and most of the LC is oriented perpendicular to the electrodes.

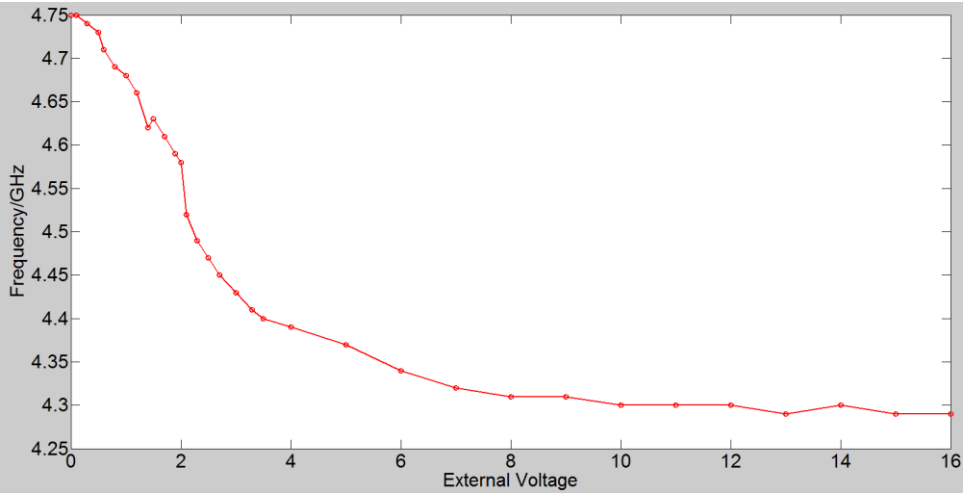

Figure 5. 28 Frequency as a function of bias voltage

Figure 5.29 shows the comparison of simulation results and measured results for the unswitched and switched states. As can be seen from Figure 5.29, the simulated and measured S_{11} show a discrepancy of 0.04 GHz (0.8%) and it can be seen as very good agreement in the unswitched state. The result in the switched state shows 4.23 GHz for the simulation along z and 4.29 GHz for the switched state. This discrepancy is 0.06 GHz and it corresponds to a difference of 1.4%, which is an acceptable discrepancy. This discrepancy may be attributed to the reason that in the actual situation, most of the LCs are switched while some LCs near the electrodes and ground plane are not switched, which results in the actual relative permittivity smaller than the permittivity used in the simulation as explained in Chapter 4. As for the fractional bandwidth (FBW), it is 10.5% at unswitched state and 12.6% at 0V, and the discrepancy is 1.9%, which is a good agreement. The FBW is 9.7% at switched state and 14% at 16V, which corresponds to a discrepancy of 5.3% and this deviation is acceptable. Therefore, based on the comparison between simulated and measured results, the general design method proposed for tunable LC devices based on microstrip configuration is verified as correct and effective to use.

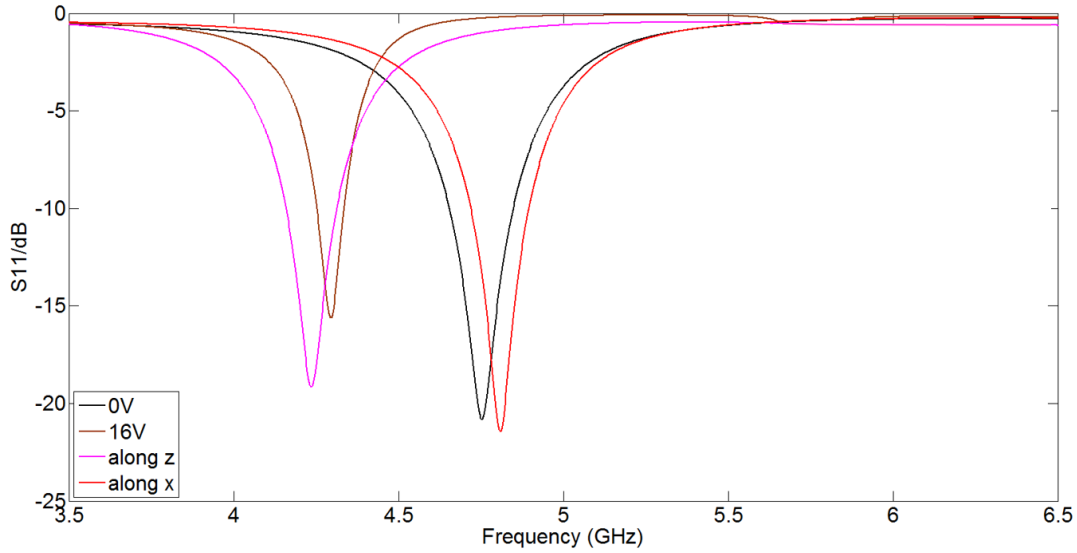

Figure 5. 29 Comparison of measured and simulated results for type I ELC resonator

5.5.2 Measurement of Tunable LC Resonator Using Type II ELC Resonator

The same fabrication procedure is used to produce electrode patterns and assemble the device, as the assemble devices shown in Figure 5.30. This device is then measured using the standard measurement setup and using bias voltage from 0V to 16V with a step of 0.5V to switch the LCs.

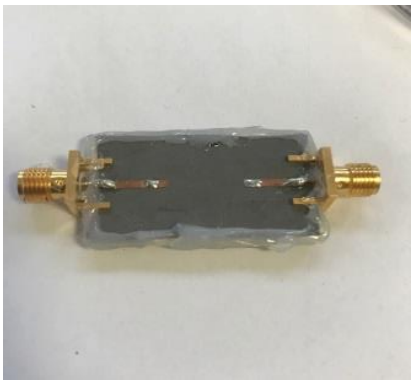

Figure 5. 30 The assemble Type II ELC resonator

Figure 5.31 shows the measured resonant frequency when applying bias voltages, and it shows that the resonant frequency shifts from 4.98 GHz to 4.51GHz with increasing the external voltage from 0V to 16V. The tuning range is 480MHz and it corresponds to a tunability of 9.6%. It also shows that with

the increasing of the voltage, the return loss shows a decrease. The decrease in the return loss can be attributed to the anisotropy of the loss tangent which is higher along the director.

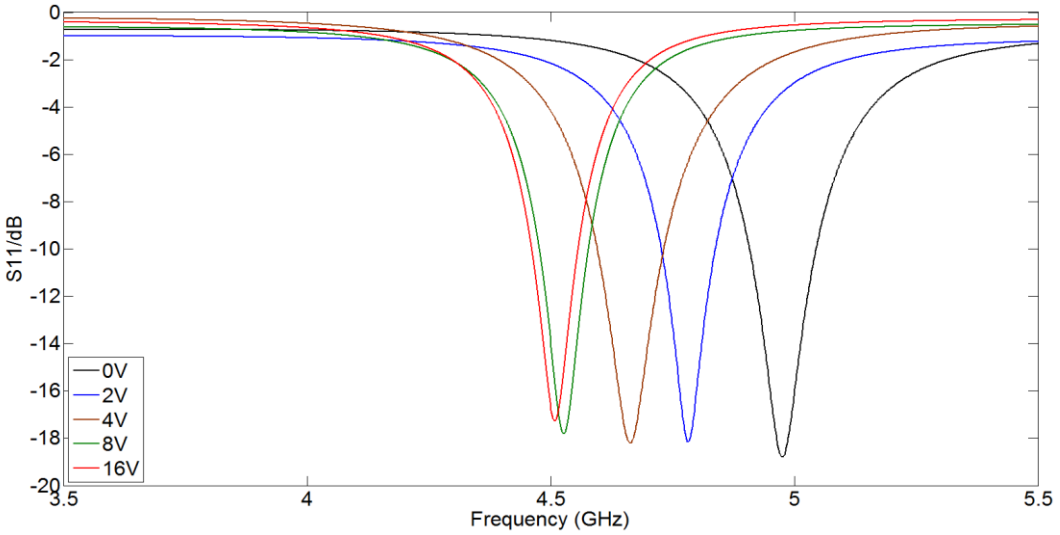

Figure 5. 31 The measured resonant frequency with external bias voltage for type II ELC

Figure 5.32 shows the resonant frequency as a function of the bias voltage. It can be seen from the Figure 5.32, the threshold voltage is about 0.5V, which is similar as the results from previous measurement. After the threshold voltage, the frequency decreases continuously and drastically between 0.5V to 8V. There is small changes in the frequency after 8V, and it means that 8V is the saturation voltage.

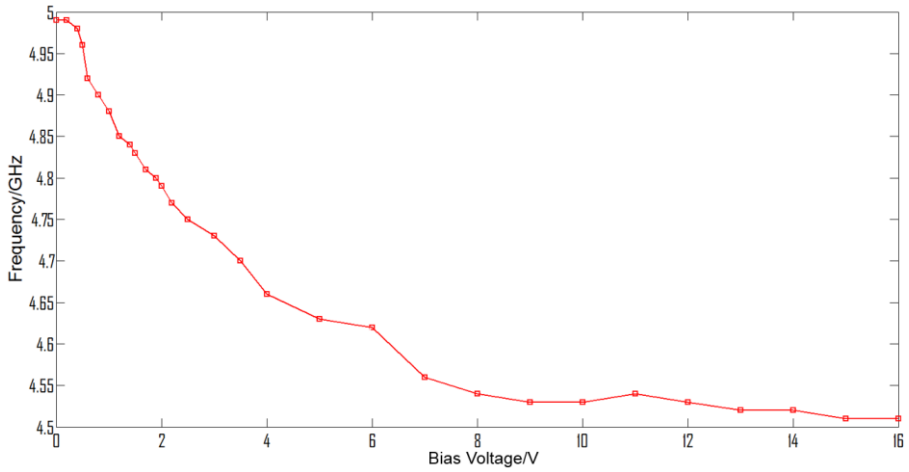

Figure 5. 32 Frequency as a function of bias voltage for type II ELC

The comparison between the measured and simulated results is shown in Figure 5.33. As can be seen from Figure 5.33, in the unswitched state, the resonant frequencies for the simulation along x and measured are 5GHz and 4.98GHz, and there is very good agreement between them. At switched state, the simulation along z is 4.47GHz while the measured result is 4.51GHz, and it shows a discrepancy of 0.04GHz. As discussed above, this discrepancy can be attributed to the difference in the relative permittivity between the simulation and actual measurement. The fractional bandwidth for the simulated and measured results shows some discrepancies. The FBW for the simulated results are almost constant, and the measured FBW for the measured results increases for 50MHz between 0V to 16V. The 3dB bandwidth for measured results is nearly double that of the simulated results. The explicit reason for the discrepancy is unknown, but it may be attributed to the fabrication error and shortcomings of the simulation software.

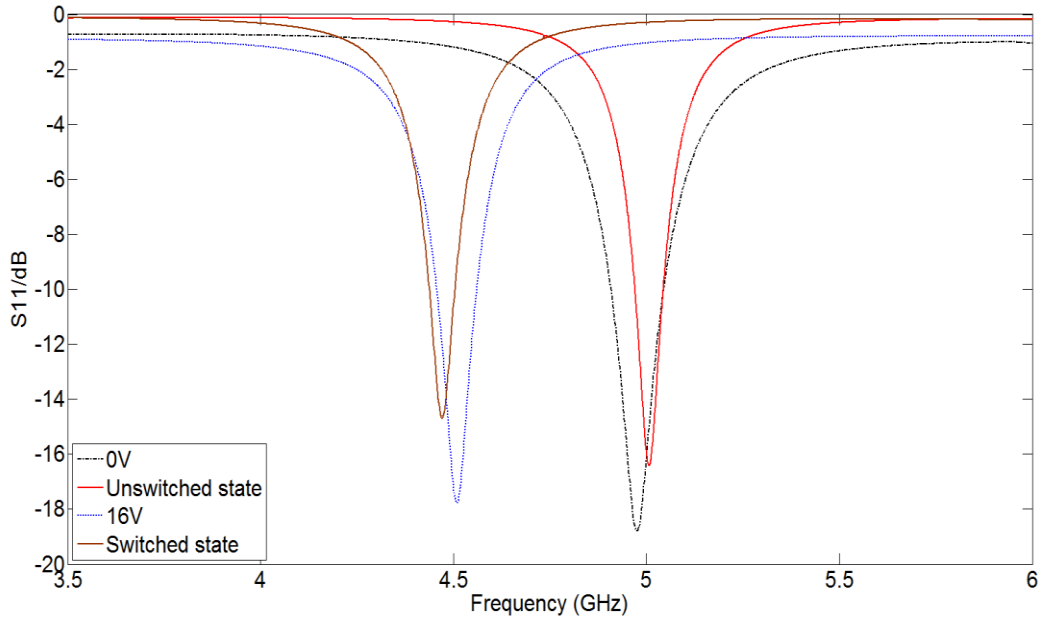

Figure 5. 33 Comparison between simulation and measured results for type II ELC

5.5.3 Measurement of Tunable LC Resonator Using Type III ELC resonator

Compared with previous two models, type III ELC resonator uses a different

configuration which uses feed lines and the resonator structure on the same side. As shown in Figure 5.34, the microstrip lines labeled with red circles are used to connect the ground plane with the connectors so that the low AC bias voltage can be applied to switch the LCs. This connection is realize by using a thin layer of the conductive material to connect the microstrip lines in the red circles with the ground plane, and the microstrip lines are then soldered with the connectors to connect the ground plane and the connectors. In this way, the connection is built and the voltage can be applied.

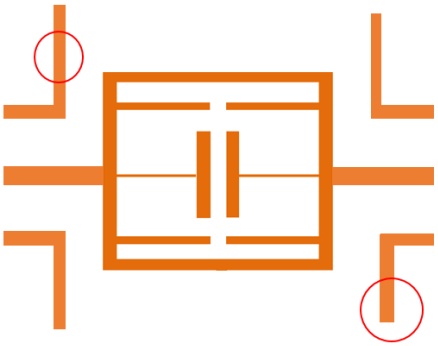

Figure 5. 34 (a) The layout of Type III ELC resonator

Figure 5.35 shows the measured results with applying the external voltage, and the resonant frequency shifts from 4.98 GHz to 4.46 GHz when the bias voltage changes from 0V to 16V. The tuning range is 520 MHz and it means a tunability of 10.5%. The return loss shows a decrease from -19.5dB to -14dB from 0V to 16V. The reason for the decrease has been discussed above.

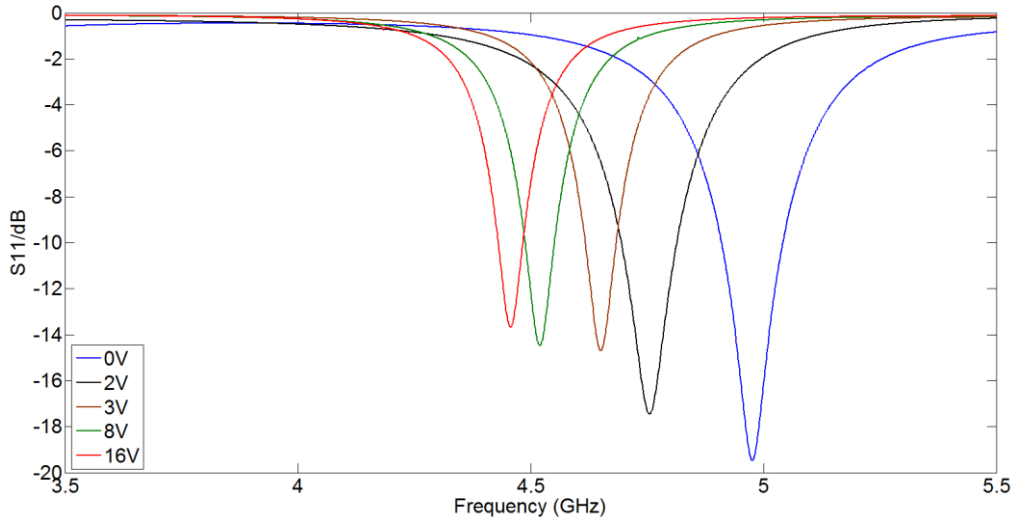

Figure 5. 35 Measured resonant frequency with different bias voltage for type III ELC

Figure 5.36 shows the resonant frequency as a function of bias voltage. As discussed above, the threshold voltage is 0.5V which can be seen from the figure. The saturation voltage is 8V, and beyond 8V, there is little change in the frequency. The main change in the frequency happens between 0.5V to 8V and this change is a continuously decrease.

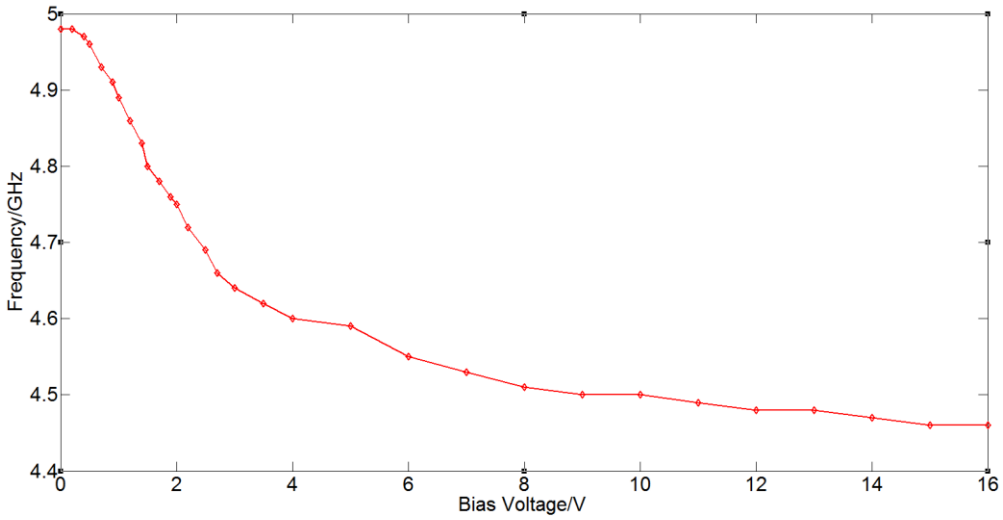

Figure 5. 36 Resonant frequency as a function of bias voltage

Figure 5.37 shows the comparison between the measured and simulated results. As can be seen from the figure, at the unswitched state, the resonant frequency from simulation along x is 5GHz while the measured results shows 4.98GHz, and it is a discrepancy of 0.02GHz (0.4%). Since the discrepancy is quite small, at the unswitched state, there is good agreement between the simulation and measured results at the resonant frequency. At switched state, for the resonant frequency, it is 4.46 GHz for the measured results and 4.42 GHz for the simulation results, which shows a small discrepancy of 0.04 GHz (0.9%). In the resonant frequency, for both unswitched and switched state, there are good agreements between measured and simulated results. However, for the magnitude, there are big discrepancies. As can be seen from Figure 5.37, the return losses are -20dB and -26dB for the unswitched state, and it can be seen as reasonable agreement. For the switched state, the return losses are -14dB for the measured results and -28dB for the simulation results, which is double in the value. The reason for this discrepancy can be attributed

to the configuration of feedline and the microtrip lines connecting the ground plane and the connectors.

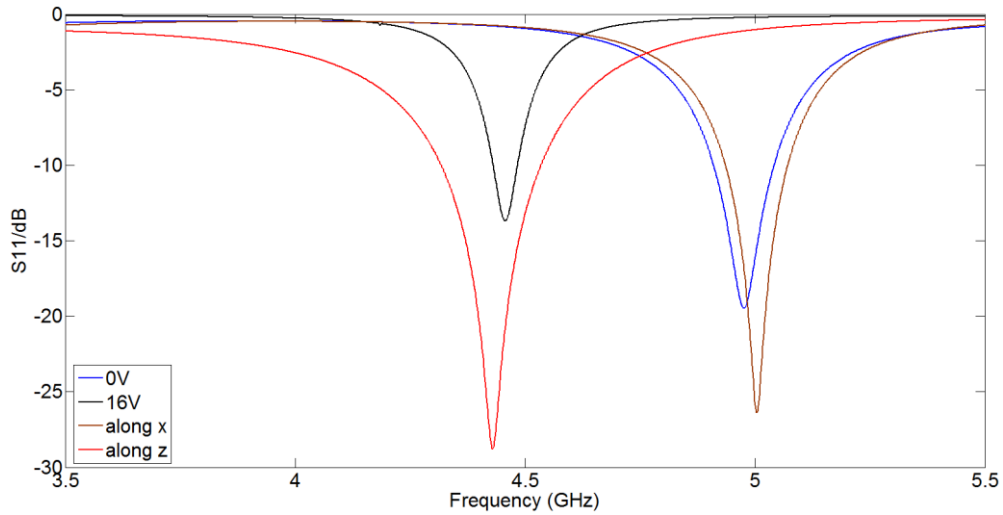

Figure 5. 37 Comparison between measured and simulated results for type III ELC

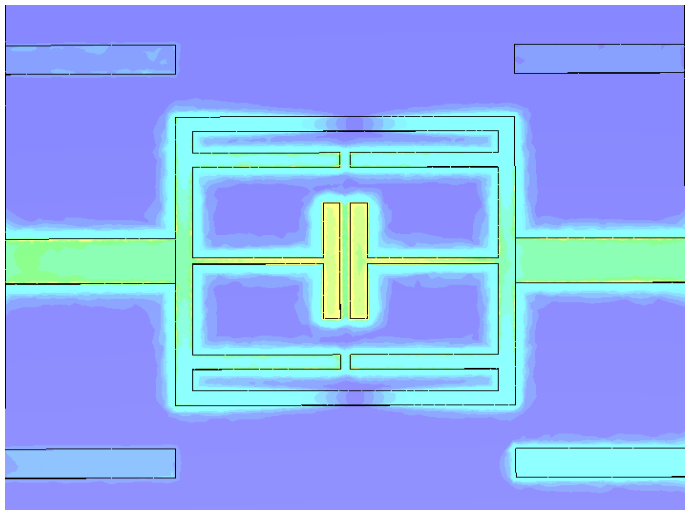

Figure 5. 38 Electric field including four additional electrodes for type III ELC

The CST simulation is used to include the four electrodes to figure out how these electrodes affect the resonant frequency. The simulation suggests that some of the electric field is generated in the additional electrodes as shown in Figure 5.38, and it makes power loss and can reduce the depth of the measured S-parameters. Therefore, this configuration is not preferred and feed lines on different side is used for the following designs.

5.6 Conclusion

The proposed design method is demonstrated with the design and fabrication of three tunable microstrip LC resonators, using an inverted microstrip structure consisting of three types of ELC resonators. The first resonator using ELC resonator is designed to work at 4.8GHz and the LC used is E7. The fabricated device is measured and shows a tuning range of 470MHz with a tunability of 9.8%, in good agreement with the predictions from CST. The biggest discrepancy of the resonant frequency between measured and simulated results is 0.06 GHz and it corresponds to a difference of 1.4%. The second and third devices used type II and III ELC resonators to form tunable resonators using LCs are designed to work at 5GHz. These two resonatorss are then fabricated and measured. The type II tunable ELC resonator using LCs has a tuning range of 480MHz and it corresponds to a tunability of 9.6%, and the type III tunable ELC resonator using LCs has a tuning range of 520 MHz and it is a tunability of 10.5%. The biggest discrepancies of resonant frequencies for type II and type III tunable ELC resonator are 40MHz and 40MHz, respectively. There are very good agreements for the three types of tunable LC resonators in the resonant frequencies between the simulated and measured results. Therefore, the general design method proposed is an effective methodology and can be used for the design of microstrip tunable devices based on LCs. However, in the type II and type III ELC resonator using LCs, there are discrepancies in the 3dB bandwidth. In the following designs, a method to control bandwidth may be proposed, if the 3dB bandwidth needs to be constant.

The merits of using ELC resonator is that this types of structure increase the tuning range and tunability. The rough estimation of the tunability for E7 LC from using the perpendicular and parallel permittivity is about 6% to 7%. However, for the three types of ELC resonators simulated and measured, the tunability are 9.8%, 9.6% and 10.5%, respectively, which are bigger than the estimation. The reason might be this structure couples strongly to the electric field and thereby increasing the tuning range and tunability.

Chapter 6 Tunable LC Resonators Using Interdigital Capacitors

In the previous chapter, the design method has been tested and verified by designing tunable resonators using ELC resonators to work at 5GHz. Since the second objective is to explore more possibilities of using LC based devices. In this chapter, a different type of tunable resonators using IDCs are investigated.

In this chapter, resonators working at 2.4GHz are investigated. The ELC resonator has been shown to be an effective structure to use with LC as a tunable device in Chapter 5. Therefore, in order to employ the characteristics of strong coupling to electric field and use the simple equivalent circuit of ELC resonator, an alternative structure needs to be proposed to make it work at 2.4GHz. In order to work at lower microwave frequencies, either a higher capacitance or inductance is needed [Bilotti, 2007]. One way of reducing the resonant frequency is to introduce more inductance in the arms [Schurig, 2006]. However, increasing the inductance using these arms means increasing the size of the resonator, as stated in previous chapter the inductive loops provide the inductance. Increasing the size is not the ideal choice, since a small size is preferred in modern wireless communication systems [Kumar, 2013b]. Another way to achieve a lower frequency resonance is to increase the capacitance. In order to increase the capacitance, interdigital capacitors (IDC) are considered to use as the alternative structure. More capacitance is achieved in this way, by increasing the length of the electrodes in a small area [Bahl, 2003].

In this chapter, tunable bandpass resonators using IDCs are designed, simulated, fabricated and tested. The first part of this chapter focuses on designing tunable resonators working at 2.4GHz. Three types of tunable resonators using different numbers of IDC fingers are designed, optimized and simulated to achieve the largest tuning range. Since using IDC can provide more capacitance and $f = \frac{1}{\sqrt{LC}}$, it means with a fixed resonant frequency, using

IDC needs smaller inductance than the ELC resonator. Smaller inductance in this type of structure mean decreased length of inductive loops as the inductive loops provide the inductance. Therefore, with the aim of size reduction, the tunable resonators using IDC are also designed to work at 5GHz. The resonators using IDCs are designed, optimized and fabricated. A comparison of the performance of the tunable resonators using LCs is made between the designed IDC resonators and other resonators from literatures.

6.1 Design Method for the IDC Resonators

The detailed structure chosen for the inverted microstrip resonator is shown in Figure 6.1(a), and follows ideas from [Yagmaee, 2013]. As long as the overall size of the resonator is small fraction of the operating wavelength, this resonator can be approximated by an inductor and capacitor in the form of a resonant circuit [Yagmaee, 2013; Hong, 2003]. As shown in Figure 6.1(a), the interdigital capacitors (IDC) provide the capacitance and the two outer branches connecting in parallel provide the inductance to the circuit. The simplified equivalent circuit for the resonator is shown in Figure 6.1(b), where *C* is the total equivalent capacitance of the IDC, L_1 is the inductance from the IDC and L_2 is the inductance of the loops. Since the effective length of IDC is long, the inductance L_1 from the IDC cannot be ignored.

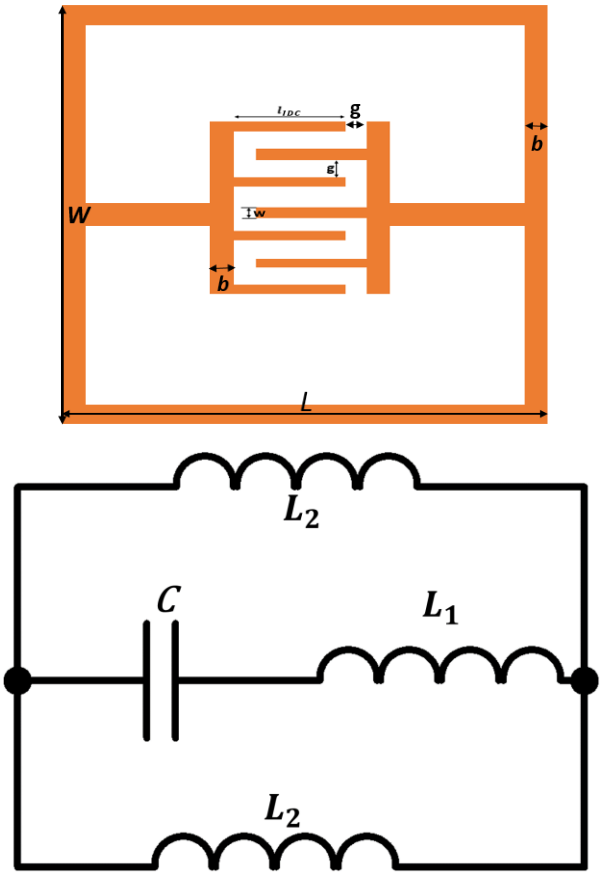

Figure 6. 1 (a) Schematic view of the resonator (for illustration) (b) Equivalent circuit of the resonator.

For the resonant circuit, the resonant angular frequency ω is given by $1/\sqrt{LC}$, therefore, *C* and *L* are needed to determine the resonant frequency. The partial capacitance method [Gevorgian, 2001; Gupta, 1996] is used to find the capacitance and inductance of the resonator, and the capacitance *C* of the IDC can be analytically calculated as follows [Gevorgian, 2001],

$$C_{IDC} = \frac{\varepsilon_{eff} 10^{-3}}{18\pi} \frac{K(k)}{K'(k)} (N-1) l_{IDC} \qquad (pF) \qquad 6\text{-}1$$

Where the capacitance of the IDC shows in Figure 6.1(a) is a function of the finger length *l*, total number of fingers *N*, line width *w*, gap width *g*, and effective dielectric constant ε_{eff}.

The ratio of complete elliptic integral of first kind $K(k)$ and its complement $K'(k)$ is given by

$$\frac{K(k)}{K'(k)} = \begin{cases} \frac{1}{\pi}\ln\left\{2\frac{1+\sqrt{k}}{1-\sqrt{k}}\right\} & for\ 0.707 \le k \le 1 \\ \frac{\pi}{\ln[\frac{1+\sqrt{k'}}{1-\sqrt{k'}}]} & for\ 0 \le k \le 0.707 \end{cases} \quad 6\text{-}2$$

and $k = tan^2(\frac{w\pi}{4(w+g)})$; $k' = \sqrt{1-k^2}$. All the lengths are in microns.

The inductance of the IDC L_1 is approximated as [Gevorgian, 2001]

$$L_1 = \frac{Z_o\sqrt{\varepsilon_{eff}}}{c} \quad 6\text{-}3$$

where $\varepsilon_{eff} = \frac{\varepsilon_r+1}{2} + \frac{\varepsilon_r-1}{\sqrt{1+12(\frac{h}{b})}}$, Z_o and ε_{eff} are calculated with the loop width *b* and thickness *h* and *c* is the velocity of light in free space.

The loop inductance L_2 is approximated as [Yagmaee, 2013]

$$L_2 = \mu_0\mu_r h(2\frac{b}{W} + 2\frac{L}{b} + \frac{L-2b-g-l}{b}) \quad 6\text{-}4$$

The permeability μ_r of the LC can be approximated by $\mu_r = 1$.

The resonant frequency for this resonator can be calculated as

$$f = \frac{1}{2\pi\sqrt{(L_2+L_1)C_{IDC}}} \quad 6\text{-}5$$

When N is 2, the IDC can be seen as an ELC resonator with two parallel strips. When the ELC resonator and IDC have the same line width, gap width, same substrate, compared the capacitance *C* from ELC resonator, the C_{idc} *can be rewritten as*

$$C_{idc} = (N-1)\frac{l_{idc}}{lelc}C \quad 6\text{-}6$$

Where l_{elc} and l_{idc} are the length of the parallel strip of ELC resonator and IDCs. The resonant frequency of IDC can be converted into

$$f_{idc} = \sqrt{\frac{l_{elc}}{l_{idc}(N-1)}}f_{elc} \quad 6\text{-}7$$

The equation 6-7 shows clear that if the ELC and IDC have the same length of parallel strips, using IDC with multiple fingers have lower resonant

frequency then ELC resonator, which shows that using IDC is an effective way to work at lower microwave frequencies.

6.1.1 Verification of C_p

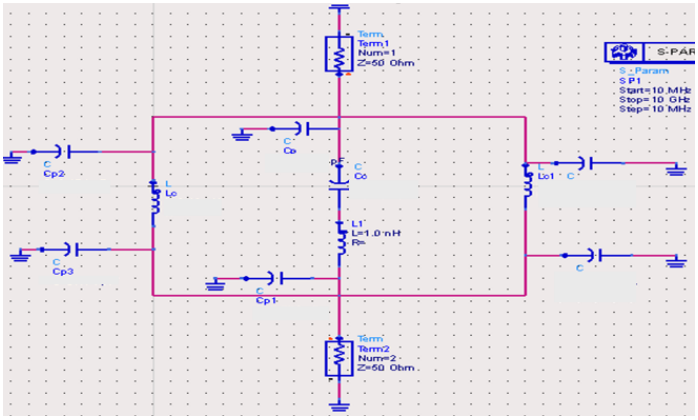

Figure 6. 2 Equivalent circuit including C_p

As stated in the previous chapter, if the capacitances C_p is not included in the design equations, whether it is reasonable to exclude the C_p needs to be verified. Figure 6.2 shows the equivalent circuit including C_p in the ADS simulation. The equivalent circuits including and excluding C_p are both simulated with ADS, and the results are shown in Figure 6.3. It is designed to work at 2.4GHz with using IDC with 5 fingers. As can be seen from Figure 6.3 (a) and (c), the resonant frequencies at unswitched state including C_p and excluding C_p are 2.38GHz and 2.36GHz, respectively. At switched state, the resonant frequencies are 2.10GHz including C_p and 2.04GHz excluding C_p. The biggest discrepancy in the simulation results is 60MHz (2.1%), and it means including the C_p changes only 2.1% of the resonant frequency, which is relatively a small change. Therefore, in the ADS simulation, C_p is not included in the simplified equivalent circuits.

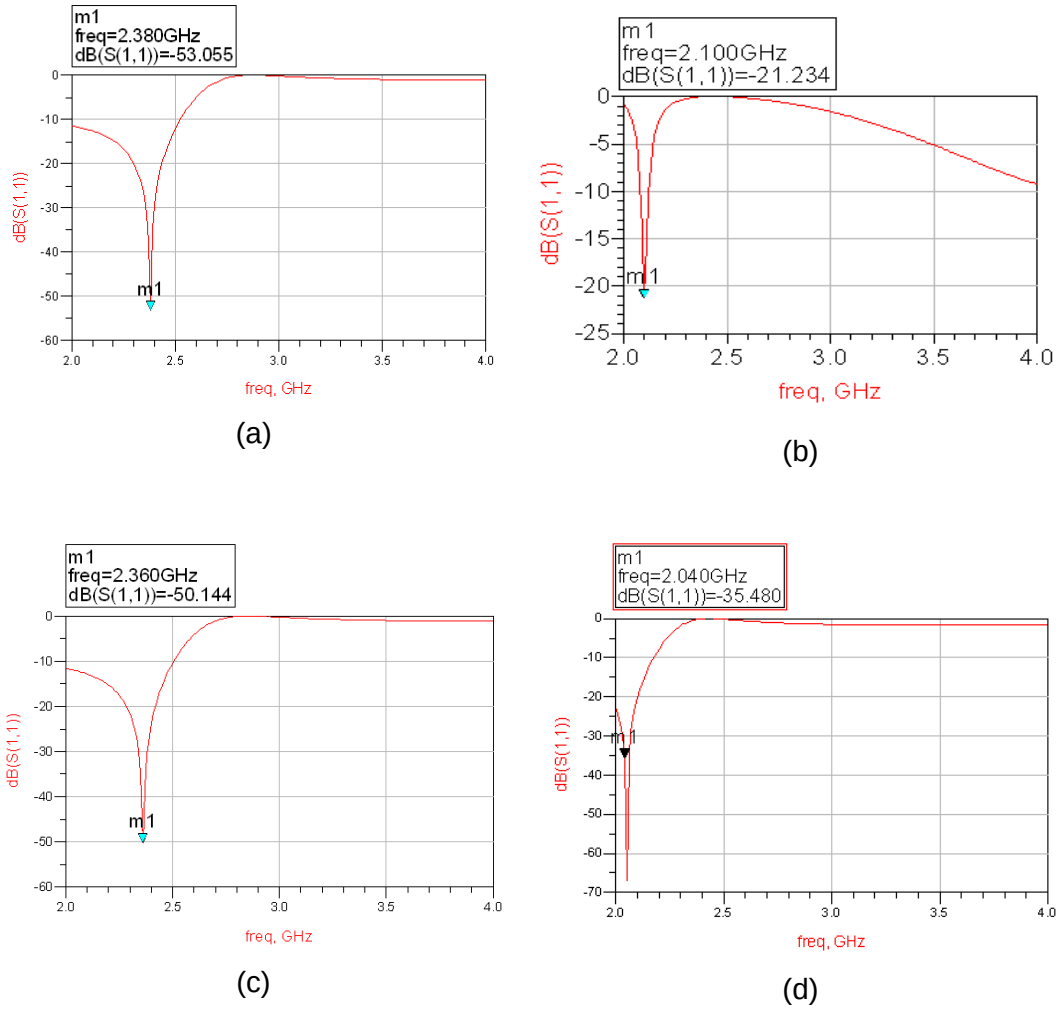

Figure 6. 3 Resonant frequency at (a) unswitched state excluding C_p (b) at switched state excluding C_p (c) at unswitched state including C_p (d) at switched state including C_p

The intention of using IDCs is to increase the capacitance without increasing the size. However, using too many numbers of IDC finger may makes it too close to the inductive loops, which leads to the consideration of coupling between fingers and inductive loops. Therefore, in order to minimize the influences of the coupling and the consideration of fabrication, such as the minimum gap between IDC fingers, the number of IDC fingers is chosen to be less than 11 fingers. The empirical calculations have been used to calculate the resonant frequency and tuning range so that there is a clear idea of how many fingers of IDC can be used to achieve better tuning range. The calculations suggests that using 2 fingers has the lowest tuning range, which is 0.15GHz. Using 9 fingers and 5 have the largest and second largest tuning range, which are 0.29GHz and 0.28GHz, respectively. IDC with 4 fingers has

the third largest tuning range of 0.24GHz. The calculation of other number of IDC fingers shows a highest of 0.18GHz, and these fingers are not considered to be designed as the fingers with larger tuning range have been found. Since the tuning range of 4 fingers is only 0.05GHz smaller than the largest tuning range of 9 fingers, it is possible that the tuning range of 4 fingers can be maximized with optimization. IDC with 4 fingers is also a simple structure to start to better understand how this type of structure responds in the lumped element modelling and full wave simulation. Therefore, tunable LC resonators using IDC with 4 fingers is first designed.

6.2 Tunable LC Resonator Using IDC with Four Fingers

The design starts with IDC using four fingers, as shown in Figure 6.4. It uses the inverted microstrip structure where feed lines and the resonator structures are connected through metallic vias, shown as the white hole in Figure 6.4. It uses the equivalent circuits in Figure 6.1(b). *W* and *L* are the width and length of structure, *w* is the width of fingers, *b* is the width of the inductive loops, *g* is the gap between fingers, *l* is the length of central plate. The dimensions using the empirical equations are shown in Table 6.1.

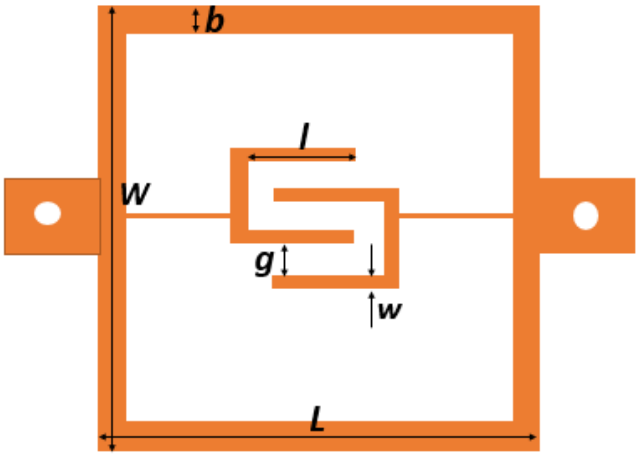

Figure 6. 4 ELC using interdigital capacitors

L	*W*	*b*	*l*	*w*	*g*
14	14	0.5	4	0.5	0.3

Table 6. 1 The dimensions after empirical equations

6.2.1 First Optimization Using ADS

As stated in the proposed design method, the first stage of the design is the lumped element modelling. In the lumped element simulation using ADS, it is important to find out how the changes in different dimensions affect the resonant frequency and the tuning range. As the aim of using IDC is to increase the capacitance while keeping the inductance, the length *L* and the width *W* are kept unchanged. The optimization focuses on the dimension affecting the capacitances, which are the width *w* of the IDC, the length *l* of the IDC, and the gap *g* between the IDC fingers.

Width of IDC *w*/mm	Tunability	Length of IDC *l*/mm	Tunability	Gap of IDC *g*/mm	Tunability
0.2	6%	2	10.5%	0.1	9.8%
0.3	7.5%	3	12.3%	0.2	11.1%
0.4	9%	4	11%	0.3	10%
0.5	11%	5	10.3%	0.4	9.9%
0.6	8.9%	6	10.5%	0.5	8.9%

Table 6. 2 Results when changing width of the resonator

Based on the fabrication consideration and coupling issues, the width *w* of the IDC is chosen to change from 0.2mm to 0.6mm, *l* is chosen to change from 2mm to 6mm and the gap *g* changes from 0.1mm to 0.5mm. Table 6.2 shows the summary of the tunability with changing each dimensions and Figure 6.5 shows the comparison of the resonant frequency with changing each dimensions.

For changing the width *w* of IDC, as can be seen from Table 6.2, the biggest tuning range is achieved when the width is 0.5mm. The Figure 6.5(a) shows that the tuning range is 0.24GHz, and it corresponds to a tunability of 11%. With increasing the width *w* of IDC, the resonant frequency gradually increases. For the switched state, the resonant frequency has greater increase from 0.4mm to 0.6mm. For the unswitched state, the greater increase happens

when changing the width from 0.2mm to 0.5mm. Therefore, in the optimization process, the width of IDC changes should concentrate from 0.3mm to 0.6mm to generate larger tuning range.

Figure 6.5(b) shows that when the length *l* of IDC is 3mm, it has the largest tuning range of 260MHz, and 210MHz is the smallest tuning ranges when using length of 5mm and 6mm, which corresponds to the tunablity of 12.3% and 10.3%, respectively, shown in Table 6.2. The difference between the largest and smallest tuning range is 50MHz, which is not a big change. The increase in the resonant frequency is nearly flat. As for the tuning range, there is small changes in the tuning range, and it means that changing the length *l* of the IDC changes the resonant frequency but it does not affect the tuning range very much.

Figure 6.5(c) shows the results from changing the gap *g* between IDC fingers. The largest tuning range 0.27GHz is achieved when the gap is used 0.2mm, and the smallest tuning range is 0.2GHz when gap is 0.5mm. The discrepancy for the tuning range is 0.07GHz, and it means that changing the gap does not change the tuning range very much. Figure 6.5(c) shows the trend of the resonant frequency when changing the gap between IDC, and it shows the resonant frequency and tuning range are more sensitive when the gap *g* is from 0.2mm to 0.4mm. Therefore, in the second optimization using CST, the gap is varied from 0.2mm to 0.4mm.

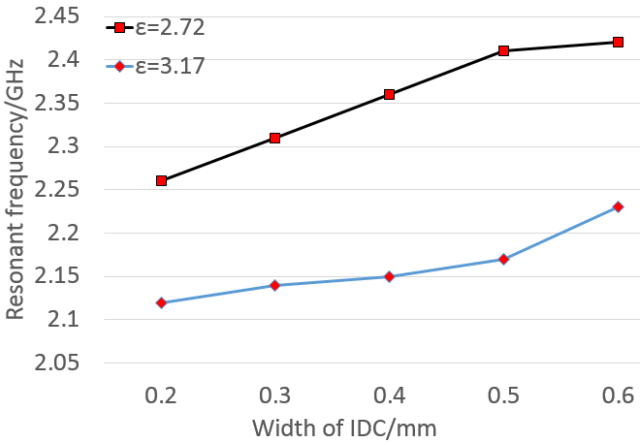

(a)

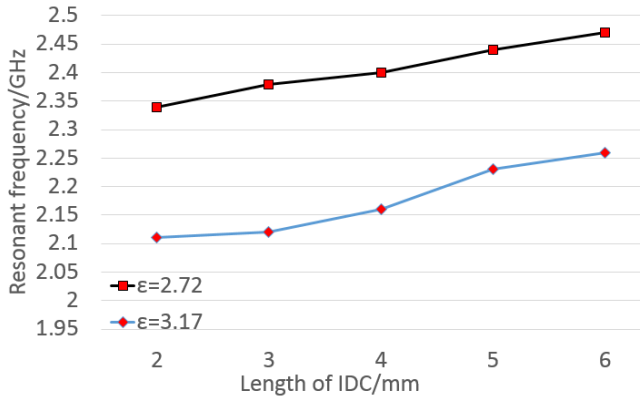

(b)

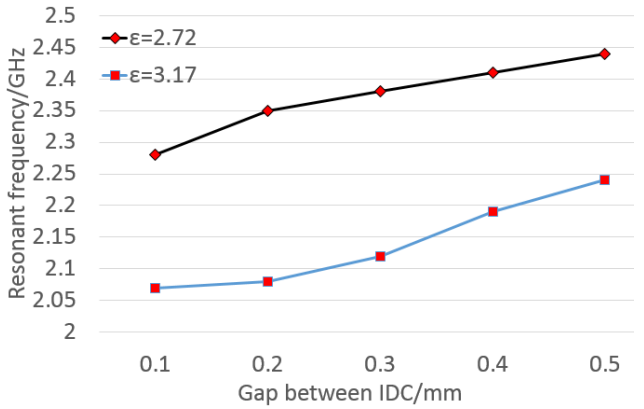

(c)

Figure 6. 5 Comparison of the resonant frequency with (a) different widths *w* of IDC (b) different length *l* of IDC (c) changing gap *g* between IDC

The first optimization using ADS is conducted after understanding the influences of the each dimensions, and it suggests that with the dimensions shown in Table 6.3, the working frequency is adjusted to 2.4GHz and the tuning range is 270MHz.

L	*W*	*b*	*l*	*w*	*g*
14	14	0.5	3.5	0.3	0.25

Table 6. 3 Dimension of the IDC after first optimization using ADS

6.2.2 Second Optimization and Full Wave Simulation Using CST

The next stage as previously is to take the optimised values from ADS and build a model for simulation in CST, and it is shown in Figure 6.6. As can be seen from Figure 6.6, the IDC structure and feed lines are patterned on two different sides of the substrate and are connected through metallic vias. The substrates supporting the feed lines, IDC structures and ground plane are shown as the outlines.

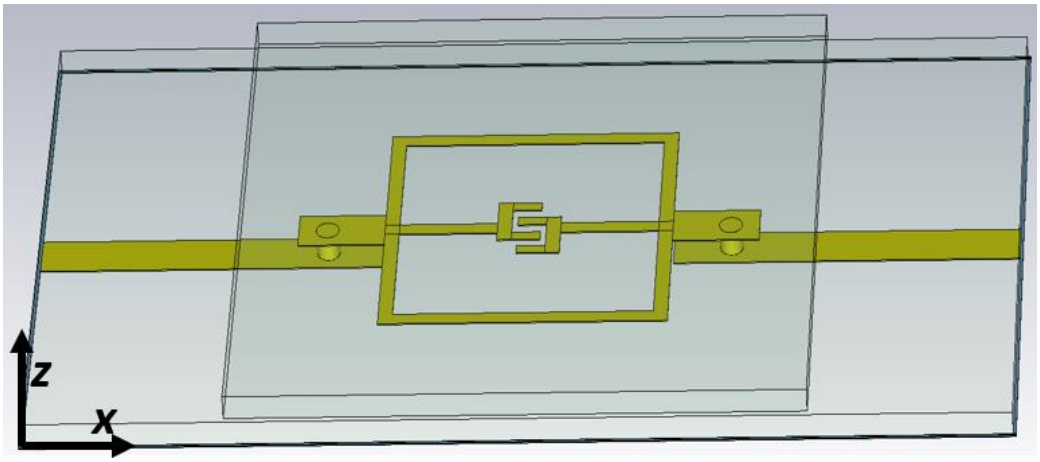

Figure 6. 6 3D structure of the IDC using four fingers

The full simulation is run with CST and it shows the results of 2.45GHz at unswitched state and 2.11GHz at switched state using $\varepsilon_{||}$ along x and z direction as shown in Figure 6.6. These results are then compared with the simulation results from ADS, which are 2.4GHz and 2.13GHz, respectively. The discrepancy between the CST and ADS results are 50MHz and 20MHz, which corresponds to the discrepancy of 2% and 0.9%. Since the discrepancy is small, there is good agreement between the ADS and CST results, which also proves the equivalent circuits for this structure is correct.

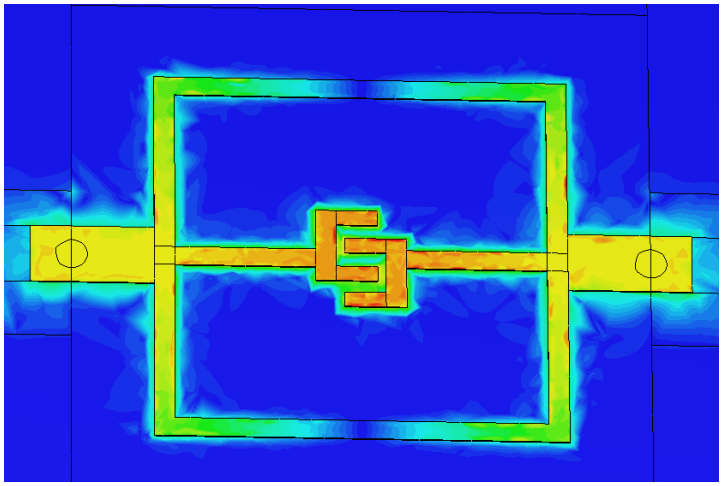

Figure 6. 7 The electric field at resonant frequency

In order to figure out which components in the IDC structures have higher intensity of electric field, the electric field at resonant frequency is observed and shown in Figure 6.7. It can be clearly seen that the IDC element has the stronger electric field, the orange and red colours show higher intensity. Therefore, the strong electric field at capacitive element also indicates that the first optimization using ADS focuses on the capacitive elements is reasonable.

In the second optimization, the length *l* of the IDC, the width *w* of the IDC and gap *g* between the IDC fingers are optimized. It starts with changing the width *w* of the IDC. The width is chosen to be changed from 0.3mm to 0.6mm, which is based on the analysis of first optimization stated above. Figure 6.7(a) shows the resonant frequency with changing the width *w* of IDC from 0.3mm to 0.6mm. As can be seen from Figure 6.8(a), the resonant frequency increases from 2.36GHz to 2.49GHz when increasing the width of IDC from 0.3mm to 0.6mm. The frequency change is 0.13GHz when changes the width of 0.3mm. Therefore, when optimizing small range of frequency, changing the width *w* is preferred. The length *l* is then optimized with CST and it changes from 2mm to 6mm. Figure 6.8(b) shows the CST results with changing the length of IDC. It can be seen from the Figure 6.8(b) that with increasing the length *l* from 2mm to 6mm, the resonant frequency increases from 2.37GHz to 2.56GHz, which shows an increase of 0.19GHz. When the length is 4mm, it has the slightly higher return loss of -21.5dB. Based on the first optimization of the gap *g* using ADS, the gap *g* is investigated with changing gap from 0.1mm to 0.4mm.

Figure 6.8(c) shows the resonant frequency with changing the gap *g* between IDC fingers. The resonant frequency increases from 2.37GHz to 2.48GHz as increasing the gap *g* from 0.1mm to 0.4mm, which corresponds to a frequency change of 110MHz. The simulation results from changing the length *l* and the gap *g* shows that the resonant frequecy is sensitive to the changes. Therefore, high resolution masks are needed to fabricate the structure.

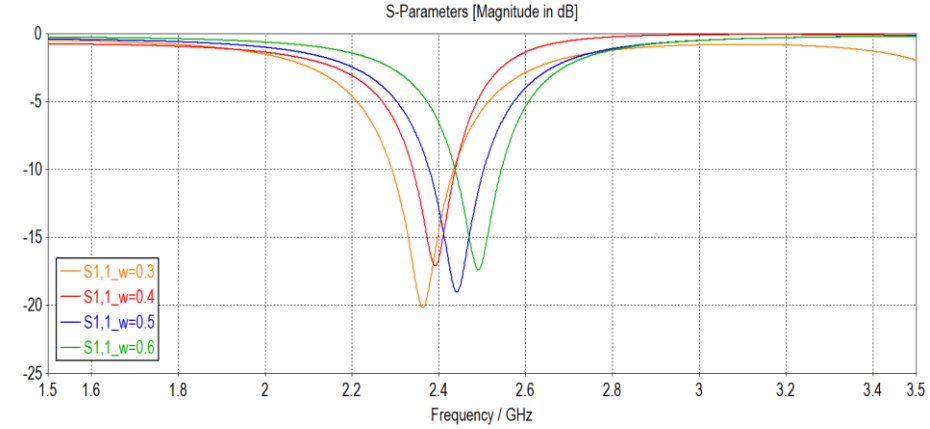

(a)

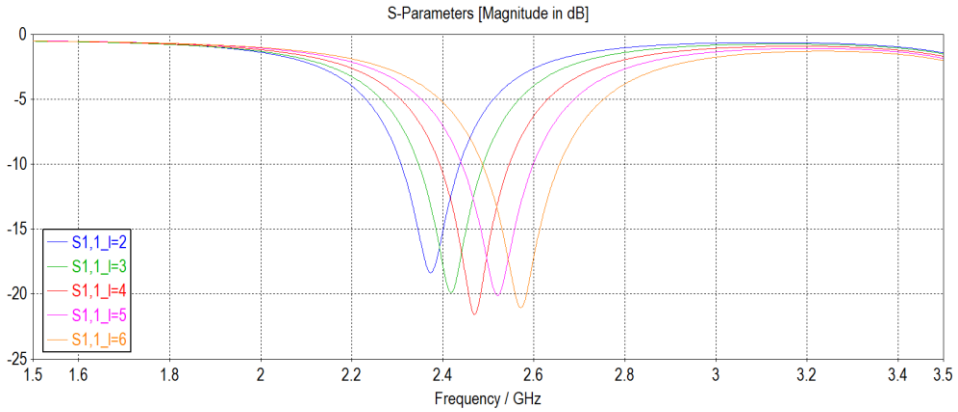

(b)

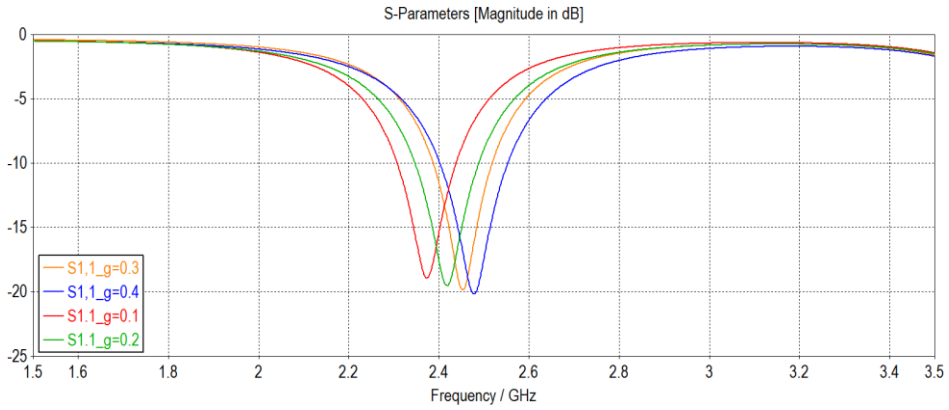

(c)

Figure 6. 8 The resonant frequency with (a) changing width *w* of IDC (b) changing length *l* of IDC (c) changing gap *g* between IDC

L	*W*	*b*	*l*	*w*	*g*
14	14	0.5	4	0.35	0.2

Table 6. 4 Dimension of the IDC after first optimization using ADS

Based on the second optimization of each dimensions, the working frequency is adjusted to 2.4GHz with the dimensions shown in Table 6.4. The full wave simuation is performanced with the final dimensions after second optimization. The LCs are aligned along x for the unswitched state and along z for the switched state, where *x* and *z* direction are shown in Figure 6.6. As can be seen from Figure 6.9, the resonant frequency shifts from 2.4GHz to 2.12GHz when LCs are switched from unswitched state to switched state. The tuning range is 280MHz and it corresponds to a tunability of 13.2%. The return loss changes from -15.5dB to -17dB, and the insertion losses are -1.5dB to -1.3dB when LCs switch from along x to along z.

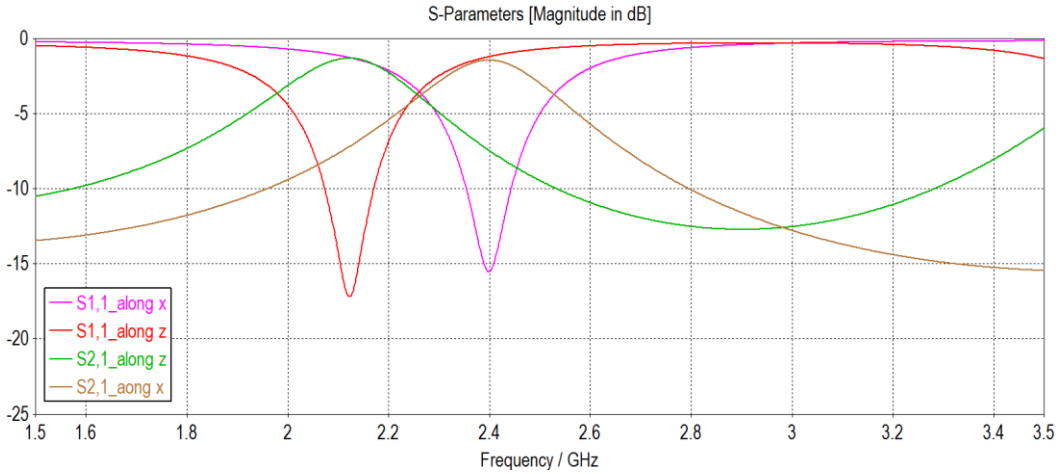

Figure 6. 9 Full wave simulation with final dimension after second optimization using CST

6.3 Tunable LC Resonator Using IDC with 5 Fingers

IDC with 5 fingers from the initial calculation has the second largest tuning range, therefore, IDC with 5 fingers needs to be designed so that it can be optimized to achieve even larger tuning range, as shown in Figure 6.10. Based on the equation 6-1, if keeping all the dimensions the same value, IDC with 5

fingers has bigger capacitance than IDC with 4 fingers. If IDC with 4 fingers and 5 fingers have the same capacitance, the dimensions for IDC with 5 fingers, namely *l*, *w*, and *g*, are smaller than the value in IDC with 4 fingers. IDC with 5 fingers also use the equivalent circuit shown in Figure 6.1(b), as increasing the fingers affects the value for capacitance and inductance, but it does not change the equivalent circuit.

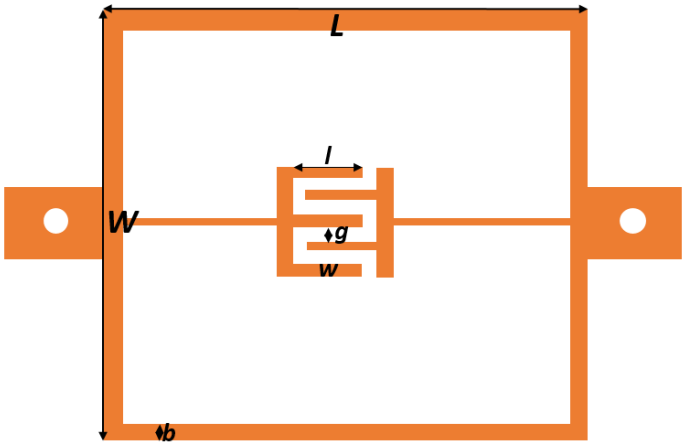

Figure 6. 10 Structure of IDC with 5 fingers

6.3.1 First Optimization Using ADS

In the previous section, the influences to the resonant frequency with varying the dimensions of the IDC for 4 fingers have been studied. Whether increasing the fingers of IDC has the similar influence for the resonant frequency when changing the dimensions of IDC needs to be found out in the ADS. Table 6.5 shows the dimensions using empirical equations to design the tunable resonators using IDC with 5 fingers to work at 2.4GHz.

L	*W*	*b*	*l*	*w*	*g*
14	14	0.5	4.5	0.4	0.15

Table 6. 5 The dimensions using empirical equations for IDC with 5 fingers

Under the consideration the resolution of fabrication and minimizing the effect of coupling to inductive loops, the width *w* of the IDC is chosen to vary from 0.2mm to 0.6mm, the length *l* of the IDC is varied from 2mm to 6mm with a

step of 0.5mm, and the gap *g* between IDC fingers, and it is chosen to change from 0.1mm to 0.5mm.

Width of IDC *w* /mm	Tunability	Length of IDC *l* /mm	Tunability	Gap of IDC *g* /mm	Tunability
0.2	11.7%	2	11.7%	0.1	13%
0.3	10.4%	2.5	12.2%	0.15	15.1%
0.4	13.3%	3	11.9%	0.2	15.5%
0.5	10.5%	3.5	12.8%	0.25	15.9%
0.6	8.4%	4	15.1%	0.3	12.6%
		4.5	13.3%	0.35	11.7%
		5	13.7%	0.4	9.6%
		5.5	12.6%	0.45	7.6%
		6	11.9%	0.5	6.2%

Table 6. 6 Results of tunability when changing dimensions of the IDC

For changing the width *w* of IDC, as can be seen from the Table 6.6, when the width is 0.4mm, it has the highest tunability of 13.3%, and when the width is 0.6mm, the lowest tunability is 8.4%. As can be seen from Figure 6.11(a), the tuning range is varied when changes the width *w* of IDC. More specifically, with increasing the width of IDC from 0.2mm to 0.6mm, the tuning range first increases from 0.2mm to 0.4mm followed by decreasing from 0.4mm to 0.6mm, where the highest tuning range is 0.28GHz and the lowest tuning range is 0.19GHz. While in the first optimization of IDC using 4 fingers, the tuning range gradually increases from 0.2mm to 0.5mm, and decreases from 0.5mm to 0.6mm. The difference in the tuning range suggests that it is necessary to run the ADS simulation for IDC with 5 fingers, since the tuning range behaves differently with different numbers of fingers. All the ADS simulation results for both IDC with 4 fingers and 5 fingers shows that with increasing the width of IDC, the resonant frequency increases.

Figure 6.11(b) shows the comparison of the resonant frequency with changing the length *l* of IDC. As can be clearly seen from the Figure 6.11(b), with increasing the length of IDC, the resonant frequency increases from 2.19GHz to 2.46GHz for $\varepsilon = 2.72$ and 1.96GHz to 2.18GHz for $\varepsilon = 3.17$. The highest tuning range is 0.31GHz when using the length of 4mm, and the lowest tuning range is 0.23GHz when using 2mm as the length of IDC, which corresponds to a tunability of 15.1% and 11.7%, as shown in Table 6.6. The difference between the highest tuning range and the lowest tuning range is 80MHz, and changing the length *l* from 2.5mm to 5.5mm shows larger tuning range.

Figure 6.11(c) shows the comparison of changing gaps *g* between IDC. As can be seen from Figure 6.11(c), with increasing the gap *g*, the resonant frequencies for using both isotropic values of LCs increase, and the resonant frequencies using $\varepsilon = 3.17$ have greater increase. As for the tuning range, it can be clearly seen from Figure 6.11 (c), the tuning range with gap *g* more than 0.4mm is smaller, which shows the lowest tuning range is 0.15GHz with a tunability of 6.2% with gap *g* of 0.5mm. When gap *g* is 0.25mm, it has the highest tuning range of 0.33GHz and it corresponds to a tunability of 15.9%, as shown in Table 6.6. Since the largest tuning range is more than double of the lowest tuning range, in the second optimization with CST, the gap *g* between IDC fingers are not chosen to beyond 0.4mm.

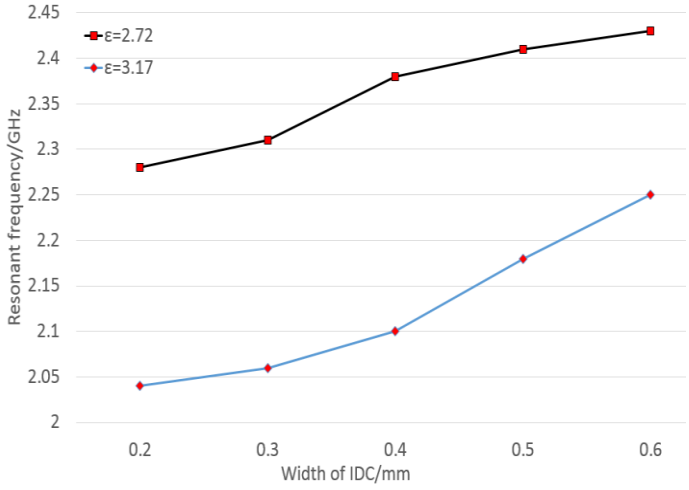

(a)

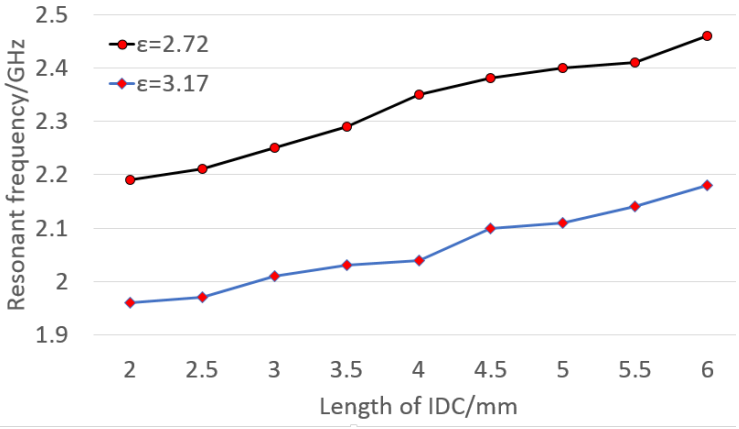

(b)

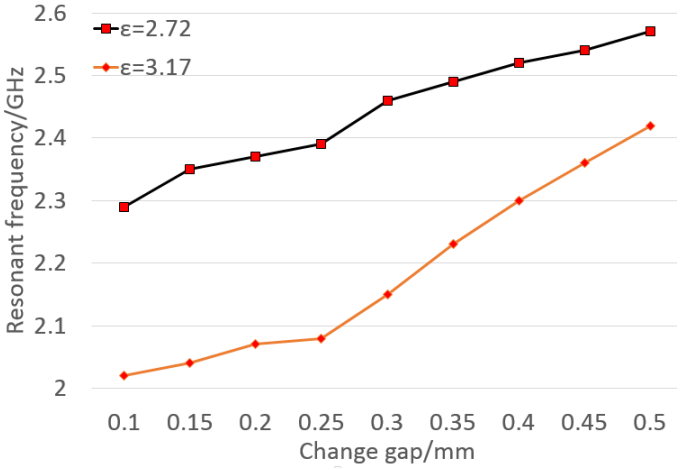

(c)

Figure 6. 11 Comparison of resonant frequency with (a) changing width *w* of IDC (b) changing length *l* of IDC (c) changing gaps *g* between IDC

After understanding the influences of each dimensions to the resonant frequency, the ADS simulation is used to adjust the working frequency and tuning range. The optimization using ADS achieves the working frequency of 2.4GHz and a tuning range of 0.33GHz with the dimensions shown in Table 6.7.

L	*W*	*b*	*l*	*w*	*g*
14	14	0.5	4	0.3	0.25

Table 6. 7 The dimensions after first optimization using ADS

6.3.2 Second Optimization Using CST

The dimensions in Table 6.7 are used to build the 3D model of IDC with 5 fingers in CST, and it is shown in Figure 6.12. As can be seen from Figure 6.12, the substrate is shown in brown colour and the top substrate is chosen to be transparent to show the resonator structure. The resonator structure is shown as the yellow colour, and feed lines are on the other side of the substrate and are connected to the resonator through the metallic vias. The material used for the substrate is the same as previous section. The full wave simulation using CST suggests that the resonant frequencies are 2.46GHz at unswitched state and 2.15GHz at switched state, where LCs are aligned along x to represent unswitched state and along z to represent switched state, respectively. Compared with the results from lumped element modelling using ADS, the discrepancies are 60MHz at unswitched state and 20MHz at switched state. The small discrepancies of 2.1% at unswitched state and 1% at switched state ensure that the equivalent circuit used in the ADS simulation is correct.

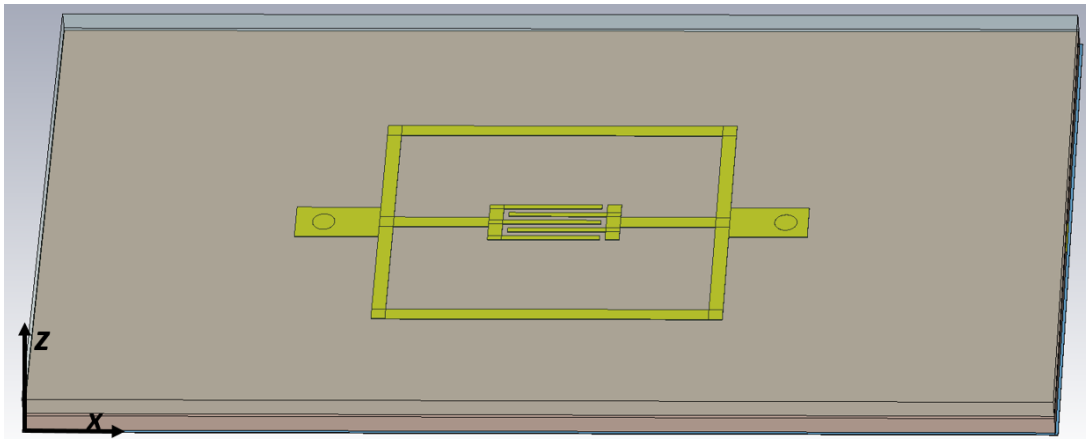

Figure 6. 12 3D model of IDC with 5 fingers in CST

The next stage is to figure out whether using 5 fingers has the same effect to the resonant frequency as 4 fingers in the CST, which also involves changing the dimensions of width *w* of the IDC, length *l* of the IDC and gap *g* between IDCs. It start with changing the width *w* of the IDC from 0.2mm to 0.5mm, as the first optimization using ADS shows that in this range, it has larger tuning range. Figure 6.13(a) shows the resonant frequency at unswitched state with changing the width of IDC from 0.2mm to 0.5mm. It can be seen that with increasing the width of IDC, the resonant frequency increases from 2.3GHz to 2.42GHz. An increase of 0.12GHz in the resonant frequency at unswitched state is achieved while it is slightly smaller than the increase of 0.15GHz in ADS simulation. The length *l* of IDC is then optimized with CST, and it varies from 2.5mm to 5.5mm based on the first optimization results in ADS.

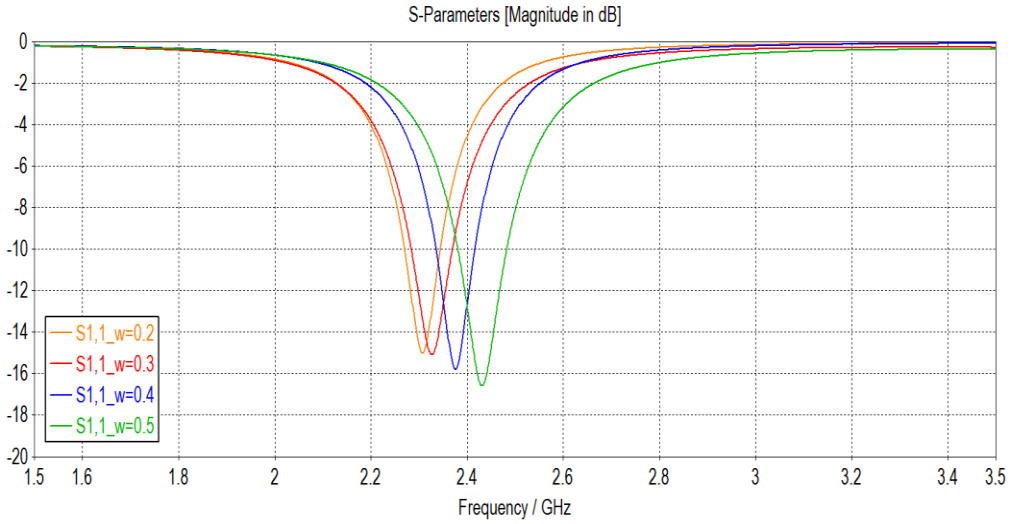

(a)

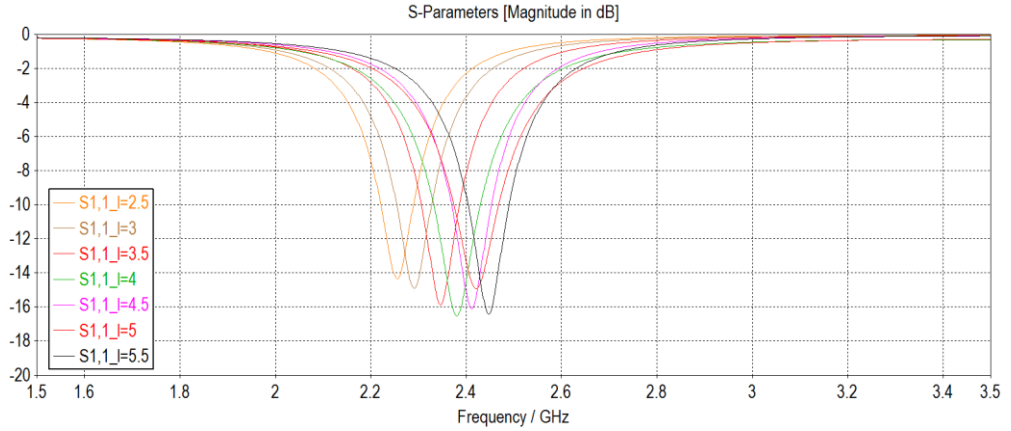

(b)

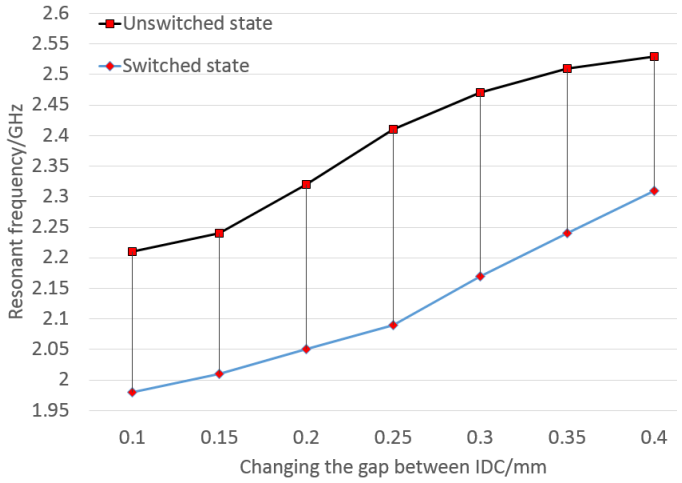

(c)

Figure 6. 13 Resonant frequency with (a) changing width *w* of IDC at unswitched state (b) changing length *l* of IDC at unswitched state (c) with changing gaps between IDC at both states

Figure 6.13(b) shows the resonant frequency with different length of IDC. The resonant frequency increases from 2.25GHz to 2.45GHz with increasing the length of IDC from 2.5mm to 5.5mm at unswitched state. The changes in length *l* of IDC in both ADS and CST simulation indicates that changing length of IDC does not affect the tuning range very much. The gap *g* between IDC fingers is the last to be optimized with CST, and it is chosen to be changed from 0.1mm to 0.4mm, as the first optimization in ADS suggests that beyond 4mm the tuning range is too small. Therefore, the simulation results of changing gap between IDC fingers using CST are shown in Figure 6.13. As can be seen from Figure 6.13(c), the tuning range varies when changing the gaps *g* between IDC. It shows higher tuning range when changing the gap from 0.15mm to 0.35mm, and it has the highest tuning range of 0.32GHz at 0.25mm of the gap. Considering both ADS and CST optimization results, the tuning range is more sensitive to the changes in gap *g* between IDCs.

Based on the optimization of the three dimensions, the optimization is carried to achieve the working frequency of 2.4GHz and the largest tuning range. Table 6.8 shows the final dimensions after optimization.

L	*W*	*b*	*l*	*w*	*g*
14	14	0.5	3.5	0.3	0.2

Table 6. 8 The dimensions after first optimization using CST

The final dimensions are then used to perform the full wave simulation using CST to show the working frequency and tuning range. Figure 6.14 shows the results of resonant frequency at unswitched and switched state. The resonant frequency shifts from 2.4GHz to 2.07GHz from unswitched state to switched state, and the tuning range is 0.33GHz which corresponds to a tunability of 16%. The return loss is -15.5dB for unswitched state and -18dB for switched state. The insertion loss is higher than -2dB in the frequency range. Compared with the tuning range of 0.28GHz for IDC with 4 fingers, IDC with 5 fingers has higher tuning range. Compared with the highest tuning range of 0.29GHz from using empirical equations, the optimized tuning range is 0.33GHz, which is

higher than the highest tuning range from empirical equations and proves the neccessity of optimizing the IDC with 5 fingers.

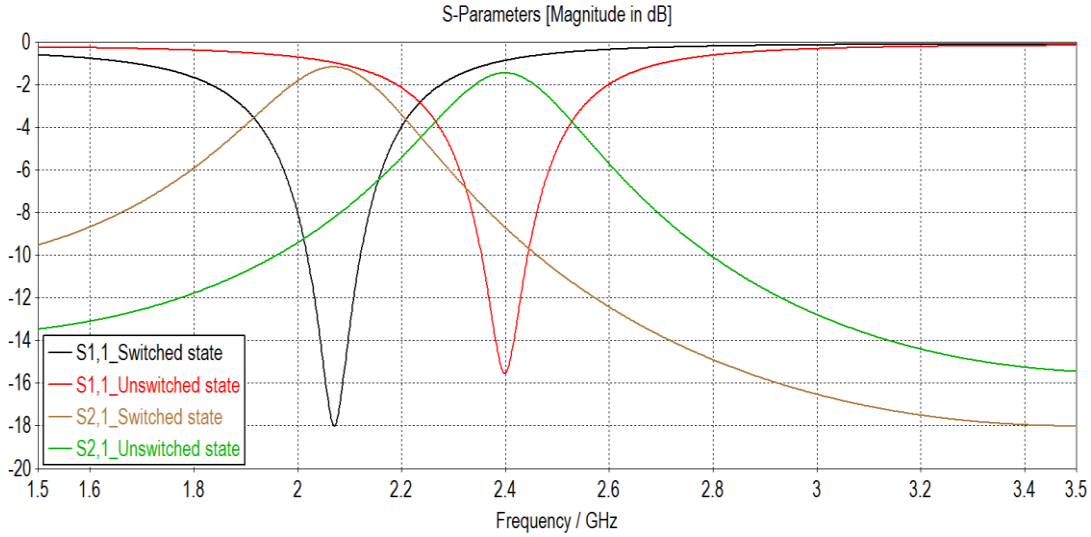

Figure 6. 14 Resonant frequency at unswitched and switched state

6.4 Tunable LC Resonator Using IDC with 9 Fingers

Based on the initial calculation of the resonant frequency and tuning range using empirical equations, IDC using 9 fingers has the largest tuning range of 0.29GHz. Therefore, IDC with 9 fingers needs to be designed and optimized to have larger tuning range.

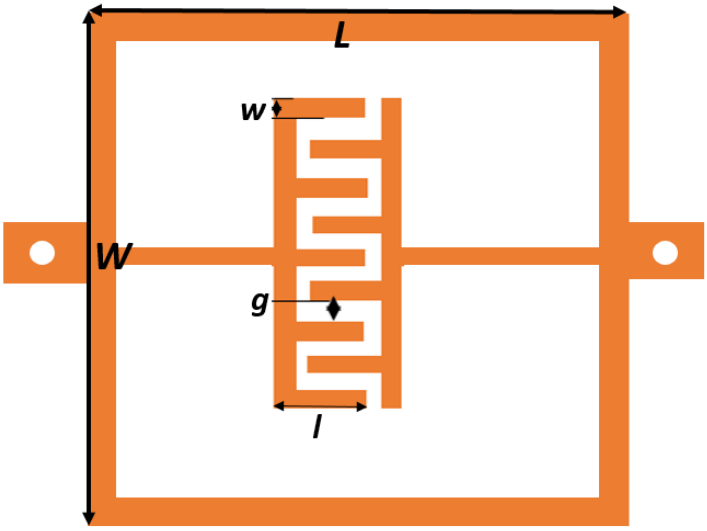

Figure 6. 15 IDC with 9 fingers

Figure 6.15 shows the IDC using 9 fingers. The initial calculation for the dimensions of this structure is shown in the Table 6.9 as the before value. The lumped element modelling using ADS suggests that the resonant frequency shifts from 2.44GHz to 2.15GHz from unswitched state to switched state, and the tuning range is 0.29GHz. Since the optimization for the IDC with 9 fingers is the same process as previous section and the same parameters for the IDC elements are optimized, the first optimization is not described in detail. The resonant frequencies after first optimization are 2.4GHz for $\varepsilon = 2.72$ and 2.10GHz for $\varepsilon = 3.17$, and it corresponds to a tuning range of 300MHz. The dimensions after the first optimization is shown as the after value in Table 6.9.

	L	*W*	*b*	*l*	*w*	*g*
Before	14	14	0.5	3	0.25	0.15
After	14	14	0.5	3.5	0.35	0.1

Table 6. 9 The dimensions after first optimization using ADS

The dimensions after first optimization are then used to build the 3D model in CST as shown in Figure 6.16 to find out the resonant frequency and tuning range in the full wave simulation. As can be seen from the 3D model, the feed lines and the resonator structure are patterned on two sides of the substrate, and they are connected through metalic vias. The blue region is the LC cavity. Two dielectric substrates are chosen to be transparent so that the resonator structure can be seen in the figure.

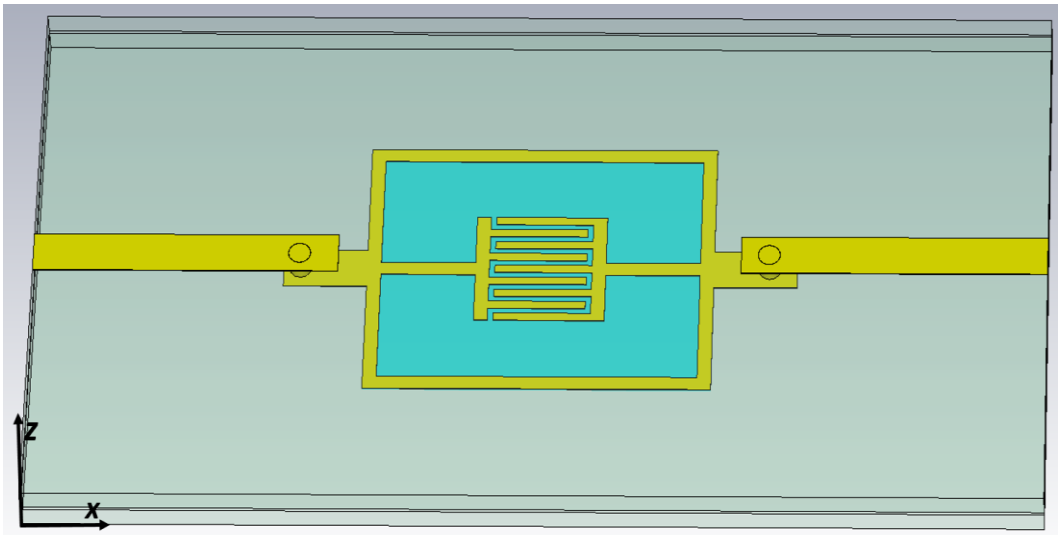

Figure 6. 16 3D structure of IDC with 9 fingers

Width of IDC *w* /mm	Tunability	Length of IDC *l* /mm	Tunability	Gap of IDC *g* /mm	Tunability
0.2	11.7%	2	11.2%	0.1	15.1%
0.3	14.4%	2.5	14.2%	0.15	14.7%
0.4	13.5%	3	15.9%	0.2	14.5%
0.5	13.1%	3.5	15.8%	0.25	14.2%
0.6	12.4%	4	15.1%	0.3	13.6%
		4.5	14.3%	0.35	12.7%
		5	13.7%	0.4	11.6%
		5.5	12.2%	0.45	9.8%
		6	11.5%	0.5	9.2%

Table 6. 10 Summary of how each dimensions influences the tuning range for IDC with 9 fingers

With the dimensions from ADS optimization, the resonant frequencies using CST are 2.45GHz and 2.16GHz, and the tuning range is 0.29GHz, which is slightly smaller than the tuning range in ADS. The comparison between ADS and CST simulation results suggests that the biggest discrepancy is 0.06GHz (2.7%), and it can be seen to have good agreement between ADS and CST results. In order to adjust the working frequency to 2.4GHz and optimize to have the largest tuning range, the second optimization is carried out by varying

the dimensions of the width *w* of the IDC, the length *l* of the IDC and the gap *g* between IDC, and the results are summarized in Table 6.10. With the understanding how each dimensions influences the resonant frequency and tuning range, the CST is then used to optimize the working frequency to 2.4GHz at unswitched state, and the largest tuning range is achieved with the dimensions shown in Table 6.11.

L	*W*	*b*	*l*	*w*	*g*
14	14	0.5	3	0.3	0.1

Table 6. 11 Final dimension after second optimization

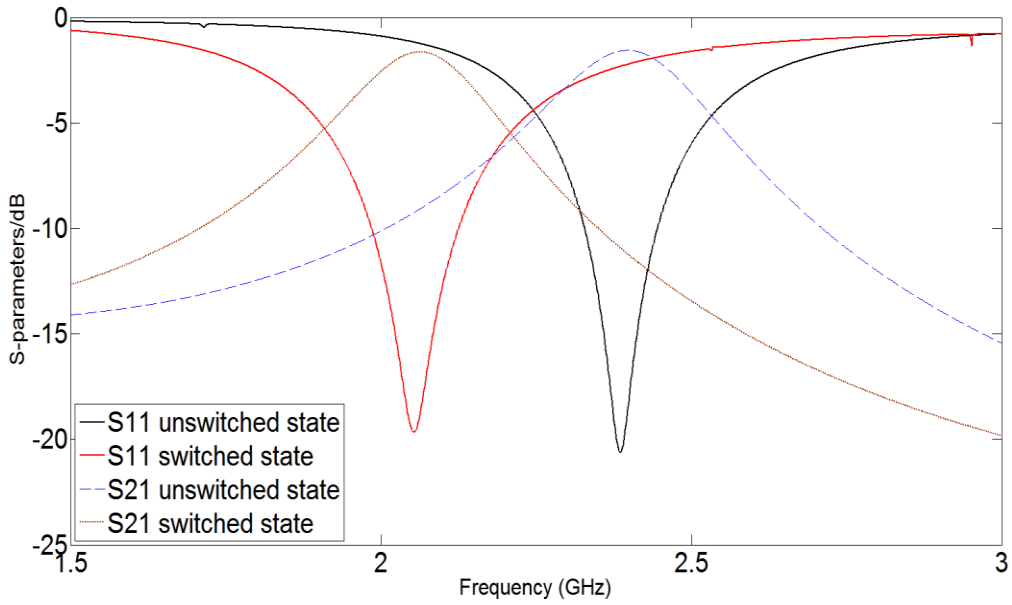

Figure 6. 17 Resonant frequency at unswitched state and switched state

The dimensions in Table 6.11 are used to update the 3D model and used to run the full wave simulation to show the working frequency and final optimized tuning range. The CST simulation results with the final optimized dimensions can be seen from Figure 6.17. The resonant frequency shifts from 2.4GHz at unswitched state to 2.05GHz at switched state, and it corresponds to a tuning range of 350MHz and a tunability of 16.6% The return loss is -21.5dB at unswitched state and -19.5dB at switched state, while the insertion loss is less than -3dB at both states. The 3dB bandwidth remains constant at both states.

The bandpass resonator has the largest tuning range among the simulated IDC with 4, 5 and 9 fingers, and it needs to be fabricated and measured.

6.5 Measurement of Tunable LC Resonators Using IDCs at 2.4GHz

6.5.1 Measurement for Tunable LC Resonators Using IDC with 4 Fingers

Figure 6.18 shows the photo of fabricated resonator using IDC with 4 fingers. As can be seen from the Figure 6.18, the dielectric substrate is Rogers Duroid 5880, and the resonator structure is patterned using copper. The silver color shown in this figure is the conductive paste to connect the resonator structure and the feed lines on the other side. The detailed dimensions for the substrate and copper are shown in Table 6.12.

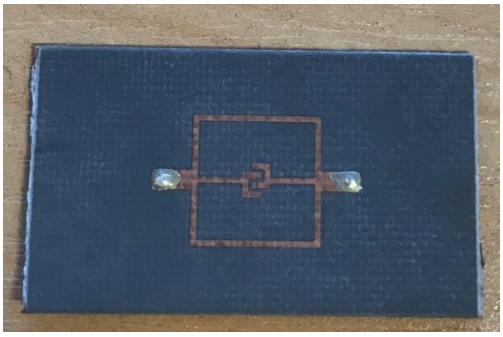

Figure 6. 18 The photo of fabricated IDC with 4 fingers

Component	Material	Thickness (mm)
Microtrip line substrate/Ground plane substrate	Rogers Duroid 5880	0.79
Microstrip line and ground plane	Copper	0.035
Spacer	Roger s Duroid 5880	0.13
Liquid Crystals	Merck E7	0.13
SMA connector	0-18GHz to use	

Table 6. 12 The dimensions for the component to build the device

The patterned resonator is then assemble using the assembly methods stated in Chapter 3 and is also measured under the measurement setup in Chapter 3. The external bias voltage uses AC voltage from 0V to 16V with a step of 0.5V. Figure 6.19 shows the measured resonant frequency with changing the applied voltage. As can be seen from the Figure 6.19, the resonant frequency shifts from 2.38GHz to 2.15GHz when the bias voltage varies from 0V to 16V. The tuning range is 0.23GHz and it corresponds to a tunability of 10.7%. The return loss moves from -22.3dB to -19.8dB, which shows a slight decrease when increasing the bias voltage.

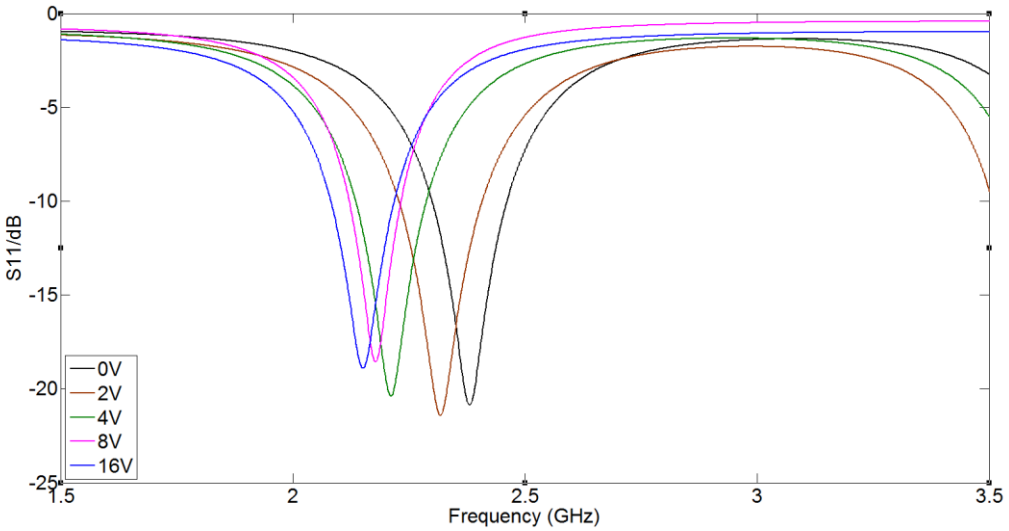

Figure 6. 19 The resonant frequency with changing the voltage

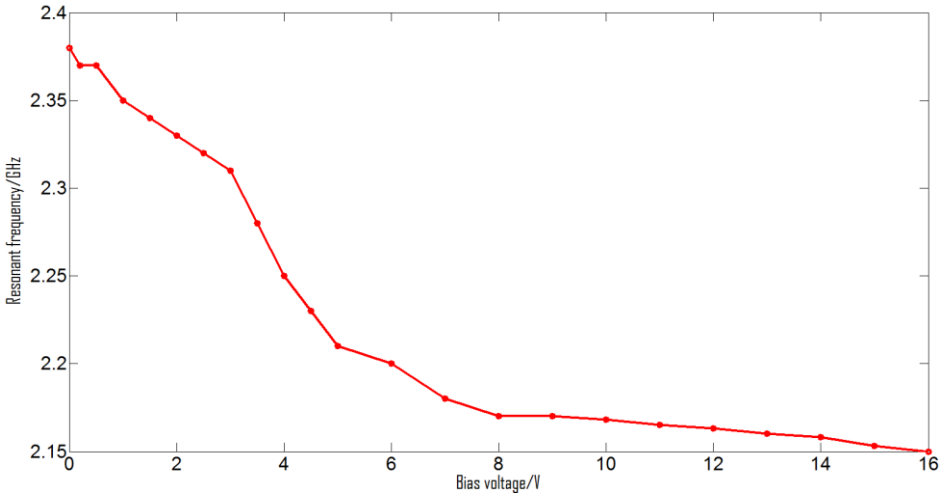

Figure 6. 20 The resonant frequency as a function of bias voltage

Figure 6.20 shows the resonant frequency as a function of the bias voltage. It can be clearly seen that with increasing the bias voltage, the resonant frequency drastically decreases from 2.38GHz to 2.17GHz when the applied bias voltage changes from 0V to 8V. After 8V, there is slightly decrease for the resonant frequency, which decreases from 2.17GHz to 2.15GHz.

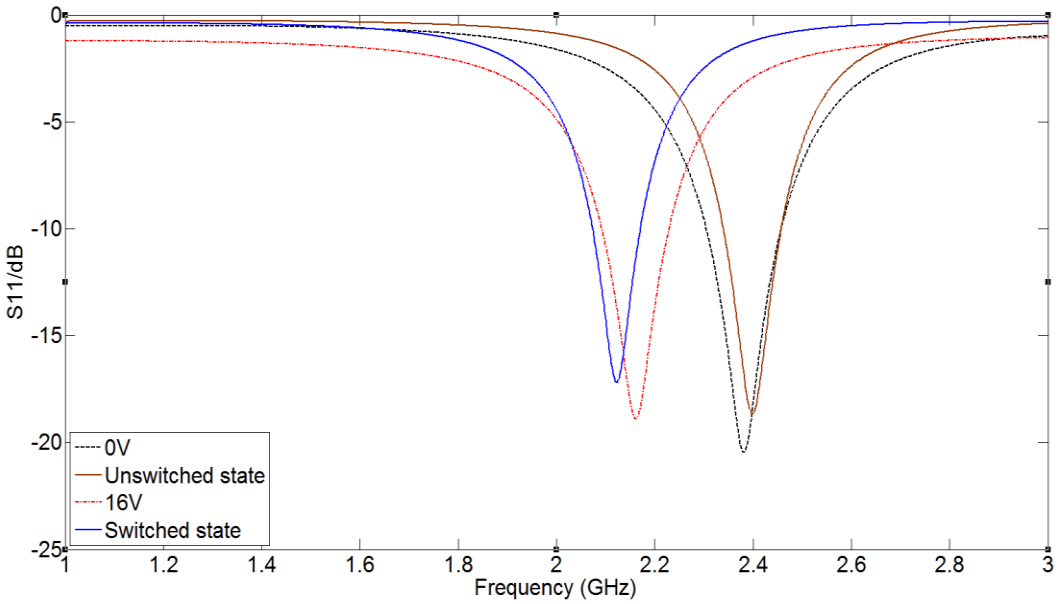

Figure 6. 21 Comparison of resonant frequency between simulated and measured results

The simulated and measured results of resonant frequency are compared in Figure 6.21. As can be seen from Figure 6.21, the resonant frequency at unswitched state is 2.4GHz and 2.38GHz when the bias voltage is 0V. The discrepancy in resonant frequency between simulated and measured is 0.02GHz (0.8%), which means a good agreement between the simulated and measured results at unswitched state. The resonant frequency at switched state is 2.12GHz and the measured results at 16V is 2.15GHz, which corresponds to a discrepancy of 0.03GHz (1.5%). The resonant frequencies at both switched and unswitched state have good agreement, as the discrepancies are small, which are 0.8% and 1.5%, respectively. The FBW of the measured results are 19% at 0V and 26% at 16V, while the FBW is 14% at unswitched state and 19% at switched state. The discrepancies are 5% and 7% between measured and simulated results at unswitched and switched state. The discrepancies are slight higher, but it is acceptable. If the

discrepancies are much higher, a methodology to control the constant FBW needs to be proposed.

6.5.2 Measurement for Tunable LC Resonator with IDC Using 5 Fingers

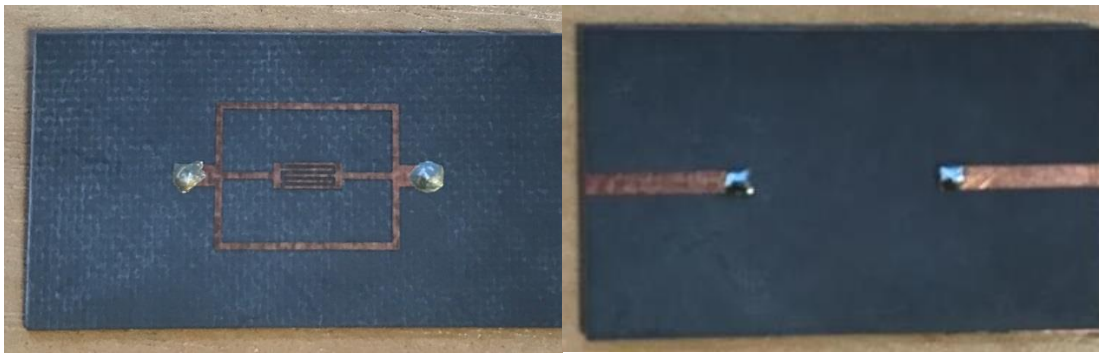

(a) **(b)**

Figure 6. 22 (a) Fabricated IDC with 5 fingers (b) Feed lines on the other side

The IDC with 5 fingers is fabricated with the etching process stated in Chapter 3, and the fabricated structure is shown in Figure 6.22 (a). Figure 6.22 (b) shows the feed lines on the other side, and feed lines and resonator structure are connected by conductive paste shown as the silver in Figure 6.22 (a).

This IDC with 5 fingers is then assemble using the proposed method and measured using the measurement setup stated in Chapter 3. Figure 6.23 shows the measured results of resonant frequency with changing the bias voltage from 0V to 16V. As can be seen from Figure 6.23, the resonant frequency shifts from 2.37GHz to 2.10GHz when varies the external bias voltage from 0V to 16V. The tuning range is 270MHz and the tunability is 12.8%. The return losses are -15.5dB at 0V and -16.4 dB at 16V.

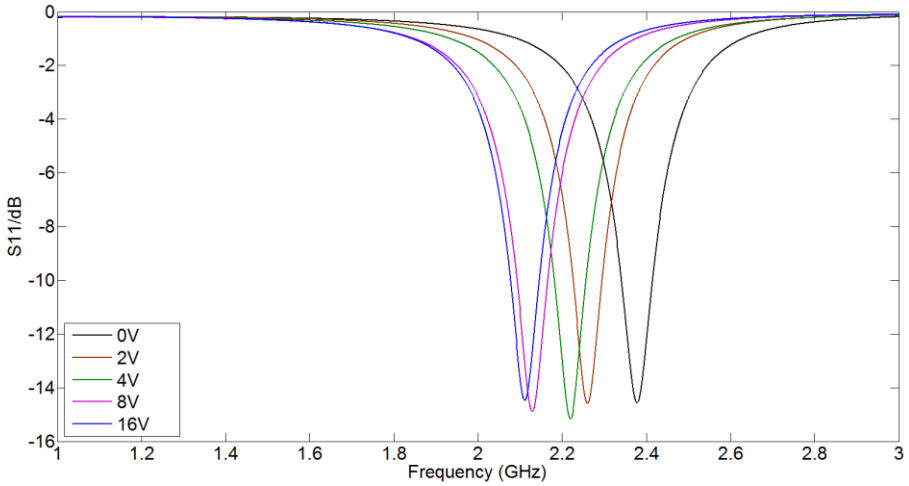

Figure 6. 23 Resonant frequency at different bias voltage

Figure 6.24 shows the resonant frequency as a function of the external bias voltage. After the threshold voltage of 0.5V, the LCs start to switch from unswitched state to switched state, and the resonant frequency gradually decreases as the bias voltage increases. After 8V, the voltage reaches the saturation voltage and the resonant frequency does not change very much after this voltage.

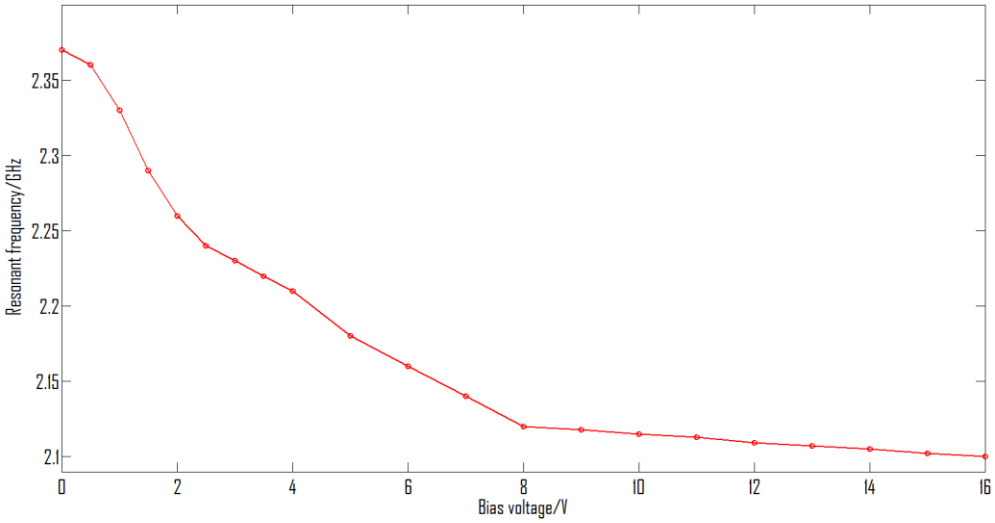

Figure 6. 24 Resonant frequency as a function of bias voltage for IDC with 5 fingers

The comparison between the simulated and measured results of the resonant frequency is shown in Figure 6.25. As can be seen from Figure 6.25, the resonant frequency at unswitched state is 2.4GHz and 2.37GHz when the bias

voltage is 0V. It corresponds to a discrepancy of 0.03GHz (1.2%), where a good agreement between simulated and measured results at unswitched state is achieved. As for the switched state, the resonant frequency is 2.07GHz and the measured resonant frequency at 16V shows 2.10GHz, where the discrepancy between them is 0.03GHz (1.4%). Therefore, with the small discrepancies of 1.2% and 1.4%, the simulated and measured results have good agreements for the resonant frequency at both unswitched and switched state. The FBW for the simulation is 12.9% at unswitched state and 16.4% at switched state, while the measured FBW is 16% at 0V and 14.3% at 16V. The comparison of FBW at unswitched and 0V shows a discrepancy of 3.1% and 2.1% for switched state and 16V. As the discrepancies in both resonant frequency and FBW is small, the good agreement is achieved between simulated and measured results.

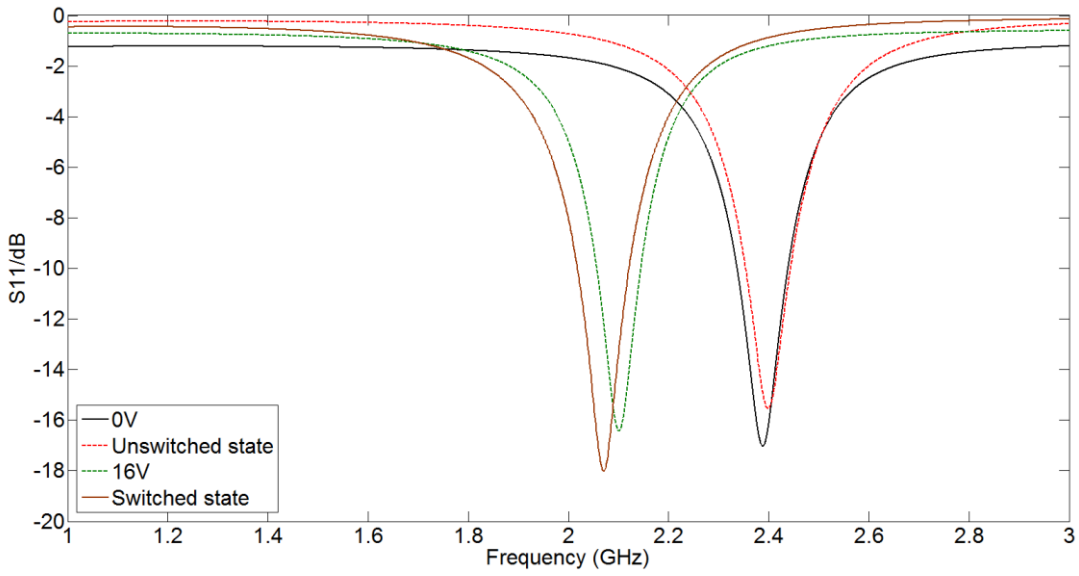

Figure 6. 25 Comparison between simulated and measured results for IDC with 5 fingers

6.5.3 Measurement for the Tunable LC Resonator Using IDC with 9 Fingers

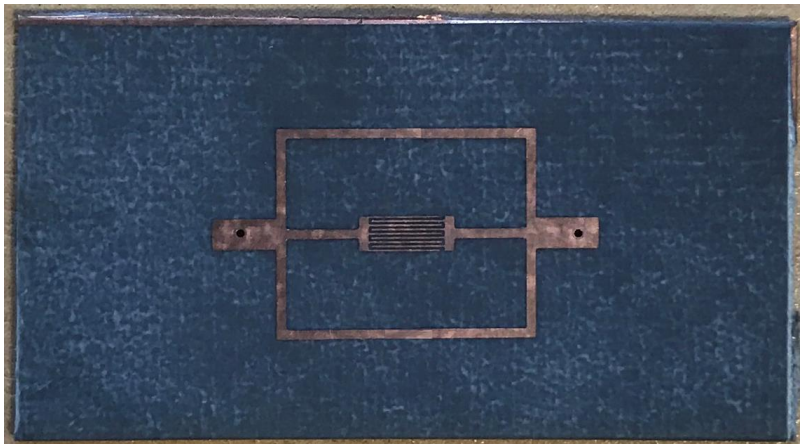

Figure 6. 26 Fabricated IDC with 9 fingers

The tunable resonator using IDC with 9 fingers is also fabricated and shown in Figure 6.26. It uses the material stated in Table 6.12 to build the fitler.

This tunable resonator using IDC with 9 fingers is assembled and measured using the standard the process developed in Chapter 3. The measured results of the resonant frequency is shown in Figure 6.27, where the resonant frequency is plotted as a function of changing external bias voltage. The resonant frequency moves from 2.39GHz to 2.08GHz when the bias voltage is changed from 0V to 16V. The tuning range for IDC with 9 fingers is 0.31GHz and it corresponds to a tunability of 14.9%, which is the largest tuning range among the three fabricated devices. The return loss is -21dB at 0V and -20dB at 16V.

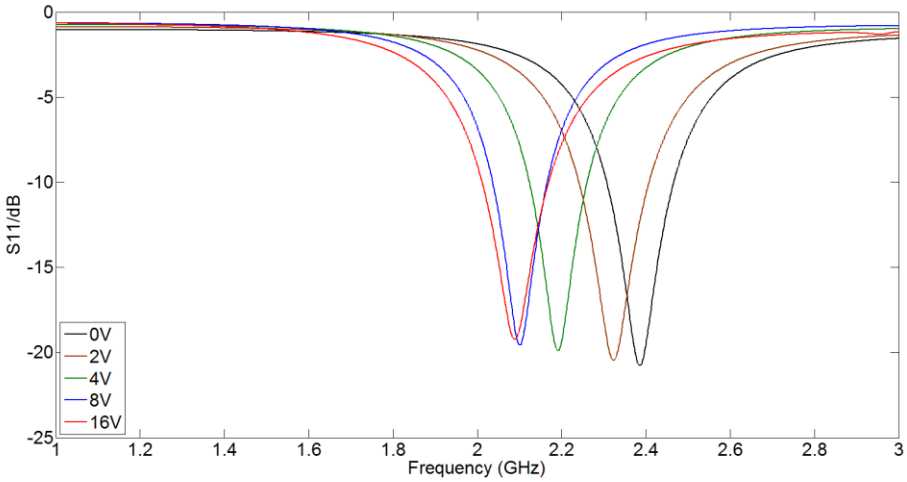

Figure 6. 27 Resonant frequency with changing bias voltage for IDC with 9 fingers

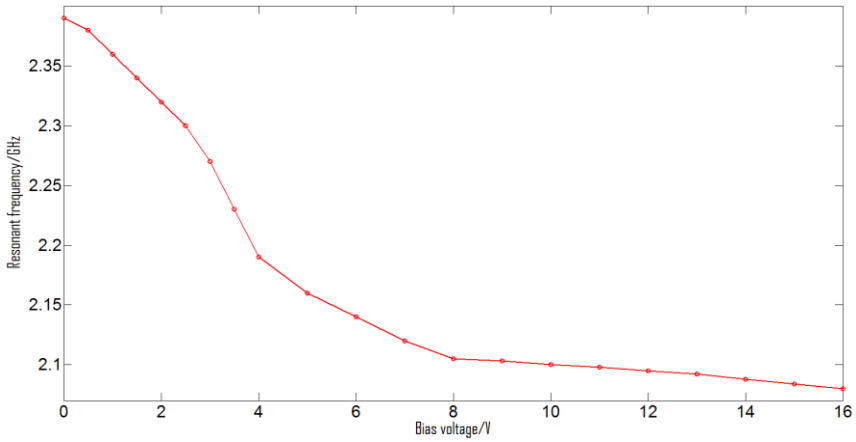

Figure 6. 28 Resonant frequency as a function of bias voltage

Figure 6.28 shows the resonant frequency when the bias voltage is changed from 0V to 16V with a step of 0.5V. As can be seen from Figure 6.28, after the threshold voltage of 0.5V, the resonant frequency starts to gradually decrease from 2.39GHz to 2.10GHz. When the voltage reaches 8V, there is very small decrease in the resonant frequency, where the resonant frequency changes from 2.10GHz to 2.08GHz with the bias voltage increasing from 8V to 16V.

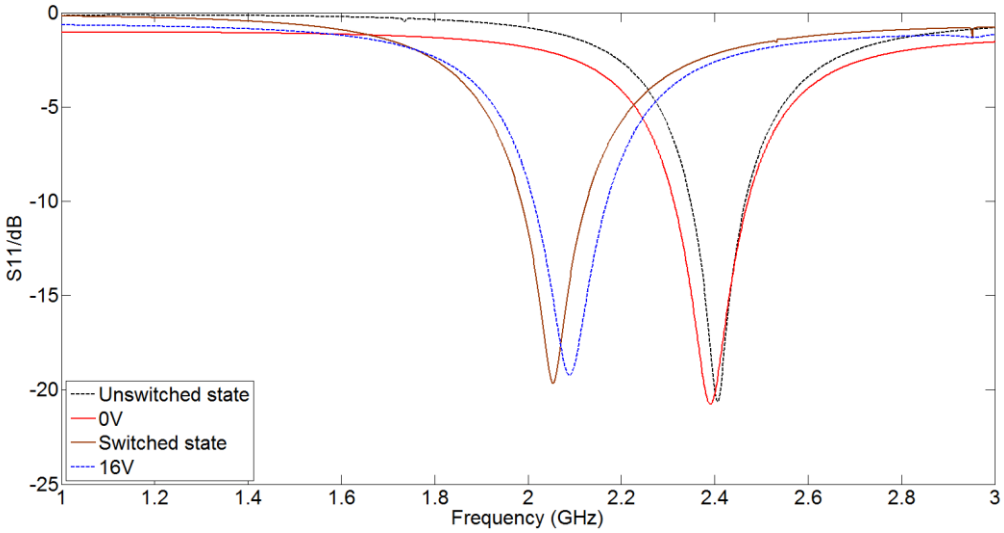

Figure 6. 29 Resonant frequency as a function of bias voltage

Figure 6.29 shows the comparison between simulation and measured results at both unswitched and switched state. The resonant frequencies are 2.4GHz and 2.39GHz at unswitched state and 0V, respectively. The resonant frequency for the switched state is 2.05GHz and the corresponding measured result at 16V is 2.08GHz. The discrepancies are 0.01GHz and 0.03GHz are unswitched and switched state, and the discrepancies prove there are good agreements for the resonant frequency at both unswitched and switched state. As for the FBW, it is 17% at unswitched state and 21% at 0V, while it is 24% at switched state and 25% at 16V. The discrepancy of FBW is 4% at unswitched state and 1% at switched state. With the small discrepancies in both resonant frequency and FBW, there is good agreement between simulated and measured results.

6.6. Microstrip Tunable LC Resonator Using IDC for 5 GHz

Tunable resonator using IDC at 2.4GHz has been studied and they have shown good performance at 2.4GHz. There are two channels for WiFi, one is 2.4GHz and the other channel is 5GHz, which has been investigated with ELC resonators in Chapter 5. Since using IDCs can achieve more capacitance then ELC resonators, it means that the length of inductive loops can be reduced and the size reduction can be realized with using IDCs. Therefore, tunable resonators using IDCs are designed at 5GHz to realize size reduction.

6.6.1 First Optimization with ADS

The resonator is designed and calculated using the methods and equations stated in Section 6.1. Based on fabrication considerations, such as the constraints of total area available for the resonator and the minimum of gap between electrodes, the fingers used are chosen from 4 fingers to 11 fingers, and the length and width of the resonator is chosen not to be less than 10mm. The tunable resonators using IDC with different fingers are designed to work at 5GHz and they are calculated using the empirical equations, which were completed using Matlab to generate the dimensions for the resonator. The comparison of the simulated results among different IDC fingers is shown in Table 6.13. As can be seen from Table 6.13, the largest tuning range is achieved when the number of fingers is 9. The results shows that the resonant frequency shifts from 5.51GHz to 5.03GHz when the (scalar) permittivity changes from 2.72 to 3.13, and the tuning range is 480MHz. Therefore, the IDC with 9 fingers is designed to work at 5GHz.

IDC with fingers	Resonant frequency (GHz) at ($\varepsilon = 2.72$)	Resonant frequency (GHz) at ($\varepsilon = 3.17$)	Tuning range (MHz)	Tunability
4	5.42	5.01	410	8.3%
5	5.46	5.02	440	8.7%
6	5.43	5.03	400	7.9%
7	5.45	5.04	410	8.1%
8	5.47	5.02	450	8.9%
9	5.51	5.03	480	9.5%
10	5.45	5.01	440	8.7%
11	5.43	5.04	390	7.7%

Table 6. 13 Comparison of the simulation results of different IDC fingers using ADS

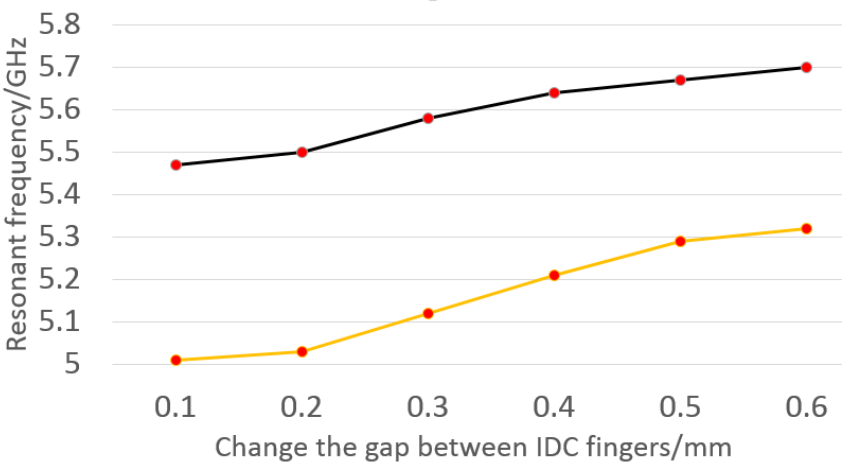

(a)

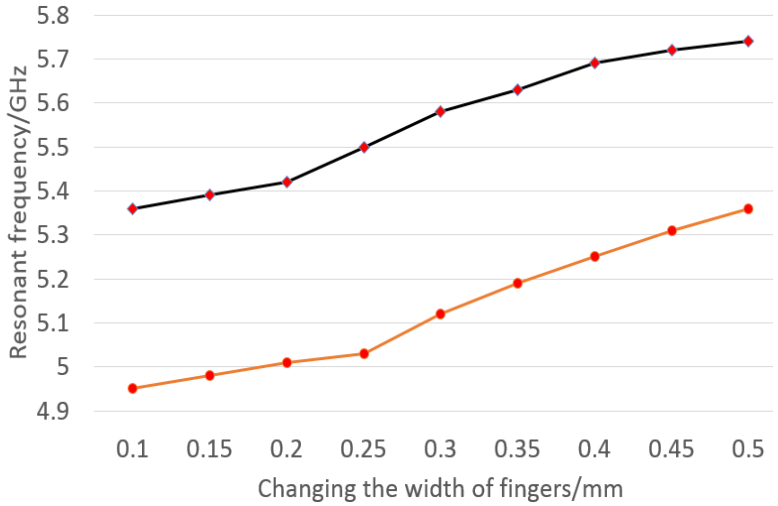

(b)

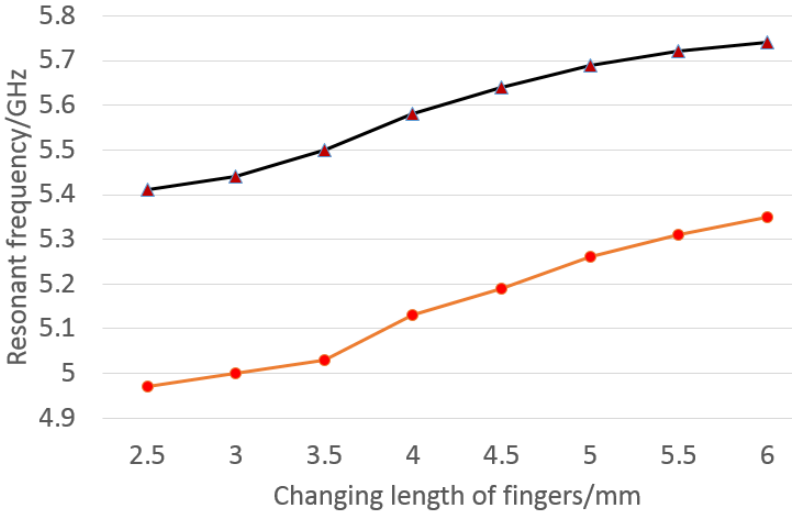

(c)

Figure 6. 30 The comparison of resonant frequencies for IDC with 9 fingers with(a) changing gap *g* between IDCs (b) changing width *w* of fingers (c) changing the length *l* of fingers

As stated in the previous sections, the optimization process focuses on the IDC element. Therefore, the length l, the width w and the gap g of the IDC are first optimized using ADS, and the results are shown in Figure 6.30. Figure 6.30(a) shows the comparison of changing gap *g*, and it can be seen that the resonant frequencies are more sensitive at both unswitched and switched state when changes the gap from 0.2mm to 0.4mm, since more tuning range can be achieved. As for changing the width *w* of the IDC finger, Figure 6.30(b) indicates that from 0.2mm to 0.4mm, there are greater increase, which changes from 5.42GHz to 5.69GHz and 5.01GHz to 5.25GHz. Figure 6.30(c) shows the resonant frequency as a function of changing length *l* of IDC fingers. The resonant frequency shifts from 5.44GHz to 5.68GHz and 5GHz to 5.26GHz when changing the length *l* from 3mm to 5mm, and it corresponds to a change of 220MHz and 260MHz, respectively.

The resonant frequency using the dimensions from empirical equations is 5.51GHz, and it is close to the required working frequency of 5GHz. Therefore, based on the comparison above, slightly changes in the dimensions can achieve the required working frequency. After the first optimization using ADS, the required working frequency of 5GHz is achieved with the dimensions shown in Table 6.14.

L	*W*	*l*	*w*	*b*	*g*
12	12	3.5	0.25	0.5	0.2

Table 6. 14 Dimensions after first optimization using ADS

6.6.2 Second Optimization with CST

The dimensions in Table 6.14 are used to build the 3D model of the proposed tunable resonator using IDCs, and it is shown in Figure 6.31. The dielectric substrate Rogers 5880 ($\varepsilon_r = 2.20$) with the thickness of 0.79 mm is used to support the inverted microstrip resonator elements and microstrip I/O ports. The feed line is placed on the upper side of the top substrate, and connected to the inverted microstrip on the inside using metalised vias with a diameter of 0.4 mm to achieve impedance matching. Another Rogers 5880 dielectric layer

with a thickness of 0.13mm is used as a spacer and is patterned to form the LC cavity between the microstrip and the ground plane, which is final piece of Rogers 5880 substrate. The inner surfaces of both substrates have a thin polymer alignment layer deposited and a fill hole in ground plane substrate is used to flow the LC into the cavity after assembly. SMA connectors are used to connect the microstrip input to the resonator, and make it easier to integrate into other microwave systems.

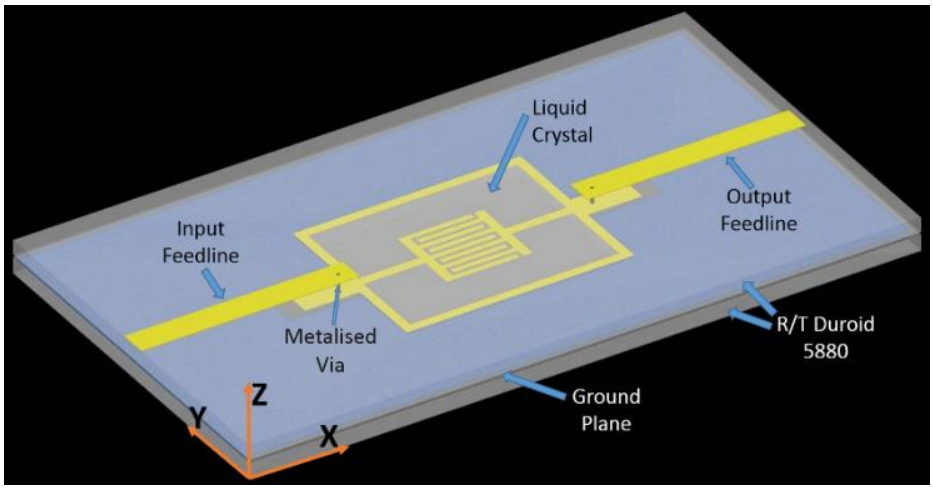

Figure 6. 31 3-D view of the inverted bandpass tunable resonator

CST Microwave Studio is used as the electromagnetic wave simulator to verify the resonant frequency from the equivalent circuit analysis and guide the optimization process. As a LC is a uniaxial anisotropic material, three orientations of the unixial anisotropy were simulated, along *x*, *y* and *z*, shown in Figure 6.31. The orientations along *x* and *y* represent the unswitched LC along either of these directions defined using an alignment layer; for the simulation the permittivity is taken to be $\varepsilon_{r\|}$ along *x* or *y* direction. If the orientation is along *z*, this corresponds to the switched LC when the LC director aligns with the applied voltage. So $\varepsilon_{r\|}$ is in the *z* direction for the fully switched state and is taken to be uniformly aligned in this one direction. CST modeling shows that selecting *x* gives the maximum tuning range, as shown in Figure 6.34 later. Also, since the direction of the unswitched state is imposed by the rubbing of the alignment layer, from the fabrication point of view it is clear that rubbing along *x*, which is the direction along the fingers of

the IDC, is more likely to produce an effective anchoring.

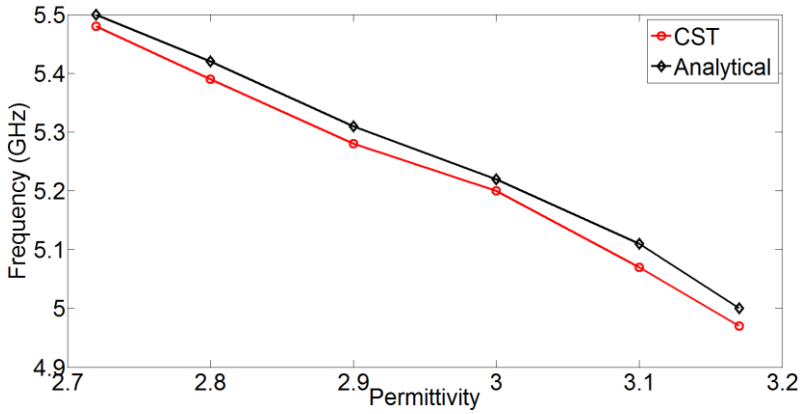

Figure 6. 32 Simulated and theoretical resonant frequency versus ε_r

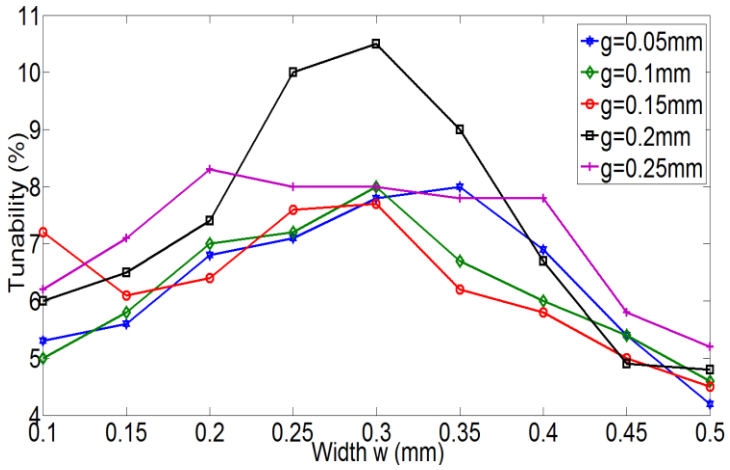

(a)

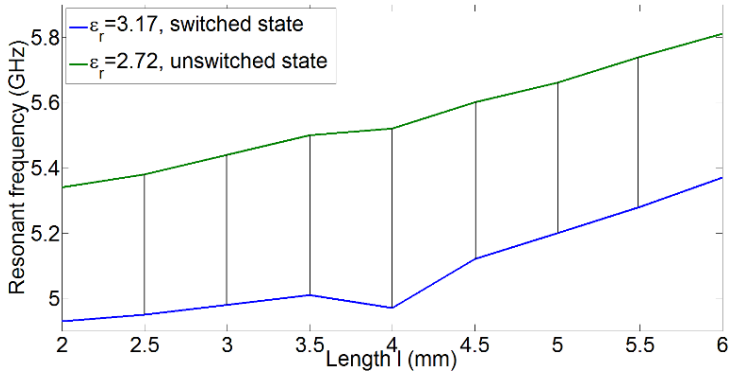

(b)

Figure 6. 33 Optimization dimensions with changing length, gap and width of IDC (a) changing gap and width (b) Comparison of changing length

In order to make sure the lumped element model is satisfactory, a comparison between the resonant frequencies from ADS simulations and from CST simulations is plotted versus ε_r in Figure 6.32, which uses the values for the device dimensions given in Table 6.14. The results from CST and ADS show a good agreement and the differences are within 1%. The small discrepancies between the theoretical and simulated resonant frequencies are due to the parasitic elements that are ignored in the analytical calculations with ADS.

The next optimization stage of the design is using CST to maximize the tuning range as the permittivity ellipsoid is changed from along *x* to along *z* assuming the LC is homogeneous, as discussed above. The optimization involves keeping the inductive loop fixed and varying three of the dimensions of the IDC, the length l, the inter-electrode gap g and the width w. The optimization starts by fixing the length l from the dimensions shown in Table 6.14, and changing *g* and *w*. With fixed l and considering the resolution limits of fabrication, the gap is changed from 0.05 mm to 0.25 mm with steps of 0.05 mm, and width is changed from 0.1 mm to 0.5 mm with steps of 0.05 mm. The optimization shows that *g* = 0.2 mm and *w* = 0.3 mm give the largest tunability. Then, *g* and *w* are kept fixed and the length l is changed with steps of 0.2 mm. With a length of 4 mm, the largest tuning range is achieved, with a tunability of 11%. The *l* is then varied with *g* and *w* found from the optimization, and the results confirm that the largest tuning is obtained with *l* equal to 4mm. The optimization results are shown in Figure 6.33. The final optimized dimensions of the proposed resonator are shown in Table 6.15. Compared with the size of tunable resonator s using ELC resonator at 5GHz, tunable resonator s using IDC with 9 fingers has a size reduction of 26.5%, which satisfies the aim of using IDC at 5GHz.

L	*W*	*l*	*w*	*b*	*g*
12	12	4	0.3	0.5	0.2

Table 6. 15 The dimensions after CST optimization

Before fabrication, modelling of the resonator with optimized dimensions was carried out to investigate the resonant frequency and tunability. It was found in Figure 6.34 that the resonant frequencies for alignment along *x* and *y* are similar, 5.52GHz and 5.49GHz respectively, and the chosen alignment along *x* made from the electric field and LC modelling, shows to be the better one since it has the slightly larger tuning range. Starting with alignment along *x*, the resonant frequency shifts from 5.52GHz to 4.97GHz on reorientation to the *z*-direction, as occurs with an applied voltage, and the fractional bandwith (FBW) are 11% and 9.6%, respectively. The frequency shift corresponds to a tuning range of 550MHz, and the tunability is 11%. The return losses at resonance are -23dB for the unswitched state and -21dB for the switched state, and the insertion losses are -0.82dB and -1.12dB respectively, shown in Figure 6.34.

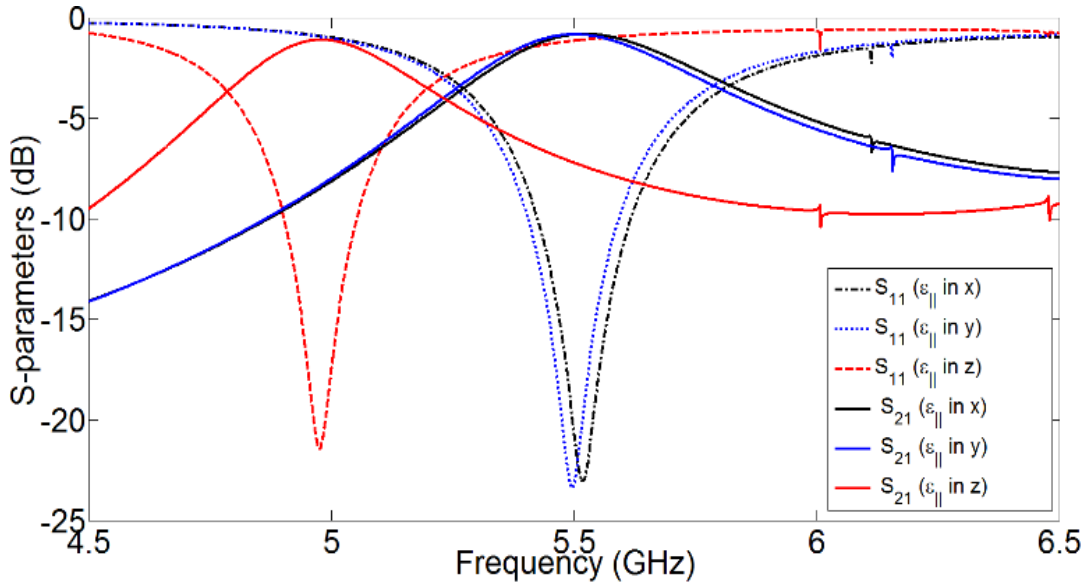

Figure 6. 34 Simulation results of insertion loss (S_{21}) and return loss (S_{11})

6.6.3 Fabrication of the Device

Standard photolithography was used to fabricate the test resonator. The feedlines and the microstrip resonator structure on the dielectric layers were masked and etched. In order to form the cavity to contain the LC, the surfaces must be initially prepared. The top and bottom surfaces of the resonator were coated with a thin layer of polyvinyl alcohol (PVA) made by Sigma-Aldrich to

planarize and provide the anchoring and alignment of the LC. The layers were mechanically rubbed longitudinally (along *x* in Figure 6.31) to control the alignment of the surface anchoring, as is standard in the fabrication of LC devices. The alignment layers produce the correct orientation of the bulk LC in the absence of the bias voltage, and restore the original planar alignment after the voltage is removed. The device was filled with LC using a fine syringe through a small hole on the bottom layer. To examine the possibility of leakage or air bubbles with this procedure, a test cell with an ITO glass plate instead of the ground plane was made to allow observation of the filling process. This showed no leakage, and examination under a microscope showed the absence of air bubbles.

6.6.4 Measurement of Tunable LC Resonator Using IDC with 9 Fingers

The fabricated and assembled device and measurement setup is shown in Figure 6.35. The frequency response was measured using a Keysight E5071C network analyser. The input port of the resonator was connected to the analyser through a Bias-Tee. A 1 kHz voltage was used and measurements were taken with the biasing voltage amplitude varying from 0 V to 16 V in 0.5 V steps.

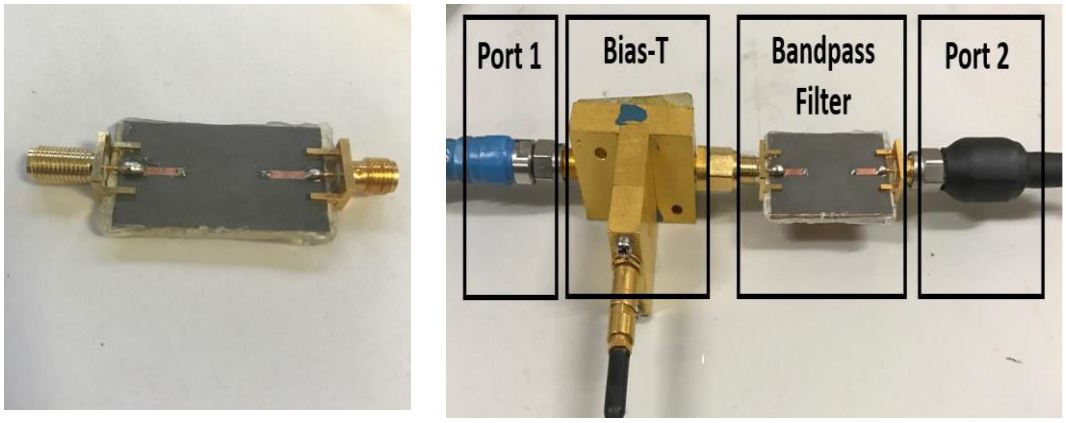

(a) (b)

Figure 6. 35 (a) Fabricated and assemble device (b) Measurement Setup for the experiment (from left: port1, bias-tee, resonator and port2)

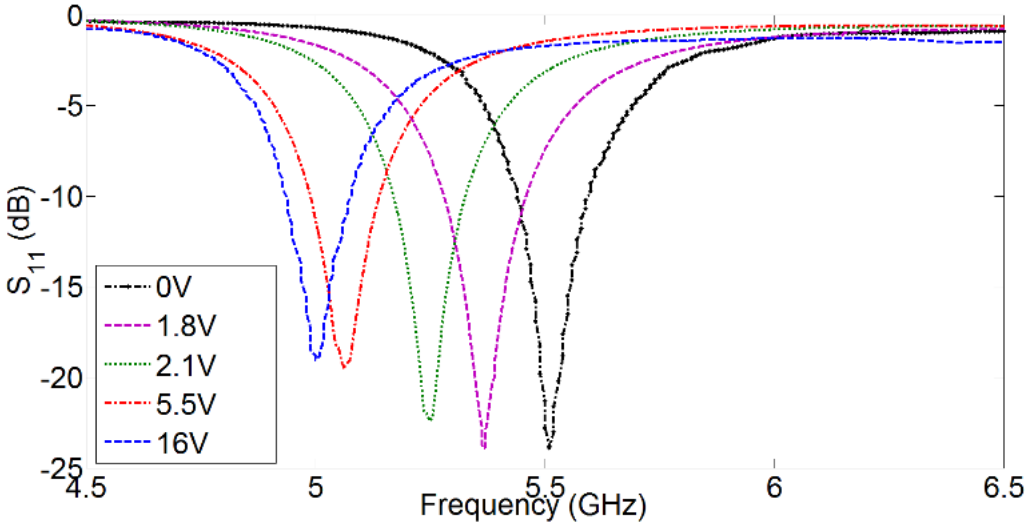

(a)

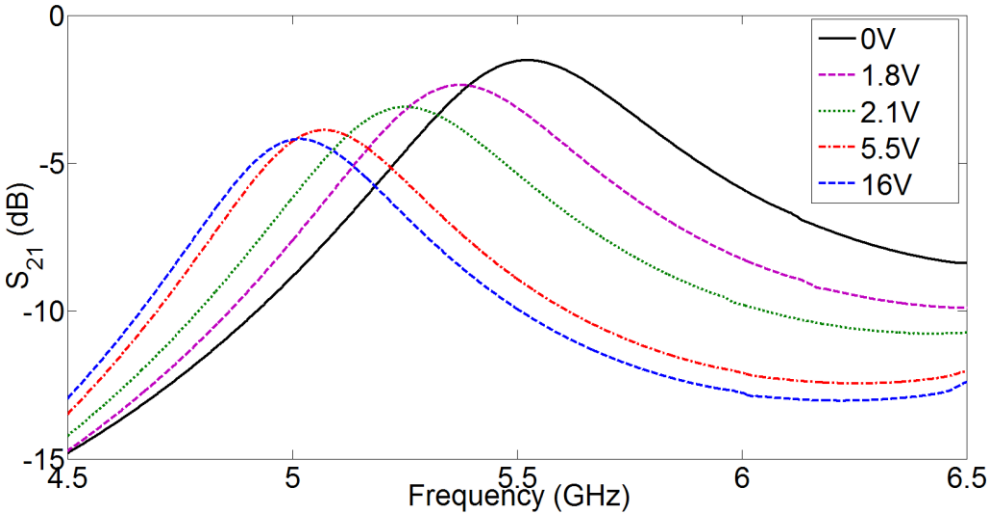

(b)

Figure 6. 36 Measured S-parameters with changing bias voltage (a) Measured S_{11} with different bias voltages (b) Measured S_{21} with different bias voltages

Figure 6.36 shows the measured S-parameters with different bias voltages. The S_{11} measured at different bias voltages for the resonator is shown in Figure 6.36 (a). A clear shift in the resonant frequency is observed in the measured response, which indicates that gradually increasing the bias voltage gradually switches the LC and reorients it from the un-switched state. As shown in Figure 6.36(a), the resonant frequency is 5.51GHz and the FBW is 8.3% with no bias voltage. By increasing the bias voltage, the LC directors start to re-orient from parallel (along the *x* direction) to perpendicular (along the *z* direction) to the electrodes. When the bias voltage achieves the saturation value, the LC is largely aligned perpendicular (along *z*) to the

electrodes. The central frequency goes to a minimum resonant frequency of 5.01GHz with a FBW of 9.5%. Therefore, the tuning range is 500MHz, which corresponds to a tunability of 10%. Figure 6.36 (b) indicates that changing the bias voltage, the insertion loss S_{21} changes from -1.5dB to -4.2dB.

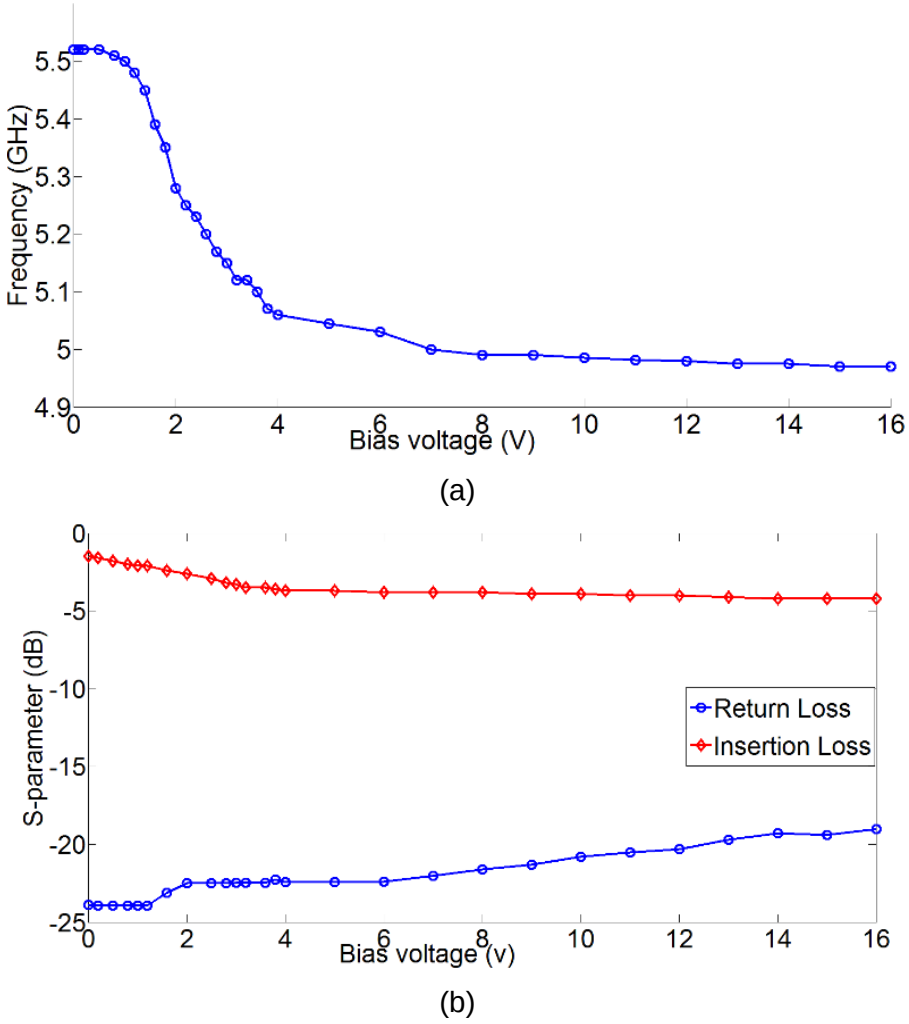

Figure 6. 37 (a) Centre frequency as a function of LC bias voltage (b) Measured insertion loss and return loss as a function of voltage

Figure 6.37 shows the centre frequency, and the measured insertion and return losses as functions of the LC bias voltage. When a voltage is applied across an LC cell there is a threshold voltage before the LC starts gradually to re-orient itself to the applied field (Fréedericksz transition).For E7 this threshold is about 0.5 V and Figure 6.37(a) shows this behaviour for the centre frequency. After 0.5V, the central frequency decreases slowly and continuously for intermediate values between 0.5V to about 7V and there is

little change after that. When the bias voltage increases to more than 7V, the LC reaches a saturation state and most of the LC is oriented perpendicular to the electrodes. Figure 6.37(b) indicates that when the bias voltage increases from 0V to 16V, the return loss is bigger than 18dB and the insertion loss changes from -1.5dB to -4.2dB. The increases in the insertion loss can be attributed to the anisotropy of the loss tangent which is higher along the director [Chandrasekhar, 1992].

Figure 6.38 shows the comparison of simulation results and measured results for the unswitched and switched states. As can be seen from Figure 6.38, the simulated and measured S_{11} show very good agreement in the unswitched state. However, the results show a small difference in the switched state, from 4.97GHz for the simulation to 5.01GHz for the measured S_{11}.

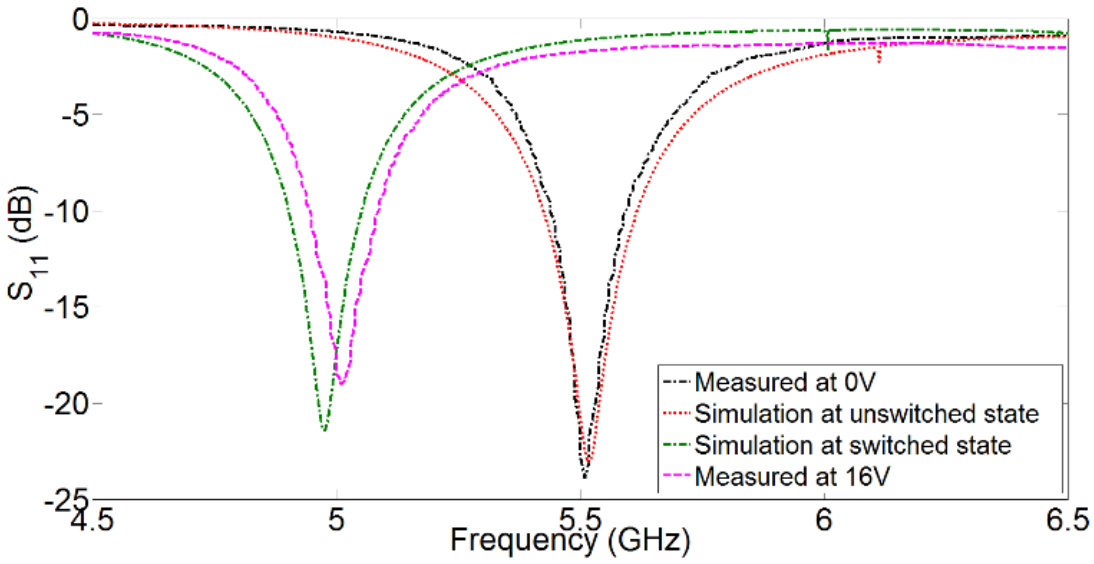

Figure 6. 38 Comparison of Measured and Simulated S_{11} at unswitched and switched state

To illustrate the reasons for this discrepancy, a finite element 3D modelling [Willman, 2007] is used to calculate the detailed LC director switching in the device. The director represents the average direction of the molecules in the LC and so shows the axis of the anisotropy. The CST simulation assumes a homogeneous anisotropic layer, but the reality is that the liquid crystals switches to a non-uniform structure. Figure 6.39 shows director profile of the switched seen that LC is not fully oriented in the cross-section of the device in

Figure 6.39(a). Furthermore, there is a narrow layer next to the alignment layers that will remain unswitched. The effective permittivity is found by summing the value of the permittivity along the field and in the switched state the value will be close to $\varepsilon_{r\|}$ but lower. Figure 6.39(b) shows that beyond the edge of the electrodes, the LC is only partially switched contributing to a lowering of the effective permittivity for this region.

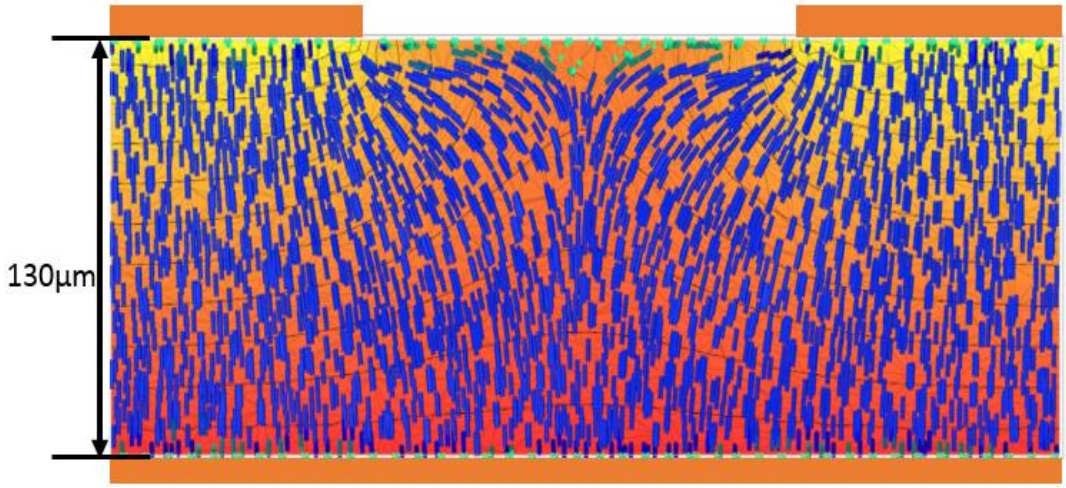

(a)

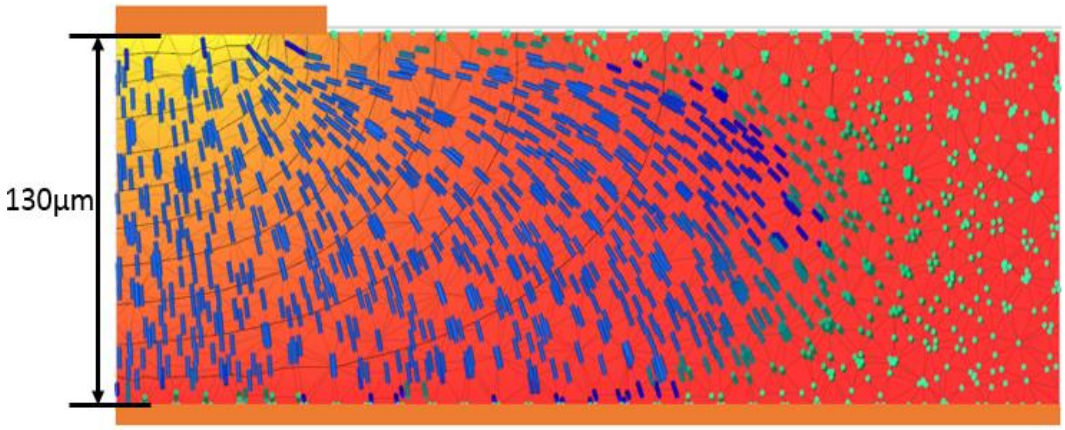

(b)

Figure 6. 39 Orientation of LC directors shown with rods with applied voltage (background colour) at (a) region between electrodes (b) at the edge of the electrodes. The ground electrode covers the whole of the bottom surface. Ground plane is the bottom layer, and its size is 40×32mm. Top electrode is half of the IDC fingers, it is around 0.15mm.

In order to provide a more accurate value for the effective permittivity, the LC director simulation results in the region between the electrodes and the ground

plane are used to calculate an approximate value of the effective permittivity ε_{eff}. It could be seen from the CST simulation that the highest microwave field was in this region and only small fields were found between the electrodes and beyond the edges of the electrodes. The effective permittivity was calculated by simply averaging the z-component of the dielectric constant. This was found to be $\varepsilon_{eff} = 3.12$, which is slightly lower than $\varepsilon_{r\|}$ for E7. The extracted value of ε_{eff} is then used in the CST simulation and the new resonant frequency is 4.99GHz with the FBW of 8.8%, and the insertion loss and return loss are -1.17dB and -23.6dB, respectively. Compared with simulation using $\varepsilon_{r\|} = 3.17$, the new resonant frequency is closer to the measured S_{11} and shows more accurate agreement with the measured results.

6.6.5 Comparison with Other Tunable Resonators Using LCs at 5GHz

Performance comparisons of the proposed tunable resonators with other tunable resonators reported in the literature are summarized in Table 6.16. The comparison involves some characteristics that indicate the performance of the resonator, such as the centre frequency, FBW, tunability, insertion loss and return loss. As can be seen from Table 6.16, our work has better performance in narrower bandwidth, lower insertion loss, better return loss and the largest tunability.

Tunable LC devices	Centre Frequency (GHz)	FBW	Tunability	Insertion Loss (dB)	Return Loss (dB)	LC
[18]	4-5	81.5%-86.4%	7.3%	4.2-4.0	Unknown	Unknown 2.88-3.26
[19]	5	22%	6%	6-9	>7	Unknown 2.4-3.2
[24]	5	12.2%-12.6%	4.8%	3-6	>18	Merck MDA-98-1602 2.62-3.06
[25]	5	41%-50%	6%	>3	>10	K15 2.72-2.9
This work	5	8.3%-9.5%	10%	1.5-4.2	>18	Merck E7 2.72-3.17

Table 6. 16 Comparison with previous tunable resonators based on LC

6.7 Conclusion

In this chapter, the tunable resonator using IDC with different numbers of fingers are have been studied. Using IDCs can generate more capacitances and therefore can work at lower frequency without increasing the size of the resonator. In the first part of this chapter, the tunable LC resonator using IDCs are designed to work at 2.4GHz. Tunable LC resonator using IDC with 4, 5 and 9 fingers are designed using the proposed general design method, and are optimized and fabricated. The tunable LC resonator using IDC with 4 fingers shows a tuning range of 0.28GHz and a tunability of 13.2%. The tunable resonator using IDC with 5 fingers shows a tuning range of 0.33GHz and a tunablity of 16%. The tunable LC resonator using IDC with 9 fingers has the best performance among the three resonators, it has a tuning range of 0.35GHz and a tunability of 16.6%. Compared with the tuning range from using empirical equations for the three resonators, the optimized simulation results all show increased tuning range. The comparisons between the simulated and

measured results for the three resonators show very good agreement in both the resonant frequency and bandwidth.

In the second part of the chapter, the tunable LC resonators using IDC are also designed to work at 5GHz. Compared with the tunable ELC resonators, using IDCs can generate more capacitances and inductance can be decreased, thereby achieving a size reduction. The results from empirical equations also suggest that tunable LC resonator using IDC with 9 fingers has the largest tuning range. Therefore, the tunable resonator using IDC with 9 fingers are designed, optimized and fabricated. The size for the optimized IDC with 9 fingers shows a size reduction of 26.5%, compared with ELC resonator working at the same frequency. The fabricated device is measured and shows a tuning range of 500MHz with a tunability of 10%, in good agreement with the predictions from CST. Accurate finite element modelling of the LC switching is used to explain the small discrepancy in measured and simulated S_{11} for the switched state. A more accurate value of the effective permittivity is estimated from the LC modelling and used in CST to give more accurate results that show a better agreement with the measured results. The comparison between this work and the literature shows that this resonator has narrower bandwidth, larger tunability, lower insertion loss and a better return loss.

Chapter 7 Tunable Ring Resonators Using LCs

In the previous chapter, the tunable LC resonators using IDCs have been investigated. In this chapter, ring resonators are proposed, which are distributed resonators having narrowband and high selectivity. The microstrip ring resonators have been widely used as microwave resonators, couplers, oscillators and antennas [Sun, 2007], and they have the advantages of high quality factor, compact size and sharp rejection [Nakhlestani, 2013; Olokede, 2017]. In this chapter, a tunable LC resonator using single ring resonator is designed to have narrow bandwidth and constant 3dB bandwidth.

7. 1 Tunable LC Resonator using Single Ring Resonator

7.1.1 Design Method for Single Ring Resonator

Figure 7.1 shows the schematic view of the ring resonator. A small gap *g* is included between the ring and each feed line. The feed lines are designed to be 50Ω to achieve impedance matching

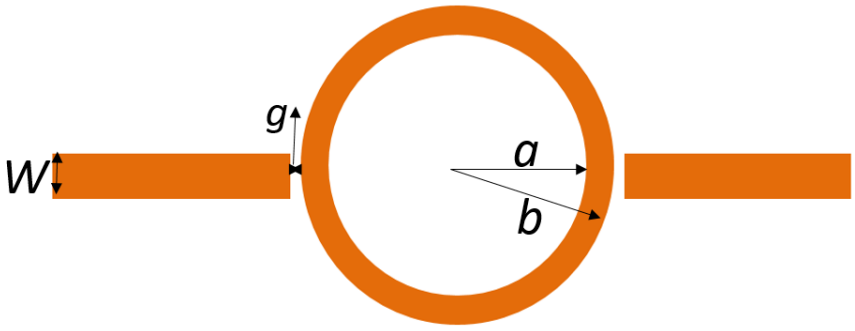

Figure 7. 1 Schematic view of the ring resonator

In order to design the ring resonator, the design method needs to be described. The analysis of ring resonator was first introduced by [Wolff, 1971], [Chang, 1996] and [Yu, 1997] developed new method to synthesis ring resonator, where closed form expressions for the ring resonator are found. The single ring resonator shown in Figure 7.1 can be represented by using three separate circuit elements cascaded together, as shown in Figure 7.2. The feed lines are

not considered in the model because they are treated as lossless lines and matched to 50Ω.

Figure 7. 2 Network circuit of planar ring resonator

[Yu, 1997] state that this gap is included to separate the resonant behavior of the ring from the feed network, and it slightly affects the resonant frequencies of the ring resonator but significantly affects the peak amplitudes of the scattering parameter of the device. Therefore, an equivalent lumped circuit is used to take these effects of coupling into account. The left and right coupling gaps of the resonator can be modelled by a parallel capacitance C_p and a series capacitance C_g, as shown in Figure 7.3.

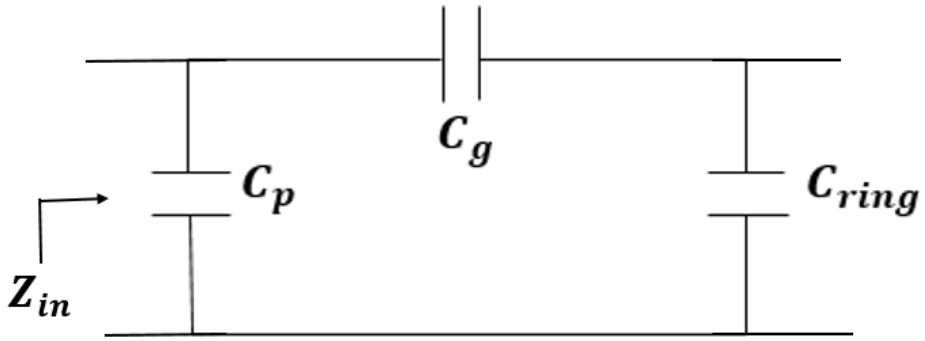

Figure 7. 3 Equivalent lumped circuit for ring and coupling

The capacitor values C_p and C_g are found by closed-form expressions of [Garg, 1978] and then modified by [Yu, 1997]:

$$\frac{C_{even}(\varepsilon_r=9.6)}{W} = 12\left(\frac{g}{W}\right)^{m_e} e^{k_e} \quad \text{7-1}$$

$$\frac{C_{odd}(\varepsilon_r=9.6)}{W} = 12\left(\frac{g}{W}\right)^{m_o} e^{k_o} \quad \text{7-2}$$

where

$$m_e = 0.8675, k_e = 2.043 - \frac{0.03}{\left(\frac{W}{h}\right)}\ 0.1 \leq g/W \leq 0.5 \quad \text{7-3a}$$

$$m_e = \frac{1.565}{(\frac{W}{h})^{0.16}} - 1, k_e = 1.97 - \frac{0.03}{(\frac{W}{h})}\ 0.5 \le g/W \le 1.0 \quad \text{7-3b}$$

$$m_o = \frac{W}{h}\left(0.619 log_{10}\frac{W}{h} - 0.3853),\right) 0.1 \le g/W \le 1.0 \quad \text{7-3c}$$

$$k_o = (4.26 - 1.453 log_{10}\frac{W}{h}\ \ 0.1 \le g/W \le 1.0 \quad \text{7-3d}$$

$$C_{even}(\varepsilon_r) = 1.167 C_{even}(\varepsilon_r = 9.6)(\frac{\varepsilon_r}{9.6})^{0.9} \quad \text{7-4}$$

$$C_{odd}(\varepsilon_r) = 1.1 C_{odd}(\varepsilon_r = 9.6)(\frac{\varepsilon_r}{9.6})^{0.8} \quad \text{7-5}$$

$$C_p = \frac{C_{even}(\varepsilon_r)}{2} \quad \text{7-6}$$

$$C_g = \frac{2C_{odd}(\varepsilon_r) - C_{even}(\varepsilon_r)}{4} \quad \text{7-7}$$

W is the width of the feed line, *g* is width of the gap, *h* is the thickness of the feed line substrate and ε_r is the dielectric constant of the substrate, respectively.

The input impedance of the ring resonator is obtained as [Yu, 1997]

$$Z_{ring} = \frac{1}{j\omega C_{ring}} \quad \text{7-8}$$

The capacitance of the ring is

$$C_{ring} = \frac{2Y_r[1 - \cos(2\pi\beta_r r)]}{\omega \sin(2\pi\beta_r r)} \quad \text{7-9}$$

Where $Y_r = \frac{1}{Z_r}$, Z_r is the characteristic impedance of the microstrip ring, and β_r is the corresponding propagation phase constant, ω is the radian frequency (rad/s) and *r* is the mean radius of the ring, and it can be determined by $2\pi r = n\lambda_g$, where λ_g is the wavelength . With explaining the input impedance of a ring resonator and coupling gaps between the feed lines and the ring, they can be integrated to form the overall equivalent circuits. The total input impedance and capacitance are obtained as

$$Z_{in} = jX_{in} = \frac{1}{j\omega C_{in}} \quad \text{7-10}$$

$$C_{in} = \frac{C_p C_g + C_p C_{ring} + C_g C_{ring}}{C_g + C_{ring}} \quad \text{7-11}$$

The resonant frequency for a circuit is the frequency that makes the

impedance seen by the source purely resistive, which means the $X_{in} = 0$. Using the equation above, the resonant frequency is calculated.

7.1.2 Optimization and Full Wave Simulation Using CST

W	*g*	*a*	*b*
2.4	0.3	11	13

Table 7. 1 Ring dimensions with initial calculation (unit:mm)

Using the method stated above, the tunable resonator using ring resonator is designed to work at 2.4GHz, and the dimensions for the ring resonator is shown in Table 7.1. Since it is difficult to find an effective equivalent lumped element model for ring resonator, and the equations 7-1 to 7-11 can give the resonant frequency directly, so there is no need to carry out the lumped element modeling using ADS. The dimensions in Table 7.1 are directly used to build 3D model in CST. Figure 7.4(a) shows the layout of the proposed ring resonator and Figure 7.4(b) presents the cross-section view of the ring resonator. It uses the same materials as the tunable devices in previous chapters.

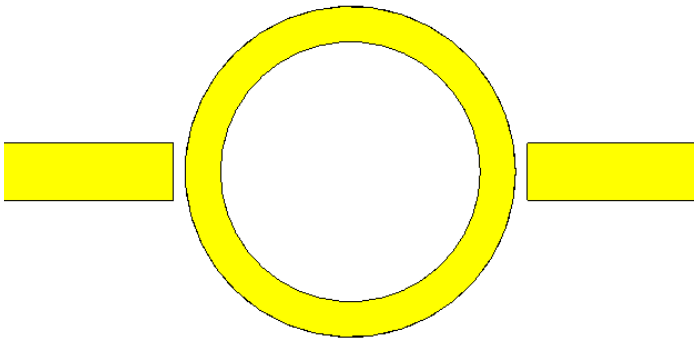

(a)

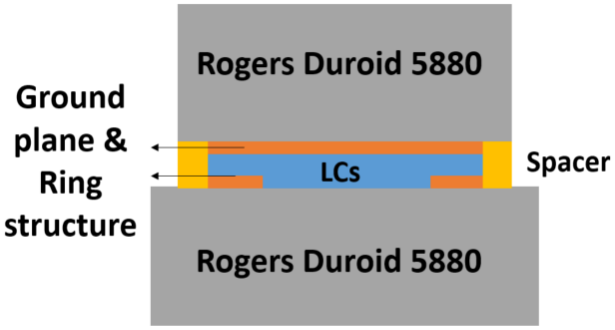

(b)

Figure 7. 4 (a) Schematic view of ring resonator (b) Cross section view of ring resonator (Not drawn to scale)

The full wave simulation is conducted using the dimensions in Table 7.5. The resonant frequencies are generated with using LCs switching from unswitched state to switched state. The simulated results of resonant frequency at unswitched and switched states are shown in Figure 7.5. As can be seen from Figure 7.5, the resonant frequency shifts from 2.35GHz to 2.11GHz from unswitched state to switched state. The tuning range is 0.24GHz and it corresponds to a tunability of 11.4%. Since the tunable bandpass ring resonator is designed to work at 2.4GHz, the optimization is carried out to adjust the working frequency and maximize the tuning range.

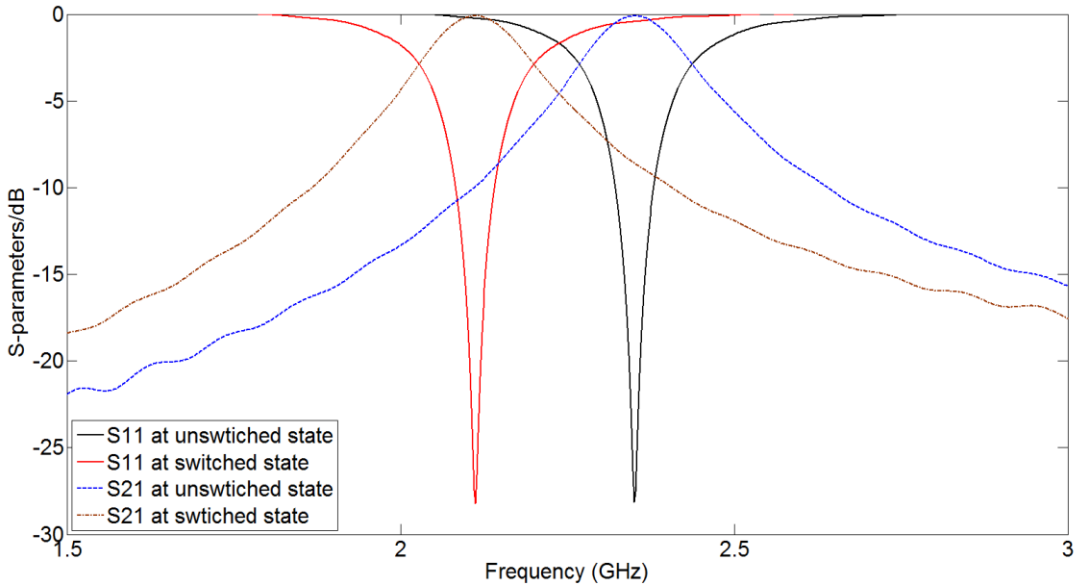

Figure 7. 5 Resonant frequency for ring resonator using CST

Before the optimization, the influences of the each dimensions to the resonant frequency needs to be investigated. There are two dimension which are important for designing the ring resonator, and they are the mean radius of the ring *r* and the gap *g* between the ring and the feed lines, respectively. The gap *g* between the ring and the feed line slightly affect the resonant frequency and mainly affects the magnitude of the resonant frequency [Bashore, 2000]. Therefore, the radius *r* of the ring and the gap *g* between ring and feed lines are investigated using CST to find out how the changes in these parameters affect the resonant frequency.

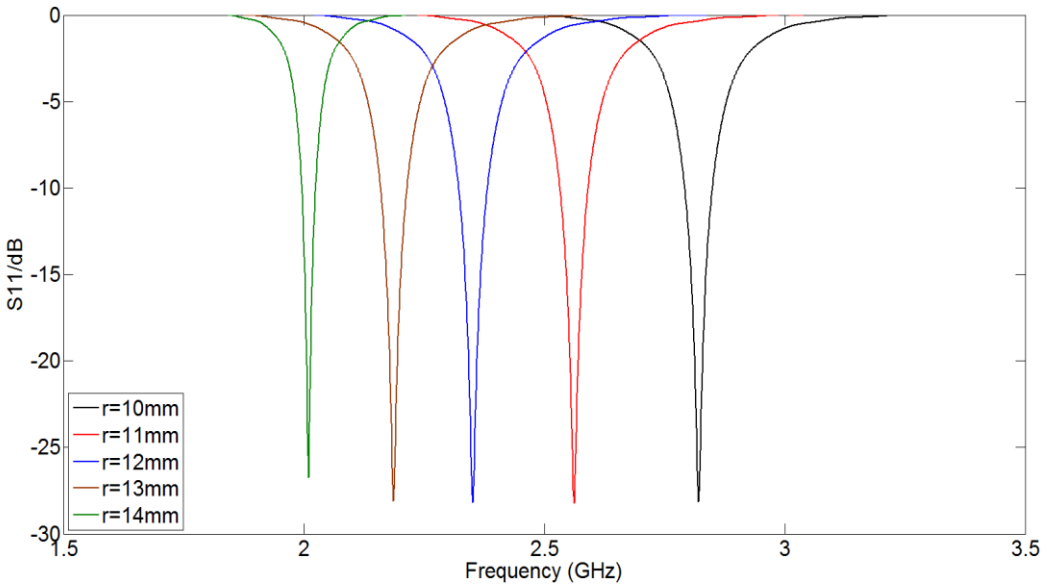

(a)

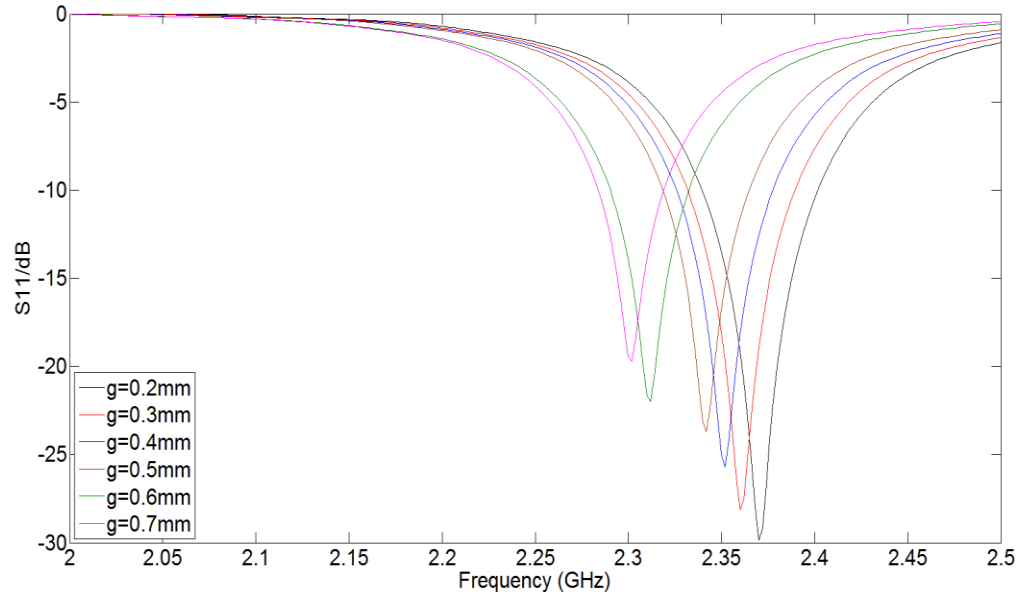

(b)

Figure 7. 6 Resonant frequency with (a) changing mean radius *r* of the ring resonator (b) changing gap *g* of the ring resonator

The mean radius *r* of the ring resonator is changed from 10mm to 14mm to find out the influences and the simulation results of the resonant frequency are shown in Figure 7.6(a). As can be seen from Figure 7.6(a), with changing the mean radius *r*, there is a clear shift in the resonant frequency. The resonant frequency changes from 2.82GHz to 2.02GHz with changing the mean radius from 10mm to 14mm with a step of 1mm. With changing every 1mm in the mean radius, the minimum resonant frequency changes is 0.18GHz and the

largest change is 0.22GHz, which means the resonant frequency is very sensitive to the mean radius *r*. Therefore, in the fabrication process, a high resolution mask is needed to fabricate this resonator so that the fabrication errors can be minimized. The gap *g* is then varied from 0.2mm to 0.7mm to find out the influences to the resonant frequency. As can be seen from the Figure 7.6(b), changing the gap *g* slightly affects the resonant frequency, which decreases from 2.37GHz to 2.30GHz with increasing the gap *g* from 0.2mm to 0.7mm. The magnitude decreases from -29.8dB to -19.7dB with increasing the gap from 0.2mm to 0.7mm, which means an average of 2dB change with changing gap of 0.1mm. In order to have a good return loss, large gap should not be chosen.

With the understanding of how each dimensions affects the resonant frequency, the optimization is carried out to adjust the working frequency and optimize the maximum tuning range. The dimensions for the ring resonator after the optimization is shown in Table 7.2, and these dimensions can be used to achieve the adjusted working frequency of 2.4GHz and the maximum tuning range.

W	*g*	*a*	*b*
2.4	0.2	12	13

Table 7. 2 Dimensions for the ring resonator after optimization

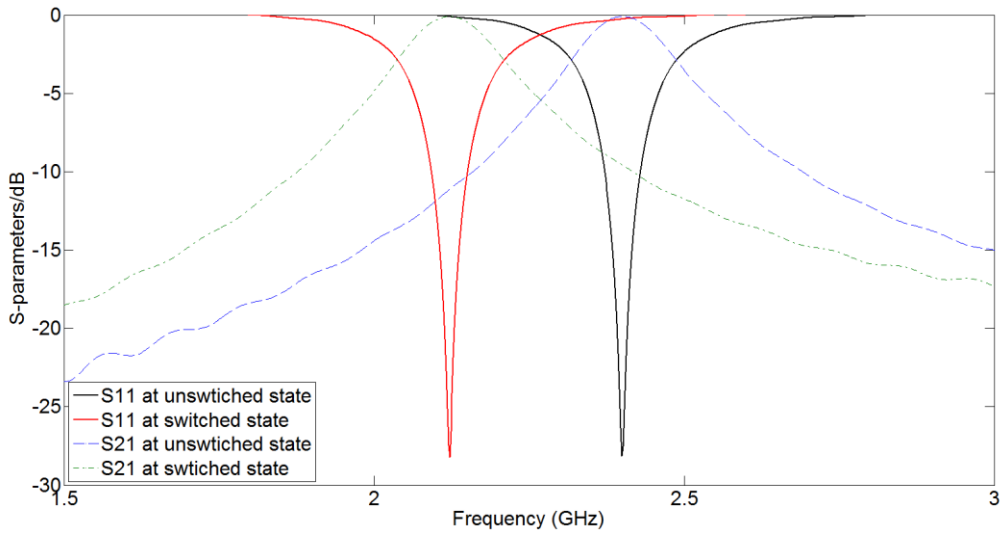

Figure 7. 7 S-parameters at unswitched and switched states using CST

The 3D model is updated with the dimensions after optimization and the full wave simulation results using CST is shown in Figure 7.7. As can be seen from Figure 7.7, the resonant frequency shifts from 2.4GHz to 2.12GHz from unswitched state to switched state. The tuning range is 0.28GHz and it is a tunability of 13.2%. The 3dB bandwidth is 170MHz and remains constant at both states. The return loss is around -28dB at both states and insertion loss is nearly 0dB. The tunable bandpass ring resonator shows very good frequency selectivity and return loss, but the area for the ring is $\pi \times 13^2 mm^2$, which is large. Therefore, this ring structure can be alternated so that a size reduction can be achieved.

7.1.3 Conclusion

The tunable LC resonator using sing ring resonator is designed and simulated. It has a tuning range of 0.28GHz and the advantages of good return loss and very low insertion loss. However, the size for the single ring resonator is relatively big. In order to reduce the size, more possible structures, such as dual mode ring resonators and split ring resonators, can be studied in the future work.

For the ring resonator, there are gaps between the feed lines and the ring structure. In order to apply bias voltage to the feed lines and the ring resonator to switch the LCs in the region, a novel approach needs to be found out. Since the bias voltage is applied separately to each elements of the tunable resonators to switch the LC, the non-uniformity of switching LCs needs to be considered and minimized to achieve the best performance.

Chapter 8 Conclusion and Future Work

8.1 Conclusion

The work presented in the thesis is firstly the design method for tunable microstrip devices using LCs and secondly applying these methods to the design of different types of tunable devices for wireless communication systems. The research presented in this thesis is summarized as follows:

Based on the advantages of low cost, low power consumption and low loss at microwave frequencies, LCs are a promising tunable material to use to build tunable devices. Therefore, the thesis focuses on the tunable LC devices at microwave frequencies. For the purpose of designing the tunable LC devices, it is important to understand the tuning mechanism of using LCs as the tunable material and how LCs are responded to external bias voltage, which are shown in Chapter 2. In order to form an aligned layer of the LCs, LC must be confined between two flat substrates, which have a polymer alignment layer to maintain a single domain in the director field. A microwave structure that is compatible with the thin flat layer uses inverted microstrip structures to propagate the microwave field between the electrodes and a ground plane. The LC layer also requires a low voltage to be applied across the layer to re-orient the director, thus changing the dielectric properties of the LC seen by the microwave field. The fabrication process of LC devices consists of two process, patterning electrodes and assembling the devices. The patterning electrodes process is developed by testing different methods, such as milling, laser cutting, microplotter and etching. The laser cutting and etching are decided to use for device which has dimension larger or smaller than 20μm, respectively. For LC devices, the alignment layers need to be deposited and rubbed to provide the pre-alignment for LCs, and it is achieved by using spin coating and dip coating.

A general design method for microstrip devices using LCs needs to be developed to design LC devices efficiently with high quality. In Chapter 4, a novel general design method for designing tunable microstrip devices using

LCs is proposed. The design method consists of two stages using lumped element modelling and full wave simulation, respectively. This method starts from choosing a microstrip configuration and turn it into equivalent circuit lumped element model through theoretical or empirical equations. The equivalent circuit is built in the ADS to perform the lumped element modelling, where the circuit dimensions are first optimized in terms of adjusting to the required working frequency and maximize the tuning range. The lumped element model is then converted back to microstrip configuration, and it is built in the CST to generate the S-parameters and electric field at resonant frequencies. The comparison between simulated S-parameters from ADS and CST is made to ensure the equivalent lumped element model is correct to use. A final check is made to verify the approximation of using LCs as a homogeneous anisotropic material by comparing the electric field at resonant frequency from CST and director profile of LCs from QLC3D, which an in-house finite element modelling.

The proposed novel design method for LC devices at microwave frequencies is then tested and verified in Chapter 5. Three types of ELC resonators, where additional inductances or capacitances are added, are designed, simulated and fabricated at the working frequency of 4.8GHz and 5GHz. The merit of using ELC resonator is that it increases the tuning range by strong coupling to the electric field. The type I ELC resonator shows a tuning range of 570MHz (11.8%) from 4.8GHz to 4.23GHz for the simulation, and the measured results shows that the resonant frequency shifts from 4.76GHz to 4.29GHz, which corresponds to a tuning range of 470MHz (9.8%). The comparison between simulation and measured results show that the biggest discrepancy for the centre frequencies is 1.9%, which is relatively a small discrepancy. Type II ELC resonator indicates that the simulated resonant frequency switches from 5GHz to 4.47GHz, and it shows a tuning range of 530MHz and a tunability of 10.6%. While the measured results shows that the resonant frequency changes from 4.98GHz to 4.51GHz with the tuning range of 480MHz (9.6%). Type III uses a different microstrip configuration of the feed lines and the method to connect to the ground plane, where the feed lines and the ELC structure are on the same side. The simulation of this structure shows that the resonant frequency

shifts from 5GHz to 4.42GHz, and it is a tuning range of 570MHz and a tunability of 11.4%. The measured resonant frequency changes from 4.98GHz to 4.46GHz, which corresponds to a tuning range of 520MHz and a tunability of 10.5%. However, this structure shows big discrepancies in the magnitude of S-parameters, which can be attributed to the loss from using this configuration. Therefore, the inverted microstrip structure is used in the whole project. Based on the comparison of the simulated and measured results for the three types of the ELC resonators, the novel design method proposed in Chapter 4 is correct and effective to use to design LC devices, and it is used to design all the LC devices proposed in this thesis.

Having developed and proved the design method, it was applied to two classes of tunable resonators in Chapter 6 and 7. The first class of tunable resonators are designed in Chapter 6 to work at lower frequency without increasing the size. An interdigital capacitor (IDC) is used to generate more capacitance in folded area. The IDCs with different number of fingers are used to design tunable resonators working at 2.4GHz in the first part of Chapter 6. The tunable resonator using IDC with 9 fingers has the largest tuning range of 0.31GHz (16.6%), which shifts from 2.4GHz to 2.05GHz for the simulation. The measured resonant frequency shows a shift from 2.39GHz to 2.08GHz, and it corresponds to a tuning range of 0.31GHz and a tunability of 14.9%. The discrepancies between the simulation and measured results are 0.01GHz and 0.03GHz, which shows good agreements for the resonant frequency at both unswitched and switched state. In the second part of Chapter 6, IDCs are used to design tunable resonators at 5GHz, allowing comparison with the ELC resonators in Chapter 5. IDC with 9 fingers is chosen to be used due to the largest tuning range from the simulation. Compared with ELC resonator working at 5GHz, using IDCs with 9 fingers can achieve a size reduction of 26.5%. The simulation results shows a frequency shift from 5.52GHz to 4.97GHz, and it is a tuning range of 550MHz and a tunability of 11%. While the measured resonant frequency shows it changes from 5.51GHz to 5.01GHz, which corresponds to a tuning range of 500MHz and a tunability of 10%. In order to achieve more accurate results, the in-house finite element modelling softeare QLC3D is used to generate more accurate value for the LC, and it

shows a resonant frequency of 4.99GHz, which shows more accurate agreement with the measured results. Compared with the reported literature of LC devices working at 5GHz, the final IDC tunable resonators using IDC at 5GHz has the largest tuning range and tunability, and good return loss and better insertion loss.

In Chapter 7, the tunable ring resonator is designed to explore more possibility of tunable LC devices. The tunable single ring resonator is designed to work at 2.4GHz, and the resonant frequency shifts from 2.4GHz to 2.12GHz, which corresponds to a tuning range of 0.28GHz and a tunability of 13.2%. More ring resonator structures will be designed and tested in the future work.

CST has been shown to give accurate simulation of the LC layer for the lower microwave frequency ranges for microwave resonators. In some ways this is surprising because the liquid crystal is a highly inhomogeneous anisotropic layer, particularly when partially switched. However in optimising the tuning range it is only necessary to model the extreme values of dielectric constant, which can be done by representing the LC layer as a homogeneous anisotropic layer. The true performance of the devices has been measured and shown to give continuous tuning of the resonant frequencies as the voltage switching the liquid crystal layer is gradually changed.

8.2 Future work

For the future work, the following are suggestions to extend the investigations based on the research presented in the thesis:

1. Since the proposed design method is effective to use at lower microwave frequency, it would be useful to consider extending the method to higher frequencies. The design method approximates the LCs to a homogeneous anisotropy material in CST. At the higher microwave frequencies, this approximation may fail, because the LCs may be switched to a very inhomogeneous state in the regions where there is a high microwave field. In these cases, an efficient method to

take the LC director modelling profile and represent this as an inhomogeneous material in CST needs to be found out. Another consideration in the higher microwave frequencies is that a coplanar waveguide (CPW) is a more suitable waveguide as SMA connectors are not suitable to use higher microwave frequencies due to loss. Thus, the resonator's input needs to be redesigned to make them compatible with CPW.

2. In the Chapter 7, the designed tunable ring resonators have gaps between the feed lines and resonator structure. Therefore, a new method needs to be developed to connect the feed lines and resonator structures without affecting the performance of the resonators. Moreover, the non-uniformity of the LC switching needs to be considered and realized in the simulation which may eliminate the discrepancies between simulation and measured results.

3. The material used in this thesis is LCs from Merck E7, which anisotropy is not high. Therefore, LCs with higher anisotropy, such as GT3 series LC can be used in these resonators to achieve more tuning. However, in the proposed design method, the impedance matching can be realized at one state, which may cause impedance mismatching at another state. Using LCs with higher anisotropy may make the mismatching at one state worse.

References

[Abbaspour-Tamijani, 2003] Abbaspour-Tamijani, A., Dussopt, L. and Rebeiz, G.M., 2003. Miniature and tunable filters using MEMS capacitors. I*EEE Transactions on Microwave Theory and Techniques, 51(7)*, pp.1878-1885.

[Adam, 202] Adam, J.D., Davis, L.E., Dionne, G.F., Schloemann, E.F. and Stitzer, S.N., 2002. Ferrite devices and materials. *IEEE Transactions on Microwave Theory and Techniques, 50(3),* pp.721-737.

[ADS, 2012] Advanced Design System (ADS). Santa Clara: Keysight Technologies; 2012. https://www.keysight.com/en/pc-1297113/advanced-design-system-ads?cc=GB&lc=eng

[Alaqil, 2018] Alaqil, H. and Hong, J., 2018. Tunable narrow bandwidth of a bandpass filter combined microstrip and suspended substrate stripline. *Microwave and Optical Technology Letters*, *60*(4), pp.983-987.

[Allen, 1961] Allen, J.E. and Segre, S.E., 1961. The electric field in single-turn and multi-sector coils. *Il Nuovo Cimento Series* 10, 21(6), pp.980-987.

[Al-Maznaee, 2007] Al-Maznaee, T. and Abd-El-Raouf, H.E., 2007, December. Design of reconfigurable patch antenna with a switchable V-slot. *In Applied Electromagnetics, 2007. APACE 2007. Asia-Pacific Conference on (pp. 1-5). IEEE.*

[Anand, 2013] Anand, A., Small, J., Peroulis, D. and Liu, X., 2013. Theory and design of octave tunable filters with lumped tuning elements. *IEEE Transactions on Microwave Theory and Techniques, 61(12),* pp.4353-4364.

[Atallah, 2015] Atallah, H.A., Abdel-Rahman, A.B., Yoshitomi, K. and Pokharel, R.K., 2015, December. Novel compact tunable bandpass filter using

capacitively loaded H-shaped resonator. In *Electronics, Circuits, and Systems (ICECS), 2015 IEEE International Conference on* (pp. 233-236). IEEE

[Baena, 2005] Baena, J.D., Bonache, J., Martin, F., Sillero, R.M., Falcone, F., Lopetegi, T., Laso, M.A., Garcia-Garcia, J., Gil, I., Portillo, M.F. and Sorolla, M., 2005. Equivalent-circuit models for split-ring resonators and complementary split-ring resonators coupled to planar transmission lines. *IEEE Transactions on microwave theory and techniques, 53(4), pp.1451-1461*.

[Bahadur, 1992] Bahadur, B. ed., 1992. *Liquid crystals: applications and uses* (Vol. 3, pp. 68-199). Singapore: World Scientific.

[Bahl, 2003] Bahl, I.J., 2003. *Lumped elements for RF and microwave circuits*. Artech house.

[Bao, 2008] Bao, P., Jackson, T.J., Wang, X. and Lancaster, M.J., 2008. Barium strontium titanate thin film varactors for room-temperature microwave device applications. Journal of Physics D: Applied Physics, 41(6), p.063001.

[Bashore, 2000] Bashore, F., 2000. RF Circuit Design: Theory and Applications. *Microwave Journal,* 43(3), pp.200-200.

[Beck, 1997] Beck, J.D., Canfield, B.L., Haddock, S.M., Chen, T.J.H., Kothari, M. and Keaveny, T.M., 1997. Three-dimensional imaging of trabecular bone using the computer numerically controlled milling technique. *Bone*, 21(3), pp.281-287.

[Berhard, 2006] Bernhard, J.T. and Balanis, C., 2006. Reconfigurable Antennas (Synthesis Lectures on Antennas and Propagation). *Morgan and Claypool.*

[Bernigaud, 2006] Bernigaud, J.F., Martin, N., Laurent, P., Quendo, C., Tanné, G., Della, B., Huret, F. and Gelin, P., 2006, September. Liquid crystal tunable

filter based on DBR topology. *In Microwave Conference, 2006. 36th European (pp. 368-371). IEEE.*

[Bilotti, 2007] Bilotti, F., Toscano, A. and Vegni, L., 2007. Design of spiral and multiple split-ring resonators for the realization of miniaturized metamaterial samples. *IEEE transactions on antennas and propagation*, *55*(8), pp.2258-2267.

[Bokhari, 1996] Bokhari, S.A., Zürcher, J.F., Mosig, J.R. and Gardiol, F.E., 1996. A small microstrip patch antenna with a convenient tuning option. *Antennas and Propagation, IEEE Transactions on,* 44(11), pp.1521-1528.

[Boutejdar, 2016] Boutejdar, A., 2016. Design of 5 GHz-compact reconfigurable DGS-bandpass filter using varactor-diode device and coupling matrix technique. *Microwave and Optical Technology Letters*, *58*(2), pp.304-309.

[Butt, 2009] Butt, K.A., Nadeem, A.E. and Hasan, A., 2009. A low cost RF oscillator incorporating a folded parallel coupled resonator. *Progress In Electromagnetics Research C,* 9, pp.75-88.

[Cameron, 2015] Cameron, R.J., Kudsia, C.M. and Mansour, R., 2015. *Microwave filters for communication systems*. John Wiley & Sons.

[Camley, 2018] Camley, R., Celinski, Z., Garbovskiy, Y. and Glushchenko, A., 2018. Liquid crystals for signal processing applications in the microwave and millimeter wave frequency ranges. Liquid Crystals Reviews, 6(1), pp.17-52.

[Chandrasekhar, 1992] Chandrasekhar, S., 1992. Liquid crystals. *Cambridge*

[Chang, 1996] Chang, K., 1996. Microwave ring circuits and antennas(Book). *New York: John Wiley & Sons, Inc, 1996.*

[Chaudhary, 2012] Chaudhary, G., Jeong, Y. and Lim, J., 2012. Harmonic suppressed dual-band bandpass filters with tunable passbands. I*EEE Transactions on Microwave Theory and Techniques, 60(7)*, pp.2115-2123.

[Chen, 2008] Chen, H.T., O'Hara, J.F., Azad, A.K., Taylor, A.J., Averitt, R.D., Shrekenhamer, D.B. and Padilla, W.J., 2008. Experimental demonstration of frequency-agile terahertz metamaterials. *Nature Photonics*, *2*(5), pp.295-298.

[Chen, 2009] Chen, H.T., Padilla, W.J., Cich, M.J., Azad, A.K., Averitt, R.D. and Taylor, A.J., 2009. A metamaterial solid-state terahertz phase modulator. *Nature Photonics*, *3*(3), pp.148-151.

[Chen, 2010] Chen, K., Chen, Z. and Zhu, L., 2010, May. Design of a high power digital tunable filter. *In Microwave and Millimeter Wave Technology (ICMMT), 2010 International Conference on (pp. 496-498). IEEE*.

[Cheng, 2011] Cheng, C.C. and Rebeiz, G.M., 2011. High-Q 4–6-GHz suspended stripline RF MEMS tunable filter with bandwidth control. *IEEE Transactions on Microwave Theory and Techniques, 59(10),* pp.2469-2476.

[Chigrinov, 1999] Chigrinov, V.G., 1999. *Liquid crystal devices: physics and applications.*

[Chin, 2008] Chin, J.Y., Lu, M. and Cui, T.J., 2008. Metamaterial polarizers by electric-field-coupled resonators. *Applied Physics Letters*, *93*(25), p.251903.

[Chiou, 2011] Chiou, Y.C. and Rebeiz, G.M., 2011. A tunable three-pole 1.5–2.2-GHz bandpass filter with bandwidth and transmission zero control. *IEEE Transactions on Microwave Theory and Techniques, 59(11)*, pp.2872-2878.

[Chrisostomidis, 2000] Chrisostomidis, C.E., Guglielmi, M., Young, P. and Lucyszyn, S., 2000, October. Application of chained functions to low-cost microwave band-pass filters using standard PCB etching techniques. *In Microwave Conference, 2000. 30th European* (pp. 1-4). IEEE.

[Chun, 2008] Chun, Y.H., Hong, J.S., Bao, P., Jackson, T.J. and Lancaster, M.J., 2008, June. BST varactor tuned bandstop filter with slotted ground structure. In *2008 IEEE MTT-S International Microwave Symposium Digest* (pp. 1115-1118). IEEE.

[Cohn, 1958] Cohn, S.B., 1958. Parallel-coupled transmission-line-resonator filters. *IRE Transactions on Microwave Theory and Techniques*, *6*(2), pp.223-231.

[Collings, 1997] Collings, P.J. and Hird, M., 1997. *Introduction to liquid crystals: chemistry and physics*. CRC Press.

[Cristal, 1972] Cristal, E.G. and Frankel, S., 1972. HairPin-Line and Hybrid HairF) in-Line/Half-Wave Parallel-Coupled-Line Filters. *IEEE Transactions on Microwave Theory and Techniques*, *20*(11).

[CST, 2017] CST Mirowave Studio. Paris: CST Computer Simulation Technology AG; 2017. www.cst.com.

[Daivd, 2005] David, M.P., 2005. Microwave engineering. *John Wiley&Son In*.

[Deo, 2015] Deo, P., Mirshekar-Syahkal, D., Seddon, L., Day, S.E. and Fernandez, F.A., 2015. Microstrip Device for Broadband (15–65 GHz) Measurement of Dielectric Properties of Nematic Liquid Crystals. *Microwave Theory and Techniques, IEEE Transactions on*, 63(4), pp.1388-1398.

[Dhouibi, 2012] Dhouibi, A., Burokur, S.N., De Lustrac, A. and Priou, A., 2012. Study and analysis of an electric Z-shaped meta-atom. *Advanced Electromagnetics,* 1(2), pp.64-70.

[Djoumessi, 2009] Djoumessi, E.E., Chaker, M. and Wu, K., 2009. Varactor-tuned quarter-wavelength dual-bandpass filter. *IET microwaves, antennas & propagation, 3(1)*, pp.117-124.

[Dolfi, 1993] Dolfi, D., Labeyrie, M., Joffre, P. and Huignard, J.P., 1993. Liquid crystal microwave phase shifter. Electronics Letters, 29(10), pp.926-928.

[Dussopt, 2003] Dussopt, L. and Rebeiz, G.M., 2003. Intermodulation distortion and power handling in RF MEMS switches, varactors, and tunable filters. *IEEE Transactions on Microwave Theory and Techniques, 51(4),* pp.1247-1256.

[Edwards, 1992] Edwards, T.C., 1992. *Foundations for microstrip circuit design*. John Wiley & Sons Incorporated.

[Fjerstad, 1970] Fjerstad, R.L., 1970. Some design considerations and realizations of iris-coupled YIG-tuned filters in the 12-40 GHz region. *IEEE Transactions on Microwave Theory and Techniques, 18(4),* pp.205-212.

[Fouladi, 2013] Fouladi, S., Huang, F., Yan, W.D. and Mansour, R.R., 2013. High-Q narrowband tunable combline bandpass filters using MEMS capacitor banks and piezomotors. *IEEE Transactions on Microwave Theory and Techniques, 61(1),* pp.393-402.

[Fourn, 2003] Fourn, E., Pothier, A., Champeaux, C., Tristant, P., Catherinot, A., Blondy, P., Tanné, G., Rius, E., Person, C. and Huret, F., 2003. MEMS switchable interdigital coplanar filter. *IEEE Transactions on microwave theory and techniques, 51(1)*, pp.320-324.

[Fritzsch, 2011] Fritzsch, C., Giacomozzi, F., Karabey, O.H., Goelden, F., Moessinger, A., Bildik, S., Colpo, S. and Jakoby, R., 2011, October. Continuously tunable W-band phase shifter based on liquid crystals and MEMS technology. *In Microwave Integrated Circuits Conference (EuMIC), 2011 European* (pp. 522-525). IEEE.

[Gaebler, 2008] Gaebler, A., Goelden, F., Mueller, S. and Jakoby, R., 2008, March. Efficiency considerations of tuneable liquid crystal microwave devices. *In Microwave Conference (GeMIC), 2008 German (pp. 1-4). VDE*.

[Gaebler, 2009] Gaebler, A., Moessinger, A., Goelden, F., Manabe, A., Goebel, M., Follmann, R., Koether, D., Modes, C., Kipka, A., Deckelmann, M. and Rabe, T., 2009. Liquid crystal-reconfigurable antenna concepts for space applications at microwave and millimeter waves. *International Journal of Antennas and Propagation,* 2009.

[Garbovskiy, 2011] Garbovskiy, Y., Reisman, L., Celinski, Z., Camley, R.E. and Glushchenko, A., 2011. Metallic surfaces as alignment layers for nondisplay applications of liquid crystals. Applied Physics Letters, 98(7), p.30.

[Garbovskiy, 2012] Garbovskiy, Y., Zagorodnii, V., Krivosik, P., Lovejoy, J., Camley, R.E., Celinski, Z., Glushchenko, A., Dziaduszek, J. and Dąbrowski, R., 2012. Liquid crystal phase shifters at millimeter wave frequencies. *Journal of Applied Physics,* 111(5), p.054504.

[Garg, 1978] Garg, R. and Bahl, I.J., 1978. Microstrip discontinuities. *International Journal of Electronics Theoretical and Experimental*, 45(1), pp.81-87.

[Genc, 2009] Genc, A. and Baktur, R., 2009. A tunable bandpass filter based on varactor loaded split-ring resonators. *Microwave and Optical Technology Letters, 51(10)*, pp.2394-2396.

[Gennes, 1995] Gennes, P.D., Prost, J. and Pelcovits, R., 1995. The physics of liquid crystals. *Physics Today,* 48(5), p.67.

[Gevorgian, 2001] Gevorgian, S. and Berg, H., 2001, September. Line capacitance and impedance of coplanar-strip waveguides on substrates with multiple dielectric layers. *In European Microwave Conference* (Vol. 31, pp. 153-156). Nexus Media Limited; 1996.

[Girbau, 2009] Girbau, D., Lázaro, A., Martínez, E., Masone, D. and Pradell, L., 2009. Tunable dual-band bandpass filter for WLAN applications. *Microwave and Optical Technology Letters, 51(9)*, pp.2025-2028.

[Goelden, 2009] Goelden, F., Gaebler, A., Goebel, M., Manabe, A., Mueller, S. and Jakoby, R., 2009. Tunable liquid crystal phase shifter for microwave frequencies. *Electronics letters,* 45(13), pp.686-687.

[Goelden, 2010] Goelden, F., Gaebler, A., Karabey, O., Goebel, M., Manabe, A. and Jakoby, R., 2010, March. Tunable band-pass filter based on liquid crystal. In *German Microwave Conference*, 2010 (pp. 98-101). IEEE.

[Goldsmith, 1999] Goldsmith, C.L., Malczewski, A., Yao, Z.J., Chen, S., Ehmke, J. and Hinzel, D.H., 1999. RF MEMS variable capacitors for tunable filters. *International Journal of RF and Microwave Computer-Aided Engineering: Co-sponsored by the Center for Advanced Manufacturing and Packaging of Microwave, Optical, and Digital Electronics (CAMPmode) at the University of Colorado at Boulder, 9(4),* pp.362-374.

[Gu, 2010] Gu, Q. and De Luis, J.R., 2010, November. RF MEMS tunable capacitor applications in mobile phones. *In Solid-State and Integrated Circuit Technology (ICSICT), 2010 10th IEEE International Conference on (pp. 635-638). IEEE*.

[Guillemin, 1957] Guillemin, E.A., 1957. *Introduction to Circuit Theory*.

[Gupta, 1996] Gupta, K.C., Garg, R., Bahl, I. and Bhartia, P., 1996. *Microstrip Lines ans Slotlines*.

[Hage-Ali, 2010] Hage-Ali, S., Tiercelin, N., Coquet, P., Sauleau, R., Preobrazhensky, V. and Pernod, P., 2010. A millimeter-wave frequency tunable microstrip antenna on ultraflexible PDMS substrate. *In 2010 IEEE Antennas and Propagation Society International Symposium.*

[Hand, 2009] Hand, T.H. and Cummer, S., 2009. Controllable magnetic metamaterial using digitally addressable split-ring resonators. *Antennas and Wireless Propagation Letters, IEEE*, *8*, pp.262-265.

[Hasan, 2008] Hasan, A. and Nadeem, A.E., 2008. Novel microstrip hairpinline narrowband bandpass filter using via ground holes. *Progress In Electromagnetics Research*, *78*, pp.393-419.

[Hashimoto, 2001] Hashimoto, K., Xu, H., Mukaigawa, T., Kubo, R., Zhu, H., Noda, M. and Okuyama, M., 2001. Si monolithic microbolometers of ferroelectric BST thin film combined with readout FET for uncooled infrared image sensor. *Sensors and Actuators A: Physical*, 88(1), pp.10-19.

[Hinojosa, 2017] Hinojosa, J., Saura-Ródenas, A., Alvarez-Melcon, A. and Martínez-Viviente, F.L., 2017. Electronically tunable microstrip bandstop filters using a varactor-loaded open ring resonator (VLORR). *Applied Physics A*, *123*(7), p.477.

[Hong, 1996] Hong, J.S. and Lancaster, M.J., 1996. End-coupled microstrip slow-wave resonator filter. Electronics Letters, 32(16), pp.1494-1496.

[Hong, 1998] Hong, J.S. and Lancaster, M.J., 1998. Cross-coupled microstrip hairpin-resonator filters. *IEEE Transactions on Microwave theory and techniques*, *46*(1), pp.118-122.

[Hong, 2000] Hong, J.S. and Lancaster, M.J., 2000, June. Microstrip triangular patch resonator filters. *In Microwave Symposium Digest. 2000 IEEE MTT-S International* (Vol. 1, pp. 331-334). IEEE.

[Hong, 2004] Hong, J.S.G. and Lancaster, M.J., 2004. *Microstrip filters for RF/microwave applications* (Vol. 167). John Wiley & Sons.

[Hornstein, 2005] Hornstein, M.K., Bajaj, V.S., Griffin, R.G., Kreischer, K.E., Mastovsky, I., Shapiro, M., Sirigiri, J.R. and Temkin, R.J., 2005. Second harmonic operation at 460 GHz and broadband continuous frequency tuning of a gyrotron oscillator. *Electron Devices, IEEE Transactions on*, 52(5), pp.798-807.

[Hu, 2006] Hu, W., Ismail, M.Y., Cahill, R., Gamble, H.S., Dickie, R., Fusco, V.F., Linton, D., Rea, S.P. and Grant, N., 2006. Tunable liquid crystal reflectarray patch element. *Electronics Letters*, 42(9), pp.509-511.

[Hu, 2007] Hu, W., Ismail, M.Y., Cahill, R., Encinar, J.A., Fusco, V.F., Gamble, H.S., Linton, D., Dickie, R., Grant, N. and Rea, S.P., 2007. Liquid-crystal-based reflectarray antenna with electronically switchable monopulse patterns. *Electronics Letters*, 43(14), pp.744-745.

[Hu,2008] Hu, W., Cahill, R., Encinar, J., Dickie, R., Gamble, H., Fusco, V. and Grant, N., 2008. Design and measurement of reconfigurable millimeter wave reflectarray cells with nematic liquid crystal. *Antennas and Propagation, IEEE Transactions on*, 56(10), pp.3112-3117.

[Huang, 2009] Huang, F. and Mansour, R.R., 2009, September. Tunable compact dielectric resonator filters. In *Microwave Conference, 2009. EuMC 2009. European* (pp. 559-562). IEEE.

[Huang, 2014] Huang, X., Feng, Q., Zhu, L., Xiang, Q. and Jia, D., 2014. Synthesis and design of tunable bandpass filters with constant absolute bandwidth using varactor-loaded microstrip resonator. *International Journal of RF and Microwave Computer-Aided Engineering*, *24*(6), pp.681-689.

[Ito, 2007] Ito, M., Sekine, N., Ishizaki, M., Kina, O. and Matsubara, R., Toppan Printing Co Ltd, 2007. *Structure, transmission type liquid crystal display, reflection type display and manufacturing method thereof*. U.S. Patent Application 11/786,494.

[Jabita, 2013] Jabita, A.N.A., 2013. *Design of singly split single ring resonator for measurement of dielectric constant of materials using resonant method*.

[Jakoby, 2012] Jakoby, R., 2012, October. Design and application of a liquid crystal varactor based tunable coupled line for polarization agile antennas. *In Microwave Conference (EuMC), 2012 42nd European* (pp. 739-742). IEEE.

[James, 2011] James, R., Fernández, F.A., Day, S.E., Bulja, S. and Mirshekar-Syahkal, D., 2011. Characterisation and Applications of Nematic Liquid Crystals in Microwave Devices. *Molecular Crystals and Liquid Crystals*, 542(1), pp.196-718.

[Jiang, 2011] Jiang, H., Lacroix, B., Choi, K., Wang, Y., Hunt, A.T. and Papapolymerou, J., 2011. Ka –and U-band tunable bandpass filters using ferroelectric capacitors. *IEEE Transactions on Microwave Theory and Techniques, 59(12),* pp.3068-3075.

[Kang, 2008] Kang, L., Zhao, Q., Zhao, H. and Zhou, J., 2008. Magnetic tuning of electrically resonant metamaterial with inclusion of ferrite. *Applied Physics Letters*, *93*(17), p.171909.

[Karabey, 2012a] Karabey, O.H., Bausch, S., Bildik, S., Strunck, S., Gaebler, A. and Jakoby, R., 2012, October. Design and application of a liquid crystal varactor based tunable coupled line for polarization agile antennas. *In Microwave Conference (EuMC), 2012 42nd European* (pp. 739-742). IEEE.

[Karabey, 2012b] Karabey, O.H., Gaebler, A., Strunck, S. and Jakoby, R., 2012. A 2-D electronically steered phased-array antenna with 2 2 elements in LC display technology. *Microwave Theory and Techniques, IEEE Transactions on*, 60(5), pp.1297-1306.

[Karabey, 2014] Karabey, O.H., 2014. Liquid crystal material for microwave applications. *In Electronic Beam Steering and Polarization Agile Planar Antennas in Liquid Crystal Technology* (pp. 9-25). Springer, Cham.

[Kelker, 1980] Kelker, H. and Hatz, R., 1980. *Handbook of liquid crystals*. Wiley-VCH.

[Khodasevych, 2012] Khodasevych, I., Rowe, W.S. and Mitchell, A., 2012. Reconfigurable fishnet metamaterial using pneumatic actuation. *Progress In Electromagnetics Research* B, 38, pp.57-70.

[Kim, 1999] Kim, H.T., Park, J.H., Kim, Y.K. and Kwon, Y., 1999, June. Millimeter-wave micromachined tunable filters. *In Microwave Symposium Digest, 1999 IEEE MTT-S International (Vol. 3, pp. 1235-1238). IEEE*.

[Kim, 2002] Kim, H.T., Park, J.H., Kim, Y.K. and Kwon, Y., 2002. Low-loss and compact V-band MEMS-based analog tunable bandpass filters. *IEEE Microwave and Wireless Components Letters, 12(11),* pp.432-434.

[Kirschning, 1981] Kirschning, M., Jansen, R.H. and Koster, N.H.L., 1981. Accurate model for open end effect of microstrip lines. *Electronics Letters,* 17(3), pp.123-125.

[Koenigsberger, 2013] Koenigsberger, F. and Tlusty, J., 2013. *Machine tool structures* (Vol. 1). Elsevier.

[Koochakzadeh, 2007] Koochakzadeh, M. and Abbaspour-Tamijani, A., 2007, June. Switchable bandpass filter for 0.3-0.6 GHz. *In Microwave Symposium, 2007. IEEE/MTT-S International (pp. 557-560). IEEE.*

[Kumar, 2017] Kumar, A. and Pathak, N.P., 2017. Varactor-incorporated bandpass filter with reconfigurable frequency and bandwidth. *Microwave and Optical Technology Letters*, *59*(8), pp.2083-2089.

[Kumar, 2013a] Kumar, A., Arya, D. and Srivastava, D.K., 2013, November. Band width of microstrip antenna improved by using mushroom type EBG

structure. *In Multimedia, Signal Processing and Communication Technologies (IMPACT), 2013 International Conference on* (pp. 159-162). IEEE.

[Kumar, 2013b] Kumar, D. and De, A., 2013. Effective Size Reduction Technique for Microstrip Filters. *Journal of Electromagnetic Analysis and Applications*, *5*(04), p.166.

[Jia, 2013] Jia, D.H., Feng, Q., Huang, X.G. and Xiang, Q.Y., 2013. A novel tri-mode bandwidth tunable filter with harmonic suppression. *Progress In Electromagnetics Research C*, 34, pp.183-194.

[Lakshminarayanan,2003] Lakshminarayanan, B. and Weller, T., 2003, June. Tunable bandpass filter using distributed MEMS transmission lines. *In Microwave Symposium Digest, 2003 IEEE MTT-S International (Vol. 3, pp. 1789-1792). IEEE*.

[Lee, 2000] Lee, S.Y. and Tsai, C.M., 2000. New cross-coupled filter design using improved hairpin resonators. *IEEE Transactions on Microwave theory and Techniques*, *48*(12), pp.2482-2490.

[Lee. 2002] Lee, Y.T., Lim, J.S., Kim, C.S., Ahn, D. and Nam, S., 2002. A compact-size microstrip spiral resonator and its application to microwave oscillator. *Microwave and Wireless Components Letters, IEEE*, 12(10), pp.375-377.

[Lee, 2004] Lee, T.H., 2004. *Planar microwave engineering: a practical guide to theory, measurement, and circuits* (Vol. 1). Cambridge University Press.

[Lei, 2012] Lei, M., 2012. *Printing Alignment for Liquid Crystal Devices for Microwave Applications.* MSc. University College London

[Li, 2012] Li, Q. ed., 2012. *Liquid crystals beyond displays: chemistry, physics, and applications*. John Wiley & Sons.

[Li, 2014] Li, C., Bian, Y., Li, G., Wu, Y., Wang, J., Wang, X., Zhang, X., Xia, F., Bai, D., Sun, L. and Li, H., 2014. A tunable high temperature superconducting bandpass filter realized using semiconductor varactors. *IEEE Trans. Appl. Supercond., 24(5)*, pp.1-5.

[Li, 2015] Li, J.S., Liu, H. and Zhang, L., 2015. Compact and tunable-multichannel terahertz wave filter. *IEEE Transactions on Terahertz Science and Technology*, *5*(4), pp.551-555.

[Liu, 2008] Liu, L. and Langley, R.J., 2008. Liquid crystal tunable microstrip patch antenna. *Electronics Letters*, 44(20), pp.1179-1181.

[Liu, 2015] Liu, X., 2015, April. Tunable RF and microwave filters. *In Wireless and Microwave Technology Conference (WAMICON), 2015 IEEE 16th Annual (pp. 1-5). IEEE*.

[LKPF, 2016] LKPF, 2016. *Micro-material processing with the LPKF ProtoLaser U3.* [pdf] Available at:< http://www.lpkfusa.com/datasheets/prototyping/317-lpkf-protolaser-u3.pdf> [Accessed 1 January, 2016]

[Long, 2011] Long, J., Li, C., Cui, W., Huangfu, J. and Ran, L., 2011. A tunable microstrip bandpass filter with two independently adjustable transmission zeros. *IEEE Microwave and Wireless Components Letters, 21(2),* pp.74-76.

[Ludwig, 2000] Ludwig, R., 2000. *RF Circuit Design: Theory & Applications, 2/e*. Pearson Education India.

[Makimoto, 1980] Makimoto, M. and Yamashita, S., 1980. Bandpass filters using parallel coupled stripline stepped impedance resonators. *IEEE Transactions on Microwave Theory and Techniques*, *28*(12), pp.1413-1417.

[Martin, 203] Martin, N., Laurent, P., Person, C., Gelin, P. and Huret, F., 2003, October. Patch antenna adjustable in frequency using liquid crystal. *In Microwave Conference, 2003. 33rd European* (Vol. 2, pp. 699-702). IEEE.

[Martin, 2004a] Martin, N., Laurent, P., Person, C., Gelin, P. and Huret, F., 2004, October. Size reduction of a liquid crystal-based, frequency-adjustable patch antenna. *In Microwave Conference*, *2004. 34th European* (Vol. 2, pp. 825-828). IEEE.

[Martin, 2004b] Martin, N., Laurent, P., Prigent, G., Gelin, P. and Huret, F., 2004. Technological evolution and performances improvements of a tunable phase-shifter using liquid crystal. *Microwave and optical technology letters*, 43(4), pp.338-341.

[Marin, 2005] Marin, R., Mössinger, A., Freese, J., Müller, S. and Jakoby, R., 2005, October. Basic investigations of 35 GHz reflectarrays and tunable unit-cells for beamsteering applications. *In Radar Conference, 2005. EURAD 2005. European* (pp. 291-294). IEEE.

[Marin, 2006] Marin, R., Freese, J., Manabe, A. and Jakoby, R., 2006, July. Realization of 35 GHz steerable reflectarray using highly anisotropic liquid crystal. *In Antennas and Propagation Society International Symposium 2006, IEEE* (pp. 4307-4310). IEEE.

[Matthaei, 1963] Matthaei, G.L., Young, L. and Jones, E.M., 1963. *DESIGN OF MICROWAVE FILTERS, IMPEDANCE-MATCHING NETWORKS, AND COUPLING STRUCTURES*. VOLUME 2. STANFORD RESEARCH INST MENLO PARK CA.

[Maune, 2003] Maune, B., Lawson, R., Gunn, C., Scherer, A. and Dalton, L., 2003. Electrically tunable ring resonators incorporating nematic liquid crystals as cladding layers. *Applied physics letters*, *83*(23), pp.4689-4691.#

[Mirfatah, 2009] Mirfatah, A. and Laurin, J.J., 2009. Tunable hairpin resonator based on liquid crystal. In 2009 *13th International Symposium on Antenna Technology and Applied Electromagnetics and the Canadian Radio Science Meeting.*

[Missaoui, 2011] Missaoui, S., Kaddour, M. and Gharbi, A., 2011. Design and simulation of tunable phase shifters based on liquid crystals. *Electromagnetics*, 31(4), pp.285-293.

[Missaoui, 2012] Missaoui, S. and Kaddour, M., 2012. Liquid crystal-reconfigurable conformal monopole antennas structures for microwave applications. J. *Eng. Technol*. Res, 3, pp.57-64.

[Meier, 2012] Meier, G., Sackmann, E. and Grabmaier, J.G., 2012. *Applications of liquid crystals*. Springer Science & Business Media.

[Moessinger, 206] Moessinger, A., Marin, R., Freese, J., Mueller, S., Manabe, A. and Jakoby, R., 2006, November. Investigations on 77 GHz tunable reflectarray unit cells with liquid crystal. *In Antennas and Propagation, 2006. EuCAP 2006. First European Conference on* (pp. 1-4). IEEE.

[Moessinger, 2010] Moessinger, A., Fritzsch, C., Bildik, S. and Jakoby, R., 2010, May. Compact tunable Ka-band phase shifter based on liquid crystals. *In Microwave Symposium Digest (MTT), 2010 IEEE MTT-S International (pp. 1020-1023). IEEE.*

[Montgomery, 1948] Montgomery, C.G., Dicke, R.H. and Purcell, E.M., 1948. *Principles of microwave circuits* (No. 25). Iet.

[Müller, 2004] Müller, S., Scheele, P., Wei, C., Wittek, M., Hock, C. and Jakoby, R., 2004, June. Tunable passive phase shifter for microwave applications using highly anisotropic liquid crystals. *In Microwave Symposium Digest, 2004 IEEE MTT-S International* (Vol. 2, pp. 1153-1156). IEEE.

[Mueller, 2006] Mueller, S., Goelden, F., Scheele, P., Wittek, M., Hock, C. and Jakoby, R., 2006, September. Passive phase shifter for W-band applications using liquid crystals. *In Microwave Conference*, 2006. 36th European (pp. 306-309). IEEE.

[Mueller, 2008] Mueller, S., Koeberle, M., Goelden, F., Penirschke, A., Gaebler, A., Lapanik, A., Haase, W. and Jakoby, R., 2008, October. W-band characterization of anisotropic liquid crystals at room temperature. *In Microwave Conference, 2008. EuMC 2008. 38th European* (pp. 119-122). IEEE.

[Munir, 2016] Munir, A., 2016, September. Development of dual-band microstrip bandpass filter based on split ring resonator. In *Electromagnetics in Advanced Applications (ICEAA), 2016 International Conference on* (pp. 712-715). IEEE.

[Mutalib, 2016] Mutalib, M.A., Zakaria, Z., Shairi, N.A. and Sam, W.Y., 2016, April. Design of microstrip bandpass filter with electronically tunable notch response. In *Radioelektronika (RADIOELEKTRONIKA), 2016 26th International Conference* (pp. 454-457). IEEE.

[Naglich, 2012] Naglich, E.J., Lee, J., Peroulis, D. and Chappell, W.J., 2012. Switchless tunable bandstop-to-all-pass reconfigurable filter. *IEEE Transactions on Microwave Theory and Techniques*, *60*(5), pp.1258-1265.

[Nakhlestani, 2013] Nakhlestani, A. and Hakimi, A., 2013. Wideband microstrip ring resonator bandpass filter with embedded rings. *Microelectronics Journal*, *44*(5), pp.462-467.

[Naoui, 2016] Naoui, S., Latrach, L. and Gharsallah, A., 2016. Equivalent circuit model of double split ring resonators. *INTERNATIONAL JOURNAL*, *11*(1), p.1.

[Nath, 2005] Nath, J., Ghosh, D., Maria, J.P., Kingon, A.I., Fathelbab, W., Franzon, P.D. and Steer, M.B., 2005. An electronically tunable microstrip bandpass filter using thin-film Barium-Strontium-Titanate (BST) varactors. *IEEE Transactions on Microwave Theory and Techniques*, *53*(9), pp.2707-2712.

[Ni, 2013] Ni, J. and Hong, J., 2013. Varactor-tuned microstrip bandpass filters with different passband characteristics. *IET Microwaves, Antennas & Propagation*, *8*(6), pp.415-422.

[Ni, 2014] Ni, J., Tang, W., Hong, J. and Geschke, R.H., 2014. Design of microstrip lossy filter using an extended doublet topology. IEEE Microwave and Wireless Components Letters, 24(5), pp.318-320.

[Olokede, 2017] Olokede, S.S. and Paul, B.S., 2017, May. Design of a narrow-band microstrip ring resonator bandpass filter. In *Progress In Electromagnetics Research Symposium-Spring (PIERS), 2017* (pp. 1835-1841). IEEE.

[Osadchiy, 2003] Osadchy, V., DuToit, C.F., Sengupta, L.C. and Kozyrev, A., BlackBerry RF Inc, 2003. *Microstrip phase shifter*. U.S. Patent 6,621,377.

[Owens, 1976] Owens, R.P., 1976. Curvature effect in microstrip ring resonators. *Electronics letters*, 12(14), pp.356-357.

[Pandey, 2014] Pandey, G.P., Kanaujia, B.K., Gupta, S.K. and Gautam, A.K., 2014. CSRR loaded tunable L-strip fed circular microstrip antenna. *Wireless personal communications, 74(2), pp.717-730.*

[Perez-Palomino, 2012] Perez-Palomino, G., Encinar, J.A., Barba, M. and Carrasco, E., 2012. Design and evaluation of multi-resonant unit cells based on liquid crystals for reconfigurable reflectarrays. *IET microwaves, antennas & propagation*, 6(3), pp.348-354.

[Perez-Palomino, 2013] Perez-Palomino, G., Baine, P., Dickie, R., Bain, M., Encinar, J.A., Cahill, R., Barba, M. and Toso, G., 2013. Design and experimental validation of liquid crystal-based reconfigurable reflectarray elements with improved bandwidth in F-band. Antennas and Propagation, *IEEE Transactions on,* 61(4), pp.1704-1713.

[Peroulis, 2001] Peroulis, D., Pacheco, S., Sarabandi, K. and Katehi, L.P., 2001, May. Tunable lumped components with applications to reconfigurable MEMS filters. *In Microwave Symposium Digest, 2001 IEEE MTT-S International (Vol. 1, pp. 341-344). IEEE*.

[Peroulis, 2005] Peroulis, D., Sarabandi, K. and Katehi, L.P., 2005. Design of reconfigurable slot antennas. *Antennas and Propagation, IEEE Transactions on*, 53(2), pp.645-654.

[Petosa, 2010] Petosa, A., 2010, July. Frequency agile antennas for wireless communications–A survey. *In 2010 14th International Symposium on Antenna Technology and Applied Electromagnetics&the American Electromagnetics Conference.*

[Petosa, 2012] Petosa, A., 2012. An overview of tuning techniques for frequency-agile antennas. *IEEE Antennas and Propagation Magazine*, 5(54), pp.271-296.

[Pothier, 2005] Pothier, A., Orlianges, J.C., Zheng, G., Champeaux, C., Catherinot, A., Cros, D., Blondy, P. and Papapolymerou, J., 2005. Low-loss 2-bit tunable bandpass filters using MEMS DC contact switches. I*EEE Transactions on Microwave Theory and Techniques, 53(1)*, pp.354-360.

[Poole, 2015] Poole, C. and Darwazeh, I., 2015. *Microwave active circuit analysis and design*. Academic Press.

[Pozar, 2005] Pozar, D.M., 2005. Microwave Engineering 3e. *Tramsmission Lines and Waveguides*, pp.143-149.

[Priestly, 2012] Priestly, E., 2012. *Introduction to liquid crystals*. Springer Science & Business Media.

[Prost, 1995] Prost, J., 1995. The physics of liquid crystals (No. 83). *Oxford university press.*

[Rebeiz, 2004] Rebeiz, G.M., 2004. *RF MEMS: theory, design, and technology*. John Wiley & Sons.

[Rebeiz, 2009] Rebeiz, G.M., Entesari, K., Reines, I.C., Park, S.J., El-Tanani, M.A., Grichener, A. and Brown, A.R., 2009. Tuning in to RF MEMS. *IEEE microwave magazine, 10(6)*.

[Rhodes, 1976] Rhodes, J.D., 1976. *Theory of electrical filters*. Wiley.

[Sagawa, 1989] Sagawa, M., Takahashi, K. and Makimoto, M., 1989. Miniaturized hairpin resonator filters and their application to receiver front-end MICs. *IEEE Transactions on Microwave Theory and Techniques*, *37*(12), pp.1991-1997.

[Salleh, 2008a] Salleh, M.K.M., Prigent, G., Pigaglio, O. and Crampagne, R., 2008. Synthesis of quarter wavelength side-coupled ring (QSCR) resonator applications to bandpass filters design. *Microwave and Optical Technology Letters*, *50*(2), pp.307-312.

[Salleh, 2008b] Salleh, M.K.M., Prigent, G., Pigaglio, O. and Crampagne, R., 2008. Quarter-wavelength side-coupled ring resonator for bandpass filters. *IEEE Transactions on Microwave Theory and Techniques*, *56*(1), pp.156-162.

[Salleh, 2008c] Salleh, M.K.M., Prigen, G., Vu, T.M. and Crampagne, R., 2008, December. Synthesis of tuneable ring-based bandpass filter. In *Microwave Conference, 2008. APMC 2008. Asia-Pacific* (pp. 1-4). IEEE.

[Sánchez-Renedo, 2005] Sánchez-Renedo, M., Gómez-García, R., Alonso, J.I. and Briso-Rodríguez, C., 2005. Tunable combline filter with continuous control of center frequency and bandwidth. *IEEE Transactions on Microwave Theory and Techniques*, *53*(1), pp.191-199.

[Sankarasubramaniam, 2007] Sankarasubramaniam, A., Shastry, P.N. and Katragadda, K., 2007. Design guidelines for tunable coplanar and microstrip patch antennas. *In 2007 European Microwave Integrated Circuit Conference.*

[Schaub, 2011] Schaub, D.E. and Oliver, D.R., 2011. A circular patch resonator for the measurement of microwave permittivity of nematic liquid crystal. *Microwave Theory and Techniques, IEEE Transactions on*, 59(7), pp.1855-1862.

[Schurig, 2006] Schurig, D., Mock, J.J. and Smith, D.R., 2006. Electric-field-coupled resonators for negative permittivity metamaterials. *Applied Physics Letters*, 88(4), p.041109.

[Singh, 2015] Singh, D.K., Kanaujia, B.K., Dwari, S., Pandey, G.P. and Kumar, S., 2015. Complementary Split Ring Resonator Based Compact Wideband Microstrip Antenna with Tunable Bands. *Wireless Personal Communications*, *80*(2), pp.635-645.

[Shafai, 2004] Shafai, C., Sharma, S.K., Shafai, L. and Chrusch, D.D., 2004. Microstrip phase shifter using ground-plane reconfiguration. *IEEE transactions on microwave theory and techniques,* 52(1), pp.144-153.

[Shimoda, 2001] Shimoda, Y., Ozaki, M. and Yoshino, K., 2001. Electric field tuning of a stop band in a reflection spectrum of synthetic opal infiltrated with nematic liquid crystal. *Applied Physics Letters*, 79(22), pp.3627-3629.

[Shrestha, 2012] Shrestha, B. and Kim, N.Y., 2012. Spurline resonators design and its implementation to microwave oscillators. *Microwave and Optical Technology Letters*, 54(1), pp.171-176.

[Skulski, 2013] Skulski, J. and Szymańska, A., 2013, July. Liquid crystal tunable microwave band stop filters. In Electron Technology Conference 2013 (pp. 89022E-89022E). *International Society for Optics and Photonics.*

[Stewart, 1956] Stewart, J.L., 1956. *Circuit theory and design*. John Wiley and Sons.

[Sun, 2007] Sun, S. and Zhu, L., 2007. Wideband microstrip ring resonator bandpass filters under multiple resonances. *IEEE Transactions on Microwave theory and techniques*, *55*(10), pp.2176-2182.

[Swanson, 2007] Swanson, D. and Macchiarella, G., 2007. Microwave filter design by synthesis and optimization. *IEEE Microwave Magazine*, 8(2), pp.55-69.

[Sydoruk, 2008] Sydoruk, O., Tatartschuk, E., Shamonina, E. and Solymar, L., 2008. Resonant frequency of singly split single ring resonators: An analytical and numerical study.

[Tao, 2008] Tao, H., Landy, N.I., Bingham, C.M., Zhang, X., Averitt, R.D. and Padilla, W.J., 2008. A metamaterial absorber for the terahertz regime: Design, fabrication and characterization. *Optics express*, 16(10), pp.7181-7188.

[Temes, 1973] Temes, G.C. and Mitra, S.K., 1973. *Modern filter theory and design*. John Wiley & Sons.

[Temes, 1977] Temes, G.C. and LaPatra, J.W., 1977. *Introduction to circuit synthesis and design*. McGraw-Hill Companies.

[Tombak, 2002] Tombak, A., Maria, J.P., Ayguavives, F., Jin, Z., Stauf, G.T., Kingon, A.I. and Mortazawi, A., 2002. Tunable barium strontium titanate thin film capacitors for RF and microwave applications. *IEEE Microwave and wireless components letters, 12(1)*, pp.3-5.

[Torrecilla, 2013a] Torrecilla, J., Avila-Navarro, E., Marcos, C., Urruchi, V., Sanchez-Pena, J.M., Arias, J. and Sanchez-Lopez, M.M., 2013. Microwave Tunable Notch Filter Based on Liquid Crystal Using Spiral Spurline Technology. *Microwave and Optical Technology Letters*, 55(10), pp.2420-2423.

[Torrecilla, 2013b] Torrecilla, J., Marcos, C., Urruchi, V. and Sanchez-Pena, J.M., 2013, October. Tunable dual-mode bandpass filter based on liquid crystal technology. *In Microwave Conference (EuMC), 2013 European (pp. 806-809). IEEE.*

[Torrecilla, 2014] Torrecilla, J., Urruchi, V., Sánchez-Pena, J.M., Bennis, N., García, A. and Segovia, D., 2014. Improving the Pass-Band Return Loss in Liquid Crystal Dual-Mode Bandpass Filters by Microstrip Patch Reshaping. *Materials*, 7(6), pp.4524-4535.

[Tsai, 1999] Tsai, M.S., Sun, S.C. and Tseng, T.Y., 1999. Effect of bottom electrode materials on the electrical and reliability characteristics of (Ba, Sr) TiO/sub 3/capacitors. *IEEE Transactions on electron devices, 46(9)*, pp.1829-1838.

[Tsai, 2009] Tsai, C.S. and Qiu, G., 2009. Wideband microwave filters using ferromagnetic resonance tuning in flip-chip YIG-GaAs layer structures. *IEEE Transactions on Magnetics, 45(2),* pp.656-660.

[Tu, 2008] Tu, W.H., 2008. Compact microstrip bandpass filter using modified stepped-impedance hairpin resonator. *Microwave and Optical Technology Letters*, *50*(8), pp.2007-2010.

[Uher, 1991] Uher, J. and Hoefer, W.J., 1991. Tunable microwave and millimeter-wave band-pass filters. *IEEE Transactions on Microwave Theory and Techniques, 39(4)*, pp.643-653.

[Urruchi, 20013] Urruchi, V., Marcos, C., Torrecilla, J., Sánchez-Pena, J.M. and Garbat, K., 2013. Note: Tunable notch filter based on liquid crystal technology for microwave applications. R*eview of Scientific Instruments*, 84(2), p.026102.

[Varactor, 2018] Varactor / varicap diode, www.radio-electronics.com.

[Varadan, 1999] Varadan, V.K., Jose, K.A. and Varadan, V.V., 1999. Design and development of electronically tunable microstrip antennas. *Smart materials and structures*, 8(2), p.238.

[Vendik, 1999] Vendik, O.G., Hollmann, E.K., Kozyrev, A.B. and Prudan, A.M., 1999. Ferroelectric tuning of planar and bulk microwave devices. *Journal of Superconductivity, 12(2)*, pp.325-338.

[Vorobiev, 2003] Vorobiev, A., Rundqvist, P., Khamchane, K. and Gevorgian, S., 2003. Silicon substrate integrated high Q-factor parallel-plate ferroelectric varactors for microwave/millimeterwave applications. *Applied Physics Letters, 83(15),* pp.3144-3146.

[Wadell, 1991] Wadell, B.C., 1991. *Transmission line design handbook*. Artech House.

[Wahab, 2010] Wahab, N.A., Muhamad, W.N.W., Hamzah, M.M.A.M., Sarnin, S.S. and Naim, N.F., 2010, June. Design a microstrip hairpin band-pass filter for 5GHZ unlicensed WiMAX. In *Networking and Information Technology (ICNIT), 2010 International Conference on* (pp. 183-186). IEEE.

[Wang, 2007] Wang, C. and Zaki, K.A., 2007. Dielectric resonators and filters. *IEEE microwave magazine, 8(5),* pp.115-127.

[Wang, 2008] Wang, X.C., Li, Z.L., Chen, T., Lok, B.K. and Low, D.K.Y., 2008. 355nm DPSS UV laser cutting of FR4 and BT/epoxy-based PCB substrates. *Optics and lasers in engineering*, 46(5), pp.404-409.

[Wang, 2011] Wang, X., Bao, P., Jackson, T.J. and Lancaster, M.J., 2011. Tunable microwave filters based on discrete ferroelectric and semiconductor varactors. IET microwaves, antennas & propagation, 5(7), pp.776-782.

[Weil, 2002] Weil, C., Luessem, G. and Jakoby, R., 2002, June. Tunable inverted-microstrip phase shifter device using nematic liquid crystals. *In Microwave Symposium Digest, 2002 IEEE MTT-S International (Vol. 1, pp. 367-371). IEEE*.

[Weil, 2003] Weil, C., Scheele, P., Best, P., Lüssem, G. and Jakoby, R., 2003. Highly-anisotropic liquid-crystal mixtures for tunable microwave devices. *Electronics letters*, 39(24), pp.1732-1734.

[Willman, 2007] Willman, E., Fernández, F.A., James, R. and Day, S.E., 2007. Modeling of weak anisotropic anchoring of nematic liquid crystals in the Landau-de Gennes theory. *IEEE T ELECTRON DEV*, *54*(10), pp.2630-2637.

[Withayachumnankul, 2010] Withayachumnankul, W., Fumeaux, C. and Abbott, D., 2010. Compact electric-LC resonators for metamaterials. *Optics express*, 18(25), pp.25912-25921.

[Wolff, 1971] Wolff, I. and Knoppik, N., 1971. Microstrip ring resonator and dispersion measurement on microstrip lines. *Electronics Letters*, *7*(26), pp.779-781.

[Wu, 2005] Wu, Q., Wu, M.F., Meng, F.Y., Wu, J. and Li, L.W., 2005. Modeling the effects of an individual SRR by equivalent circuit method. In *Antennas and Propagation Society International Symposium, 2005 IEEE* (Vol. 1, pp. 631-634). IEEE.

[Wu, 2006] Wu, B., Li, B., Su, T. and Liang, C.H., 2006. Study on transmission characteristic of split-ring resonator defected ground structure. *PIERS online*, *2*(6), pp.710-714.

[Yaghmaee, 2012a] Yaghmaee, P., Fumeaux, C., Bates, B., Manabe, A., Karabey, O.H. and Jakoby, R., 2012. Frequency tunable S-band resonator using nematic liquid crystal. *Electronics letters*, 48(13), pp.798-800.

[Yaghmaee, 2012b] Yaghmaee, P., Kaufmann, T., Bates, B. and Fumeaux, C., 2012, March. Effect of polyimide layers on the permittivity tuning range of liquid crystals. In Antennas and Propagation (EUCAP), 2012 6th European Conference on (pp. 3579-3582). IEEE.

[Yaghmaee, 2013] Yaghmaee, P., Karabey, O.H., Bates, B., Fumeaux, C. and Jakoby, R., 2013. Electrically tuned microwave devices using liquid crystal technology. International Journal of Antennas and Propagation, 2013.

[Yang, 2009] Yang, G.M., Xing, X., Daigle, A., Liu, M., Obi, O., Stoute, S., Naishadham, K. and Sun, N.X., 2009. Tunable miniaturized patch antennas with self-biased multilayer magnetic films. A*ntennas and Propagation, IEEE Transactions on*, 57(7), pp.2190-2193.

[Yang, 2010] Yang, Q., Xiong, X.Z., Wu, Y.L., Wang, L.P. and Xiao, H.Q., 2010, May. Design of microstrip tapped-hairpin dual-band pass filter for Ku-band application. In *Microwave and Millimeter Wave Technology (ICMMT), 2010 International Conference on* (pp. 772-774). IEEE.

[Yang, 2014] Yang, D.K., 2014. *Fundamentals of liquid crystal devices*. John Wiley & Sons.

[Yasar-Orten, 2010] Yasar-Orten, P., Ekmekci, E. and Turhan-Sayan, G., 2010, July. Equivalent circuit models for split-ring resonator arrays. In *PIERS Proceedings* (pp. 534-537).

[Yazdanpanahi, 2010] Yazdanpanahi, M., Bulja, S., Mirshekar-Syahkal, D., James, R., Day, S.E. and Fernandez, F.A., 2010. Measurement of dielectric constants of nematic liquid crystals at mm-wave frequencies using patch

resonator. Instrumentation and Measurement, *IEEE Transactions on*, 59(12), pp.3079-3085.

[Yazdanpanahi, 2012] Yazdanpanahi, M. and Mirshekar-Syahkal, D., 2012, January. Millimeter-wave liquid-crystal-based tunable bandpass filter. *In Radio and Wireless Symposium (RWS), 2012 IEEE (pp. 139-142). IEEE.*

[Yi, 2009] Yi, X. and Minasian, R.A., 2009. Microwave photonic filter with single bandpass response. *Electronics letters*, 45(7), pp.362-363.

[Yu, 1997] Yu, C.C. and Chang, K., 1997. Transmission-line analysis of a capacitively coupled microstrip-ring resonator. *Microwave Theory and Techniques, IEEE Transactions on*, 45(11), pp.2018-2024.

[Yun, 2002] Yun, T.Y. and Chang, K., 2002. Piezoelectric-transducer-controlled tunable microwave circuits. *IEEE Transactions on Microwave Theory and Techniques*, *50*(5), pp.1303-1310.

[Yunker, 2011] Yunker, P.J., Still, T., Lohr, M.A. and Yodh, A.G., 2011. Suppression of the coffee-ring effect by shape-dependent capillary interactions. *Nature*, 476(7360), pp.308-311.

[Zhang, 2008] Zhang, X.Y. and Xue, Q., 2008. Novel centrally loaded resonators and their applications to bandpass filters. *IEEE Transactions on Microwave Theory and Techniques, 56(4),* pp.913-921.

[Zhang, 2012] Zhang, X.Y., Chan, C.H., Xue, Q. and Hu, B.J., 2012. RF tunable bandstop filters with constant bandwidth based on a doublet configuration. *IEEE Transactions on Industrial Electronics*, *59*(2), p.1257.

[Zhang, 2016] Zhang, D., Xiang, Q.Y., Fu, M.Y., Tian, D.Y. and Feng, Q.Y., 2016, August. A constant absolute bandwidth tunable bandpass filter based on mixed coupled varactor loaded open ring resonators. *In Progress in Electromagnetic Research Symposium (PIERS) (pp. 3464-3467). IEEE*.

[Zhu, 2010] Zhu, B., Feng, Y., Zhao, J., Huang, C. and Jiang, T., 2010. Switchable metamaterial reflector/absorber for different polarized electromagnetic waves. *Applied Physics Letters*, *97*(5), p.051906.

[Ziolkowski, 2003] Ziolkowski, R.W. and Engheta, N., 2003. Metamaterial special issue introduction. *Antennas and Propagation, IEEE Transactions on*, *51*(10), pp.2546-2549.